I. Dynamics of Subduction Initiation
and
II. Constraining Sedimentary Basin Structure with Seismic Ambient Noise

Thesis by
Yida Li

In Partial Fulfillment of the Requirements for the
degree of
Doctor of Philosophy

CALIFORNIA INSTITUTE OF TECHNOLOGY
Pasadena, California

2023
Defended November 17

© 2023

Yida Li
ORCID: 0000-0003-0664-0247

All rights reserved except where otherwise noted

ACKNOWLEDGEMENTS

My five-year doctoral journey at Caltech has been an invaluable chapter in my life. I'm fortunate to have met with so many exceptional individuals during my time at Caltech, and I want to extend my gratitude to each one of them.

First and foremost, I wish to express my deepest appreciation to my primary advisor, Mike Gurnis. Mike has been not only my academic mentor but also a guiding light in the field of geodynamics. His academic enthusiasm and wisdom have a life-long impact on my career. I am continually inspired by Mike's philosophy that geodynamics is not just a study of modelling; but also a study of data analysis. Without Mike's mentorship, this thesis couldn't have been possible.

Secondly, I want to extend my sincere thanks to my secondary advisor, Rob Clayton. Rob introduced me to the world of seismology and patiently steered me through each step of my research project, and his mentorship allowed me a remarkable degree of freedom to explore my research interests. It was a joyful and rewarding experience to work with Rob.

I would like to thank Joann Stock for her role as my academic advisor and for teaching the plate tectonics. Our discussions and coursework greatly enriched my understanding of my Puysegur project. My gratitude also goes to Zach Ross for serving as a committee member and for his insightful courses on machine learning and seismicity. I also want to thank many faculty members in the Seismo Lab, including Zhongwen, Jennifer, Mark, and many others, from whom I learned a lot during the courses, seminars and coffee hours. I am appreciative of Donna, Rosemary, Kim, Scott, Ken, and the entire Caltech staff for their support and consideration throughout my journey.

I'd also like to extend my gratitude to my undergraduate advisor, Wei Leng, who introduced me to the field of Geodynamics during my earlier academic journey. Special thanks to Chris Grose, my mentor during my summer internship at Caltech. That initial research experience during my undergraduate studies solidified my commitment to pursuing research in geodynamics. Additionally, I want to express my appreciation to Patricia Persaud, my collaborator on the BASIN project. Patricia provided valuable insights, suggestions, and assistance that greatly contributed to our work.

My experience at Caltech was made even better by the friendships I formed. I

want to thank my office mates in RM 364, Valeria, Caifeng, Mo and Victor, Jiaqi, Erin, Jack. Sharing a warm and welcoming office with such wonderful individuals transformed my Ph.D. experience in the most positive way. I'm also thankful to my friends, Cijin, Yan, Tobi, Pond, Zhe, Zhichao, Wei, Qian, Jiashun, Ettore, Jorge, Weiqiang, and all the friends in the seismolab family.

Additionally, I'd like to express my appreciation to my friends outside the Seismolab—Sihe, Yiheng, Yangchen, Junjie, Xiuqi, Yanlong, Wenzheng, Sizheng, Linhao, Xiyuan, and Jian. Your presence in my life has made it special. To all my friends, even those not mentioned here, I'm grateful for your companionship and the impact you've had on my journey.

Finally, I want to extend my deepest thanks to my family, especially my parents and my grandma, for their unconditional love and support. They are the reason I'm here, and I can never thank them enough.

ABSTRACT

Subduction initiation, the inception of a subduction zone, heralds dramatic changes in tectonic plate kinematics and dynamics. In the first half of the thesis, I focus on understanding the dynamics of the subduction initiation process through a synthesis of numerical computations and theoretical frameworks. In Chapter 2, we employ force balance analysis and 2D geodynamic models to yield an analytical solution on the force evolution of the subducting plate. This formulation illuminates a pivotal phase in subduction initiation —- the compression-to-extension transition of plate forces -— as a defining milestone. In Chapter 3, we extend this analytical framework into a sliced 3D context (2.5D) while incorporating the influence of strike-slip motion. Modified from Chapter 2, the analytical solution validates that strike-slip motion facilitates subduction initiation by accelerating the process of weakening. Chapter 4 ventures into 3D geodynamic modeling, focusing on the Puysegur trench -— a living example of subduction initiation. The models demonstrate a capability to match multiple geophysical and geological observations quantitatively with mechanical models. With a parametric search, we discover the best-fitting models require a relatively fast strain weakening rate, which can be explained by pore-pressure weakening at shallow depths and grain-size reduction at greater depths.

The second part of this thesis transitions to ambient seismic noise correlation. In Chapter 5, we conduct an ambient noise tomography in northern Los Angeles basins with a newly obtained, dense seismic data set. The new shear wave velocity model exhibits a lower velocity in the basins than previous community models, which can potentially resolve the inconsistency between observed and calculated ground motions. In Chapter 6, we introduce a new method to identify the near-field noise sources from the spurious arrivals in ambient noise correlations. The correlation between the inverted noise sources and geological features in northern LA basins suggests the viability of this technique as a novel means of identifying geological structures, including faults.

PUBLISHED CONTENT AND CONTRIBUTIONS

Li, Yida and Michael Gurnis (Sept. 16, 2022). "A simple force balance model of subduction initiation". In: *Geophysical Journal International* 232.1, pp. 128–146. DOI: 10.1093/gji/ggac332.
Y.L. participated in the conception of the project, performed the calculation and derivation, analyzed the data, and participated in the writing of the manuscript.

Li, Yida and Michael Gurnis (Apr. 17, 2023). "Strike slip motion and the triggering of subduction initiation". In: *Frontiers in Earth Science* 11, p. 1156034. DOI: 10.3389/feart.2023.1156034.
Y.L. participated in the conception of the project, performed the calculation and derivation, analyzed the data, and participated in the writing of the manuscript.

Li, Yida, Valeria Villa, et al. (July 2023). "Shear Wave Velocities in the San Gabriel and San Bernardino Basins, California". In: *Journal of Geophysical Research: Solid Earth* 128.7, e2023JB026488. DOI: 10.1029/2023JB026488.
Y.L. participated in the conception of the project, analyzed the data, and participated in the writing of the manuscript.

TABLE OF CONTENTS

Acknowledgements . . . iii
Abstract . . . v
Published Content and Contributions . . . vi
Table of Contents . . . vi
List of Illustrations . . . ix
List of Tables . . . xxii
Chapter I: Introduction . . . 1
Chapter II: A Simple Force Balance Model of Subduction Initiation . . . 3
2.1 Abstract . . . 3
2.2 Introduction . . . 4
2.3 Force Balance . . . 4
2.4 Model Setup . . . 10
2.5 Validation . . . 13
2.6 Discussion . . . 30
2.7 Supplementary Material . . . 41
Chapter III: Strike Slip Motion and the Triggering of Subduction Initiation . . . 52
3.1 Abstract . . . 52
3.2 Introduction . . . 52
3.3 Model Formulation . . . 54
3.4 Results . . . 57
3.5 Discussion . . . 64
3.6 Conclusion . . . 69
3.7 Supplementary material . . . 70
3.8 Analytical Solution . . . 70
3.9 Model Resolution . . . 70
Chapter IV: Bounds on Fault Weakening and Dynamic Processes During Subduction Initiation . . . 77
4.1 Methods . . . 92
Chapter V: Shear Wave Velocities in the San Gabriel and San Bernardino Basins, California . . . 110
5.1 Abstract . . . 110
5.2 Introduction . . . 110
5.3 Data . . . 113
5.4 Method . . . 114
5.5 Results . . . 122
5.6 Discussion . . . 126
5.7 Conclusion . . . 135
5.8 Model Product . . . 135

5.9 Appedix A: Instrumental response for seismogram to accelerometer correlation. 136
5.10 Appendix B: ZZ and ZR phase difference is the same as Z and R phase difference. 137
5.11 Supplementary Material 138
Chapter VI: Mapping the Near-field Scattering Energy from Ambient Noise Spurious Arrival in Sedimentary Basins 145
6.1 Introduction 145
6.2 Ambient Noise Correlation and Inversion Method 146
6.3 Result and Discussion 152
Chapter VII: Conclusions and Future Direction 160

LIST OF ILLUSTRATIONS

Number *Page*

2.1 Cross–sectional schematic of the force balance showing a. the initial condition and b. during an advanced stage of subduction initiation with details shown in c. (illustrating the local $(z - s)$ coordinate system). WZ denotes the weak zone. 5

2.2 The model setup for models with a. velocity boundary conditions and b. force boundary conditions. Plate 1 and Plate 2 corresponding to the overriding plate and subducting plate. 11

2.3 a–c. The effective viscosity (as $\log_{10}(\eta_{eff})$) is color coded and overlain by the velocity vector at different time from velocity boundary model u = 1 cm/yr. d–f. The second invariant of stress σ_{II}(as $\log_{10}(\sigma_{II})$) is color–coded and overlain by the stress bar, from the same model as a–c. The length of the stress bar represent the difference between the largest and smallest principal stress, σ_{diff}, and the direction is the direction of the smallest principal stress (compression axis). 14

2.4 For the velocity boundary models, the force within the plate, F_{xx}, versus the amount of plate displacement, ℓ. a. Results from the numerical model with a visco–plastic rheology and different rates of imposed convergence. b. As in a, except from the analytical solution. c. As in a, except for a visco–elasto–plastic rheology. d. Comparison of visco–plastic (solid) and visco–elasto–plastic (dotted) rheologies for large and small convergences. The applied plate velocity is encoded by different colors. 15

2.5 a. Outline of the thermal plate (in black) and mechanical plate (in red), as well as a curve denoting the plate center determined from the mechanical plate. b. The total stress F_{ss} along the plate from numerical and analytical. c. The different components making up the bending force predicted by the analytical solution. By the definition of F_{ss}, positive means compression and negative means extension. As the analytical solution only predicts the change of normal force, all the components of normal force in c are fixed on the right end, such that the change along the curves are ΔN_{NB} or ΔN_b. The analytical solution in b is the summation of all the component in c, but a constant is added to align the analytical solution in b with the numerical model. The numerical model is with visco-plastic rheology. Static pressure $P = \int \rho g dz$ is removed in all the measurement of stress. 17

2.6 Plate displacement ℓ vs time from force boundary condition with a, c: $\varepsilon_{P0} = 1$ and b, d: $\varepsilon_{P0} = 2$. The color represent applied force. a, b: comparison between analytical solution (dashed) and numerical model (solid) with visco–plastic rheology. c, d: the comparison between visco-plastic (solid) and visco–elasto–plastic model (dotted). 18

2.7 a–c. The effective viscosity (as $\log_{10}(\eta_{\text{eff}})$) and the velocity vector from force boundary model $F_{xx} = 9.24 \times 10^{12}$ N/m. d–f. The second invariant of stress σ_{II}(as $\log_{10}(\sigma_{II})$) is color–coded and overlain by the direction , from the same model as a to c. 20

2.8 a–d. $\frac{dk}{ds}$ vs x from velocity boundary model with $u = 1$ cm/yr at four different times. e–h. strain rate (as $\log_{10}(\dot{\varepsilon})$) at the same time as a–d. Peaks and troughs in a–d correlate with the hinge zone areas in e–h. . 21

2.9 a. $\frac{dk}{ds}$ and b k vs s at different times from velocity boundary condition models with $u = 1$ cm/yr. s is the distance from the right end of the plate. Λ (on the right axis of b) is the radius of the curvature, so that $\Lambda = \frac{1}{k}$. 21

2.10 a. The normal force change N_b due to plate bending from velocity boundary models with different u but the same plate motion ℓ(= 120km). b. Average viscosity $\bar{\eta}$ (as $\log_{10} \bar{\eta}$) from the same snapshots as a. c. $\log_{10}(\bar{\eta}u)$ from the same snapshots as a. Due to plasticity, $\bar{\eta} \sim \frac{1}{u}$, $\bar{\eta}u$ is supposed to be a constant independent on u. 23

2.11 The total work W done by F_{xx} with respect to plate motion ℓ from velocity boundary models with different convergent rates with visco-plastic rheology(solid) and visco-elasto-plastic rheology(dotted). . . . 25

2.12 a–c. Contours of t_{SI} from analytical solution for velocity boundary models. d–f. The same contours for the force boundary models. The varying parameter include plate velocity u for velocity boundary models and boundary force F_{xx} for force boundary models. The age of subduction plate (a, d), plate strength τ_{max} (b, e) and weakening rate ε_{P0} (c, f) are varied. The gray area in d–f denotes parameter domains where there is no initiation. When the parameters are not varied, the default values are plate age = 40 Myr, τ_{max} = 150 MPa, $\varepsilon_{P0} = 1$. 26

2.13 a. The work done to initiate subduction, W_{SI}, from models with different convergent velocities at $\varepsilon_{P0} = 1$. Solid line is for analytical solutions, open circles for visco-plastic models, and filled triangles for visco-elasto-plastic models. b. Analytical prediction of W_{SI} vs u with different ε_{P0}'s (color-coded) for visco-plastic rheologies. 27

2.14 The integration of pressure over depth in the lithosphere, $F_p = \int_0^H p dz$. Here the pressure p is the dynamic pressure (non-hydrostatic), and H the plate thickness. The plate boundary is at x = 450 km. . . . 28

2.15 F_{xx} vs ℓ from visco-plastic model(solid) and visco-elasto-plastic model(dotted) with velocity boundary with yielding stress τ_{max} equals a. 150 MPa, b. 300 MPa, c. 600 MPa and d. 1200 MPa. 31

2.16 ℓ vs t from visco-plastic model(solid) and visco-elasto-plastic model(dotted) with force boundary with yielding stress τ_{max} equals a. 150 MPa and b. 300 MPa. 32

2.17 Illustration of the hinge zone geometry and stress. The local coordinate system(s, z) is defined in Figure 1. Two sectors draw the yielding area bounded by $z = \pm z_1(s)$. Every sector area is symmetric along the central axis $s = s_c$. Red, blue, and green represent the central, edge and out of the yielding area. 39

2.18 F_{xx} vs ℓ from visco-elasto-plastic model with a. Δt_e = 1Myr and b. Δt_e = 1.5kyr $\approx \Delta t$. a is the same as Fig 2.4c. 43

2.19 An example of measuring plate curvature k and its derivative $\frac{dk}{ds}$ from numerical model. a. the geometry of the plate. Red and green curves are the upper and lower interfaces of the mechanical plate measured from temperature contour $T = 600°C$. Blue curve is the mid-point curve of the red and green curve. b. Direct forward difference (orange) and TVRegDiff method (blue) of the blue curve in a. Direct forward difference represent the ground truth of the numerical derivative, and TVRegDiff represent the smoothed derivative. c. Direct forward difference (orange) and TVRegDiff method (blue) of the blue curve in b. d. Direct forward difference (orange) and TVRegDiff method (blue) of the blue curve in c. 45

3.1 Three Cenozoic subduction initiation events that occurred in the western Pacific showing a substantial component of relative, strike-slip motions at the nascent trench just prior to initiation. A. Present-day western Pacific with the structures against which subduction initiated shown in brown. Regions of detail shown with boxes. B. Magnitude of strike slip motion (above) and convergence direction (below, with 0 being normal to the strike of the trench) before onset of initiation. Izu-Bonin-Mariana (IBM) shown at 55 Ma (red) and 50 Ma (black solid) with values for intermediate times shown with with grey shading, Vanuatu at 15 Ma (blue dashed) and Puysegur (black, dot-dashed) using the plate model of Müller et al. (2019). C. Conditions at IBM at 55 Ma, 5 Myr before the onset of SI. D. Vanuatu at 15 Ma, 1-3 Myr before onset. E. Puysegur at 15 Ma, 1-3 Myr before onset. Abbreviations for plates: PA-Pacific Plate, AU-Australia Plate, PS-Philippine Sea Plate 55

3.2 The model configuration of velocity boundary model A and force boundary model B. 56

3.3 A. An example of model with 1cm/yr convergent velocity. Color shows the effective viscosity. Vectors show the in-plane component velocity and contours show strike slip velocity in cm/yr. B. The integrated horizontal compressional force in the plate F_{xx} as a function of plate motion ℓ for models with different strike slip velocity V_{SS} under $\varepsilon_{P0} = 1$. Solid line for numerical model results and dashed line for analytical results. C. Same as B but with slower weakening rate $\varepsilon_{P0} = 2$. D. The work done to initiate a subduction W_{SI} of every numerical model(color-coded solid circle) in the parametric grid search varying the strike slip velocity V_{SS} and ε_{P0}. Contours show the prediction of W_{SI} from analytical model. 58

3.4 Analytical prediction of initiation time t_{SI} under different convergent velocity Vx and subducting plate age with A. $V_{SS} = 0$, $\varepsilon_{P0} = 1$, B. $V_{SS} = 3$cm/yr, C. $V_{SS} = 6$cm/yr, $\varepsilon_{P0} = 1$. D to F are the same as A to C except $\varepsilon_{P0} = 2$. Red, magenta, blue and green box show the parameter range of IBM (50Ma), IBM (55Ma), Puysegur (PU) and Vanuatu (VT) subduction initiation from the given V_{SS} with a $\pm$1cm/yr range. 60

3.5 Cases with applied compression and with three different strike–slip velocities. A. Strike slip velocity along the the top of the domain. The parameters [ε_{P0}, V_{SS} , f_{xx}] for the three case are: B. Case M2_24, [2, 0 cm/yr, 8.57×10^{12} N/m]. C. Case M0_01, [1, 0, 8.57×10^{12}]. D. Case M0_28, [2, 2, 8.57×10^{12}]. In B-D Contours show the strike slip velocity in cm/yr 61

3.6 The parametric grid search result of models with different driving force F_{xx}, strike slip velocity V_{SS} and weakening rate ε_{P0}. Triangles for cases with subduction initiation and solid dots for cases with no subduction initiation. The color of triangles present the $log_{10}t_{SI}$, where the t_{SI} is the time when the slab tip reach 60 km depth, the characteristic depth when F_{xx} turns into 0 in velocity boundary models. 62

3.7 Equivalent figure with figure 3.6 but with lower resolution. 62

3.8 Fault evolution of a high resolution models with [ε_{P0}, V_{SS} , V_p]=[2, 6 cm/yr, 4 cm/yr]. A–D, Red and blue for oceanic and continental crust. Background color for temperature. E–H, Second invariant of strain rate ($\dot{\varepsilon}_{II}$). 63

3.9 Fault evolution of a high resolution models with [ε_{P0}, V_{SS} , V_p]=[2, 6 cm/yr, 4 cm/yr], equivalent to Fig 3.8 but with weaker quartzitic crust rheology. A–D, Compositional domains. E–H, Second invariant of strain rate ($\dot{\varepsilon}_{II}$). 65

4.1 Observation summary of Puysegur trench. A. Fracture zones and seafloor magnetic lineations (color-coded with age). Black box shows the geodynamic model domain. B. Focal mechanisms from GCMT catalogue (Ekstrom, Nettles, and Dziewoński, 2012) with classified fault types (Alvarez-Gomez, 2019) for shallow earthquake(< 30 km deep), and seismicity under Fiordland(colored dots near AA' line). C, the cross-section AA' of seismicity (Seebeck et al., 2023) under Fiordland. 78

4.2 Plate reconstruction of Australia-Pacific boundary south of New Zealand. A. Reconstructed features at 15Ma. Magnetic lineations are color-coded with age. Black segments are located spreading centers and transform faults according to the magnetic lineations and curve fracture zones. B,C,D, the reconstruction with age grid at 15Ma, 25Ma and 40Ma. Age grid are color-coded with seafloor age newly generated from the spreading centers since 40Ma using *Track Tec*(Karlsen et al., 2020). 79

4.3 Time evolution of the case $\varepsilon_{P0} = 0.5, \tau_u = 500MPa$. Three columns represent the beginning (14.3Ma), middle(10Ma), and final stage(0Ma) of the model evolution. The top two rows are the cross sections at line a, b, c, and d. In line a, b, and c, vectors are in-plane velocity, contours are normal-to-plane(strike-slip) velocity, and temperature is color-coded. In line d, density is color-coded. 81

4.4 Model fitting to observations. A, the correlation coefficient of topography between models and observation. The values range from -1 to 1, with -1 being anti-correlated and 1 being perfectly correlated. B, the correlation coefficient of stress evolution between models and data. C, the correctness of location of seismicity, evaluated as the proportion of intermediate depth seismicity falling within the seismogenic zone predicted by models. The value ranges from 0 to 1, with 1 being a perfectly predicted seismogenic zone. D, correctness of focal mechanism prediction, evaluated as the proportion of correct fault types predicted by the model with respect to the GCMT catalog. 82

4.5 Comparisons between observation and models at present day. A. observed bathymetry topography (background color), seismicity (dots color-coded with depth), and stress evolution (sub-panel) modified from (Shuck et al., 2022). B. modeled present-day bathymetry topography, depth of seismogenic zone (contours color-coded with depth using the same colormap as the seismicity in A), and measured stress evolution at a,b,c (sub-panel) from case $\varepsilon_{P0} = 0.5, \tau_u = 500MPa$. C. same as B but from case $\varepsilon_{P0} = 2, \tau_u = 500MPa$. D. the total model correctness with varied ε_{P0} and τ_u. "X" stands for no subduction initiation. The correctness ranges from 0 to 1, with 1 being a perfect fit to observed data. PT, Puysegur trench; PR, Puysegur ridge; PB, Puysegur bank; SZ, Snares zone; SB, Solander basin. 83

4.6 Time evolution of the case $\varepsilon_{P0} = 2, \tau_u = 150MPa$ where subduction fails to initiate. 84

4.7 Comparison of focal mechanisms. A. focal mechanisms from GCMT((Ekstrom, Nettles, and Dziewoński, 2012)) catalog. B. focal mechanisms at the same hypocenters as A from case $\varepsilon_{P0} = 0.5, \tau_u = 500MPa$. C. same as B but from the case $\varepsilon_{P0} = 2, \tau_u = 500MPa$. D. same as B but from the case $\varepsilon_{P0} = 0.5, \tau_u = 300MPa$. 86

4.8 Equivalent to Figure 4.5 but from the cases with dry feldspar (strong) crust model. 87

4.9 Equivalent to Figure 4.4 but from the cases with dry feldspar(strong) crust model. 88

4.10 Physical models for strain-weakening. A. Shear heating with ε_{P0} (contoured in black). Blue contours represent the density distribution of T & $\dot{\varepsilon}$ in the lithosphere from the Puysegur model (beginning at 15 Ma for case $\varepsilon_{P0} = 0.5, \tau_u = 300$ MPa). T_0 is the initial temperature. B. ε_{P0} by grain-size reduction (black contours). Colored contours are the same as A except from the end (0 Ma) of case $\varepsilon_{P0} = 0.5, \tau_u = 300$ MPa. Dark gray shaded regions in B represent the grain-size reduction is either unneeded or insufficient. C. The averaged weakening rate $\bar{\varepsilon}$ from pore pressure weakening; σ^* is the pressure-permeability exponential scaling factor and $\bar{\Gamma}$ the average fluid production rate in the top 10 km. D. Typical strain weakening paths for different weakening mechanisms compared with the best fitting Puysegur models. Three physical mechanisms' parameters are taken from 3 stars with corresponding colors in A, B, and C. The paths of pore pressure and best fitting numerical model sample a point at the depth of 5 km. The light gray shaded regions are for $0.1 \leq \varepsilon_{P0} \leq 1$. 89

4.11 Roughness evolution r from grain-size evolution model. Background color for log scale roughness reduction rate $log_{10}(-\frac{dr}{dt})$ for A, constant stress $\tau = 150MPa$ and B, constant strain rate $\dot{\varepsilon} = 10^{-15}s^{-1}$. Dashed contours for A, strain rate in s^{-1} and B, stress in MPa. Solid curves for the contours of the desired final stress or strain rate after weakening. 90

4.12 Fluid content phase diagram modified from (Fagereng et al., 2018) Figure 7. The colors of the contours and dots represent fluid content in percentage. Contours for the average fluid content in MORB (Mid-ocean ridge basalt) and GLOSS(global subducting sediment). Dots are the sampled dots at the slab interface from the last step of the case $\varepsilon_{P0} = 0.5, \tau_u = 300MPa$. 91

5.1 Distribution of BASIN nodal arrays (colored dots), broadband stations (black and blue triangles), and SCSN accelerometers (black dots). Color represents the deployment time for the temporary node stations. Black triangles are the permanent Southern California Seismic Network (SCSN) stations. Black lines (AA' to EE') are geological cross-sections, and red stars in the San Gabriel basin are boreholes with well logs used in this study. 113

5.2 Intra-array correlation function from the SG1 dense linear array. a. The ZZ component depicts Rayleigh waves. b. The TT component with virtual source SG1120 shows Love waves. Correlation functions are filtered between 0.2 and 2 Hz. 114
5.3 An example of Rayleigh wave group velocity dispersion analysis in the frequency-time domain. a. Hilbert transform of the ZZ correlation function. b. Phase difference δ between ZR and ZZ from the Wavelet transform. Red for δ between [0, π], retrograde particle motion. Blue for δ between [-π, 0], prograde particle motion. c. Combination of a and b. Red and blue lines are inferred retrograde fundamental mode and prograde first higher mode dispersion curves, respectively. The correlation is from station pair SG102-SG160. . . . 117
5.4 Ray coverage of the Rayleigh wave fundamental mode group velocity at T=1s. The rays are color-coded by picked group velocity. 118
5.5 a. ZZ and ZR ambient noise correlation functions from G. Li et al., 2016. b. The Hilbert-wavelet transformation of a. c. and d. the particle motion of the blue and red parts of (b). In c and d, the time of the particle motion is color-coded, from blue (t = 0) to red. 119
5.6 An example of phase velocity dispersion picking. The red line is the reference fundamental mode phase velocity evaluated from the group velocity model. The black dots are the picks. 120
5.7 Color-coded background map is the prior basin depth model from (Villa et al., 2023). White lines are the nodal arrays. Numbered green diamonds are boreholes. 121
5.8 Group velocity maps for Rayleigh wave (a, c, e) and Love wave (b, d, f) at periods of 1, 2, and 3 s. 121
5.9 V_{SH} inverted from Love wave tomography at depths of 0.5, 1, 1.5, and 2 km. 122
5.10 V_{SV} inverted from Rayleigh wave tomography at depths of 0.5, 1, 1.5, and 2 km. 123
5.11 Vs model at the depths of 0.5, 1, 1.5, and 2 km. 123
5.12 Radial anisotropy at depths of 0.5, 1, 1.5, and 2 km. 124
5.13 Intra-array TT, RR, and ZZ correlation functions from the SB1 dense linear array using SB1-1018 as a virtual source. Colored lines are Eikonal travel times from the group velocity map at different frequencies (color-coded by period). 125

5.14 Intra-array TT, RR, and ZZ correlation functions from the SB1 dense linear array using SB1-1088 as a virtual source. Colored lines are Eikonal travel times from the group velocity map at different frequencies (color-coded by period). 126
5.15 Intra-array TT, RR, and ZZ correlation functions from the SB1 dense linear array using SB1-1248 as a virtual source. Colored lines are Eikonal travel times from the group velocity map at different frequencies (color-coded by period). 127
5.16 Ray paths (white curves) of the Love wave group velocity model at 1 s period from the Eikonal method. Gray straight lines represent straight ray path. Travel times of Eikonal ray path (white) and straight ray path (gray) are marked for comparison. 127
5.17 Cross-sections of Vs model compared against prior basin model (dashed line) and basin model constraint from other references (dotted line). Locations of the cross-sections are shown in Figure 5.1 with black lines. Abbreviations for faults: SJF-San Jacinto fault; LLF-Loma Linda fault; RF-Raymond fault; SMF-Sierra Madre fault; BJ-Barrier J; FQ- fault Q. 128
5.18 Love wave group velocity dispersion curves in the San Gabriel basin predicted by our model (black solid line) and CVMS model (black dashed line). The background is the envelope from the correlation function, and the red curves are the actual picks. 130
5.19 Rayleigh wave group velocity dispersion curves in the western San Gabriel basin (SG1-SG2) predicted by our model (black solid line) and CVM-S model (black dashed line). The background is the envelope from the correlation function, and the red curves are the actual picks. 130
5.20 Love wave group velocity dispersion curves in the eastern San Gabriel basin (SG3-SG4) predicted by our model (black solid line) and CVM-S model (black dashed line). The background is the envelope from the correlation function, and the red curves are the actual picks. . . . 131
5.21 Rayleigh wave group velocity dispersion curves in the eastern San Gabriel basin (SG3-SG4) predicted by our model (black solid line) and CVM-S model (black dashed line). The background is the envelope from the correlation function, and the red curves are the actual picks. 131

5.22 Love wave group velocity dispersion curves in the San Bernardino and Chino basins (SB2-SB3) predicted by our model (black solid line) and CVM-S model (black dashed line). The background is the envelope from the correlation function, and the red curves are the actual picks. 132
5.23 Rayleigh wave group velocity dispersion curves in the San Bernardino and Chino basins (SB2-SB3) predicted by our model (black solid line) and CVM-S model (black dashed line). The background is the envelope from the correlation function, and the red curves are the actual picks. 132
5.24 Love wave group velocity dispersion curves in the San Bernardino basin (SB2-SB6) predicted by our model (black solid line) and CVM-S model (black dashed line). The background is the envelope from the correlation function, and the red curves are the actual picks. . . . 133
5.25 Rayleigh wave group velocity dispersion curves in the San Bernardino basin (SB2-SB6) predicted by our model (black solid line) and CVM-S model (black dashed line). The background is the envelope from the correlation function, and the red curves are the actual picks. . . . 133
5.26 Love and Rayleigh wave resolution test from ray coverage of TT and ZZ correlation at T=2s. 134
5.27 VS derived from sonic well logs from the Ferris, LOP, and CRP boreholes compared with our Vs model (black dashed lines for starting model, black solid lines for final model) and CVMS 4.26 (red). Locations of the boreholes are shown with red stars in Figure 5.1. . 135
5.28 Compilation and distribution of Vs with depth in the Raymond, San Gabriel, Chino, and San Bernardino basins (gray lines) from our Vs model (upper panels) and CVMS 4.26 (lower panels). The black shaded regions show the distribution of Vs values at different depths. 136
5.29 Example of correlation functions folded at t = 0 s from a) a seismogram-to-seismogram cross correlation and b) a seismogram-to-accelerometer cross correlation. In a) the causal and anti-causal branch show coherent phase, and in b) the causal and anti-causal display a half period (π phase) shift. 137

6.1 a. Mapview of study area with dense array distribution. In total 750 stations in 10 lines wer4e deployed Li, Villa, R. W. Clayton, et al., 2023 b. An example of SG1-SG1 intra-array correlations using SG130 as a virtual source. c. An example of SG1-SG2 inter-array correlations using SG130 as a virtual source. Yellow, green and blue curves for the estimated direct arrival at speed of 0.5, 1 and 2km/s respectively. Black arrows mark the possible spurious arrivals. . . . 147

6.2 Illustration of the inversion method. Triangle i and j stand for the station i,j. Color-coded hyperbolas are the contours of the travel time difference. Each contour contributes to the same time point in the cross-correlation between station i and j. Solid circles stand for dense noise source S_{lm} at the location of (x_l, y_m), with the color-coded travel time difference from each source to station i and j. The dashed square depicts a domain of sparser noise source R_{pq}, with all the dots interior the square governed by the four corners' R. 148

6.3 A benchmark test of intra-array correlation. a. Noise source(red stars), stations(black circles) and velocity model(background color) in map view. b. Inverted noise source distribution(background color). c. Correlation functions from finite difference model(black) as an input for the inversion vs. synthetic wave envelops from inversion output. The virtual source of c is the black star in b. 151

6.4 A benchmark test of inter-array correlation. Equivalent to Figure 6.3 but using the inter-array correlation for the inversion. 151

6.5 a. The combined inverted noise source distribution from correlation SG1-SG2, SG3-SG4, SB2-SB6, and SB3-SB6. b. The combined model sensitivity from the same correlation dataset as a. 152

6.6 a. Zoom-in of inverted noise source distribution from SG1-SG2 region. b. Waveform amplitude of ambient noise correlation(black) vs. synthetic correlation(red). The virtual source is SG1-150(black star in a.) and the virtual receivers are the nodes of SG2 line. Yellow, green and blue lines are the direct arrivals at the speed of 0.5, 1 and 2km/s. All waveforms(black) in b. are filtered by a bandpass filter with a frequency band of 2 Hz to 3 Hz. 155

6.7 a. Zoom-in of inverted noise source distribution from SG3-SG4 region. b. Waveform amplitude of ambient noise correlation(black) vs. synthetic correlation(red). The virtual source is SG3-315(black star in a.) and the virtual receivers are the nodes of SG4 line. Yellow, green and blue lines are the direct arrivals at the speed of 0.5, 1 and 2km/s. All waveforms in b. are filtered by a bandpass filter with a frequency band of 2 Hz to 3 Hz. 155
6.8 a. Zoom-in of inverted noise source distribution from SB2-SB6 region. b. Waveform amplitude of ambient noise correlation(black) vs. synthetic correlation(red). The virtual source is SB2-201(black star in a.) and the virtual receivers are the nodes of SB6 line. Yellow, green and blue lines are the direct arrivals at the speed of 0.5, 1 and 2km/s. All waveforms in b. are filtered by a bandpass filter with a frequency band of 2 Hz to 3 Hz. 156
6.9 a. 1D noise source distribution from SG1-SG1 correlation with different periods color-coded. Black arrows mark the two possible peaks of noise source in high frequency. b. Zoom in of the noise source distribution near SG1 from the SG1-SG2 correlation. c. Love wave group velocity sensitivity kernels in the San Gabriel basin with different periods. 156

LIST OF TABLES

Number *Page*

2.1 Model Parameters 13

3.1 Model Parameters mainly inherit from Y. Li and Gurnis, 2022 with an addition of weak overriding plate cases. Non-Newtonian parameters of Olivine mantle, Quartzitic crust and Eclogite are from Karato and Wu, 1993; Gleason and Tullis, 1995; Jin et al., 2001. 71

4.1 Model Parameters mainly inherit from Li and Gurnis, 2022Li and Gurnis, 2023 with an addition of weak overriding plate cases. Non-Newtonian parameters of Olivine mantle, Quartzitic crust, and Eclogite are from Karato and Wu, 1993Gleason and Tullis, 1995Jin et al., 2001Rybacki et al., 2006. Symbol A's with different composition represent pre-exponents of viscosity, i.e. $\eta = Ae^{\frac{E}{nRT}}(\dot{\varepsilon}_{II})^{\frac{1-n}{n}}$. A_{diff} and A_{disl} are the pre-exponents of strain rate(eq 4.10,4.11). 92

Chapter 1

INTRODUCTION

The subduction zone is a geological setting characterized by various geological phenomena, including earthquakes and volcanoes. It plays an important role in plate tectonics, acting as a significant driver of plate motion through slab pull. Moreover, subduction zones exhibit a fundamental characteristic, their "weakness." Compared to plate interiors, the subduction interface is typically much weaker, featuring a lower yield stress. The weakness at the slab interface leads to the localization of deformation within narrow shear zones and is associated with the occurrence of large mega-thrust earthquakes along subduction interfaces.

Subduction initiation, the beginning phase of the subduction zone, marks a critical turning point of plate tectonics. During this process, plate kinematics and tectonic dynamics undergo rapid transformations within a relatively short timeframe. In the first half of this thesis (Chapter 2,3,4), we study the dynamic mechanisms governing subduction initiation using both theoretical frameworks and numerical computations.

In Chapter 2, we present an analytical solution for a subduction initiation system derived from the force balance analysis of a subducting plate. Combining theoretical insights with numerical models, we establish that a crucial characteristic of induced subduction initiation systems is the compression-extension transition within the plate force. We identify two primary factors governing the force evolution of the subducting plate: plate convergence and weakening rate.

Building upon the theory introduced in Chapter 2, Chapter 3 extends our analysis into the realm of 2.5D, considering the influence of strike-slip motion. Our research demonstrates that strike-slip motion expedites the subduction initiation process by accelerating strain weakening, and we can quantify this effect by adjusting the weakening rate. Besides, we validate our theory using a few subduction initiation examples from the Cenozoic history of the Pacific hemisphere. Through a simple closed-form equation, we predict subduction initiation timescales consistent with observations.

In Chapter 4, we return to the complexities of the 3D world. Our focus shifts to the Puysegur Trench, a living example of subduction initiation on the southern tip

of New Zealand. Employing 3D, time-dependent geodynamic models starting from 15 million years ago, we explore various model parameters. By comparing model outcomes with the geophysical and geological observations, including topography, stress evolution derived from stratigraphy, seismicity patterns, and earthquake focal mechanisms, we discover that the models with a fast weakening rate align with a range of geophysical and geological observations. We further investigate the primary mechanism driving strain weakening and discover that fluid pore pressure emerges as a plausible mechanism for rapid weakening at shallow depths while weakening at deeper depths could be mainly governed by grain-size reduction. These models exemplify the excellent alignment of geodynamic models with a diverse array of geophysical and geological observations, and the well-constrained geodynamic models not only reveal the dynamics behind Earth's history but also provide crucial inputs for understanding the present-day stress field.

The latter half of this thesis shifts focus to ambient noise analysis using dense seismic array data from the northern Los Angeles basins. This endeavor is driven by the aim of enhancing our understanding of how a major earthquake originating from the San Andreas fault might impact the densely populated Los Angeles region. To achieve this, we construct a new velocity model from the newly obtained dense array data (Chapter 5). Our tomography model, which integrates ambient noise correlation, receiver function, gravity, and borehole data, exhibits lower velocities compared to the previous community model. This suggests that previous assessments may have underestimated the potential ground shaking.

In the final chapter (Chapter 6), we focus on a prominent feature within correlation functions – spurious precursory arrivals. We introduce a novel method for mapping 2D near-field ambient noise sources. Applying this method to the data set from Chapter 5, we observe a clear correlation between the spatial distribution of the inverted noise source and geological features. Moreover, given that high-frequency components dominate the spurious arrivals, we conclude that the noise source is associated with scattering from structures with significant velocity contrasts at shallow depths, such as sedimentary basin edges and faults. This new technique offers a new way of identifying geological structures, particularly faults.

Chapter 2

A SIMPLE FORCE BALANCE MODEL OF SUBDUCTION INITIATION

Li, Yida and Michael Gurnis (Sept. 16, 2022). "A simple force balance model of subduction initiation". In: *Geophysical Journal International* 232.1, pp. 128–146. DOI: 10.1093/gji/ggac332.

2.1 Abstract

The initiation and development of subduction zones are associated with substantial stress changes both within plates and at plate boundaries. We formulate a simple analytical model based on the force balance equation of a subduction zone, and validate it with numerical calculations of highly non–linear, coupled thermo–mechanical system. With two kinds of boundary conditions with either fixed velocity or fixed force in the far field, we quantitatively analyze the role of each component in the force balance equation, including slab pull, inter–plate friction, plate bending, and basal traction, on the kinematics and stress state of a subducting plate. Based on the numerical and analytical models, we discuss the evolution of plate curvature, the role of plastic yielding and elasticity, and how different factors affect the timing of subduction initiation. We demonstrate with the presence of plastic yielding for a plate of thickness, H, that the bending force is proportional to H^2, instead of H^3 as previously thought. Although elasticity increases the force required to start nucleating subduction it does not substantially change the total work required to initiate a subduction zone when the yielding stress is small. The analytical model provides an excellent fit to the total work and time to initiate subduction and the force and velocity as a function of convergence and time. Plate convergence and weakening rate during nucleation are the dominant factors influencing the force balance of the plate, and 200 km of plate convergence is typically required to bring a nascent subduction zone into a self-sustaining state. The closed–form solution now provides a framework to better interpret even more complex, time–dependent systems in three–dimensions.

2.2 Introduction

The balance of forces within subduction zones is a key determinant governing plate motions instantaneously and over time as plates evolve. The force balance likely changes substantially with commensurate changes in the state–of–stress within plates in time and space, especially during the initiation of a new subduction zone. As deduced from field observations and mechanical models, a subducting plate may experience a change from compression to extension during subduction initiation, which could suggest a transfer of driving force from far-field compression to slab pull. In addition to driving forces, there are factors that resist plate motion, such as friction at the subduction interface and rigid plate bending. While bending, the viscous plate experiences deformation within the plate hinge zone, with considerable energy dissipated with a force required to counterbalance the bending torque. Other sources of driving and resisting forces, including a traction from flow beneath lithosphere and horizontal pressure changes from the lateral variations of isostatic columns, might also be important components of the force balance.

Despite a considerable literature documenting the key forces which may exist as a function of time using sophisticated numerical methods (Gurnis, C. Hall, and Lavier, 2004; Nikolaeva, T. V. Gerya, and F. O. Marques, 2010; Leng and Gurnis, 2015; Zhong and Zhong-Hai Li, 2019; Arcay et al., 2020), we are not aware of a simple closed form, analytical model of the force balance as a function of time. Although earlier work described instantaneous force balances (McKenzie, 1977; Mueller and Phillips, 1991), none has been formulated in time. Such a model provides a guide to better understand the complex, time–dependent phenomena that occur in the full solution of the coupled non-linear conservation equations. Here we derived the relationship between forces and plate motion in a trench perpendicular cross section based on a force balance equation, and later validate the result against the full solution of the coupled system of equations with a suite of numerical computations. The role of elasticity is shown through comparison of solutions with and without elasticity.

2.3 Force Balance

At any instant of time, the force balance for a viscously dominated plate is

$$F_{xx} + \Delta N_{NB} = \Delta N_b + T_S + F_a + F_I \tag{2.1}$$

where F_{xx} is an applied far–field compression, ΔN_b and ΔN_{NB} are the change in the normal force arising from the bending of the slab and negative buoyancy,

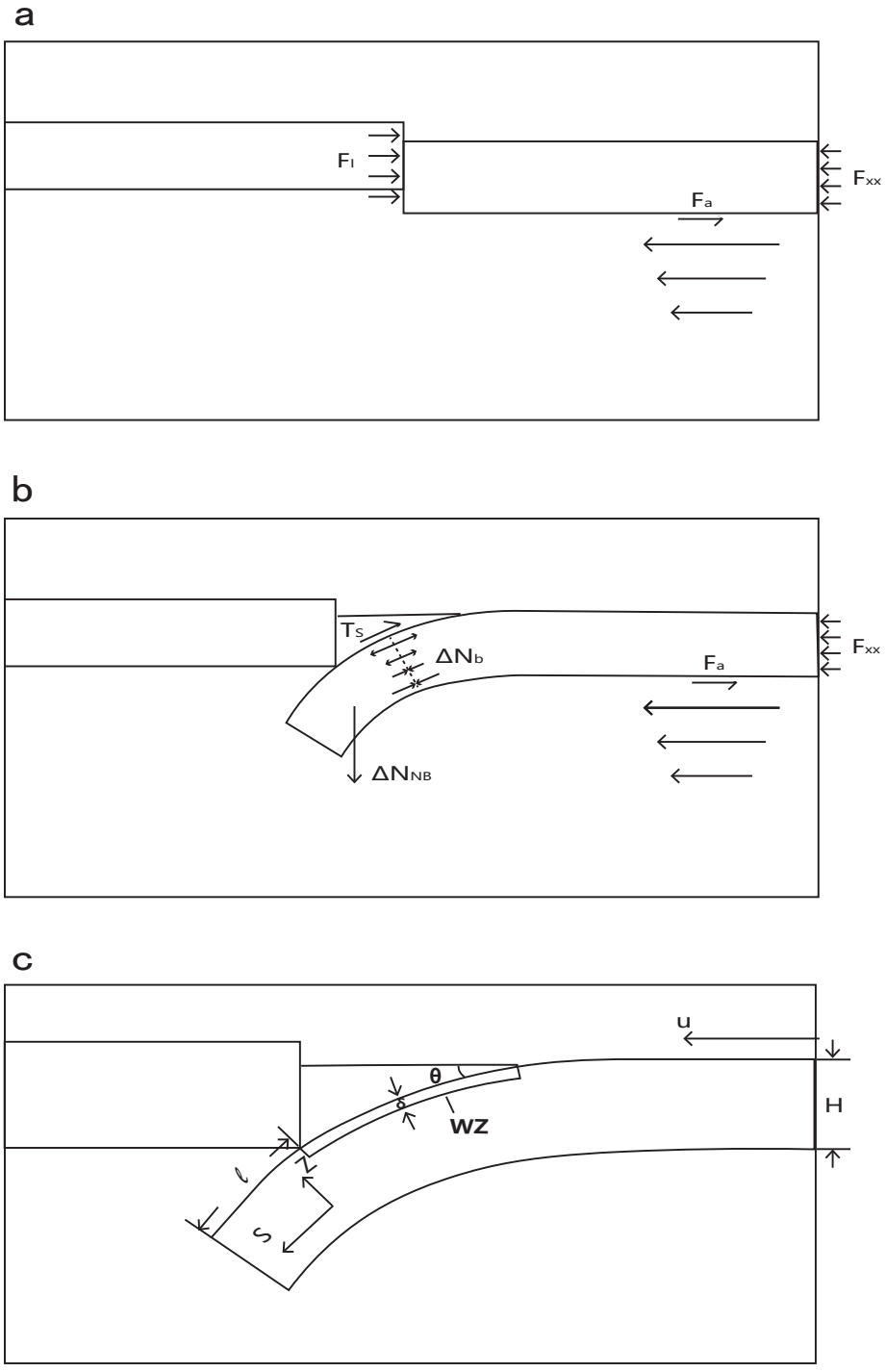

Figure 2.1: Cross–sectional schematic of the force balance showing a. the initial condition and b. during an advanced stage of subduction initiation with details shown in c. (illustrating the local $(z - s)$ coordinate system). WZ denotes the weak zone.

respectively, from the slab tip to the surface (Buffet, 2006), T_S is the frictional resistance between the slab and the over-riding plate, F_a is resistance from viscous shear in the asthenosphere, and F_I is a resistance from a horizontal pressure gradient across the plate boundary arising from differing isostatic columns (Fig. 2.1A). In Appendix A, we provide a detailed derivation of this equation. One can see that F_I has been added as a resisting force, not as a driving force for subduction initiation, as previously considered in the literature (Nikolaeva, T. V. Gerya, and F. O. Marques, 2010; Leng and Gurnis, 2015). Below, we will discuss this further, but detailed computations in 2-D show that F_I initially causes the in-coming plate to slow.

There are two forces within the slab (Fig. 2.1B) that act in the down-dip direction. The first is a driving force from the negative buoyancy of the slab

$$\Delta N_{NB} = H\Delta\rho g \sin\theta \cdot \ell \tag{2.2}$$

where H is the plate thickness, g the acceleration of gravity, $\Delta\rho$ the density difference between slab and ambient mantle, θ dip angle of the slab (typically increasing from 0 at the trench to 45° in the subduction zone), and ℓ the horizontal cumulative slab (plate) displacement. The second is a resisting force generated from bending, which has previously been considered, for example in Buffet, 2006 as an equation tracking the total normal force change attributed to the bending of a thin viscous plate of constant viscosity

$$\Delta N_b = \frac{1}{3}\eta H^3 \int_0^L \left(\frac{dk}{ds}\right)^2 ds \cdot u = K_b u \tag{2.3}$$

where k is the local curvature of the bending slab, η the viscosity of the slab, u the convergence velocity at the nascent trench (so that, $u = \dot{\ell}$), s the distance along the plate's center line (Fig. 2.1c), and L the total length of center line. A single coefficient, which we call K_b, can be used to collapse all coefficients associated with bending into a single term that multiplies u. As the effective viscosity of the bending plate could change as the new subduction zone develops, the constant viscosity assumption (and hence the validity of the equation) will be critically evaluated with detailed computations. In calculations, we will consider the more realistic case when the effective viscosity of the plate no longer remains constant, specifically when the plate experiences brittle failure. We consider a constant yield stress for the plate, accomplished through a reduction in viscosity.

For the plate bending problem, the hinge zone is where a great amount of deformation occurs, and it experiences a reduction of effective viscosity due to plastic failure.

In Appendix B, we show that the contribution of a bending torque from the hinge zone is no longer proportional to the convergent velocity u, but rather a constant independent of u. Combining the contributions of brittle and ductile deformation, the total bending torque is

$$\Delta N_b = K_b u + N_{HZ} \tag{2.4}$$

where N_{HZ} is the bending torque from the hinge zone, a parameter independent of u. $K_b u$ accounts for the contribution of bending force from the area where the bending is not large enough to cause plasticity. For a relatively small yielding stress, plasticity occurs almost everywhere in the bending area, therefore $N_{HZ} >> K_b u$. The bending torque in the hinge zone is expressed as

$$N_{HZ} = \frac{1}{6} H^2 (dk/dz)_{max} s_{HZ} \tau_{max} \tag{2.5}$$

where $(dk/ds)_{max}$ is the maximum rate of plate curvature change. s_{HZ} is the width of the hinge zone, and τ_{max} the maximum yield stress in the plate.

The resistance at the base of the subducting plate during convergence is

$$F_a = 2\eta_a \dot{\varepsilon} L_p = \eta_a \frac{u}{d_a} \cdot L_p = \eta_a \frac{L_p}{d_a} u \tag{2.6}$$

where η_a is the viscosity of the asthenosphere, d_a the thickness of the asthenosphere, and L_p the length of the plate.

The plate is also resisted by the total friction at the plate boundary, T_S, a process that is primarily limited by the yield stress which in turn is controlled by strain weakening. In the numerical model, we consider plastic failure to be governed by a Drucker-Prager yielding criterion with a maximum stress as the upper limit, $\tau_y = \min(\mu_y p + C, \tau_{y0})$, where p is hydrostatic pressure. For the weakening, we use a simplified two-stage process to represent the strain weakening: Initially the yielding parameters μ_y and C decrease linearly with the accumulation of plastic strain, but once the plastic strain saturates, i.e. the plastic strain exceeds the reference plastic strain, ε_{P0}, the yielding stress remains at $\tau_{yf}(\mu_{yf} = 0, C_f = \tau_{yf})$. For the analytical solution, the two stage process is further simplified as $\tau_y = \tau_{max}$ prior to plastic saturation and $\tau_y = \tau_{yf}$ after saturation. This approximation is valid because p is typically much greater than τ_{y0} so that the non-saturated yield stress ($\mu_y > 0$) is mostly cutoff by τ_{y0}. Prior to strain saturation of the fault, the total shear stress from the fault is

$$T_S = \int_0^{\frac{H}{\sin\theta}} \tau_y ds = (\tau_{y0} + \frac{(\tau_{yf} - \tau_{y0})\ell}{\delta\varepsilon_{P0}}) \frac{H}{\sin\theta} + \ell \frac{\tau_{y0} - \tau_{yf}}{\delta\varepsilon_{P0}} \ell = A - B\ell + C\ell^2 \tag{2.7}$$

Where $A = \frac{\tau_{y0}H}{\sin\theta}$, $B = \frac{\tau_{y0}}{\delta\varepsilon_{P0}} \cdot \frac{H}{\sin\theta}$, and $C = \frac{\tau_{y0}}{\delta\varepsilon_{P0}}$. After the strain saturates, i.e. $s > \delta\varepsilon_{P0}$, where δ is the fault thickness, T_S becomes

$$T_S = \int_0^{\frac{H}{\sin\theta}} \tau_y ds = \tau_{yf}\frac{H}{\sin\theta} + \delta\varepsilon_{P0}(\tau_{y0} - \tau_{yf}) = D \tag{2.8}$$

The isostatic force, F_I, is caused by the horizontal pressure difference across the different density columns making up the plate boundary. As a result of isostasy, the horizontal pressure gradient is zero below the compensation depth, d_{comp}, at the base of the lithosphere. However, above the compensation depth, the pressure at the same depth is not usually equal because of density differences in adjacent columns. Here, the density arises from both thermal and compositional differences. Assuming the plate thermal structure obeys a half-space cooling model, the total thermal plate boundary force is the integration of pressure differences from the thermal contrast over depth (Turcotte and Schubert, 1982 eq. 6.405)

$$F_{\text{therm}} = \int_0^{d_{\text{comp}}} \Delta P dz = g\rho_m\alpha\Delta T(1 + \frac{2\rho_m\alpha\Delta T}{\pi(\rho_m - \rho_w)})\kappa(t_2 - t_1) \tag{2.9}$$

Where ρ_m is the mantle reference density, ρ_w is the water density, α is the coefficient of thermal expansion, ΔT is the temperature difference between mantle and surface, κ is the thermal diffusivity, and t_1 and t_2 are the plate age of plate 1 and plate 2, corresponding to the overriding plate and subducting plate, respectively. The other factor contributing to the pressure gradient is the difference in composition between the two plates, assumed to be limited to the crust for simplicity. Similarly, we obtain the boundary force from compositional density differences

$$F_{\text{comp}} = \int_0^{d_{\text{comp}}} \Delta P dz = \frac{1}{2}g\frac{(\rho_m - \rho_{C1})(\rho_{C1} - \rho_w)}{\rho_m - \rho_w}\Delta C_1^2 - \frac{1}{2}g\frac{(\rho_m - \rho_{C2})(\rho_{C2} - \rho_w)}{\rho_m - \rho_w}\Delta C_2^2 \tag{2.10}$$

Where ρ_{C1}, ρ_{C2} are the crustal density of plate 1 and plate 2, and ΔC_1 and ΔC_2 are the crustal thickness of plate 1 and plate 2. With the joint contribution of thermal and compositional density differences across the plate boundary, the total isostatic force at the plate boundary is

$$F_I = F_{\text{therm}} + F_{\text{comp}} \tag{2.11}$$

Substituting in the expressions of ΔN_b, F_{NB}, T_S,and F_a as given above, eq. 2.1 yields

$$F_{xx} + H\Delta\rho g\sin\theta \cdot \ell = T_S + \eta_a\frac{L_P}{d_a} \cdot u + F_I + K_b u + N_{HZ} \tag{2.12}$$

The completeness of the force balance equation is examined with solutions as time progresses during subduction initiation, assuming two typical scenarios, one with plate convergence driven by velocity boundary conditions and another driven by force boundary conditions. These will form the basis for comparison against solutions for the fully coupled, non–linear equations.

Velocity Boundary Condition

With a velocity boundary condition, $u = u_0$, the plate convergence is driven by a fixed, constant velocity and eq. 2.12 becomes

$$F_{xx} = (2\eta\frac{L_P}{d_a} + K_b)u + T_S - H\Delta\rho \sin\theta\ell + N_{HZ} + F_I \tag{2.13}$$

With eq. 2.7 and 2.8, 2.13 yields

$$F_{xx} = \begin{cases} A\ell^2 - (B + H\Delta\rho \sin\theta)\ell + C + (2\eta\frac{L_P}{d_a} + K_b)u_0 + T_S + N_{HZ} + F_I, & \ell < \delta\varepsilon_{P_0} \\ -H\Delta\rho \sin\theta \cdot \ell + D + (2\eta\frac{L_P}{d_a} + K_b)u_0 + T_S + N_{HZ} + F_I, & \ell > \delta\varepsilon_{P_0} \end{cases} \tag{2.14}$$

We will discuss the nature of these solutions when comparisons are made to the full solution of the governing equations from the numerical model.

Force Boundary Condition

Alternatively, we apply a constant far–field compression F_{xx} that drives the plate motion, so that the convergence velocity becomes

$$u = \frac{F_{xx} + H\Delta\rho g\ell \sin\theta - T_S - F_I - N_{HZ}}{K_b + \eta_a\frac{L_P}{d_a}} \tag{2.15}$$

Based on this equation, we obtain the relationship between time t taken to reach a horizontal displacement of ℓ through the integration $t = \int_0^\ell \frac{d\ell'}{u}$. The expression of t with respect to ℓ depends on how much strain has accumulated within the fault zone: When $\ell < \varepsilon_{P_0}\delta$

$$t \approx \frac{4K_1C\ell}{B_1^2 + 4C(F_{xx} - A - F_I - N_{HZ})} \tag{2.16}$$

Where $K_1 = K_b + \frac{L_P}{d_a} \cdot \eta_a$.

When $\ell > \delta\varepsilon P_0$

$$t \approx \frac{4K_1\tau_{y0}}{B_1^2 + 4C(F_{xx} - A - F_I - N_{HZ})} + \frac{K_2(\ell - \delta\varepsilon_{P0})}{F_{xx} - D - F_I - N_{HZ}} \tag{2.17}$$

Where $B_1 = B + H\delta\rho g \sin\theta$, $K_2 = K_b + \frac{L_P}{d_a} \cdot \eta_a$. K_1 and K_2 follow the same definition, but because the asthenosphere viscosity η_a is non-Newtonian, the second stage ($\ell > \delta\varepsilon_{P0}$) has an overall lower η_a due to the higher plate speed, and K_2 is thereby smaller than K_1. In eq. 2.16 and 2.17 we only present the approximate forms, with the detailed derivations and full expressions given in the supplementary material (eq. 2.28, 2.29). We will discuss solutions of these equations with the force boundary conditions when comparing against the solution of the full equations with the numerical models.

2.4 Model Setup

We have formulated a series of computations in a two-dimensional (2D) domain with the finite element method using the *Underworld* package (Mansour et al., 2020) to validate the simple force balance. Computational models with both visco-plastic and visco-elasto-plastic rheologies are used to isolate the role of elasticity during subduction initiation. Initial temperature field is from half-space-cooling model with given subducting and upper plate age. Models are computed with both imposed velocities and imposed forces, so as to mimic the routes taken in the simple analytical force balance. The models with imposed velocities are implemented using a Dirichlet condition on the right wall through the depth of the plate (Fig. 2.2a). The models with imposed forces are implemented by applying a horizontally-acting body force through a narrow column (Fig. 2.2b) on the right edge of the subducting plate, following (Leng and Gurnis, 2011), and the thermal age of the rightmost 100 km lithosphere is set to be 0, decoupling the subducting plate from the model domain boundary. With the large topographic gradients rapidly developing during subduction initiation, the topography is tracked as a free surface, as in previous studies (Toth and Gurnis, 1998; Gurnis, C. Hall, and Lavier, 2004; Nikolaeva, T. V. Gerya, and F. O. Marques, 2010). Here, the free surface is approximated by overlaying the plates with a 40 km thick, low viscosity (e.g. sticky–air) layer (Crameri et al., 2012). The material has a non–Newtonian and temperature–dependent rheology

$$\eta(T, \dot{\varepsilon}) = \eta_0 e^{\frac{E}{nRT} - \frac{E}{nRT_0}} \left(\frac{\dot{\varepsilon}}{\dot{\varepsilon_0}} \right)^{\frac{1-n}{n}} \tag{2.18}$$

where E is the activation energy, R the ideal gas constant, and n the exponent of non-Newtonian flow. η_0 is the reference viscosity at a the reference temperature, T_0, and reference strain rate, $\dot{\varepsilon_0}$. In addition to the non-Newtonian viscosity, the material yields (plastic failure) by imposing an upper limit on the stress; the effective

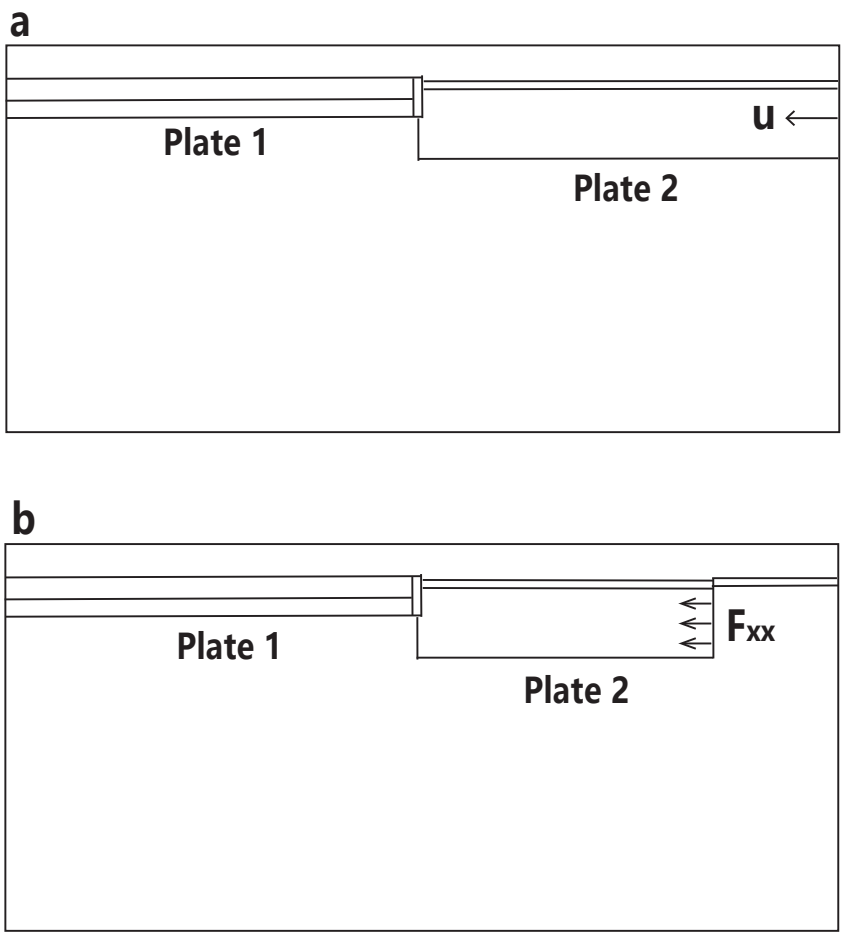

Figure 2.2: The model setup for models with a. velocity boundary conditions and b. force boundary conditions. Plate 1 and Plate 2 corresponding to the overriding plate and subducting plate.

viscosity becomes

$$\eta_{\text{eff}} = \min\left(\eta(T), \tau_y/\dot{\varepsilon}_{II}\right) \tag{2.19}$$

where τ_y is the yield stress, and $\dot{\varepsilon}_{II}$ is the square root of the second invariant of strain rate tensor. The effective viscosity is confined by minimum and maximum values (see Table 2.1). The yield stress follows the Drucker-Prager yielding criterion with an upper cutoff, $\tau_y = \min(\mu_y p + C, \tau_{y0})$.

Weakening processes are approximated by reducing the yield stress with plastic strain, following a two-stage process: Prior to a strain saturation, C and μ_y linearly decrease with accumulation of plastic strain ε_P, and afterwards τ_y remains constant.

$$\tau_y = \begin{cases} \mu_y p + C, & \varepsilon_P \leq \varepsilon_{P0} \\ \tau_{yf}, & \varepsilon_P > \varepsilon_{P0} \end{cases} \tag{2.20}$$

where ε_{P0} is the reference plastic strain that controls the rate of weakening. C and μ_y are cohesion and friction coefficient, $C = (\tau_{yf} - C_0)\frac{\varepsilon_P}{\varepsilon_{P0}} + C_0$ and $\mu_y = \mu_{y0} - \mu_{y0}\frac{\varepsilon_P}{\varepsilon_{P0}}$. The material within the majority of the domain is governed by non-Newtonian flow, indicating the dominance of ductile deformation. In two regions, the weak zone and hinge zone, where the strain rate is large, the yielding dominates, indicating the deformation makes a transition into brittle failure. Three materials are present within the domain: An 8 km thick basaltic crust on top of the subducting plate that can metamorphose to eclogite at depth (Hacker, Abers, and Peacock, 2003); a 25 km thick granitic crust on top of the over-riding plate; and an olivine mantle composing the remainder of the domain. The density varies with composition, but the rheological parameters are invariant so as to validate the simple force balance equations.

For models with a velocity boundary condition, we determine the total horizontal compressional force within the plate, $F_{xx} = -\int_{-\frac{H}{2}}^{\frac{H}{2}} \sigma_{xx} dz$, with plate convergence ℓ, and compare against the evaluation of eq. 2.13. For models driven with a force boundary, the plate convergence ℓ *vs.* time from numerical models are compared against evaluation of eq. 2.16 and 2.17. In the first set of models (Fig. 2.2a), the boundary velocity controls plate convergence and the plate motion remains constant with time. In the force boundary model (Fig. 2.2b), the compression F_{xx} is applied via a body force in a thin layer on the right end of the subducting slab, and a ridge with 0 thermal age is connected to the right of the subducting slab to decouple the subducting slab from the right wall. The presence of thermal ridge also naturally generate an additional "ridge push" compression.

Symbol	Definition	Value	Symbol	Definition	Value
n	non-Newtonian exponent	3	τ_{y0}	maximum yield stress	150 MPa
E	Activation energy	540 kJ/mol	τ_{yf}	minimum yield stress	3 MPa
η_{min}	minimum viscosity	10^{19} Pa $\cdot$ s	ε_{P0}	reference plastic strain	1 or 2
η_{max}	maximum viscosity	10^{25} Pa $\cdot$ s	t_1	overriding plate age	20 Myr
μ	shear modulus	3×10^{10} Pa	t_2	subducting plate age	40 Myr
$\dot{\varepsilon}_0$	reference strain rate	10^{-15} s^{-1}	ΔC_1	continental crustal thickness	25 km
α	thermal expansivity	3×10^{-5} C^{-1}	ΔC_2	oceanic crustal thickness	8 km
κ	thermal diffusivity	10^{-6} m$^2 \cdot$ s^{-1}	H	plate mechanical thickness	60 km
T_0	Surface temperature	0°C	δ	fault thickness	20 km
T_1	mantle temperature	1400° C	θ	fault dip angle	45°
C_0	intial cohesion	44 MPa	μ_{y0}	initial friction coefficient	0.6
η_{st}	sticky air viscosity	10^{19}Pa $\cdot$ s	μ_{st}	sticky air shear modulus	3×10^{10} Pa
d_{st}	sticky air thickness	40km	κ_{st}	sticky air thermal diffusivity	10^{-5} m$^2 \cdot$ s^{-1}

Table 2.1: Model Parameters

2.5 Validation

Velocity boundary

Subduction initiation with imposed velocity evolves through a pathway (Fig. 2.3) similar to published models (Gurnis, C. Hall, and Lavier, 2004; Zhong and Zhong-Hai Li, 2019; Maunder et al., 2020). In the case with an imposed velocity of u_0 = 1 cm/yr, the viscosity (Fig. 2.3a-c) is strongly influenced by temperature, but several features stand out. The first is a conspicuous reduction of viscosity beneath the subducting plate and around the slab due to the non-linearity of viscosity. The second is a reduction of viscosity at the plate boundary weak zone and hinge zone due to yielding. Despite yielding and non-linear viscosity, the simple force balance appears to capture the principal physics (Fig. 2.4).

The horizontal compression within the plate interior, F_{xx}, shows three stages as a function of plate convergence, ℓ , in both the numerical and analytical solutions (Fig. 2.4). The parameters used in the analytical solution are given in Table 2.1. In the earliest stage, F_{xx} drops steeply with plate motion during the first 30 km, followed by a relatively slow drop, and finally after 150 km of convergence the drop accelerates again. The initial rapid stress drop is caused by a reduction of resistant stress from the weak zone, T_S, due to the plastic weakening and the increase of negative buoyancy. In this stage, the whole plate experiences horizontal compression (Fig. 2.3d). After around 30 km of convergence, the fault zone has been fully weakened and the yield stress no longer decreases. With the reduction of T_S, F_{xx} becomes governed by the accumulation of negative buoyancy from plate convergence. By 150 km of

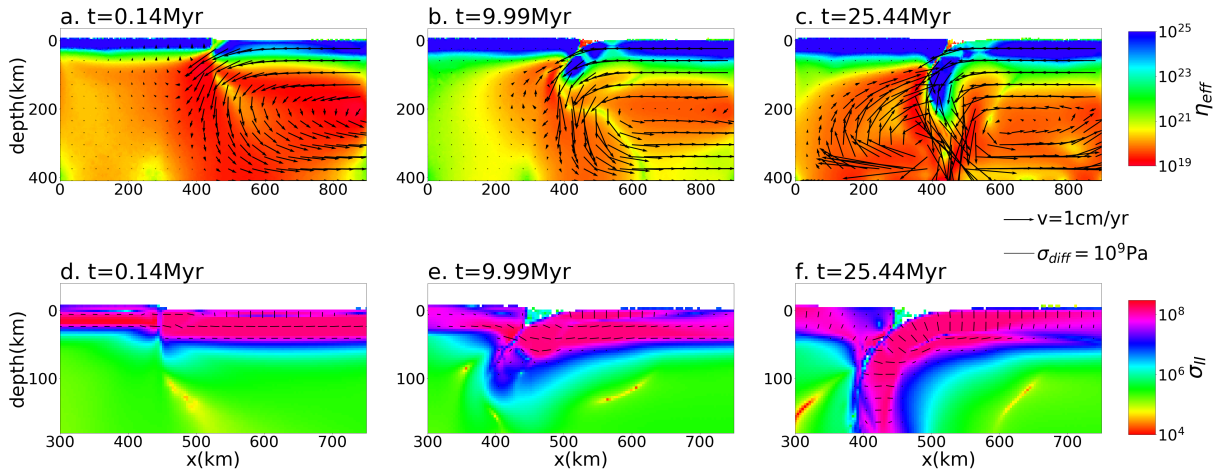

Figure 2.3: a–c. The effective viscosity (as $\log_{10}(\eta_{eff})$) is color coded and overlain by the velocity vector at different time from velocity boundary model u = 1 cm/yr. d–f. The second invariant of stress σ_{II}(as $\log_{10}(\sigma_{II})$) is color–coded and overlain by the stress bar, from the same model as a–c. The length of the stress bar represent the difference between the largest and smallest principal stress, σ_{diff}, and the direction is the direction of the smallest principal stress (compression axis).

convergence, the subducted oceanic crust starts to metamorphose to dense eclogite, accelerating the drop of F_{xx}. By 200 km convergence, F_{xx} drops to 0, and the state–of–stress in the slab and in the in–coming plate becomes extensional (Fig. 2.3e, f). The flip in sign of F_{xx} indicates that subduction has become self-sustaining, the end of the period of subduction initiation, t_{SI}.

In addition to changes associated with plate convergence, ℓ, F_{xx} systematically changes with the convergence velocity, u_0. From eq. 2.13, the u–dependence comes from the basal shear F_a and the bending torque, ΔN_b. The non-Newtonian viscosity influences the shear resistance from the base of subducting slab, and with a constant plate velocity (e.g. a constant strain rate at the base of the plate), its role can be more easily isolated. In this model, the effective viscosity at the base of lithosphere is 10^{19} to 10^{20} Pa·s and the estimated basal shear force F_a, is 10^{11} to 10^{12} N/m (for several cm/yr plate velocity). The normal force from bending, ΔN_b, consists of two term: N_{HZ} from the hinge zone and $K_b u$ outside of the hinge zone. In the hinge zone, where the flow is dominated by plasticity, the change of normal force

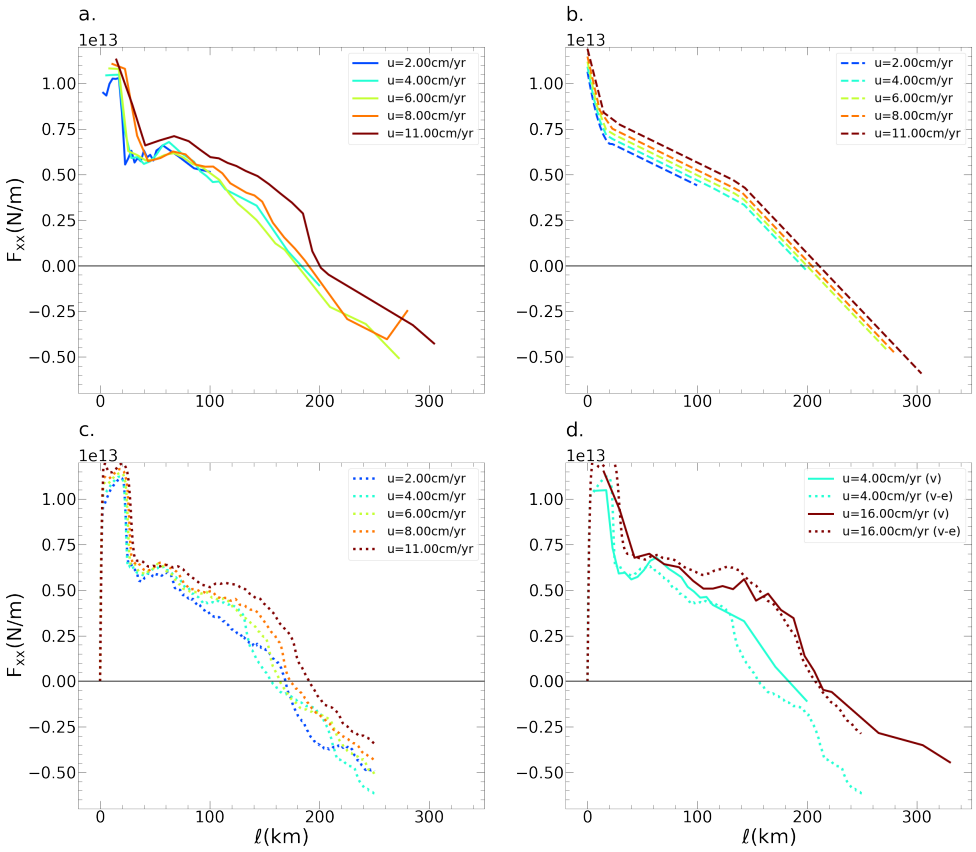

Figure 2.4: For the velocity boundary models, the force within the plate, F_{xx}, versus the amount of plate displacement, ℓ. a. Results from the numerical model with a visco–plastic rheology and different rates of imposed convergence. b. As in a, except from the analytical solution. c. As in a, except for a visco–elasto–plastic rheology. d. Comparison of visco–plastic (solid) and visco–elasto–plastic (dotted) rheologies for large and small convergences. The applied plate velocity is encoded by different colors.

is independent of u (Appendix B). Outside of the hinge zone, the plate viscosity is mainly governed by temperature and thereby a constant through the plate, so that the normal force change is only controlled by $K_b u$. As the bending barely takes place outside the hinge zone, the contribution of normal force change outside hinge zone is negligible with a fairly small yielding stress ($K_b u \ll \Delta N_{HZ} \approx 10^{12}$N/m). For estimating the value, we chose $K_1 = K_b + \frac{L_P}{d_a}\eta_a \approx \frac{L_P}{d_a}\eta_a \approx 4\times10^{20} Pa \cdot s$ (Fig. 2.4b). In the domain of $F_{xx} - \ell$, K_1 determines the spacing between curves as plate velocity varies (Fig. 2.4b).

The analytical model is further validated by comparing the spatial variation of the compressional plate normal force $F_{ss} = -\int_{-H/2}^{H/2} \sigma_{ss} dz$ within the plate for the case $u_0 = 1$ cm/yr at 15 Myr (Fig. 2.5). As shown in Appendix A, the change of the compressional plate normal stress $F_{ss}(= -N_b)$ is a consequence of basal traction, inter-plate traction, negative buoyancy, bending torque, and isostatic force. We compare the change of F_{ss} along the plate from numerical and analytical solutions (Fig. 2.5b). Different components contributing to the changing F_{ss} are evaluated analytically (Fig. 2.5c). The evaluation of ΔN_{NB}, F_a, T_s and F_I follows the formulations we derived in eq. 2.2, 2.6, 2.7, 2.8 ,and 2.11. For the ΔN_b, we follow Buffet, 2006 and Ribe, 2001:

$$\frac{dN}{ds} = k\frac{dM}{ds} \tag{2.21}$$

Where M is the bending torque $M = \int_{-H/2}^{H/2} \sigma_{ss} z dz$, and $N = -F_{ss}$. Note that the validation of the analytical solution contains the plate curvature k, which is based upon the slab geometry from numerical models. As an example along the center line temperature contour ($T = 600^\circ$ C), the measured curvature of the plate is shown in Figure 2.5a, with details in supplementary material section Evaluating Plate Curvature(Section 2.7).

Three principal stages emerge from the variation of F_{ss} with s (Fig. 2.5b): From $s = 500$ to 450 km (note that s is a function of x in Fig. 2.5a, as denoted with the colored filled circles), the plate stress F_{ss} decrease from 0 at the slab tip into a negative F_{ss}, an extensional stage driven by negative buoyancy; from $s = 450$ to 300 km, despite a large negative buoyancy (N_{NB}), the inter-plate friction (T_s), is the dominant resisting term, and together with F_I and N_b, causes a transition in state–of–stress from extension to compression. For $s < 300$ km, there is no substantial bending or slab pull, and so the only term present is the basal shear resistance, which is responsible for the slow increase of F_{ss} from the plate boundary to its plate interior.

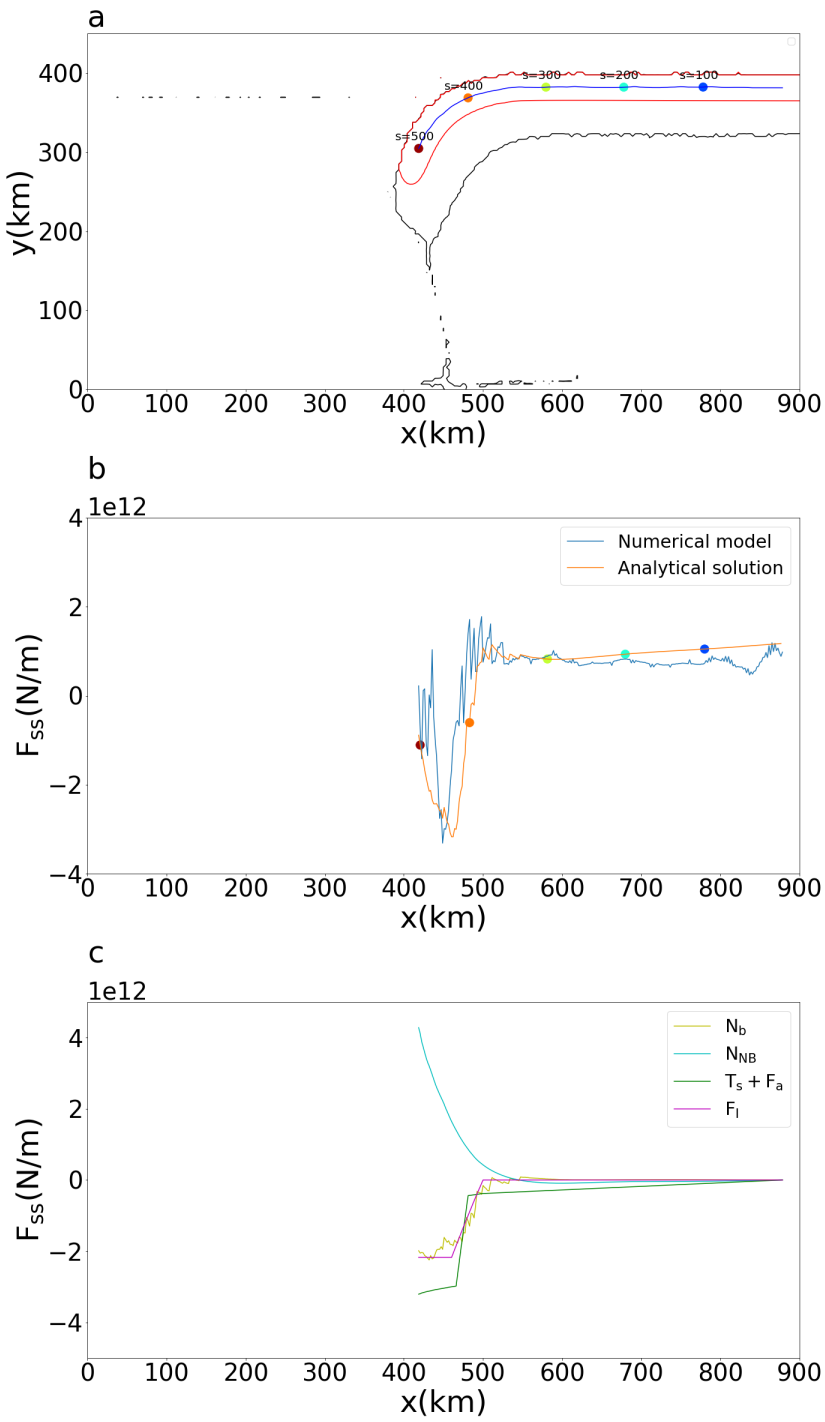

Figure 2.5: a. Outline of the thermal plate (in black) and mechanical plate (in red), as well as a curve denoting the plate center determined from the mechanical plate. b. The total stress F_{ss} along the plate from numerical and analytical. c. The different components making up the bending force predicted by the analytical solution. By the definition of F_{ss}, positive means compression and negative means extension. As the analytical solution only predicts the change of normal force, all the components of normal force in c are fixed on the right end, such that the change along the curves are ΔN_{NB} or ΔN_b. The analytical solution in b is the summation of all the component in c, but a constant is added to align the analytical solution in b with the numerical model. The numerical model is with visco-plastic rheology. Static pressure $P = \int \rho g dz$ is removed in all the measurement of stress.

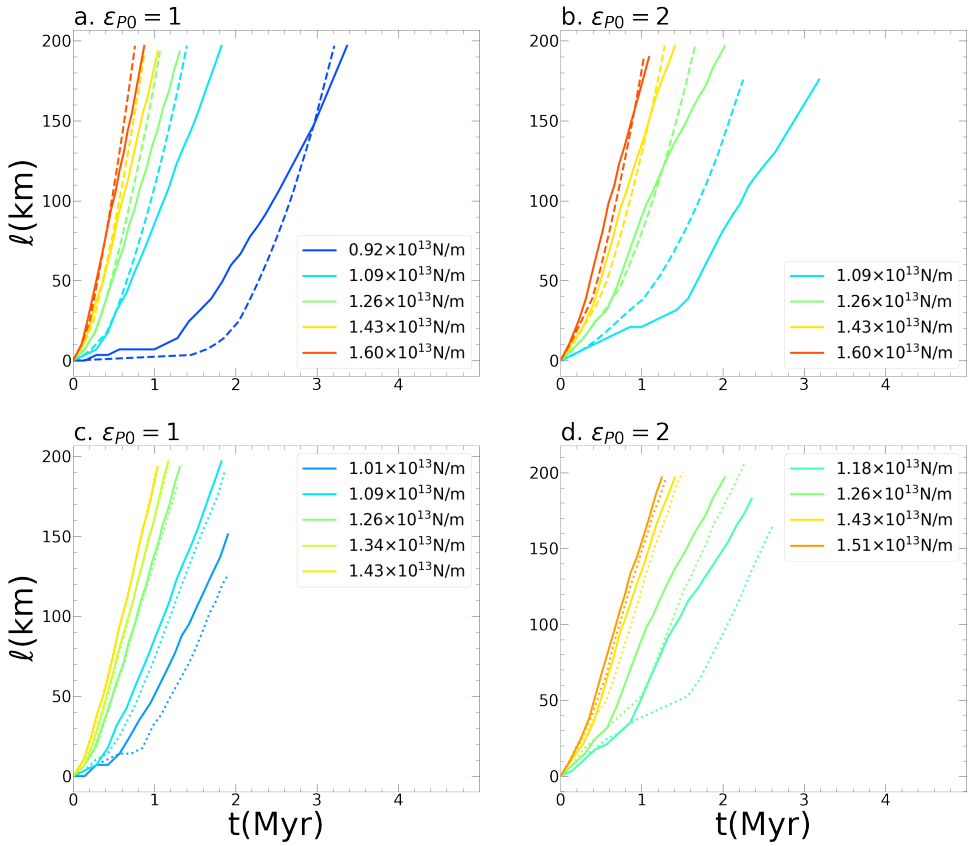

Figure 2.6: Plate displacement ℓ vs time from force boundary condition with a, c: $\varepsilon_{P0} = 1$ and b, d: $\varepsilon_{P0} = 2$. The color represent applied force. a, b: comparison between analytical solution (dashed) and numerical model (solid) with visco–plastic rheology. c, d: the comparison between visco-plastic (solid) and visco–elasto–plastic model (dotted).

Force boundary

We now turn to the case where a force boundary is used. The dynamics of a nascent boundary evolves with the primary features in viscosity (Fig. 2.7a-c) being similar to when velocity boundary conditions are used. A relatively high asthenospheric viscosity is used ($\sim 10^{20}$ Pa· s) allowing reasonable plate velocities with a relatively short plate length. The small domain is a reflection of the need to systematically sweep through the parameter range at a reasonable computational cost, and with the relatively large asthenospheric viscosity $\eta_a \approx 10^{20}$Pa · s acting on the short plate ($\sim$ 400 km), the total F_a is equivalent to the plate with realistic length scale (L_P = 4000 km) and viscosity ($\eta_a = 10^{19}$Pa · s). In the force boundary scenario, the plate interior stresses (Fig. 2.7d–f) remain in compression, unlike the velocity boundary ones where the plate stress experiences a rapid conversion from compression to extension. The evolutionary pathway branches in two directions: For small applied forces the plate boundary remains stable and subduction never initiates, while for forces that exceed the threshold $F_{xx} > T_S + F_I + N_{HZ}$ (when $u > 0$ in eq. 2.15), subduction initiates. Displacement accelerates with time for a variety of applied forces and weakening rates, with close agreement between the finite element and analytical solutions (eqs. 2.16 and 2.17; Fig. 2.6). The parameters used in the analytical solution see Table 2.1. Despite most of the parameters for the force boundary being the same as the ones used in the velocity boundary model, several differ. The K_1 term governs the resistance associated with plate velocity, and is dominated by F_a, i.e. $K_1 \approx \eta_a \frac{L_P}{d_a}$. Although we set pre–factor for the viscosity law in the mantle to a higher value in the force boundary models, the effective viscosity does decrease with the non–linearity as plate velocity increases. Therefore, unlike the velocity boundary model with a constant $K_1 = 4.4 \times 10^{20}$ Pa · s, the force boundary has two stages: prior to the plate boundary being fully weakened ($\ell < \delta\varepsilon_{P0}$), $K_1 = 2.6 \times 10^{21}$Pa · s, and after the weakening with a higher plate velocity and lower η_a, $K_2 = 1.9 \times 10^{21}$Pa · s.

Plate Curvature

Plate curvature, k, is a key factor in evaluating plate bending. In a bending plate, the strain rate is $\dot{\varepsilon}_{ss} = -zu\frac{dk}{ds}$ (Buffet, 2006), and the stress $\sigma_{ss} = -4\eta zu\frac{dk}{ds}$, so that plate curvature directly reflects plate deformation due to bending. Details on the measurement of plate curvature is provided in Supplementary Material section S3. A comparison of $\frac{dk}{ds}$ with maps of second invariant in strain rate from a case with u = 1 cm/yr (Fig. 2.8), shows two plateaus of $\frac{dk}{ds}$, one positive and one negative, that

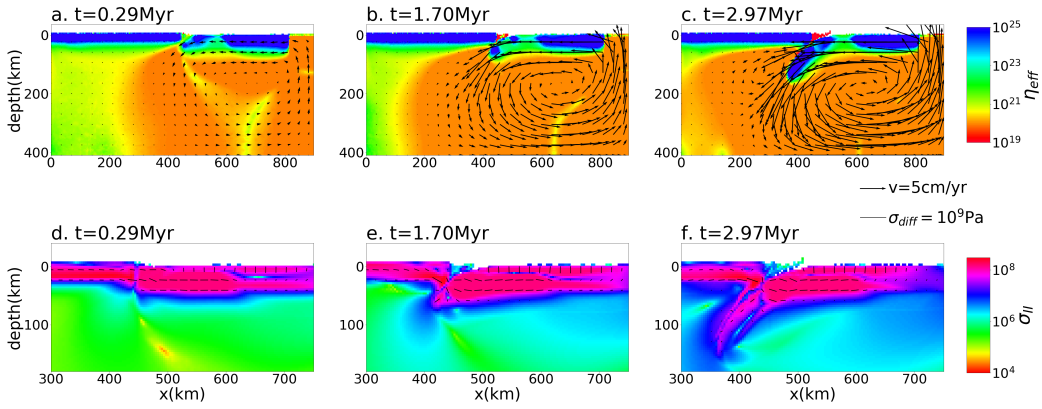

Figure 2.7: a–c. The effective viscosity (as $\log_{10}(\eta_{\text{eff}})$) and the velocity vector from force boundary model $F_{xx} = 9.24 \times 10^{12}$ N/m. d–f. The second invariant of stress σ_{II}(as $\log_{10}(\sigma_{II})$) is color–coded and overlain by the direction , from the same model as a to c.

correlate with two yielding area (bending and unbending) in the hinge zone, where the $\dot{\varepsilon}_{II}$ is 2 orders of magnitude higher than in other regions. The spatial correlation between areas of high strain rate and the $\frac{dk}{ds}$ peaks verifies the relation between strain rate and curvature. In previous studies, including Buffet, 2006, the plate bending force is simplified as $\Delta N = -\frac{1}{6}(\frac{H}{\Lambda_{\min}})^3 \eta u$, based upon the assumption that k linearly increases from 0 to $\frac{1}{\Lambda_{\min}}$, and then linearly decreasing from $\frac{1}{\Lambda_{\min}}$ to 0 with the same rate. This assumption has k changing with s linearly and symmetrically, and $\frac{dk}{ds}$ is similar to a single period of a square–wave–like function in terms of s. The measured $\frac{dk}{ds}$ versus s (Fig. 2.9b) shows negative and positive plateaus of $\frac{dk}{ds}$ with roughly the same amplitudes validating the simple assumption. The symmetrical shape of k agrees with measurement in earlier studies (F. A. Capitanio, Morra, and Goes, 2009; Farrington, L.-N. Moresi, and F. A. Capitanio, 2014). This behavior of $\frac{dk}{ds}$ reflects symmetry of the bending and unbending of the plate. The maximum slab curvature is about 5 to 8×10^{-6} m^{-1} (Fig. 2.9a), so that the minimum radius of curvature, $\Lambda_{\min} = \frac{1}{k_{\max}}$, is 100 to 200 km. Although k with s is linear and symmetric, the relationship $\Delta N = -\frac{1}{6}(\frac{H}{\Lambda_{\min}})^3 \eta u$ may not apply as η is spatially heterogeneous due to plastic yielding, a point examined in the next section.

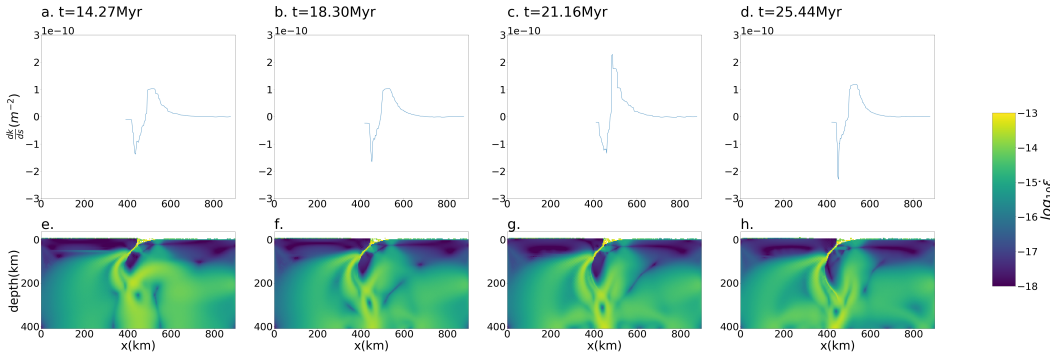

Figure 2.8: a–d. $\frac{dk}{ds}$ vs x from velocity boundary model with $u = 1$ cm/yr at four different times. e–h. strain rate (as $\log_{10}(\dot{\varepsilon})$) at the same time as a–d. Peaks and troughs in a–d correlate with the hinge zone areas in e–h.

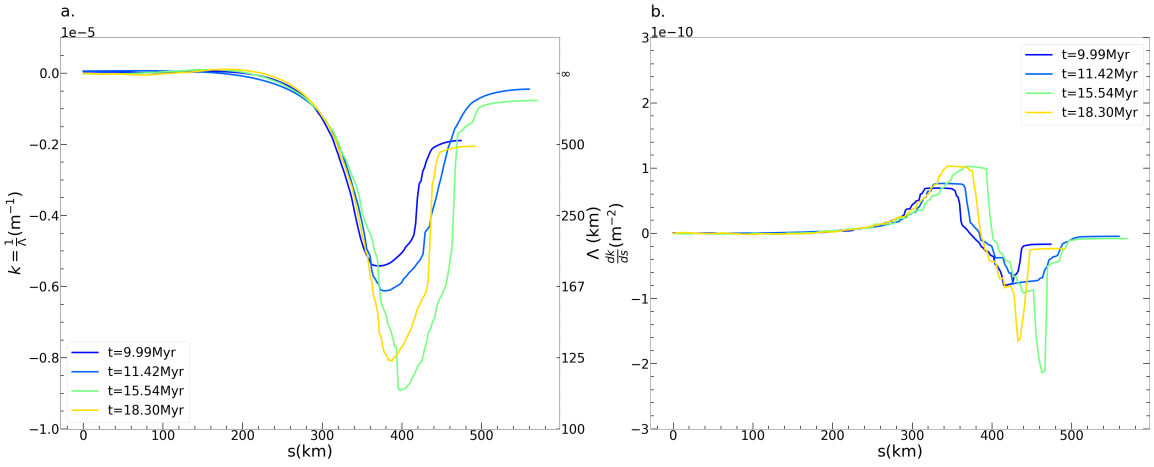

Figure 2.9: a. $\frac{dk}{ds}$ and b k vs s at different times from velocity boundary condition models with $u = 1$ cm/yr. s is the distance from the right end of the plate. Λ (on the right axis of b) is the radius of the curvature, so that $\Lambda = \frac{1}{k}$.

Hinge zone

A prominent feature of the hinge zone is the reduction in viscosity there (Fig. 2.3 and Fig 2.7), specially where the subducting slab experience substantial bending with a reduction in viscosity due to plastic yielding. In the hinge zone, there are typically two symmetric sectors with large deformation. The upper sector is typically in extension while the lower sector is in compression. Positive and negative peaks of $\frac{dk}{ds}$ correlate with where the plate bends and unbends (Fig. 2.8). With the previously assumed constant slab viscosity, the resistance from plate bending is proportional to plate velocity $\Delta N_b = K_b u$, while when the hinge zone yields by plastic failure, the bending torque is independent of plate velocity. The analytical solution, $N_{HZ} = \frac{1}{6} H^2 S_{HZ} \tau_y (\frac{dk}{ds})_{\max}$, and measurement in numerical model (Fig. 2.5c) consistently predicts $N_{HZ} \approx 2 \times 10^{12}$N/m. For the numerical models, the bending resistance is derived from $dN_b = k dM$, where M is bending moment. N_b only changes substantially near the bending area, $450 < x < 550$ km, and the total bending resistance across the hinge zone is $\Delta N_b = N_b(450) - N_b(550)$. ΔN_b is independent of plate velocity u (Fig. 2.10a), agreeing with a bending torque in the hinge zone(s), N_{HZ}, that remains constant. This result, in contrast to ΔN_b being proportional to u with a constant η, reflects the dominance of plasticity within the hinge zone. With an increased plate velocity and higher strain rates, assuming plate curvature remains invariant, the hinge zone viscosity is reduced. The influence of plastic yielding on effective viscosity is quantified with an average viscosity in an analogous way a bending moment is defined (e.g. a weighting over $\dot{\varepsilon} \times z$)

$$\bar{\eta} = \frac{\int_{-H/2}^{H/2} \eta z^2 dz}{\int_{-H/2}^{H/2} z^2 dz} = \frac{12}{H^3} \int_{-H/2}^{H/2} \eta z^2 dz \tag{2.22}$$

This then leads to the compact expression for $M = -\frac{1}{3} \bar{\eta} u H^3 \frac{dK}{ds}$. On the other hand, due to plastic yielding, $M = \frac{\tau_y H^2}{4}$, a constant independent on u, we expect $\bar{\eta} \sim \frac{1}{u}$. For the quantity $\bar{\eta}$ with s (shown with a log scale in Fig. 2.10b), the most prominent features are the dips, one between $x = 500$ and 600 km and the other between $x = 400$ and 500 km where $\bar{\eta}$ varies by 2 orders of magnitude. These two low $\bar{\eta}$ areas are the hinge zone areas where the strongest bending and unbending happens due to the plate yielding. In the hinge zones, the $\bar{\eta}$ decrease with increased u, and the product of $\bar{\eta}$ and u remain generally constant as u changes (Fig. 2.10c), verifies that the reduction of $\bar{\eta}$ due to plastic yielding cancels the variation of strain rate due to varied plate velocity and the bending torque is generally independent of u.

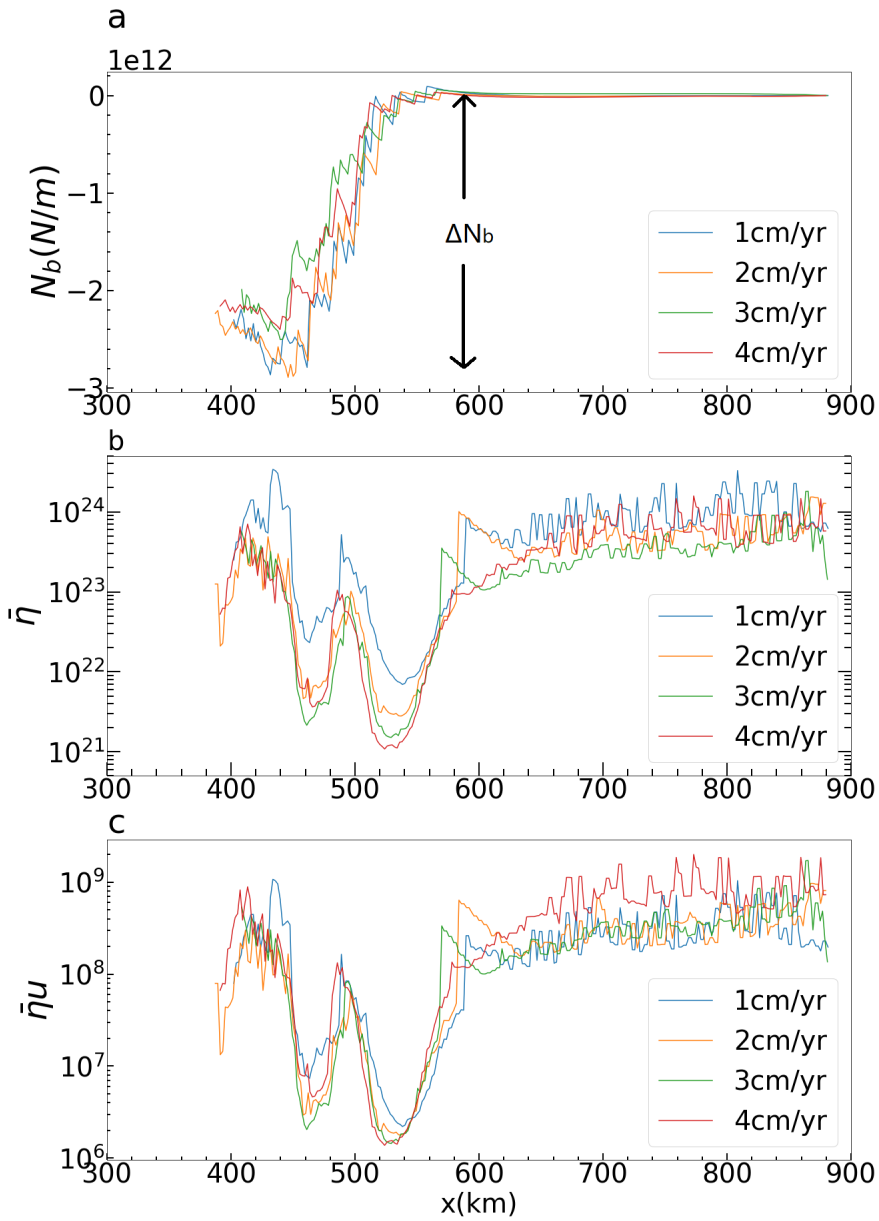

Figure 2.10: a. The normal force change N_b due to plate bending from velocity boundary models with different u but the same plate motion $\ell(= 120\text{km})$. b. Average viscosity $\bar{\eta}$ (as $\log_{10}\bar{\eta}$) from the same snapshots as a. c. $\log_{10}(\bar{\eta}u)$ from the same snapshots as a. Due to plasticity, $\bar{\eta} \sim \frac{1}{u}$, $\bar{\eta}u$ is supposed to be a constant independent on u.

Initiation time

Plate stress and plate motion evolve in velocity–imposed and force–imposed scenarios, with the principal driving force experiencing a transition from an initial external compression to dominance by slab pull. Consequently, we define an initiation time when slab pull becomes dominant. For velocity boundary models, F_{xx} decreases with time, and we define the time when $F_{xx} = 0$ to be the time of initiation, t_{SI}. After t_{SI}, the internal driving force (negative buoyancy), is able to overcome all the resistance and the plate can move without any external driving force. From eq. 2.14 we obtain $\ell_{SI} = (D + (2\eta\frac{L_P}{d_a} + K_b)u_0 + N_{HZ} + F_I)/(\Delta\rho \sin\theta)$. Initially, the thermal contraction is the major source for negative buoyancy as no metamorphism takes place. At $\ell \approx 150$km, the density anomaly from eclogite metamorphism augments the negative buoyancy (Fig. 2.4). As plate convergence reaches about 200 km, F_{xx} becomes less than zero, and with the inclusion of eclogite metamorphism, we obtain

$$\ell_{SI} = \frac{D + (2\eta\frac{L_P}{d_a} + K_b)u_0 + N_{HZ} + F_I + d_c\Delta\rho_e g \sin\theta \times (150 \text{ km})}{\frac{1}{2}H\rho_0\alpha\Delta T g \sin\theta + d_c\Delta\rho_e g \sin\theta} \tag{2.23}$$

As $t_{SI} = \frac{\ell_{SI}}{u}$, we see that that this time–scale is primarily influenced by plate velocity, and secondarily plate age and plate strength through the bending toque and isostatic force (Fig. 2.12a–c). The increase of ε_{P0} slows the weakening, thereby delaying the onset of a state of neutral stress.

Unlike the velocity boundary where the F_{xx} changes with time, for the constant force boundary, as the plate interior stress is governed by the boundary condition, F_{xx} equals the applied boundary force. Together with the accumulation of negative buoyancy and weakening, the plate speed u accelerates with time. Therefore, we define the initiation time as the time when the plate convergence reaches a certain quantity ℓ_{SI}. With eq. 2.24

$$t_{SI} \approx \frac{4K_1\tau_{y0}}{B_1^2 + 4C(F_{xx} - A - F_I - N_{HZ})} + \frac{K_1(\ell_{SI} - \delta\varepsilon_{P0})}{F_{xx} - D - F_I - N_{HZ}} \tag{2.24}$$

The exact solution of t_{SI} see equation 2.30.Here we choose $\ell_{SI} = 200$km, roughly equal to the ℓ_{SI} for velocity boundary models. Maps show the prediction of the initiation time from equation 2.30, with force, plate age, τ_{max}, and ε_{P0} (Fig. 2.12d–f). Due to the nature of the force boundary condition, the plate experience continuous speedup, and together with the increasing negative buoyancy, the t_{SI} is relatively small compared to the velocity boundary models where the plate velocity is confined with the boundary condition. Despite of the absolute t_{SI}, the changing of t_{SI} with

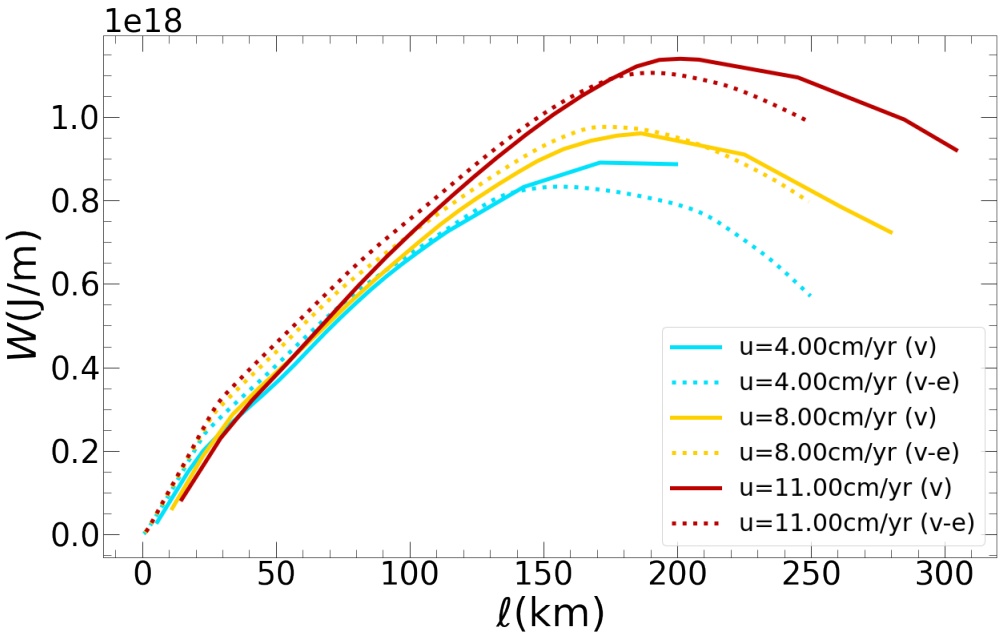

Figure 2.11: The total work W done by F_{xx} with respect to plate motion ℓ from velocity boundary models with different convergent rates with visco-plastic rheology(solid) and visco-elasto-plastic rheology(dotted).

respect to the plate age, τ_{max} and ε_{P0} obey the same trend as found for velocity models (Fig 2.12a–c). The No SI domains (the shaded regions in Fig. 2.12d–f) predicted from equation 2.30 are consistent with the numerical models, that is when an insufficient force applied to the boundary fails to induce subduction initiation.

Work done to initiate subduction

Having established the time to initiate subduction, we can now turn to the total work done by the compression up to this time. In the imposed velocity configuration, the in–plate force is integrated with plate convergence

$$W(\ell) = \int_0^{\ell} F_{xx}(\ell')d\ell' \tag{2.25}$$

in which W reflects the work done on the system by the boundary condition. Initially, W increases with ℓ as F_{xx} is compressional and the plate motion is driven by boundary velocity (Fig. 2.11). However, as negative buoyancy accumulates and the plate boundary weakens, W eventually peaks when $F_{xx} = 0$, the same criteria defining t_{SI}. Consequently, at the peak of $W(\ell)$, we define W_{SI}, the total work done to initiate subduction. As expected, we find a close agreement between the work

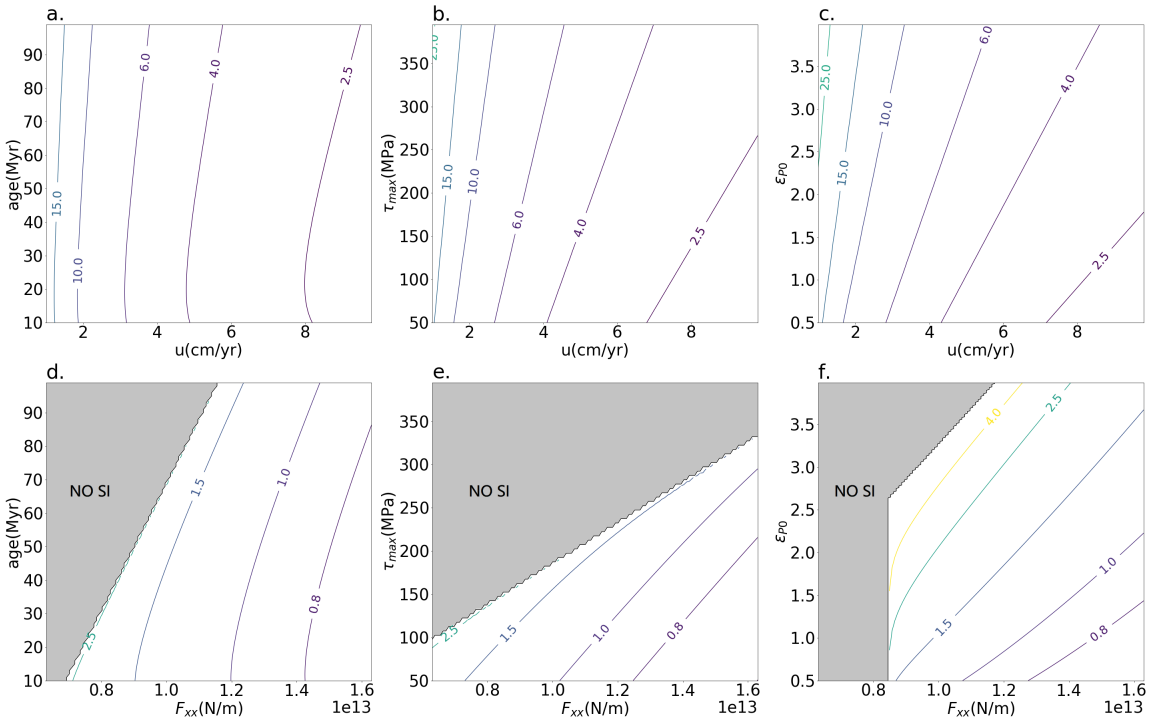

Figure 2.12: a–c. Contours of t_{SI} from analytical solution for velocity boundary models. d–f. The same contours for the force boundary models. The varying parameter include plate velocity u for velocity boundary models and boundary force F_{xx} for force boundary models. The age of subduction plate (a, d), plate strength τ_{max} (b, e) and weakening rate ε_{P0} (c, f) are varied. The gray area in d–f denotes parameter domains where there is no initiation. When the parameters are not varied, the default values are plate age = 40 Myr, τ_{max} = 150 MPa, ε_{P0} = 1.

predicted by the simple force balance model with the full numerical results for the same rate of weakening, controlled through $\varepsilon_{P0} = 1$ (Fig. 2.13a). On average, the simple model slightly over–predicts the work done as a function of convergence velocity.

As an increased convergent velocity u incurs greater dissipation in the system, the numerical models and analytical models consistently predict an increase of W_{SI} with larger u (Fig. 2.13a). In addition to the plate velocity u, the dissipation is strongly influenced by the weakening process, therefore we evaluate the W_{SI}-u with different weakening rate from the analytical solution using eq 2.14 and eq 2.25 (Fig 2.13b). With an increase in u from 1 to 10 cm/yr, W_{SI} only increases by less than 5×10^{17} J/m, while an increase of ε_{P0} by a step of 1 can lead to 1×10^{18}J/m increase in W_{SI}. Compared to plate velocity, the plate weakening caused by the plate motion has a larger impact on the total energy dissipation in the system and demonstrates

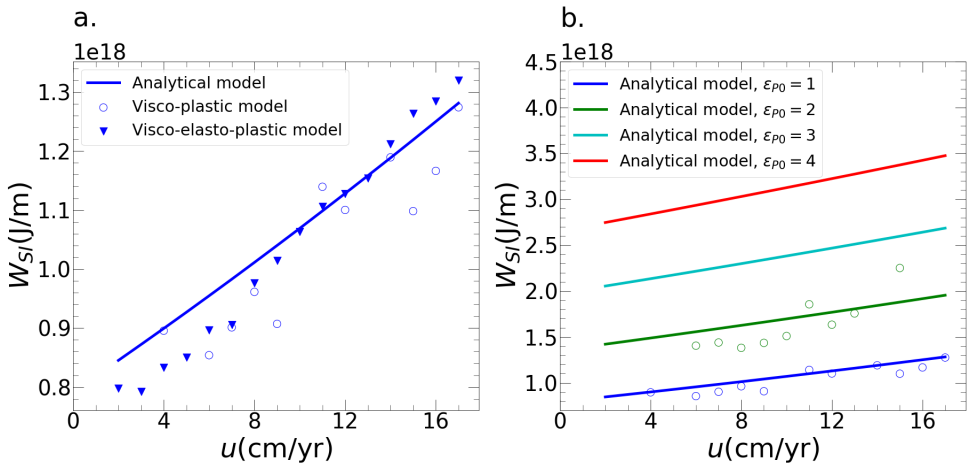

Figure 2.13: a. The work done to initiate subduction, W_{SI}, from models with different convergent velocities at $\varepsilon_{P0} = 1$. Solid line is for analytical solutions, open circles for visco-plastic models, and filled triangles for visco-elasto-plastic models. b. Analytical prediction of W_{SI} vs u with different ε_{P0}'s (color-coded) for visco-plastic rheologies.

the importance of the rate of subductin zone nucleation in determining how hard, or how much work it takes, to make a new subduction zone.

Isostatic Force

The isostatic force F_I, defined in eq. 2.11, is the normal force due to lateral pressure gradients across the plate boundary where the plate's thermal and compositional structure change sharply. The integration of pressure over depth with respect to x, $F_p = \int_0^H p dz$, across the plate boundary in the numerical model shows large fluctuations due to plate bending and inter–plate friction, but with a clear offset between overriding and subducting plates (Fig. 2.14). Analytically, the estimated combination of thermal and compositional isostatic forces, F_I (eq. 2.9 and 2.10), is 2.07×10^{12} N/m, close to the measured difference across the plate boundary (Fig. 2.14). In different scenarios of subduction initiation, F_I can function as either a driving or resistance term. In the model, the subduction initiation is induced by a horizontal driving force, and F_I pushes against the far field driving forces and resists plate motion, hence inhibits subduction initiation. In the other mode of subduction initiation, so called spontaneous subduction initiation (R. Stern, 2004), the slab founders vertically into the mantle without external compression, and F_I acts as a force that drives local compression against plate bending (Nikolaeva, T. V. Gerya, and F. O. Marques, 2010; Leng and Gurnis, 2015). In our cases, an F_I of $\approx 2 \times 10^{12}$

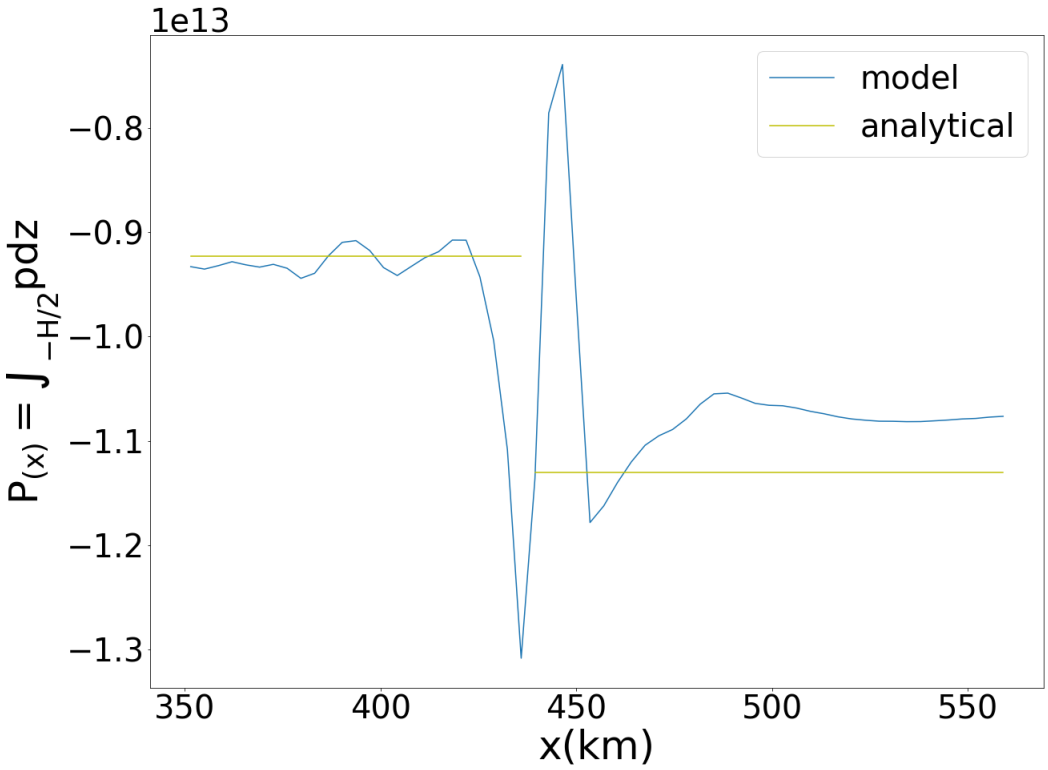

Figure 2.14: The integration of pressure over depth in the lithosphere, $F_p = \int_0^H p dz$. Here the pressure p is the dynamic pressure (non-hydrostatic), and H the plate thickness. The plate boundary is at $x = 450$ km.

N/m is roughly equal to the estimated bending torque but smaller than the initial plate boundary friction; consequently F_I is insufficient to overcome the resisting forces and no spontaneous subduction initiation occurs in the model, consistent with the finite elements computations.

Elasticity

Thus far, the calculations have been based on a fluid constitutive relation, but the lithosphere experiences elastic deformation, which can be bridged with visco–elastic models. Here we compare visco–plastic results with ones with visco–elasticity to isolate the role of elasticity during subduction initiation. This is important because both constitutive relations have been used in prior studies, including those using visco–elasto–plastic (Toth and Gurnis, 1998; Gurnis, C. Hall, and Lavier, 2004; Nikolaeva, T. V. Gerya, and F. O. Marques, 2010; Leng and Gurnis, 2015) and those assuming visco–plastic (Zhou, Zhong-Hai Li, et al., 2018; Arcay et al., 2020;

Maunder et al., 2020). We assume the material deforms as a Maxwell body, with a shear modulus μ, $\dot{\boldsymbol{\varepsilon}} = \dot{\boldsymbol{\varepsilon}}_e + \dot{\boldsymbol{\varepsilon}}_v = \frac{\dot{\tau}}{2\mu} + \frac{\tau}{2\eta}$ which has a relaxation time $t_e = \frac{\eta}{\mu}$ (Ranalli, 1995). For a lithosphere with $\eta = 10^{24}$ P$a \cdot s$ (Fig. 2.10) and $\mu = 3 \times 10^{10}$ Pa, $t_e \approx 1$ Myr, on the same order as subduction initiation. However, with the presence of plasticity, the effective viscosity can drop by orders of magnitude within the hinge zone after the nucleation stage, when the plate bending becomes more fully developed and the interplate boundary weakens. With a hinge zone viscosity $\approx 10^{23}$ P$a \cdot s$, $t_e \approx 0.1$ Myr , smaller than the time–scale for subduction initiation. This suggests that elasticity is likely to diminish as plastic yielding comes to dominate.

The role of elasticity is examined by re–calculating models presented earlier, while keeping all parameters the same except substituting a viscous with a Maxwell body (L. N. Moresi, Dufour, and Mühlhaus, 2003). From the relation F_{ss} vs. ℓ (Fig. 2.4c), we observe how elasticity changes the stress evolution. With visco–elasticity, the force starts at 0 and increases with convergence as elastic stresses buildup. Later, as the plate bends and the hinge zone yields, the relaxation time drops by orders of magnitude, and the governing rheology turns from visco-elastic to dominantly viscous. The drop of η_{eff} and t_e weakens the role of elasticity, and the evolution of the visco–elasto–plastic model closely follows the visco–plastic model after the elastic stress buildup stage (Fig. 2.4d). The work done by the compression to initiate subduction, W_{SI}, is computed for the visco–elasto–plastic cases as for the visco–plastic ones. Although the pattern of W_{SI} vs. ℓ is not strongly influenced by the elasticity (Fig. 2.13a), visco–elasto–plastic models have systematically higher W_{SI} when u is large ($u > 10$ cm/yr). With small u, as the time–scale of subduction initiation is much greater than the Maxwell relaxation time, the viscous deformation dominantly governs the visco-elastic system and the role of elasticity is negligible. In contrast, with a sufficiently large u, the time scale of subduction initiation becomes smaller than the Maxwell time, allowing the elasticity to play a larger role. Care must be taken with the elastic time steps Δt_e in the numerical model, which can influence the stress evolution, as discussed in the Supplementary Material. With an appropriately small Δt_e (a domain where visco–elastic benchmarks show that *Underworld* solutions converge to analytical ones (L. N. Moresi, Dufour, and Mühlhaus, 2003; Farrington, L.-N. Moresi, and F. A. Capitanio, 2014)), the computations show that the role of elasticity can be minor (Fig. 2.4c).

When force boundary conditions are used there are also some differences between models with and without elasticity. With elasticity, the amount of convergence rate slows with time and is associated with a systematic increase in the resisting force due to the addition of elasticity (Fig. 2.6c–d). The difference caused by elasticity is minor for cases with large F_{xx}. A larger force leads to more yielding and a smaller relaxation time. For a smaller F_{xx}, the elasticity makes a larger difference, as the initiation process occurs over a time–scale that is comparable to the Maxwell time.

The addition of elasticity provides an additional force after bending becomes developed, with the elastic stress adding an additional resistance force which slows the incoming plate. However, elasticity does not cause a substantial difference in most cases due to plasticity, which we verify by varying the yielding stress τ_{max} in velocity boundary models (Fig. 2.15) and force boundary models (Fig. 2.16). With velocity boundary conditions and a low yield stress (150 to 300 MPa, Fig. 2.15a,b) the hinge zone deformation is dominated by plastic yielding, and the visco–elasto–plastic and visco–plastic models produce nearly indistinguishable $F_{xx} \sim \ell$ curves. When yield stress increases (600 MPa to 1.2 GPa), the hinge zone viscosity is less affected by the yielding, and the elasticity causes a more prominent difference (Fig. 2.15) when the subduction zone is fully developed ($\ell \approx 300$ km). For the force boundary model (Fig. 2.16), the difference in $\ell \sim t$ due to elasticity is distinct only when the applied force is small, and the increased yield stress (300 MPa, Fig. 2.16b) makes the elasticity more prominent. The diminished role of elasticity with decreased yield stress confirms the influence of elasticity is governed by plastic yielding: With a small yield stress (τ_{max} = 150 to 300 MPa), the role of elasticity during subduction initiation seems limited.

2.6 Discussion

We have developed a simple, time–dependent analytical model tailored to induced subduction initiation with two different boundary conditions – velocity and force – corresponding to different tectonic settings. With velocity boundary conditions, plate motion is regulated by the boundary conditions regardless of the state–of–stress, and such a scenario would reflect subduction initiation localized along a small segment of strike of a nascent plate boundary. As the nascent segment is small, the resistance against plate motion from subduction initiation is similarly small compared to the far–field forces driving convergence; consequently, the plate motion is mostly unaffected by the abrupt changes of resistance during initiation, thereby maintaining a constant velocity. The Puysegur subduction zone south of

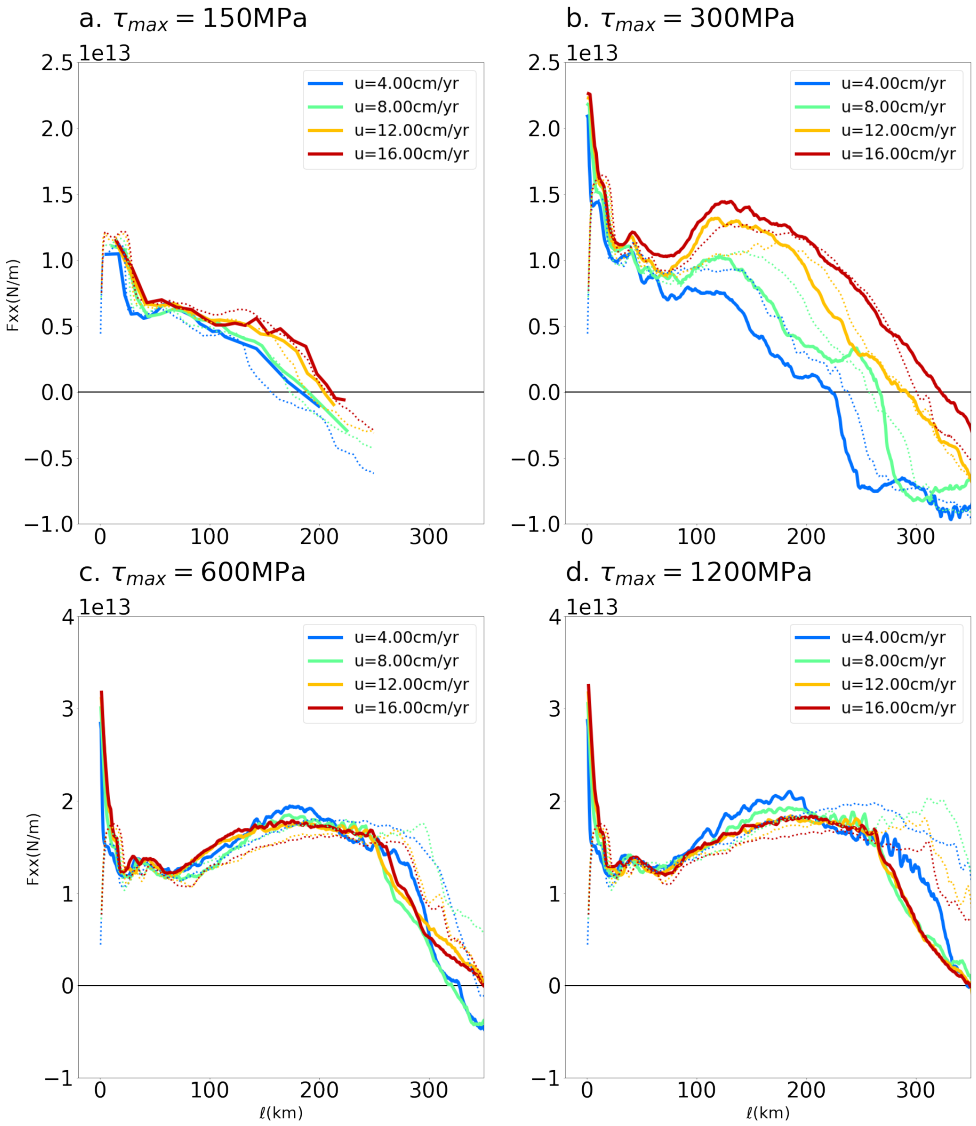

Figure 2.15: F_{xx} vs ℓ from visco-plastic model(solid) and visco-elasto-plastic model(dotted) with velocity boundary with yielding stress τ_{max} equals a. 150 MPa, b. 300 MPa, c. 600 MPa and d. 1200 MPa.

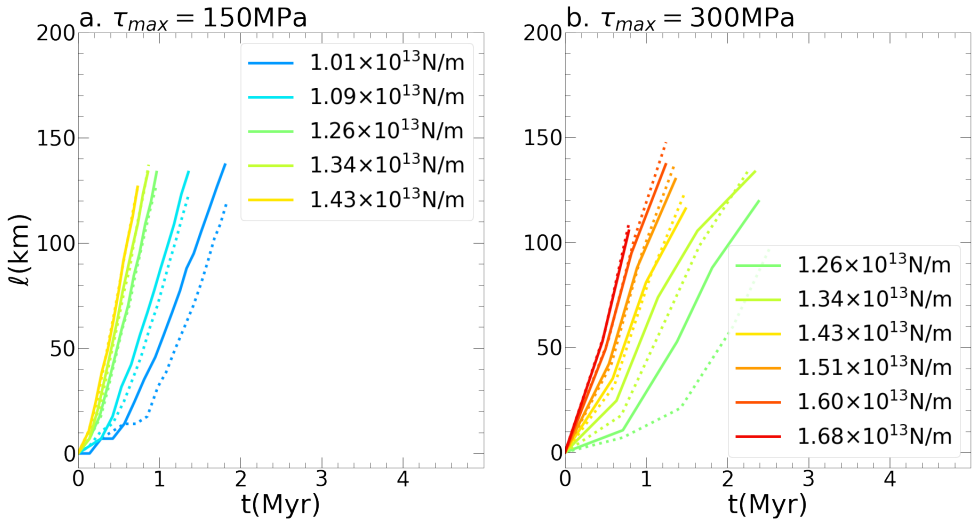

Figure 2.16: ℓ vs t from visco-plastic model(solid) and visco-elasto-plastic model(dotted) with force boundary with yielding stress τ_{max} equals a. 150 MPa and b. 300 MPa.

New Zealand (J.-Y. Collot et al., 1995; Gurnis, Van Avendonk, et al., 2019; B. Shuck et al., 2021) is in such a state. Here, the Australian Plate subducts under the Pacific Plate over a lateral extent of ≈400 km, small compared to the more fully developed subduction zones over thousands of km pulling Australia to the north. In this example, the Australia–Pacific plate kinematics are not expected to experience a substantial change due to the Puysegur subduction initiation which started at ≈ 15 Ma (Lebrun, Lamarche, and J.-Y. Collot, 2003; Sutherland, Barnes, and Uruski, 2006; Brandon Shuck et al., 2022) and the model developed here is applicable to this setting.

In contrast, the force boundary reflects the extreme where the plate kinematics are initially governed by the applied far field stress, but as the initiated boundary grows it can cause a change in plate kinematics. The reorganization of Pacific Plate motion at ≈ 50 Ma inferred from the Hawaiian–Emperor seamount Bend (HEB), and global plate circuits (Muller et al., 2016; Torsvik et al., 2017), serves as an example of changing plate kinematics that could be influenced by subduction initiation. The initiation of subduction zones in the western and southwest Pacific at around 50 Ma, including Izu-Bonin-Mariana (Reagan et al., 2019) and Tonga–Kermadec (Sutherland, Dickens, et al., 2020), is the potential cause for the rearrangement of Pacific Plate motion. The hypothesis that IBM initiation causes a change in

Pacific Plate motion is widely discussed and is based on the view that IBM initiated spontaneously (R. J. Stern and Bloomer, 1992; Reagan et al., 2019). However, it takes time for sufficient driving force to accumulate in the upper mantle and this time has to be larger than t_{SI} derived here. The quantity t_{SI} reflects the time when the forces local to a subduction zone have switched from resisting to driving but plate motion will be a function of both down dip slab length and along strike distance of a subduction zone. These were addressed in fully dynamic global calculations (J. Hu et al., 2022). Those calculations show that the initiation of the Izu–Bonin–Mariana subduction zone is insufficient for Pacific Plate rearrangement at 50 Ma. However, by 47 Ma, the IBM slab would have a down–dip length of 400 km (using the estimate of Reagan et al., 2019 for forearc extension as a proxy for convergence), considerably larger than the $\approx$ 200 km we find here for the transition from forced to self–sustaining subduction. J. Hu et al., 2022 found that the total change in Pacific Plate direction from IBM initiation would be about 10°. The HEB angle by itself reflects about 60° change, but about half of of this is likely due to the rapid motion of the Hawaiian plume to the south between 80 and 50 Ma (Tarduno et al., 2003). Instead of just IBM initiation, J. Hu et al., 2022 propose the demise of Kronotsky subduction zone in the north Pacific is the key factor, and IBM a secondary factor, leading to the rearrangement of Pacific Plate motion in the Eocene. IBM is an example of the setting described by the models with the force boundary conditions.

The viscosity of the asthenosphere can play a role in resisting subduction initiation. In the model with imposed velocity boundary conditions, the effective viscosity at the base of lithosphere is 10^{19} to 10^{20} Pa·s. The asthenospheric viscosity is governed by the non–Newtonian flow, eq. 2.18, and agrees with an estimate of viscosity in the asthenosphere beneath the Indian Plate from post seismic relaxation (Y. Hu et al., 2016). F_a is estimated to be 10^{11} to 10^{12} N/m with several cm/yr plate motion. For the force boundary models, with a relatively large asthenospheric viscosity ($\eta_a \approx 10^{20}$ Pa· s), the total shear force is $F_a \approx 10^{12}$ N/m. From the force boundary model, we obtain a good approximation of the resistance from asthenosphere for a plate with a much more realistic length scale (thousands of km). The resistance from the asthenosphere is a small but non-negligible component in the force balance.

Elasticity plays a role in subduction initiation. Visco–elastic rheologies have been widely applied in geodynamic models (Toth and Gurnis, 1998; L. N. Moresi, Dufour, and Mühlhaus, 2003; Gurnis, C. Hall, and Lavier, 2004; Taras V. Gerya, Connolly, and Yuen, 2008; F. A. Capitanio, Morra, and Goes, 2009; Fernando O. Marques

et al., 2013; Farrington, L.-N. Moresi, and F. A. Capitanio, 2014) to accommodate the long–term fluid flow and short–term elastic deformation. We compare the visco–plastic with equivalent visco–elasto-plastic models, and show that the presence of plasticity effectively reduces the Maxwell time, reducing the importance of elasticity during subduction initiation, but a conclusion dependent on the yield stress. With larger yield stresses elasticity becomes more important and stores energy that contributes to resistance against bending, as in the models of Farrington, L.-N. Moresi, and F. A. Capitanio, 2014 where a strong (non-plastic) layer is embedded within the core of the slab. When the yield stress is small, yielding occurs at the edges of the slab, the visco-elasto-plastic models are not distinguishable from visco–plastic ones in terms of either stress or strain. Although there has long been evidence for deformation within the outer portions of the bending slab through seismicity and normal faulting within the trench (Watts, 2001) and in some numerical models(F. Capitanio, G Morra, and Goes, 2007; F. A. Capitanio, Morra, and Goes, 2009; Farrington, L.-N. Moresi, and F. A. Capitanio, 2014) a strong core embedded in the slab is assumed to account for the temperature dependent viscosity and low strain rate in the center of a bending plate, there is also evidence that the core of the slab might be weak. Relatively small yield stresses within the core of slab is supported by plate rigidities that drop by more than 3 orders of magnitude near the trench (Billen, 2005). Large earthquakes (with moment magnitude 8 or larger) can rupture a substantial part of the lithosphere near the hinge zone (Kikuchi and Kanamori, 1995), suggesting that there could be little elastic strength of the bending plate. However, the arguments in Kikuchi and Kanamori, 1995 and Billen, 2005 follow from measurements made in fully developed subduction zones and we currently do not have direct evidence on the strength of the incoming plate in nascent subduction settings. Overall, the elasticity provides an extra resistance against subduction initiation especially during the nucleation stage, and slows plate motion, but elasticity does not appear to be a first order factor governing the time to initiate or the total work done to initiate subduction.

From geophysical observations offshore and from the geological on– and offshore, two modes of subduction initiation are inferred: Spontaneous and induced (Gurnis, C. Hall, and Lavier, 2004; R. Stern, 2004; Arculus et al., 2015; Sutherland, J. Collot, et al., 2017; Guilmette et al., 2018; Reagan et al., 2019; Brandon Shuck et al., 2022). With the spontaneous initiation scenario, the plate is pulled downward (bent) spontaneously without a strong far–field compression (that is $F_{xx} \approx 0$ in our formulation); in other words, the local buoyancy forces within the nascent

plate boundary are sufficient to over come the resisting forces. Interpretation of the IBM forearc (R. J. Stern and Bloomer, 1992; Reagan et al., 2019) and computational models (Dymkova and T. Gerya, 2013; Leng and Gurnis, 2015; R. J. Stern and Taras Gerya, 2018; Maunder et al., 2020) suggest that over–riding plate extension and rapid trench roll back are prominent outcomes of spontaneous subduction initiation. Our numerical models with the full solution of the coupled non–linear system never produced spontaneous initiation; in the force boundary model, a small F_{xx} results in a stable plate boundary while a large F_{xx} results in an induced mode of subduction initiation in which the slab is coupled with the overriding plate during the subduction. In the analytical model, for spontaneous initiation ($F_{xx} = 0$), the only possible driving force would be F_I. We note that F_I in eq. 2.1 is treated as a resistant force as it is a horizontal compression pushing against the incoming plate (and the computational models support this assumption). However, for the spontaneous initiation scenario, the future subducting plate is not moving forward and consequently F_I acts as a local compression which could initiate subduction. If we make this assumption, then a criteria for spontaneous initiation is $F_I > \Delta N_b$. Numerically, we estimate a typical bending force to be $\sim 2 \times 10^{12}$ N/m (Fig. 2.10a). This is close to that from the analytical model where we estimate the bending torque across the hinge zone, eq. 2.5, to be 1.8×10^{12} N/m (with $s_{HZ} \approx 100$ km, $H = 60$ km, $(dk/dz)_{max} \approx 10^{-10}\text{m}^{-2}$, and $\tau_{max} = 300$ MPa). The computational and analytical results both show ΔN_b to be 2×10^{12} N/m, roughly equal to F_I ($\approx 2 \times 10^{12}$ N/m), so the condition for spontaneous subduction initiation is only marginally possible with the model setup. However, with other sources of resistance from plate boundary friction and asthenospheric shear that would need to occur when the new shear zone forms, the observation that we never observe spontaneous initiation in our full non–linear computations is consistent with the analytical model. This theoretical result is also consistent with the models of Zhou and Wada, 2021 who argued that models with induced versus spontaneous initiation better explained the thermal history of the metamorphic soles of ophiolites.

With the half space cooling model, H is proportional to (plate age)$^{1/2}$, so that the thermal isostatic force $F_{thermal} \sim H^2$. Unlike previous work suggesting that plate rigidity, with constant viscosity, is proportional to H^3, we show that with plastic yielding, plate bending resistance is proportional to H^2. Together these indicate that the scaling of F_I and ΔN_b with subducting plate thickness is of the same order, so that the subducting plate age might not be a determining factor for subduction initiation. Both young and old plates have a chance to initiate subduction, in agreement with

the computational models of Arcay et al., 2020. Two sites of Cenozoic subduction initiation are IBM and the Matthews–Hunter (M. Patriat et al., 2015; Martin Patriat et al., 2019) which initiated with widely different subduction plate ages: 70 Myr old for IBM (C. E. Hall et al., 2003) and about 20 Myr for Matthews–Hunter using the reconstructions in Seton et al., 2016. Evidence from some ophiolites have suggested very young ages for the age of plates during subduction initiation (Hinsbergen et al., 2015; Maffione et al., 2015).

Despite the absence of spontaneous initiation in the full numerical models, we suggest that several conditions could lead to this possibility. First, a buoyant overriding plate, either through its composition or with a young thermal age, which is able to produce a large F_I. An even weaker subducting plate, with a low τ_{max} can essentially reduce the plate bending force, and may lead to a propensity of spontaneous initiation. In principle, an even weaker plate boundary, e.g. a weak inter plate friction T_s, might allow subduction to unfold spontaneously.

Another means to initiate subduction is through a vertical force during subduction propogation. One potential source of the additional vertical force is the shear force from the along-strike propagation of subduction associated with the 3D "unzipping" behavior of a subduction zone (Maunder et al., 2020). In contrast to the free slip boundary widely used in computational models, models with open boundaries at their base (Zhou, Zhong-Hai Li, et al., 2018; Arcay et al., 2020) are more likely to produce spontaneous initiation.

The time–scale for initiating a new subduction zone is a key outcome of the mechanical models and can be constrained with geological observations. By definition, t_{SI} describes the duration it takes for the local forces to exceed the external driving forces. When this change in the force balance occurs, we showed that the state–of–stress within the plate margins switches from compression to extension. Recently, detailed analysis of seismic images in the context of biostratigraphic ages from an existing borehole within the Solander Basin on the over–riding plate proximal to the Puysegur Trench (Patel et al., 2021; B. Shuck et al., 2021), demonstrated a transition from compression to extension between 15 Ma and 5 Ma as the new subduction zone formed (Brandon Shuck et al., 2022). An initial burst of compression at 15 Ma is interpreted as the initial compression during subduction nucleation (Brandon Shuck et al., 2022), in close agreement with the well–constrained relative motion between the Australian and Pacific Plates (Sutherland, Barnes, and Uruski, 2006; Gurnis, Van Avendonk, et al., 2019). The transition from compression to

extension is interpreted as the transition in the local force balance. This lead to a 10 Myr time-scale for the initiation of the Puysegur subduction zone, although Brandon Shuck et al., 2022 also show that this transition is changing along strike and comparing these observations against models will require a three–dimensional domain. The dating of ophiolites provides another constraint on the time–scale for subduction initiation (Hacker, 1994). In Oman, the geochronological dating of the Semail ophiolite indicates that initial thrusting predates the upper plate extension by at least 8 Myr (Guilmette et al., 2018). These different observations independently indicate in evolving subduction zones, the time for the stress state to become neutral is $\sim$ 10 Myr. This estimate matches the velocity boundary models with $u = 2$ to 4 cm/yr (Fig. 2.12a–c), but do not fall within the regime provided by the force boundary models (Fig. 2.12d–f).

Appendix A: Force Balance

Here we derive the force balance equation 2.1. We start from Ribe, 2001 equation 2.5b derived from the conservation of momentum and bending torque of a thin viscous sheet with constant plate thickness:

$$\frac{dN}{ds} = k\frac{dM}{ds} - Hg_s\delta\rho(1 + \frac{k^2H^2}{12}) - F_s^+ - F_s^- + \frac{1}{2}Hk(F_s^+ - F_s^-) \tag{2.26}$$

where F_s reflect the component from plate surface traction in a curved plate, $F_s^\pm = (\pm 1 - \frac{Hk}{2})T^\pm$ with a constant plate thickness and $T^\pm$ is the shear traction at top and bottom surface of the plate. N and M are the plate normal force and plate bending moment. The component of gravity in the s direction is g_s, or $g\sin\theta$. Consequently, 2.26 yields

$$\frac{dN}{ds} = k\frac{dM}{ds} - Hgsin\theta\delta\rho(1 + \frac{k^2H^2}{12}) - (\frac{Hk}{2} - 1)^2T^+ + (\frac{Hk}{2} + 1)^2T^- \tag{2.27}$$

From this equation we see that the changing of plate normal force can be decomposed into a bending, body, and boundary force. The presence of the product Hk complicates the formulation, and Buffet, 2006 states that Hk can be ignored as it is much smaller than 1, indicating the plate can function as a stress guide transmitting the stress in the s direction. The full numerical solutions show that the maximum plate curvature k can be as large as 10^{-5} m^{-1} (Fig. 2.9), so that the upper limit of Hk can be as large as 0.5, which is not negligible. However, the k reaches 10^{-5} m^{-1} only in the hinge zone area of well–developed subduction. For negative buoyancy term, θ in the hinge zone is small. Shear traction $T^\pm$ is significant only at

the beginning of the subduction initiation, when plate curvature is small, but after subduction becomes well developed $T^{\pm}$ becomes quite small in response to plate weakening. Therefore, the Hk term is negligible when both negative buoyancy and shear traction are dominant. With Hk vanishing, eq.2.27 simplifies to

$$\frac{dN}{ds} = k\frac{dM}{ds} - Hgsin\theta\delta\rho - T^{+} + T^{-}$$

By integrating this equation from one end of the slab to the other, we obtain $F_1 - F_2 = \int_0^L k dM - \int_0^L Hg\sin\theta\delta\rho ds + \int_0^L (T^{-} - T^{+})ds$. Further, with boundary conditions ($F_2 = -F_{xx}$, $F_1 = -F_I$) and substituting from eq. 2.2, 2.6, 2.7, 2.8, and 2.11, we obtain

$$F_{xx} + \Delta N_{NB} = \Delta N_b + T_s + F_a + F_I$$

verifying eq. 2.1.

Appendix B: Hinge zone yielding

In eq. 2.3, $\Delta N_b = K_b u + N_{HZ}$, we state that the bending torque ΔN_b consist of two parts: A bending torque inside the hinge zone (independent of plate velocity) and one outside the hinge zone (proportional to plate velocity). Here we demonstrate this result. The shear stress within the bending slab, τ_{ss} in the local coordinate system will be evaluated at center, edge and outside of the hinge zone (red, blue, and green cross sections in Fig. 2.17). Following Buffet, 2006, we know that the strain rate in the bending area is $\dot{\varepsilon}_{ss} = -zu\frac{dk}{ds}$, where z and s are the local coordinate system.

Outside the hinge zone, without plastic yielding the stress–strain relationship is linear $\tau_{ss} = 4\eta\dot{\varepsilon}_{ss} = -4\eta zu\frac{dk}{ds}$, and the moment is $M = \int_{-\frac{H}{2}}^{\frac{H}{2}} \tau_{ss} z dz = -\frac{1}{3}H^3\eta u\frac{dk}{ds}$. In the hinge zone, an upper limit is applied to the stress, so $\tau_{ss} = \max(\min(-4\eta zu\frac{dk}{ds}, \tau_y), -\tau_y)$. Near $z = 0$ the stress is small and so linear with strain rate and proportional to z, but with the yielding stress function as an upper limit for τ_{ss} when $|z| >> 0$. We define the intersect between a linear viscosity and plastic yielding as $z = \pm z_1$. The quantity z_1 is a function of s, $z_1 = z_1(s)$, that in the center of hinge zone the z_1 is smallest, define as $z_1 = z_1(s_c)$. As $z = z_1$ is the intersection of the linear viscosity with yielding, we have $\tau_y = 4\eta z_1 u\frac{dk}{ds}$, and we obtain $z_1 = \frac{\tau_y}{4\eta u dk/ds}$. Assuming the hinge zone is symmetric along $s = s_c$, and the width of hinge zone to be s_{HZ}, we approximate z_1 with $z_1 \approx \frac{\tau_y}{4\eta u(\gamma - \beta(s-s_c)^2)}$ where γ and β are parameters to be determined. At the edge of the hinge zone, the boundary of yielding ($z_1 = z_1(s)$) intersects with the slab boundaries and $z_1(s + s_{HZ}/2) = \frac{H}{2}$. On the other hand, in

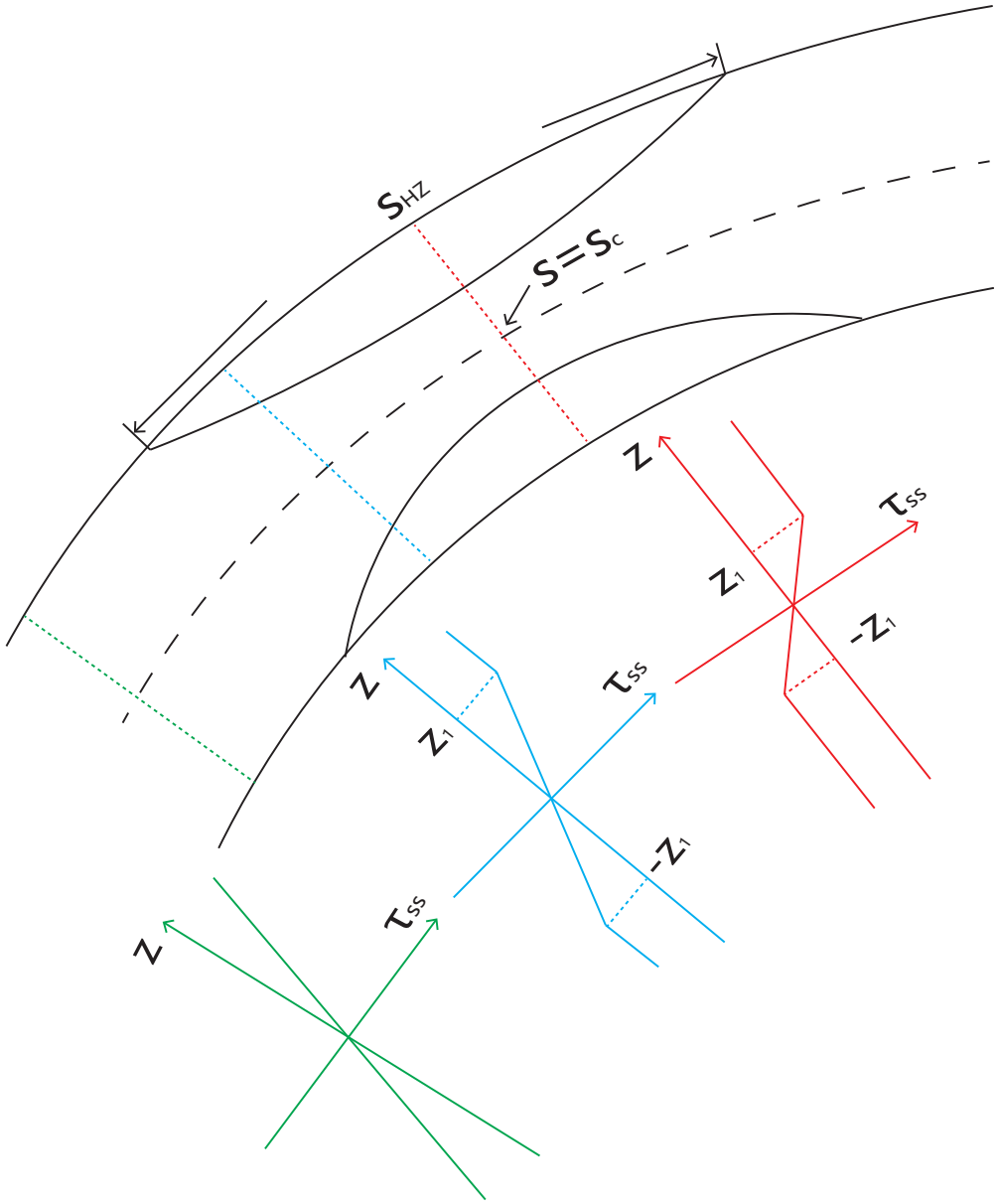

Figure 2.17: Illustration of the hinge zone geometry and stress. The local coordinate system(s, z) is defined in Figure 1. Two sectors draw the yielding area bounded by $z = \pm z_1(s)$. Every sector area is symmetric along the central axis $s = s_c$. Red, blue, and green represent the central, edge and out of the yielding area.

the center of the hinge zone, we have the smallest z_1, corresponding to a largest $\frac{dk}{ds}$. With these two constraints, we can evaluate γ and β to be $\gamma = (\frac{dk}{ds})_{max}$ and $\beta = ((\frac{dk}{ds})_{max} - \frac{\tau_y}{2\eta H u})\frac{4}{s_{HZ}^2}$. The derivation of total normal force change follows Buffet, 2006,

$$\Delta N = \int_0^L k dM = -\int_0^L M dk$$

where k is the plate curvature, and M is the moment ($M = \int_{-\frac{H}{2}}^{\frac{H}{2}} \tau_{ss} z dz$). The second part of the equation followings from the integration by parts, assuming $k(s=0) = k(s=L) = 0$. By substituting the expression of M into the equation we obtain

$$\begin{aligned}
\Delta N &= -\int_0^L \int_{-\frac{H}{2}}^{\frac{H}{2}} \tau_{ss} \frac{dk}{ds} z dz ds \\
&= -\int_{s\in C_{[0,L]}[s_c-\frac{s_{HZ}}{2}, s_c+\frac{s_{HZ}}{2}]} \int_{-\frac{H}{2}}^{\frac{H}{2}} \tau_{ss} \frac{dk}{ds} z dz ds - \int_{s_c-\frac{s_{HZ}}{2}}^{s_c+\frac{s_{HZ}}{2}} \int_{-\frac{H}{2}}^{\frac{H}{2}} \tau_{ss} \frac{dk}{ds} z dz ds \\
&= \int_{s\in C_{[0,L]}[s_c-\frac{s_{HZ}}{2}, s_c+\frac{s_{HZ}}{2}]} \frac{1}{3} H^3 \eta u (\frac{dk}{ds})^2 ds - \int_{s_c-\frac{s_{HZ}}{2}}^{s_c+\frac{s_{HZ}}{2}} \int_{-\frac{H}{2}}^{\frac{H}{2}} max(min(-4\eta z u \frac{dk}{ds}, \tau_y), -\tau_y) z \frac{dk}{ds} dz ds \\
&= K_b u + N_{HZ}
\end{aligned}$$

Here the integration is split into two parts: The first being the area outside the hinge zone where no plastic yielding occurs, and the second corresponds to the hinge zone bending torque N_{HZ}. With symmetry, the second term can be further rewritten as

$$\begin{aligned}
N_{HZ} &= 2\int_{s_c-\frac{s_{HZ}}{2}}^{s_c+\frac{s_{HZ}}{2}} \int_0^{\frac{H}{2}} min(4\eta z u \frac{dk}{ds}, \tau_y) z \frac{dk}{ds} dz ds \\
&= 2\int_{s_c-\frac{s_{HZ}}{2}}^{s_c+\frac{s_{HZ}}{2}} \int_0^{z_1} 4\eta z^2 u (\frac{dk}{ds})^2 dz ds + 2\int_{s_c-\frac{s_{HZ}}{2}}^{s_c+\frac{s_{HZ}}{2}} \int_{z_1}^{\frac{H}{2}} \tau_y z \frac{dk}{ds} dz ds \\
&= 2\int_{s_c-\frac{s_{HZ}}{2}}^{s_c+\frac{s_{HZ}}{2}} \frac{4}{3} \eta z_1^3 u (\frac{dk}{ds})^2 ds + 2\int_{s_c-\frac{s_{HZ}}{2}}^{s_c+\frac{s_{HZ}}{2}} \frac{1}{2} (\frac{H^2}{4} - z_1^2) \tau_y \frac{dk}{ds} ds
\end{aligned}$$

With $z_1 = \frac{\tau_y}{4\eta u(\gamma - \beta(s-s_c)^2)}$, $\frac{dk}{ds} = \gamma - \beta(s-s_c)^2$ the equation yields

$$\begin{aligned}
&2\int_{s_c-\frac{s_{HZ}}{2}}^{s_c+\frac{s_{HZ}}{2}} (\frac{1}{8} H^2 \tau_y (\gamma - \beta(s-s_c)^2) - \frac{\tau_y^3}{96\eta^2 u^2 (\gamma - \beta(s-s_c)^2)}) ds \\
=&\frac{1}{48} \tau_y (H^2 s_{HZ} (12\gamma - \beta s_{HZ}^2) - \frac{2\tau_y^2 \text{arctanh}[\sqrt{\frac{\beta}{\gamma}} \frac{s_{HZ}}{2}]}{\sqrt{\beta\gamma}})
\end{aligned}$$

Recalling $\beta = (\gamma - \frac{\tau_y}{2\eta Hu})\frac{4}{s_{HZ}^2}$, we obtain

$$N_{HZ} = \frac{1}{6}\tau_y H^2 s_{HZ}\gamma(1 + \frac{\tau_y}{4\gamma\eta Hu}) - \frac{\tau_y^3 \text{arctanh}[\sqrt{\frac{\beta}{\gamma}}\frac{s_{HZ}}{2}]}{24\eta^2 u^2\sqrt{\beta\gamma}}$$

We can define a dimensionless quantity $\zeta = \frac{z_1(s=s_c)}{z_1(s=s_c\pm\frac{s_{HZ}}{2})} = \frac{\tau_y}{2\gamma\eta Hu}$ which describe the ratio between minimum and maximum width of the non-yielding area in the hinge zone. With typical quantities from the models, $\tau_y = 300\text{M}Pa(\tau_{II} \leq 150MPa)$, $\gamma = 1\times10^{-10}\text{m}^{-2}$ from figure 2.9, $H = 60\text{k}m$, $u = 2\text{c}m/yr$ and $\eta = 10^{25}\text{P}a\cdot s$, we can estimate ζ to be 4×10^{-3}. Therefore $\beta = (\gamma - \frac{\tau_y}{2\eta Hu})\frac{4}{s_{HZ}^2} = (1-\zeta)\frac{4\gamma}{s_{HZ}^2} \approx \frac{4\gamma}{s_{HZ}^2}$.

$$\begin{aligned}
N_{HZ} &= \frac{1}{6}\tau_y H^2 s_{HZ}\gamma(1+\zeta) - \frac{\tau_y^3 s_{HZ}\text{arctanh}[\sqrt{1-\zeta}]}{48\gamma\eta^2u^2} \\
&= \frac{1}{6}\tau_y H^2 s_{HZ}\gamma(1+\zeta - \frac{\tau_y^2\text{arctanh}[\sqrt{1-\zeta}]}{8\gamma^2\eta^2H^2u^2}) \\
&= \frac{1}{6}\tau_y H^2 s_{HZ}\gamma(1+\zeta - \frac{\zeta^2}{2}\text{arctanh}[\sqrt{1-\zeta}]) \\
&\approx \frac{1}{6}\tau_y H^2 s_{HZ}\gamma
\end{aligned}$$

The small ζ indicates that plastic yielding pervasively occurs in the hinge zone, so that mostly the hinge zone has $\tau_{ss} = \tau_y$.

2.7 Supplementary Material

Formulation

Formulation of the $t \sim \ell$ relationship in the force balance model. Following Section 2.2, we know that for each given moment with a given plate motion, ℓ, we compute the plate velocity in terms of ℓ, $u = u(\ell)$, based on the force balance equation, and the total time for the plate motion to reach certain value (ℓ) is thereby $t = \int_0^\ell dt = \int_0^\ell \frac{d\ell'}{u}$.

With equation (7), (8), (12) and (15), we get: When $\ell < \varepsilon_{P_0}\delta$

$$
\begin{aligned}
t &= \int_0^{\ell} \frac{d\ell'}{u} = \int_0^{\ell} \frac{(K_b + \eta_a \cdot \frac{L_P}{d_a})}{F_{xx} - A - F_I - N_{HZ} + (B + H\Delta\rho g \sin\theta) \cdot \ell' - C\ell'^2} d\ell' \\
&= \frac{2K_1}{\sqrt{B_1^2 + 4C(F_{xx} - A - F_I - N_{HZ})}} (\operatorname{arctanh} \frac{B_1}{\sqrt{B_1^2 + 4C(F_{xx} - A - F_I - N_{HZ})}} \\
&\quad - \operatorname{arctanh} \frac{B_1 - 2C\ell}{\sqrt{B_1^2 + 4C(F_{xx} - A - F_I - N_{HZ})}}) \\
&\approx \frac{4K_1 C\ell}{B_1^2 + 4C(F_{xx} - A - F_I - N_{HZ})}
\end{aligned}
\tag{2.28}
$$

When $\ell > \delta\varepsilon P_0$

$$
\begin{aligned}
t &= \int_0^{\delta\varepsilon_{P0}} \frac{d\ell'}{u} + \int_{\delta\varepsilon_{P0}}^{\ell} \frac{d\ell'}{u} \\
&= \int_0^{\delta\varepsilon_{P0}} \frac{(K_b + \eta_a \cdot \frac{L_P}{d_a}) d\ell'}{F_{xx} - A - F_I - N_{HZ} + (B + H\Delta\rho g \sin\theta) \cdot \ell' - C\ell'^2} \\
&= + \int_{\delta\varepsilon_{P0}}^{\ell} \frac{(K_b + \eta_a \cdot \frac{L_P}{d_a}) d\ell'}{F_{xx} - D - F_I - N_{HZ} + H\Delta\rho g \sin\theta \cdot \ell'} \\
&= \frac{2K_1}{\sqrt{B_1^2 + 4C(F_{xx} - A - F_I - N_{HZ})}} (\operatorname{arctanh} \frac{B_1}{\sqrt{B_1^2 + 4C(F_{xx} - A - F_I - N_{HZ})}} \\
&\quad - \operatorname{arctanh} \frac{B_1 - 2\tau_{y0}}{\sqrt{B_1^2 + 4C(F_{xx} - A - F_I - N_{HZ})}}) \\
&\quad + K_1 \frac{\ln(F_{xx} - D - F_I - N_{HZ} + H\Delta\rho g \sin\theta\ell) - \ln(F_{xx} - D - F_I - N_{HZ} + H\Delta\rho g \sin\theta\delta\varepsilon_{P0})}{H\Delta\rho g \sin\theta} \\
&\approx \frac{4K_1\tau_{y0}}{B_1^2 + 4C(F_{xx} - A - F_I - N_{HZ})} + \frac{K_2(\ell - \delta\varepsilon_{P0})}{F_{xx} - D - F_I - N_{HZ}}
\end{aligned}
\tag{2.29}
$$

With the calculation above, we obtain the formulation of initiation time t_{SI}, defined as the time for plate motion to reach certain value ℓ_{SI} (ℓ_{SI} is typically greater than

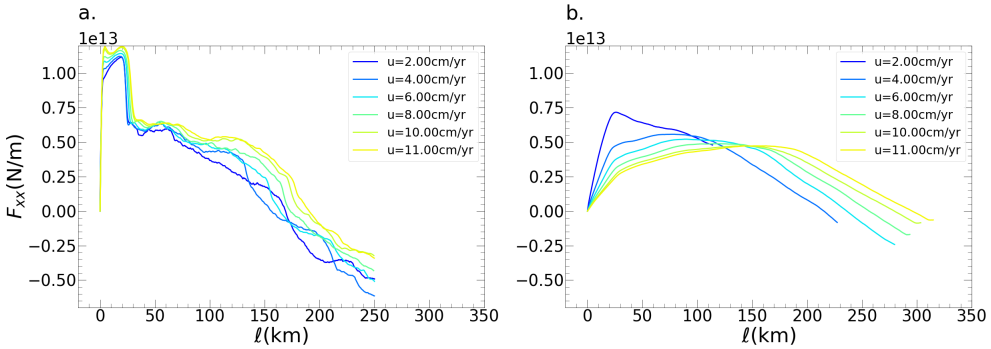

Figure 2.18: F_{xx} vs ℓ from visco-elasto-plastic model with a. Δt_e = 1Myr and b. Δt_e = 1.5kyr $\approx \Delta t$. a is the same as Fig 2.4c.

$\delta\varepsilon P_0$).

$$
\begin{aligned}
t_{SI} = & \frac{2K_1}{\sqrt{B_1^2 + 4C(F_{xx} - A - F_I - N_{HZ})}}(\operatorname{arctanh}\frac{B_1}{\sqrt{B_1^2 + 4C(Fxx - A - F_I - N_{HZ})}} \\
& - \operatorname{arctanh}\frac{B_1 - \tau_{y0}}{\sqrt{B_1^2 + 4C(F_{xx} - A - F_I - N_{HZ})}}) \\
& + K_1 \frac{\ln(F_{xx} - D - F_I - N_{HZ} + H\Delta\rho g \ell_{SI} \sin\theta) - \ln(F_{xx} - D - F_I - N_{HZ} + H\Delta\rho g \sin\theta \delta\varepsilon_{P0})}{H\Delta\rho g \sin\theta} \\
\approx & \frac{4K_1\tau_{y0}}{B_1^2 + 4C(F_{xx} - A - F_I - N_{HZ})} + \frac{K_1(\ell_{SI} - \delta\varepsilon_{P0})}{F_{xx} - D - F_I - N_{HZ}}
\end{aligned}
\tag{2.30}
$$

Visco-elastic time step

The implementation of elasticity in the numerical model is highly dependent on the elastic time step Δt_e. Following L. N. Moresi, Dufour, and Mühlhaus, 2003, two independent time steps, the numerical time step Δt and elastic time step Δt_e, are introduced to the model, and $\Delta t \leq \Delta t_e$. Δt is the actual time step that the modelled time move forward, while the Δt_e is the characteristic time step for the Maxwell body. When $\Delta t_e \neq \Delta t$, an interpolation scheme is needed to project the calculated stress with Δt_e onto Δt. The typical choice of Δt_e is based on the Maxwell relaxation time of lithosphere ($\Delta t_e = \frac{\eta_{lithto}}{10\mu}$), which is much greater than Δt, and the stress evolution is thereby greatly influenced by the interpolation scheme. To avoid the artifact from interpolation, we force Δt_e to be as small as the Δt in models of Fig 2.4c. With a larger Δt_e, the build up stage becomes a more prominent feature and the elasticity plays a greater role (Fig 2.18). However, we view the big difference introduced by the large Δt_e an artifact from the interpolation scheme.

Evaluating Plate Curvature

In the analytical solution, the plate curvature is a variable that we directly evaluate from the plate geometry in the numerical models. Here, we show how plate curvature and its derivative is measured. The evaluation of plate curvature k requires the first and second order derivative of a plate curve function f with respect to x defining the center of the plate, $y = f(x)$. We can evaluate $f' = \frac{df}{dx}$ and tangent angle : $\theta = \arctan(f')$ and plate curvature $k = \frac{1}{\Lambda} = \frac{d\theta}{ds} = \frac{d\theta}{dx}\frac{1}{\sqrt{1+f'^2}}$, the changing rate plate curvature, $\frac{dk}{ds} = \frac{dk}{dx}\frac{1}{\sqrt{1+f'^2}}$. In the numerical model, the center of the plate is measured from the plate interfaces with the upper and lower interface of the plate defined from the 600° C temperature contour (red and green curve in Fig. 2.19.a). As both upper and lower plate interfaces are concave functions, for each point from the upper interface, we find the nearest point from the lower interface, and define the middle point as the center between that point on the upper and that on the lower. The set of all center points form the plate center curve (blue curve, Fig. 2.19a), described by the formulation $y = f(x)$. As the measured curve is noisy, the method for numerical derivatives need to be treated carefully. Here we use total–variation regularization (Chartrand, 2011) to take a smoothed derivative from noisy data (`TVRegDiff`). In this method, we choose the two regularization parameters, α and ϵ, to be 0.02 and 5×10^{-5} so that the numerical derivatives are neither so noisy as to be unstable nor over–regularized.

Figure 2.19a–d show the sequence of numerical derivatives using this method (blue curves) vs. forward difference method(orange curves). From Figure 2.19a to d, every level is from the numerical derivative from the previous level, and both blue and orange curves are derived from the blue curve in the previous level using the `TVRegDiff` method and forward difference method. Apparently the orange curves(the forward difference method) is more noisy than the blue curves (`TVRegDiff`), but the overall trends of the `TVRegDiff` method agree well with the forward differences, indicating the accuracy and smoothness are guaranteed in `TVRegDiff` with appropriate choice of regularization parameters.

References

Arcay, D. et al. (2020). "Can subduction initiation at a transform fault be spontaneous?" In: *Solid Earth* 11.1, pp. 37–62. DOI: 10.5194/se-11-37-2020. URL: https://se.copernicus.org/articles/11/37/2020/.

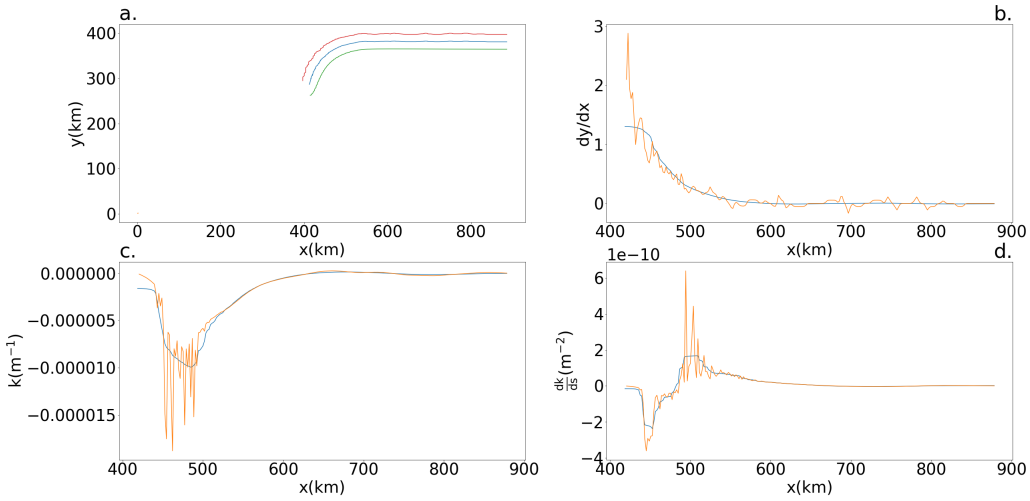

Figure 2.19: An example of measuring plate curvature k and its derivative $\frac{dk}{ds}$ from numerical model. a. the geometry of the plate. Red and green curves are the upper and lower interfaces of the mechanical plate measured from temperature contour $T = 600°C$. Blue curve is the mid-point curve of the red and green curve. b. Direct forward difference (orange) and TVRegDiff method (blue) of the blue curve in a. Direct forward difference represent the ground truth of the numerical derivative, and TVRegDiff represent the smoothed derivative. c. Direct forward difference (orange) and TVRegDiff method (blue) of the blue curve in b. d. Direct forward difference (orange) and TVRegDiff method (blue) of the blue curve in c.

Arculus, R. J. et al. (2015). "A record of spontaneous subduction initiation in the Izu-Bonin-Mariana arc". In: *Nature Geoscience* 8, pp. 728–733. DOI: 10.1038/ngeo2515.

Billen, Magali I. (2005). "Constraints on subducting plate strength within the Kermadec trench". In: *Journal of Geophysical Research* 110 (B5), B05407. ISSN: 0148-0227. DOI: 10.1029/2004JB003308. URL: http://doi.wiley.com/10.1029/2004JB003308 (visited on 07/19/2022).

Buffet, B.A. (2006). "Plate force due to bending at subduction zones". In: *J. Geophys. Res.* 111.B09405, pp. 1–9. DOI: 10.1029/2006JB004295.

Capitanio, F., G. G Morra, and S. Goes (2007). "Dynamic models of downgoing plate-buoyancy driven subduction: Subduction motions and energy dissipation". In: *Earth and Planetary Science Letters* 262, pp. 284–297. DOI: 10.1016/j.epsl.2007.07.039.

Capitanio, F. A., G. Morra, and S. Goes (Apr. 2009). "Dynamics of plate bending at the trench and slab-plate coupling: PLATE BENDING AND SLAB-PLATE COUPLING". In: *Geochemistry, Geophysics, Geosystems* 10.4, n/a–n/a. ISSN:

15252027. DOI: 10.1029/2008GC002348. URL: http://doi.wiley.com/10.1029/2008GC002348 (visited on 05/03/2022).

Chartrand, Rick (May 11, 2011). "Numerical Differentiation of Noisy, Nonsmooth Data". In: *ISRN Applied Mathematics* 2011, pp. 1–11. ISSN: 2090-5564, 2090-5572. DOI: 10.5402/2011/164564. URL: https://www.hindawi.com/journals/isrn/2011/164564/ (visited on 07/19/2022).

Collot, Jean-Yves et al. (1995). "Morphostructure of an incipient subduction zone along a transform plate boundary: Puysegur Ridge and Trench". In: *Geology* 23.6, p. 519. ISSN: 0091-7613. DOI: 10.1130/0091-7613(1995)023<0519:MOAISZ>2.3.CO;2. URL: https://pubs.geoscienceworld.org/geology/article/23/6/519-522/206344 (visited on 10/26/2023).

Crameri, F. et al. (2012). "A comparison of numerical surface topography calculations in geodynamic modelling: an evaluation of the 'sticky air' method". In: *Geophysical Journal International* 189.1. _eprint: https://academic.oup.com/gji/article-pdf/189/1/38/17364460/189-1-38.pdf, pp. 38–54. ISSN: 0956-540X. DOI: 10.1111/j.1365-246X.2012.05388.x. URL: https://doi.org/10.1111/j.1365-246X.2012.05388.x.

Dymkova, D. and T. Gerya (2013). "Porous fluid flow enables oceanic subduction initiation on Earth". In: *Geophys. Res. Lett.* 40.21, pp. 5671–5676. DOI: 10.1002/2013GL057798.

Farrington, R. J., L.-N. Moresi, and F. A. Capitanio (Nov. 2014). "The role of viscoelasticity in subducting plates". In: *Geochemistry, Geophysics, Geosystems* 15.11, pp. 4291–4304. ISSN: 15252027. DOI: 10.1002/2014GC005507. URL: http://doi.wiley.com/10.1002/2014GC005507 (visited on 05/03/2022).

Gerya, Taras V., James A.D. Connolly, and David A. Yuen (2008). "Why is terrestrial subduction one-sided?" In: *Geology* 36.1, p. 43. ISSN: 0091-7613. DOI: 10.1130/G24060A.1. URL: https://pubs.geoscienceworld.org/geology/article/36/1/43-46/129999 (visited on 02/16/2024).

Guilmette, Carl et al. (Sept. 2018). "Forced subduction initiation recorded in the sole and crust of the Semail Ophiolite of Oman". In: *Nature Geoscience* 11.9, pp. 688–695. ISSN: 1752-0894, 1752-0908. DOI: 10.1038/s41561-018-0209-2. URL: http://www.nature.com/articles/s41561-018-0209-2 (visited on 07/19/2022).

Gurnis, Michael, Chad Hall, and Luc Lavier (July 2004). "Evolving force balance during incipient subduction: EVOLVING FORCE BALANCE". In: *Geochemistry, Geophysics, Geosystems* 5.7. ISSN: 15252027. DOI: 10.1029/2003GC000681. URL: http://doi.wiley.com/10.1029/2003GC000681 (visited on 07/19/2022).

Gurnis, Michael, Harm Van Avendonk, et al. (Aug. 2019). "Incipient subduction at the contact with stretched continental crust: The Puysegur Trench". In: *Earth and Planetary Science Letters* 520, pp. 212–219. ISSN: 0012821X. DOI: 10.

1016/j.epsl.2019.05.044. URL: https://linkinghub.elsevier.com/retrieve/pii/S0012821X19303267 (visited on 02/16/2024).

Hacker, Bradley R. (Sept. 9, 1994). "Rapid Emplacement of Young Oceanic Lithosphere: Argon Geochronology of the Oman Ophiolite". In: *Science* 265.5178, pp. 1563–1565. ISSN: 0036-8075, 1095-9203. DOI: 10.1126/science.265.5178.1563. URL: https://www.science.org/doi/10.1126/science.265.5178.1563 (visited on 02/16/2024).

Hacker, Bradley R., Geoffrey A. Abers, and Simon M. Peacock (Jan. 2003). "Subduction factory 1. Theoretical mineralogy, densities, seismic wave speeds, and H $_2$ O contents: SUBDUCTION ZONE MINERALOGY AND PHYSICAL PROPERTIES". In: *Journal of Geophysical Research: Solid Earth* 108 (B1). ISSN: 01480227. DOI: 10.1029/2001JB001127. URL: http://doi.wiley.com/10.1029/2001JB001127 (visited on 07/19/2022).

Hall, Chad E. et al. (July 2003). "Catastrophic initiation of subduction following forced convergence across fracture zones". In: *Earth and Planetary Science Letters* 212.1, pp. 15–30. ISSN: 0012821X. DOI: 10.1016/S0012-821X(03)00242-5. URL: https://linkinghub.elsevier.com/retrieve/pii/S0012821X03002425 (visited on 02/16/2024).

Hinsbergen, Douwe J. J. van et al. (June 2015). "Dynamics of intraoceanic subduction initiation: 2. Suprasubduction zone ophiolite formation and metamorphic sole exhumation in context of absolute plate motions: SSZ OPHIOLITES AND METAMORPHIC SOLES". In: *Geochemistry, Geophysics, Geosystems* 16.6, pp. 1771–1785. ISSN: 15252027. DOI: 10.1002/2015GC005745. URL: http://doi.wiley.com/10.1002/2015GC005745 (visited on 10/20/2022).

Hu, J. et al. (2022). "Dynamics of abrupt change in Pacific Plate motion around 50 Ma". In: *Nature Geoscience* 15, pp. 74–78. DOI: 10.1038/s41561-021-00862-6.

Hu, Yan et al. (Oct. 2016). "Asthenosphere rheology inferred from observations of the 2012 Indian Ocean earthquake". In: *Nature* 538.7625, pp. 368–372. ISSN: 1476-4687. DOI: 10.1038/nature19787. URL: https://doi.org/10.1038/nature19787.

Kikuchi, Masayuki and Hiroo Kanamori (May 1, 1995). "The Shikotan Earthquake of October 4, 1994: Lithospheric earthquake". In: *Geophysical Research Letters* 22.9, pp. 1025–1028. ISSN: 00948276. DOI: 10.1029/95GL00883. URL: http://doi.wiley.com/10.1029/95GL00883 (visited on 07/19/2022).

Lebrun, Jean-Frédéric, Geoffroy Lamarche, and Jean-Yves Collot (Sept. 2003). "Subduction initiation at a strike-slip plate boundary: The Cenozoic Pacific-Australian plate boundary, south of New Zealand". In: *Journal of Geophysical Research: Solid Earth* 108 (B9). ISSN: 01480227. DOI: 10.1029/2002JB002041. URL: http://doi.wiley.com/10.1029/2002JB002041 (visited on 07/19/2022).

Leng, Wei and Michael Gurnis (Dec. 2011). "Dynamics of subduction initiation with different evolutionary pathways: DIFFERENT SUBDUCTION INITIATION PATHWAYS". In: *Geochemistry, Geophysics, Geosystems* 12.12, n/a–n/a. ISSN: 15252027. DOI: 10.1029/2011GC003877. URL: http://doi.wiley.com/10.1029/2011GC003877 (visited on 07/19/2022).

Leng, Wei and Michael Gurnis (Sept. 16, 2015). "Subduction initiation at relic arcs". In: *Geophysical Research Letters* 42.17, pp. 7014–7021. ISSN: 0094-8276, 1944-8007. DOI: 10.1002/2015GL064985. URL: https://onlinelibrary.wiley.com/doi/10.1002/2015GL064985 (visited on 07/19/2022).

Maffione, Marco et al. (2015). "Dynamics of intraoceanic subduction initiation: 1. Oceanic detachment fault inversion and the formation of supra-subduction zone ophiolites". In: *Geochemistry, Geophysics, Geosystems* 16.6. _eprint: https://agupubs.onlinelibrary.wiley. pp. 1753–1770. DOI: https://doi.org/10.1002/2015GC005746. URL: https://agupubs.onlinelibrary.wiley.com/doi/abs/10.1002/2015GC005746.

Mansour, J. et al. (2020). "Underworld2: Python Geodynamics Modelling for Desktop, HPC and Cloud". en. In: *Journal of Open Source Software* 5.47. DOI: 10.21105/joss.01797. URL: https://doi.org/10.21105/joss.01797.

Marques, Fernando O. et al. (Nov. 2013). "Testing the influence of far-field topographic forcing on subduction initiation at a passive margin". en. In: *Tectonophysics* 608, pp. 517–524. ISSN: 00401951. DOI: 10.1016/j.tecto.2013.08.035. URL: https://linkinghub.elsevier.com/retrieve/pii/S0040195113005349 (visited on 02/10/2022).

Maunder, B. et al. (Dec. 2020). "Rapid subduction initiation and magmatism in the Western Pacific driven by internal vertical forces". In: *Nature Communications* 11.1, p. 1874. ISSN: 2041-1723. DOI: 10.1038/s41467-020-15737-4. URL: http://www.nature.com/articles/s41467-020-15737-4 (visited on 07/19/2022).

McKenzie, D.P. (1977). "The initiation of trenches: A finite amplitude instability". In: *Maurice Ewing Series*. Ed. by Manik Talwani and Walter C. Pitman. Vol. 1. Washington, D. C.: American Geophysical Union, pp. 57–61. ISBN: 978-0-87590-400-9. DOI: 10.1029/ME001p0057. URL: http://www.agu.org/books/me/v001/ME001p0057/ME001p0057.shtml (visited on 02/17/2024).

Moresi, L. N., F. Dufour, and H.-B. Mühlhaus (2003). "A Lagrangian integration point finite element method for large deformation modeling of viscoelastic geomaterials". In: *J. Comp. Phys* 184, pp. 476–497. DOI: 10.1016/S0021-9991(02)00031-1.

Mueller, Steve and Roger J. Phillips (Jan. 10, 1991). "On The initiation of subduction". In: *Journal of Geophysical Research: Solid Earth* 96 (B1), pp. 651–665. ISSN: 0148-0227. DOI: 10.1029/90JB02237. URL: https://agupubs.onlinelibrary.wiley.com/doi/10.1029/90JB02237 (visited on 02/17/2024).

Muller, R. D. et al. (2016). "Global-scale plate reorganization events since Pangea breakup". In: *Annu. Rev. Earth Planet. Sci.* 44, pp. 107–138. DOI: 10.1146/annurev-earth-060115-012211.

Nikolaeva, K., T. V. Gerya, and F. O. Marques (2010). "Subduction initiation at passive margins: numerical modeling". In: *J. Geophys. Res.* 115. Section: B03406. DOI: 10.1029/2009JB006549.

Patel, Jiten et al. (Feb. 2021). "Stratigraphic architecture of Solander Basin records Southern Ocean currents and subduction initiation beneath southwest New Zealand". In: *Basin Research* 33.1, pp. 403–426. ISSN: 0950-091X, 1365-2117. DOI: 10.1111/bre.12473. URL: https://onlinelibrary.wiley.com/doi/10.1111/bre.12473 (visited on 02/17/2024).

Patriat, M. et al. (Sept. 2015). "Propagation of back-arc extension into the arc lithosphere in the southern New Hebrides volcanic arc: PROPAGATION OF BACK-ARC EXTENSION IN ARC". In: *Geochemistry, Geophysics, Geosystems* 16.9, pp. 3142–3159. ISSN: 15252027. DOI: 10.1002/2015GC005717. URL: http://doi.wiley.com/10.1002/2015GC005717 (visited on 07/19/2022).

Patriat, Martin et al. (Feb. 2019). "Subduction initiation terranes exposed at the front of a 2 Ma volcanically-active subduction zone". In: *Earth and Planetary Science Letters* 508, pp. 30–40. ISSN: 0012821X. DOI: 10.1016/j.epsl.2018.12.011. URL: https://linkinghub.elsevier.com/retrieve/pii/S0012821X18307209 (visited on 02/17/2024).

Ranalli, G. (1995). *Rheology of the Earth*. New York: Chapman and Hall.

Reagan, Mark K. et al. (Jan. 2019). "Forearc ages reveal extensive short-lived and rapid seafloor spreading following subduction initiation". In: *Earth and Planetary Science Letters* 506, pp. 520–529. ISSN: 0012821X. DOI: 10.1016/j.epsl.2018.11.020. URL: https://linkinghub.elsevier.com/retrieve/pii/S0012821X18306794 (visited on 02/17/2024).

Ribe, N. M. (Apr. 25, 2001). "Bending and stretching of thin viscous sheets". In: *Journal of Fluid Mechanics* 433, pp. 135–160. ISSN: 0022-1120, 1469-7645. DOI: 10.1017/S0022112000003360. URL: https://www.cambridge.org/core/product/identifier/S0022112000003360/type/journal_article (visited on 02/17/2024).

Seton, Maria et al. (2016). "Melanesian back-arc basin and arc development: Constraints from the eastern Coral Sea". In: *Gondwana Research* 39, pp. 77–95. ISSN: 1342-937X. DOI: https://doi.org/10.1016/j.gr.2016.06.011. URL: http://www.sciencedirect.com/science/article/pii/S1342937X16301320.

Shuck, B. et al. (2021). "Strike-slip enables subduction initiation beneath a failed rift: New seismic constraints from Puysegur Margin, New Zealand". en. In: *Tectonics* 40, pp. 1–33. DOI: 10.1029/2020TC006436.

Shuck, Brandon et al. (Feb. 2022). "Stress transition from horizontal to vertical forces during subduction initiation". In: *Nature Geoscience* 15.2, pp. 149–155. ISSN: 1752-0894, 1752-0908. DOI: 10.1038/s41561-021-00880-4. URL: https://www.nature.com/articles/s41561-021-00880-4 (visited on 02/17/2024).

Stern, R (Oct. 15, 2004). "Subduction initiation: spontaneous and induced". In: *Earth and Planetary Science Letters* 226.3, pp. 275–292. ISSN: 0012821X. DOI: 10.1016/S0012-821X(04)00498-4. URL: https://linkinghub.elsevier.com/retrieve/pii/S0012821X04004984 (visited on 08/22/2023).

Stern, Robert J. and Sherman H. Bloomer (Dec. 1992). "Subduction zone infancy: Examples from the Eocene Izu-Bonin-Mariana and Jurassic California arcs". In: *Geological Society of America Bulletin* 104.12, pp. 1621–1636. ISSN: 00167606. DOI: 10.1130/0016-7606(1992)104<1621:SZIEFT>2.3.CO;2. URL: https://pubs.geoscienceworld.org/gsabulletin/article/104/12/1621-1636/182637 (visited on 02/17/2024).

Stern, Robert J. and Taras Gerya (Oct. 2018). "Subduction initiation in nature and models: A review". In: *Tectonophysics* 746, pp. 173–198. ISSN: 00401951. DOI: 10.1016/j.tecto.2017.10.014. URL: https://linkinghub.elsevier.com/retrieve/pii/S0040195117304390 (visited on 02/17/2024).

Sutherland, R., P. Barnes, and C. Uruski (2006). "Miocene-Recent deformation, surface elevation, and volcanic intrusion of the overriding plate during subduction initiation, offshore southern Fiordland, Puysegur margin, southwest New Zealand". In: *New Zealand J. Geol. Geophys* 49, pp. 131–149. DOI: 10.1080/00288306.2006.9515154.

Sutherland, R., J. Collot, et al. (Apr. 2017). "Widespread compression associated with Eocene Tonga-Kermadec subduction initiation". In: *Geology* 45.4, pp. 355–358. ISSN: 0091-7613, 1943-2682. DOI: 10.1130/G38617.1. URL: https://pubs.geoscienceworld.org/geology/article/45/4/355-358/195450 (visited on 02/17/2024).

Sutherland, R., G. R. Dickens, et al. (2020). "Continental scale of geographic change across Zealandia during subduction zone initiation". en. In: *Geology* 48, pp. 419–424. DOI: 10.1130/G47008.1. URL: https://doi.org/10.1130/G47008.1,.

Tarduno, John A. et al. (Aug. 22, 2003). "The Emperor Seamounts: Southward Motion of the Hawaiian Hotspot Plume in Earth's Mantle". In: *Science* 301.5636, pp. 1064–1069. ISSN: 0036-8075, 1095-9203. DOI: 10.1126/science.1086442. URL: https://www.science.org/doi/10.1126/science.1086442 (visited on 02/17/2024).

Torsvik, T.H. et al. (2017). "Pacific plate motion change caused the Hawaiian-Emperor Bend". In: *Nature Communications* 8, 15660, p. 15660. DOI: 10.1038/ncomms15660.

Toth, John and Michael Gurnis (Aug. 10, 1998). "Dynamics of subduction initiation at preexisting fault zones". In: *Journal of Geophysical Research: Solid Earth* 103 (B8), pp. 18053–18067. ISSN: 01480227. DOI: 10.1029/98JB01076. URL: http://doi.wiley.com/10.1029/98JB01076 (visited on 07/19/2022).

Turcotte, D. L. and G. Schubert (1982). *Geodynamics*. New York: Wiley.

Watts, A. B. (2001). *Isostasy and Flexure of the Lithosphere*. Section: 458. Cambridge University Press.

Zhong, Xinyi and Zhong-Hai Li (Oct. 28, 2019). "Forced Subduction Initiation at Passive Continental Margins: Velocity-Driven Versus Stress-Driven". In: *Geophysical Research Letters* 46.20, pp. 11054–11064. ISSN: 0094-8276, 1944-8007. DOI: 10.1029/2019GL084022. URL: https://agupubs.onlinelibrary.wiley.com/doi/10.1029/2019GL084022 (visited on 02/17/2024).

Zhou, Xin, Zhong-Hai Li, et al. (July 1, 2018). "Subduction initiation dynamics along a transform fault control trench curvature and ophiolite ages". In: *Geology* 46.7, pp. 607–610. ISSN: 0091-7613. DOI: 10.1130/G40154.1. URL: https://pubs.geoscienceworld.org/gsa/geology/article/46/7/607/531973/Subduction-initiation-dynamics-along-a-transform (visited on 02/17/2024).

Zhou, Xin and Ikuko Wada (Dec. 2021). "Differentiating induced versus spontaneous subduction initiation using thermomechanical models and metamorphic soles". In: *Nature Communications* 12.1, p. 4632. ISSN: 2041-1723. DOI: 10.1038/s41467-021-24896-x. URL: http://www.nature.com/articles/s41467-021-24896-x (visited on 07/19/2022).

Chapter 3

STRIKE SLIP MOTION AND THE TRIGGERING OF SUBDUCTION INITIATION

Li, Yida and Michael Gurnis (Apr. 17, 2023). "Strike slip motion and the triggering of subduction initiation". In: *Frontiers in Earth Science* 11, p. 1156034. DOI: 10.3389/feart.2023.1156034.

3.1 Abstract

Plate tectonic reconstructions of three of the best-defined Cenozoic subduction initiation (SI) events in the western Pacific, Izu-Bonin-Mariana, Vanuatu, and Puysegur subduction zones, show substantial components of strike-slip motion before and during the SI. Using computational models, we show that strike-slip motion has a large influence on the effective strength of incipient margins and the ease of SI. The parameter space associated with visco-elasto-plastic rheologies, plate weakening, and plate forces and kinematics is explored and we show that subduction initiates more easily with a higher force, a faster weakening, or greater strike-slip motion. With the analytical solution, we demonstrate that the effect of strike-slip motion can be equivalently represented by a modified weakening rate. Along transpressive margins, we show that a block of oceanic crust can become trapped between a new thrust fault and the antecedent strike-slip fault and is consistent with structural reconstructions and gravity models of the Puysegur margin. Together, models and observations suggest that SI can be triggered when margins become progressively weakened to the point that the resisting forces become smaller than the driving forces, and as the negative buoyancy builds up, the intraplate stress eventually turns from compressional into extensional. The analytical formulation of the initiation time, t_{SI}, marking the moment when intraplate stress flips sign, is validated with computational models. The analytical solution shows that t_{SI} is dominated by convergence velocity, while the plate age, strike-slip velocity, and weakening rate all have a smaller but still important effect on the time scale of SI.

3.2 Introduction

Consensus on a unified description of subduction initiation has been slow to develop as initiation is a transient process whose record is generally obscured by subsequent

subduction zone processes, notably burial, overprinting, uplift, and compression and over-thrusting. Nevertheless, there is a substantial geological record with nearly all ocean-ocean subduction zones having initiated since the end of the Mesozoic and about half of all ocean-continent ones having re-initiated since the mid-Mesozoic (Hu and Gurnis, 2020). Subduction initiation, moreover, occurs nearby existing subduction zones (Crameri et al., 2020), is a fundamental component of plate tectonics, and is putatively associated with key changes in the force balance of tectonic plates. For example, the Pacific Plate changed its direction of motion from NNW to NW at around 50 Ma (Whittaker et al., 2007; Torsvik et al., 2017), synchronously with the initiation of two major subduction zones in the western Pacific, the Izu-Bonin-Mariana (IBM) (Ishizuka et al., 2018; Reagan et al., 2019) and Tonga-Kermadec (Sutherland, Dickens, et al., 2020). However, why new subduction zones form remains poorly understood, as subduction initiation appears to be mechanically unfavorable with initial slab pull being insufficient to overcome resistance from the friction between plates and bending of the slab (McKenzie, 1977; Toth and Gurnis, 1998; Y. Li and Gurnis, 2022). An external force, or low initial strength between plates, is required to start subduction, with scenarios for initiation described as either spontaneous (Stern and Bloomer, 1992; Nikolaeva, Gerya, and Marques, 2010) (with no external force but low strength) or induced (Gurnis, C. Hall, and Lavier, 2004; Toth and Gurnis, 1998) (with an external force).

With theoretical and computational approaches, the thermal age of plates, compositional variations, trench-normal convergence and in–plane stress (Gurnis, C. Hall, and Lavier, 2004; Nikolaeva, Gerya, and Marques, 2010; Leng and Gurnis, 2011) and fault strength, fault weakening and plate bending (McKenzie, 1977; Toth and Gurnis, 1998; Thielmann and Kaus, 2012; Qing et al., 2021) having been identified as key mechanical factors which respectively drive and limit subduction initiation. Independent of spontaneous and induced scenarios, driving forces must overcome frictional resistance between plates and bending of the high, effective viscosity plate. If the plate boundary does not weaken sufficiently fast, the oceanic plate will not slide into the mantle to allow the negative thermal buoyancy to grow quickly enough. Constitutive models with strength that weakens with deformation, due to grain size reduction, grain damage, or volatile ingestion, have been identified (Thielmann and Kaus, 2012; Bercovici and Ricard, 2014; Hirth and Kohlstedt, 1996) and can lead to rapid instability (Leng and Gurnis, 2015; Zhou et al., 2018). Models exhibiting spontaneous initiation start in a critical state that verges on instability (Leng and Gurnis, 2015; Zhou et al., 2018), an unsatisfactory condition to address causes for

the onset of initiation. If a plate boundary is in a state close to instability, the question arises as to why the boundary initiated at that point in time and not earlier.

Strike-slip motion might be one reason plate boundaries are brought closer to a state favorable for subduction initiation. Plate tectonic reconstructions of the IBM, Vanuatu and Puysegur subduction zones, three of the best constrained subduction initiation events in the western Pacific during the Cenozoic, each show a substantial component of strike-slip motion before and during initiation (Fig. 3.1). The Puysegur subduction zone extending south from the South Island of New Zealand has a well-documented component of strike-slip motion during subduction initiation which continues to the present (G. Lamarche and J.-F. Lebrun, 2000; Sutherland, Barnes, and Uruski, 2006). The initiation of IBM, among the best studied and often used as a point of comparison with other subduction zones, ophiolite–origin models, and mechanical models (Arculus et al., 2019). Although less discussed, IBM experienced a strong component of strike slip motion during the well-documented period of initiation (Gurnis, 2023). The Vanuatu subduction initiation also saw a strong component of strike-slip motion during the interval 15 to 12 Ma when the new subduction zone was forming through a polarity reversal with velocities of about 5 to 6 cm/yr (Fig. 1B, D). In addition to the the main Vanuatu subduction zone, a new segment of the plate boundary is initiating at its southern boundary, referred to as the Matthew and Hunter subduction zone, with a small 2 cm/yr convergence and a subtantially larger strike-slip motion along the Hunter Ridge since 2 Ma (Patriat et al., 2019). All of these subduction initiation events must have been shaped by strike-slip motion, but do large components of strike-slip motion influence the mechanics of initiation?

3.3 Model Formulation

We solve for the Stokes equations using traditional formulations used in geodynamics (Moresi, Gurnis, and S. Zhong, 2000; Ismail-Zadeh and Tackley, 2010) and show that a component of strike-slip motion can substantially reduce the strength of a nascent plate boundary while providing a triggering mechanism to nucleate a new subduction zone. The idea that strike-slip motion produces a more favorable condition for the far-field compression to induce subduction is examined by Xinyi Zhong and Z.-H. Li (2023) with 3D models. Here, we address this problem with a sliced 3D geometry extended from the trench-perpendicular cross-section (x-z dimension), with an additional trench-parallel dimension (y-dimension) that accounts for the strike-slip motion (Fig 3.2). In the trench-perpendicular (x-z) dimension,

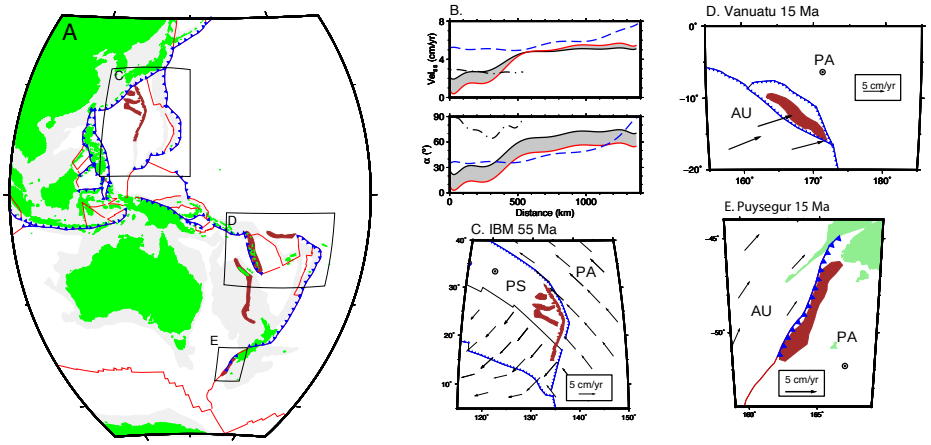

Figure 3.1: Three Cenozoic subduction initiation events that occurred in the western Pacific showing a substantial component of relative, strike-slip motions at the nascent trench just prior to initiation. A. Present-day western Pacific with the structures against which subduction initiated shown in brown. Regions of detail shown with boxes. B. Magnitude of strike slip motion (above) and convergence direction (below, with 0 being normal to the strike of the trench) before onset of initiation. Izu-Bonin-Mariana (IBM) shown at 55 Ma (red) and 50 Ma (black solid) with values for intermediate times shown with with grey shading, Vanuatu at 15 Ma (blue dashed) and Puysegur (black, dot-dashed) using the plate model of Müller et al. (2019). C. Conditions at IBM at 55 Ma, 5 Myr before the onset of SI. D. Vanuatu at 15 Ma, 1-3 Myr before onset. E. Puysegur at 15 Ma, 1-3 Myr before onset. Abbreviations for plates: PA-Pacific Plate, AU-Australia Plate, PS-Philippine Sea Plate

we apply either a convergent velocity or a convergent force on the right side of the subducting plate to induce subduction initiation. In the trench-parallel dimension, a strike-slip velocity is applied on the right wall of the subducting plate to drive the strike-slip velocity. For the two boundaries normal to the strike direction, we apply a periodic boundary condition, which allows the material to flow through the two boundaries freely. As the width of the trench parallel dimension is small ($\approx$ 6 km) with only two layers of elements and periodic boundary conditions enforcing the strike-slip velocity, the models virtually solve for a plane strain problem with no variation along strike.

A younger overriding plate is to the left of an old oceanic plate with either a compressional force or a convergent velocity added on the right edge of the older plate. A pre-existing weak zone with yielding stress being reduced by half is located at the plate boundary. As plate convergence and strike-slip motion accumulates, the strain will eventually localize at the plate boundary.

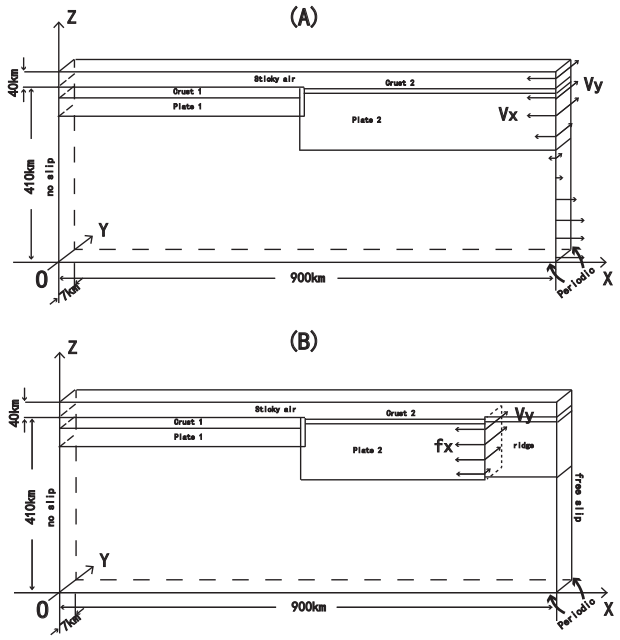

Figure 3.2: The model configuration of velocity boundary model A and force boundary model B.

The deformation of a visco-elasto-plastic material is computed with the finite element code *Underworld* (Mansour et al., 2019). The constitutive relationship between strain rate, $\dot{\varepsilon}$, and deviatoric stress, τ, is defined through a visco-elastic Maxwell body (Moresi, Dufour, and Muhlhaus, 2003),

$$\dot{\varepsilon} = \frac{\dot{\tau}}{2\mu} + \frac{\tau}{2\eta} \tag{3.1}$$

Viscosity follows the non-Newtonian Arrhenius law

$$\eta = \eta_0 \left(\frac{\dot{\varepsilon}_{II}}{\dot{\varepsilon}_0}\right)^{\frac{1}{n}-1} e^{\frac{E}{nR}\left(\frac{1}{T}-\frac{1}{T_0}\right)} \tag{3.2}$$

where μ is the shear modulus, η the viscosity, T the temperature, and $\dot{\varepsilon}_{II}$ the second invariant of strain rate tensor. E, n and R are activation energy, non-linear exponent, and ideal gas constant. $\dot{\varepsilon}_0$, η_0 and T_0 are reference strain rate, reference viscosity and reference temperature.

Plasticity, describing the strength of the rock, is an essential component of subduction initiation. We assume a yielding envelope given by the Drucker-Prager failure

criterion bounded by a maximum stress

$$\tau = \min(C\cos\phi + P\sin\phi, \tau_{max}) \tag{3.3}$$

where τ is the yielding envelop, C and ϕ are cohesion and friction angle and τ_{max} the maximum stress the rock can sustain. With the accumulation of plastic strain, the yielding envelope is reduced through rock damage or grain size reduction. The weakening is approximated as a two-stage process: The yielding envelope first reduces linearly with increasing plastic strain until saturation at which point the plastic parameters C and ϕ remain constant.

$$C = C_0 + (C_f - C_0)\min(1, \frac{\varepsilon_P}{\varepsilon_{P0}}) \tag{3.4}$$

$$\phi = \phi_0 + (\phi_f - \phi_0)\min(1, \frac{\varepsilon_P}{\varepsilon_{P0}}) \tag{3.5}$$

The reference plastic strain, ε_{P0}, controls the weakening rate with rocks weakening faster with smaller ε_{P0} and vice versa. With a lack of consensus on the underlying mechanisms responsible for weakening (Thielmann and Kaus, 2012; Bercovici and Ricard, 2014; Hirth and Kohlstedt, 1996), ε_{P0} is varied as an unknown along with other key parameters including the external compression, F_{xx}, and strike-slip velocity, V_{SS}. Details of model parameters are in Supplementary Table 3.1.

In addition to the numerical models, we formulate an analytical solution modified from Y. Li and Gurnis (2022) considering the extra influence of the strike-slip motions. The formulation of the analytical solution is based on the horizontal force balance of the subducting plate between the forces that drive the plate motion and forces that resists plate motion. The strike-slip motion affects the force balance equation through accelerating the weakening process, thereby reducing the frictional resistance at the plate boundary. By varying modeling parameters of interest, like the strike-slip velocity and weakening rate, we measure quantities like the plate force, F_{xx}, initiation time, t_{SI}, and total work, W_{SI}, from numerical models, that are compared with the analytical predictions.

3.4 Results

Kinematic boundary condition

We use a kinematic boundary condition with a constant convergent velocity on the right end of the subducting plate to initiate subduction (Fig 3.2A, Fig 3.3A). The different conditions controlling the evolution of subduction are evaluated by tracking the vertically–integrated horizontal compressional stress in the plate, i.e.

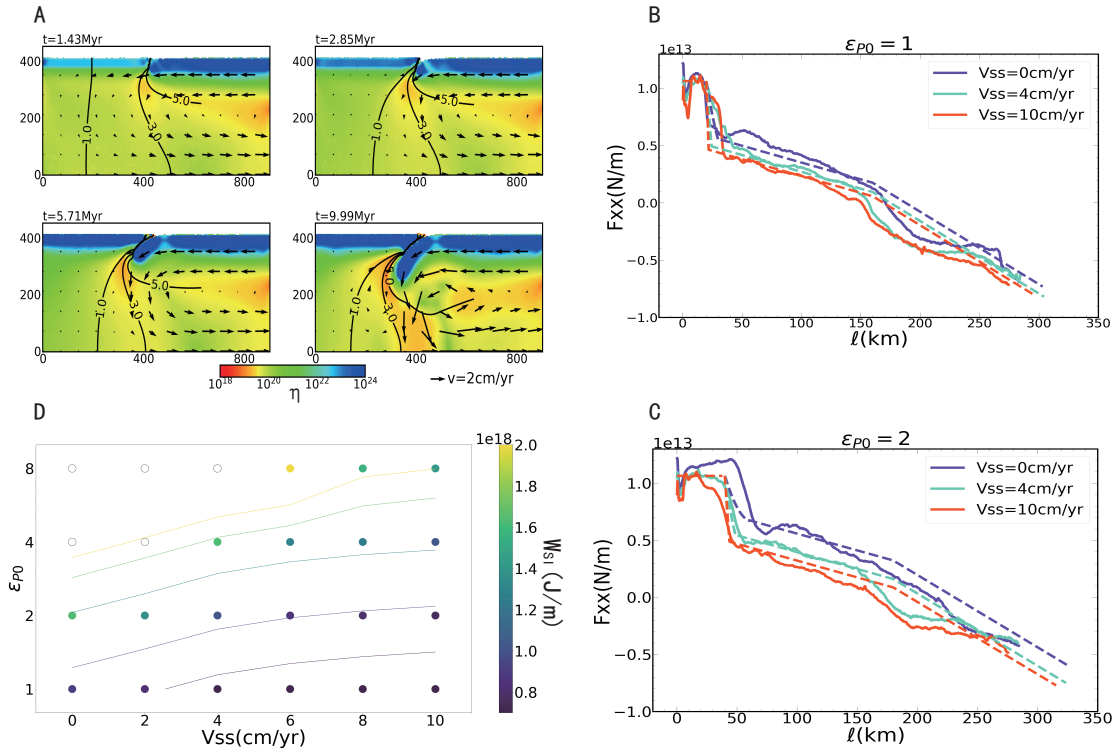

Figure 3.3: A. An example of model with 1cm/yr convergent velocity. Color shows the effective viscosity. Vectors show the in-plane component velocity and contours show strike slip velocity in cm/yr. B. The integrated horizontal compressional force in the plate F_{xx} as a function of plate motion ℓ for models with different strike slip velocity V_{SS} under $\varepsilon_{P0} = 1$. Solid line for numerical model results and dashed line for analytical results. C. Same as B but with slower weakening rate $\varepsilon_{P0} = 2$. D. The work done to initiate a subduction W_{SI} of every numerical model(color-coded solid circle) in the parametric grid search varying the strike slip velocity V_{SS} and ε_{P0}. Contours show the prediction of W_{SI} from analytical model.

$F_{xx} = \int_0^{d_{lith}} -\sigma_{xx} dz$, where d_{lith} is the thickness of lithosphere. Prior to initiation, plate motion is resisted by a large coupling stress at the plate boundary. Later, F_{xx} drops with plate convergence, ℓ, through plastic weakening and decoupling of the two plates and accumulation of negative buoyancy (Y. Li and Gurnis, 2022). Eventually, F_{xx} becomes negative (extensional), indicating that subduction has become self-sustaining and driven by the negative buoyancy of the slab instead of external forces (Fig. 3.3B-C), and we define the time when F_{xx} drops to 0 as the initiation time t_{SI}. Following Y. Li and Gurnis (2022), we define the total work, W_{SI}, done by the boundary velocity to induce a subduction initiation until t_{SI} (i.e. $W_{SI} = \int_0^{t_{SI}} F_{xx} V_x dt$), characterizing the total resistance that the driving force overcomes.

The tracking of plate force, initiation time, and total work quantitatively reflect the difficulty to induce subduction initiation. A larger F_{xx}, t_{SI} and W_{SI} indicate the subduction initiation encounters greater resistance. We develop an analytical solution of the strike-slip subduction initiation model, validate it with the numerical results, and expand the parametric space via the analytical solution.

In 2D cross-sectional models (with no strike-slip motion), F_{xx} can be formulated analytically via a force balance analysis on the subducting plate, such that F_{xx}, together with slab pull as the driving force, is balanced by the resistance from plate bending, inter-plate friction, isostatic gradients at the boundary, and shear from mantle flow (Y. Li and Gurnis, 2022). The addition of the third dimension (strike-slip) mainly changes the system by enhancing the weakening process. To analytically address the role of strike slip motion, we modify the formulation of inter-plate friction by enhancing the weakening as a result of the strike-slip velocity (see Supplementary material section S1). The contribution of strike-slip motion is analytically shown to be equivalent to reducing the effective weakening rate $\varepsilon_{P0\_eff} = \varepsilon_{P0}\frac{V_x}{\sqrt{{V_x}^2+{V_{SS}}^2}}$ and thereby reduce the inter-plate friction. This friction is balanced by the driving force, F_{xx}, and the analytical model (dashed line in Fig 3.3B-C) predicts a decrease of F_{xx} with increasing V_{SS}, in agreement with the numerical models (solid line in Fig 3.3B-C). Increasing strike-slip velocity and weakening rate consistently lowers F_{xx}, as both reduce the resistance inhibiting subduction initiation. A grid search of V_{SS} and ε_{P0} shows how these parameters influence W_{SI} (Fig. 3.3 D). In the limit of a small V_{SS} and a large ε_{P0}, convergence is insufficient to nucleate a weak zone and initiate a subduction (open circles, Fig. 3.3 D). Outside of that domain, subduction initiates and the resistance has a consistent trend: Increased V_{SS} and decreased ε_{P0} tend to lower W_{SI}.

Finally, we evaluate t_{SI} from the analytical model varying V_x, V_{SS}, ε_{P0} and subducting plate age (Fig 3.4). As discussed in Y. Li and Gurnis (2022), the initiation time is dominantly controlled by the total plate convergence, so that convergence rate V_x has a first-order control on the predicted t_{SI}. Subducting plate age determines the plate thickness, which controls both the plate bending resistance and the slab pull. The plate age affects the force balance in two ways, the slab pull and plate bending because the plate thickness changes. As the dependence of slab pull on plate thickness is first order while plate rigidity (with plasticity) second order, the change of t_{SI} is dominated by slab pull when plate is young ($<$ 10 Ma), and for an old plate ($>$ 20 Ma) the t_{SI} is governed by plate bending. Therefore, below 10Ma we

see a decrease of t_{SI} as the plate gets older due to increased slab pull that drives plate motion, while above 20 Ma t_{SI} increases with plate age due to increased bending resistance. Both V_{SS} and ε_{P0} influence t_{SI} via the term of inter-plate friction. Both increase of V_{SS} and decrease of ε_{P0} lead to an acceleration of subduction initiation, thereby reducing the t_{SI}. However, compared to V_x, the impact of the plate age, V_{SS} and ε_{P0} is minor.

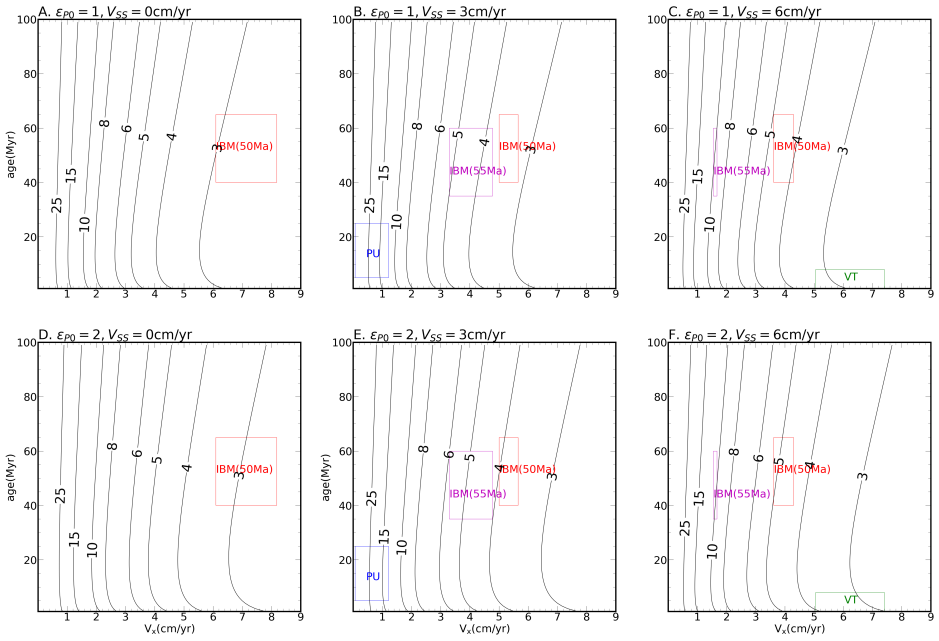

Figure 3.4: Analytical prediction of initiation time t_{SI} under different convergent velocity Vx and subducting plate age with A. V_{SS} = 0, ε_{P0} = 1, B. V_{SS} = 3cm/yr, C. V_{SS} = 6cm/yr, ε_{P0} = 1. D to F are the same as A to C except ε_{P0} = 2. Red, magenta, blue and green box show the parameter range of IBM (50Ma), IBM (55Ma), Puysegur (PU) and Vanuatu (VT) subduction initiation from the given V_{SS} with a ±1cm/yr range.

Force Boundary Conditions

Besides an applied convergent velocity, subduction initiation can be induced through applying a force on the edge of the plate (Fig. 3.2B). We use a geometry approximating a mid-ocean ridge and a compressional force F_{xx} at the ridge edge of the subducting plate (Fig. 3.2). The total compression driving the plate motion is composed of the internal ridge push from the thermal contrast and the external force F_{xx}.

When F_{xx} is sufficiently large, plate bending and resistance by shearing between plates at the nucleating boundary are overcome with subduction initiation (Leng and Gurnis, 2011; X. Zhong and Z.-.-H. Li, 2019); the minimum force needed for initiation is determined through systematic variation of parameters.

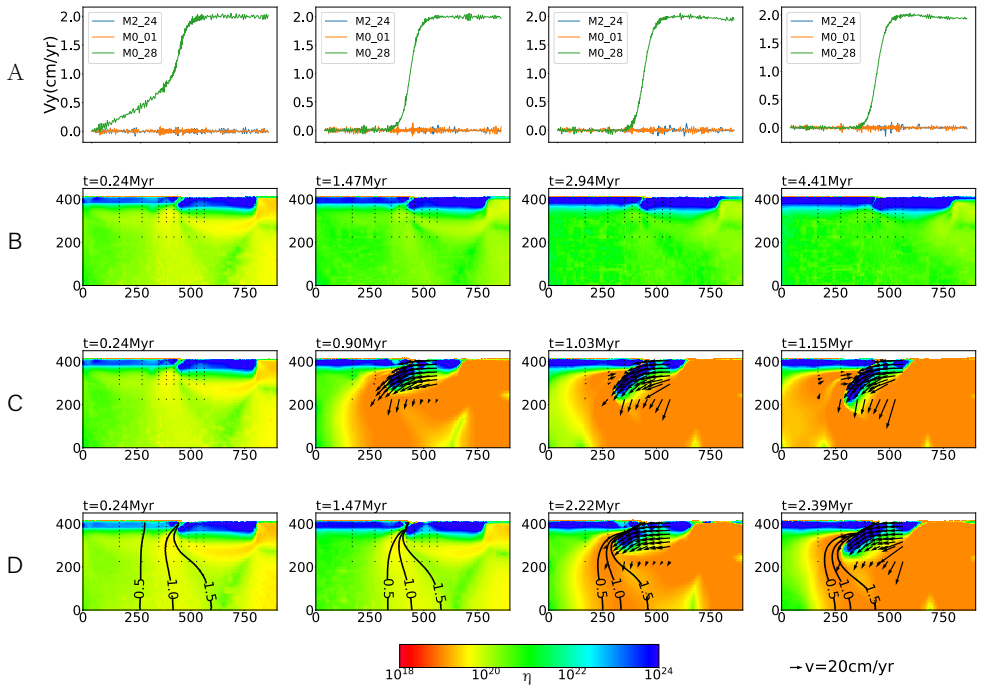

Figure 3.5: Cases with applied compression and with three different strike–slip velocities. A. Strike slip velocity along the the top of the domain. The parameters [ε_{P0}, V_{SS} , f_{xx}] for the three case are: B. Case M2_24, [2, 0 cm/yr, 8.57×10^{12} N/m]. C. Case M0_01, [1, 0, 8.57×10^{12}]. D. Case M0_28, [2, 2, 8.57×10^{12}]. In B-D Contours show the strike slip velocity in cm/yr

All prior models of subduction initiation in the literature have no strike-slip motion, and so we start with a case with no strike-slip velocity with [ε_{P0}, V_{SS} , f_{xx}]=[2, 0 cm/yr, 8.57×10^{12} N/m], as a reference (Fig. 3.5B) In this case, due to the insufficient compression to induce subduction initiation ($F_{xx} = 8.57\times10^{12}$ N/m) under a relatively low weakening rate ($\varepsilon_{P0} = 2$, larger ε_{P0} meaning slower weakening), the subduction initiation fails to occur and the plate boundary remains stable (Fig. 3.5B). Typical ridge push forces range from 2 to 4×10^{12} N/m (Bott, 1991; Toth and Gurnis, 1998) and so the F_{xx} used is not particularly small. Over time, the plate boundary remains stable with no subduction being induced. By taking this case as a reference, and then by either adding a V_{ss} of 2 cm/yr (Fig. 3.5C), or decreasing ε_{P0}

from 2 to 1 (such that the fault weakens faster), the plate boundary initiates into a subduction zone (Fig. 3.5D). This shows that the presence of strike-slip motion and acceleration of the weakening process independently facilitate subduction initiation.

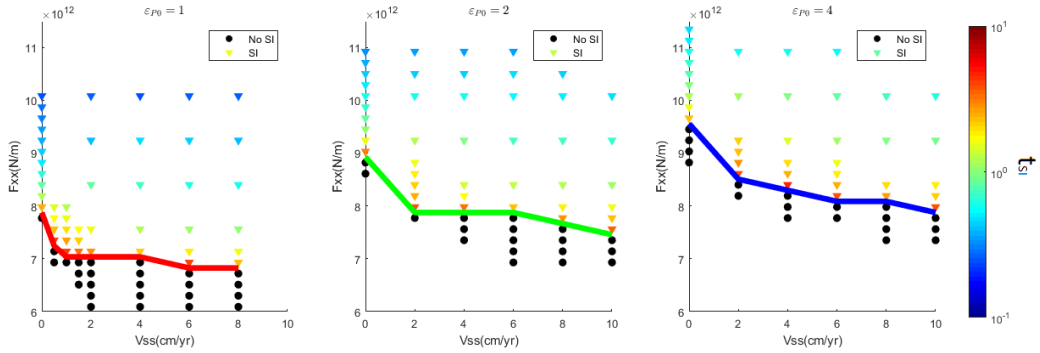

Figure 3.6: The parametric grid search result of models with different driving force F_{xx}, strike slip velocity V_{SS} and weakening rate ε_{P0}. Triangles for cases with subduction initiation and solid dots for cases with no subduction initiation. The color of triangles present the $log_{10}t_{SI}$, where the t_{SI} is the time when the slab tip reach 60 km depth, the characteristic depth when F_{xx} turns into 0 in velocity boundary models.

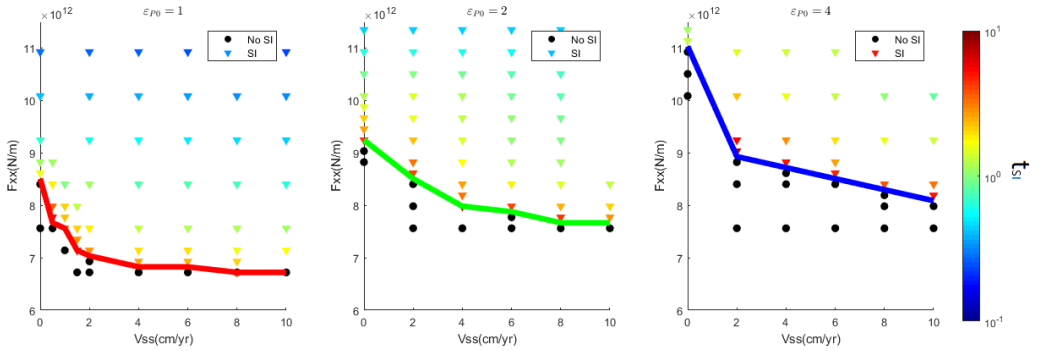

Figure 3.7: Equivalent figure with figure 3.6 but with lower resolution.

The key parameters, including strike-slip velocity, external compression, and the weakening rate, are systematically varied while computing the initiation time (Fig. 3.6). The grid search shows that regardless of the choice of weakening rate and resolution, increased strike-slip velocities lower the minimum required compressional force (Fig. 3.6 thick lines) for subduction to initiate. A lower ε_{P0} (faster weakening) always reduces the required external force, therefore facilitating subduction initiation. Unlike the velocity boundary model where the strike-slip velocity has a minor influence on plate stress and initiation time, the addition of strike-slip motion significantly reduces the stress required to initiate a subduction zone (solid curves

in Fig 3.6, 3.7), indicating the strike-slip motion provide a more favorable condition for subduction initiation.

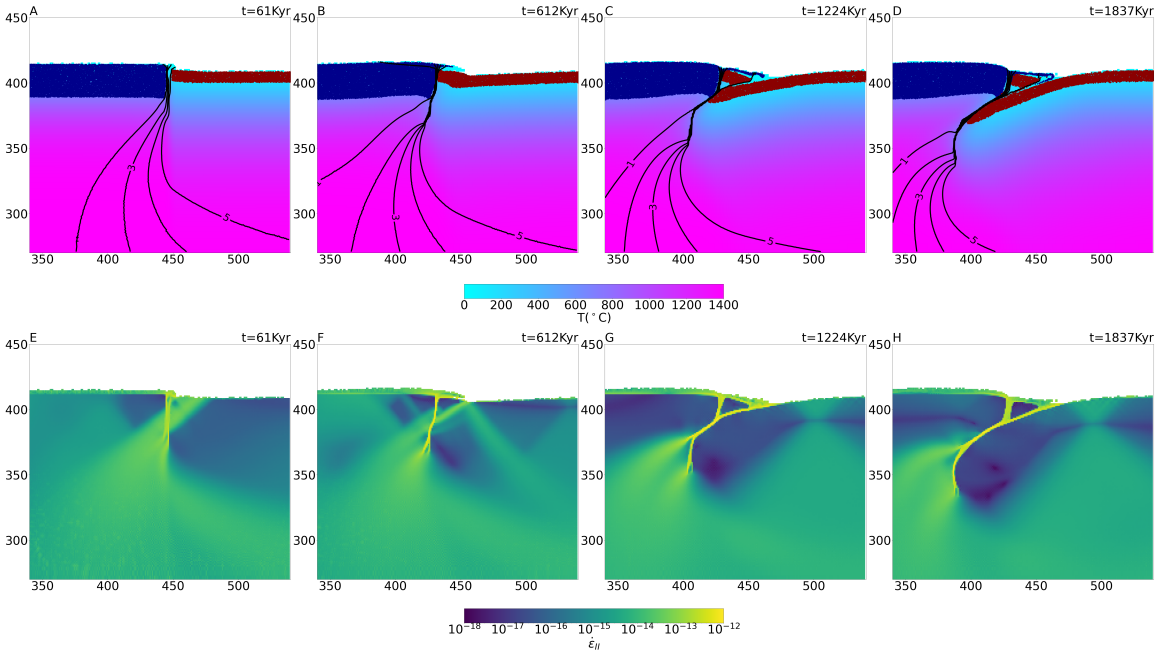

Figure 3.8: Fault evolution of a high resolution models with [ε_{P0}, V_{SS} , V_p]=[2, 6 cm/yr, 4 cm/yr]. A–D, Red and blue for oceanic and continental crust. Background color for temperature. E–H, Second invariant of strain rate ($\dot{\varepsilon}_{II}$).

Fault Evolution

The computations yield a fault system that evolves from a single strike-slip fault into a strain partitioned system composed of a vertical strike-slip fault and a dipping oblique thrust fault with partitioning of strike-slip velocity between the two (Fig. 3.8). Initially, the plate boundary fault is vertical, and will remain so with only subsequent strike-slip motion; however, subduction requires a dipping thrust fault to decouple the two plates. In those cases where the system evolves into a subduction zone, we have found that the thrust fault emerges through the combined reuse of the strike-slip fault and new fault formation. The upper part of a trapped block is bound by a vertical strike-slip fault and an oblique thrust fault as the upper lithosphere has a high viscosity and brittle failure (faulting) is the dominant mechanism that accommodates the compression. The lower part of the vertical strike-slip fault rotates with compression of the somewhat lower viscosity, ductile lower lithosphere. Through this process, the lower part of the vertical strike-slip fault is transferred and becomes the lower part of the oblique thrust fault. The reuse of a vertical fault weakened by strike-slip motion is a primary reason why strike-slip motion can lower the required force to induce subduction and therefore facilitate subduction initiation.

In the case shown above, we choose a high yield stress (300 MPa) which makes the crust of the overriding plate strong. However, with a continental upper plate with a weaker crustal layer, the resultant morphology is different (Fig. 3.9). In this case, the rheology yields a typical continental strength envelope (Kohlstedt, Evans, and Mackwell, 1995), with a weak layer present at the base of the continental crust, decoupling the lithosphere from the crust. Unlike the strong plate case where a new dipping fault emerges in the upper part of the subducting plate in response to the far–field compression, in the case of weak continental crust, the overriding plate severely deforms to accommodate the compression. In the overriding plate, the lower lithosphere delaminates at the base of the buoyant continental crust. The compression forces the subducting plate and the lower lithosphere of the upper plate to bend simultaneously, and a vertical strike-slip fault emerges in the upper plate crustal layer to reconcile the strike-slip motion. Consequently, a strain partitioning system emerges, but the wedge trapped between the strike-slip fault and the dipping thrust fault is composed of continental crust.

3.5 Discussion

With the numerical models that extend a traditional 2D trench perpendicular cross-sectional domain with orthogonal strike–slip motion, such motion influences sub-

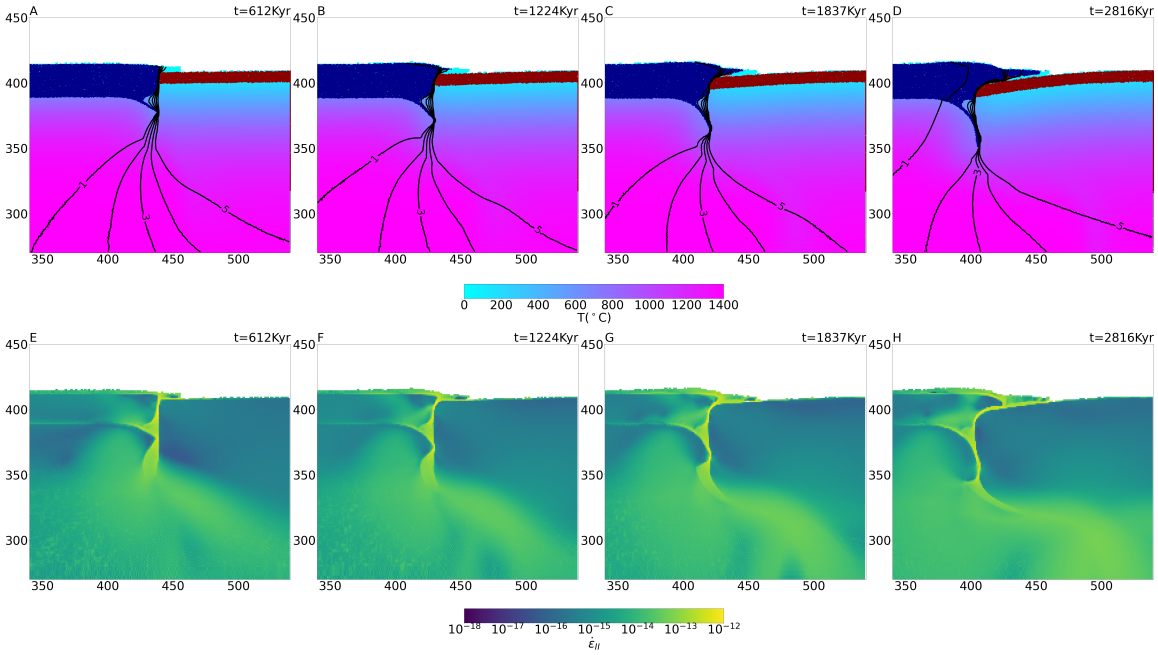

Figure 3.9: Fault evolution of a high resolution models with [ε_{P0}, V_{SS} , V_p]=[2, 6 cm/yr, 4 cm/yr], equivalent to Fig 3.8 but with weaker quartzitic crust rheology. A–D, Compositional domains. E–H, Second invariant of strain rate ($\dot{\varepsilon}_{II}$).

duction initiation. This builds on the concept that mature strike-slip faults like the San Andreas Fault (SAF) are weak (as revealed through stress indicators (Zoback et al., 1987) and heat flow (Brune, Henyey, and Roy, 1969)) and that the damage around faults grows with increasing fault displacement (Faulkner et al., 2011; Savage and Brodsky, 2011). A common conceptual idea is that a strike-slip fault will have local irregularities along the strike such there will be zones of convergence that could be sites for subduction initiation. A well-known example where local transpression leads to downwelling, although not subduction initiation, is the Miocene evolution of the San Andreas Fault (SAF) and Transverse Ranges of southern California in North America. Here, it is thought that the clear convergence across the Big Bend segment of the SAF north of Los Angeles has led to crustal and lithospheric thickening and convective instability (Humphreys and Clayton, 1990). However, we present a scenario that is distinctly different from this one, advancing the hypothesis that even with no irregularities in the orientation of faults along strike, subduction initiation is enhanced by strike-slip motion.

Can the models be applied to specific subduction initiation events? An obvious

application is along the boundary between the Pacific and Australian Plates, south of New Zealand, the Puysegur subduction zone (Fig. 3.1E). Here, a major strike-slip fault immediately to the east of the trench accommodates some of the relative plate motion (J. Y. Collot et al., 1995; G. Lamarche and J.-F. Lebrun, 2000). The age of the Puysegur subduction zone has been estimated in two ways. First is through a reconstruction using a combination of the depth extent of the seismic slab and plate kinematics, which date the onset of subduction to between 15 and 12 Ma (Sutherland, Barnes, and Uruski, 2006). Second, the age has been estimated through detailed seismic imaging of the stratigraphy on the overriding Pacific Plate which shows basin inversion (Shuck, Gulick, et al., 2022). In the northern section of Puysegur, the compression starts at 15 Ma and transitions to mild extension by 8 Ma. During this interval, most of the relative motion between the Australian and Pacific Plates was strike-slip with velocities of about 3 cm/yr (Fig. 3.1B). The subducting plate at Puysegur Trench formed along the Macquarie Ridge Complex (MRC) system, where sea–floor spreading was active since the Eocene (about 40 Ma) but terminating at about 15 Ma (Jean-Frédéric Lebrun, Geoffroy Lamarche, and J.-Y. Collot, 2003). The subducting plate age ranges from 25 Ma (north) to 5 Ma (south). With the given range of V_x, V_{SS}, and plate age for Puysegur, we predict a range of t_{SI} from the analytical model (Fig 3.4, blue box). The northern Puysegur trench corresponds to the top right corner of the blue box (V_x = 1 cm/yr, plate age = 25 Ma), yielding a model $t_{SI} \approx 12$ Myr which roughly agrees with the observed 8 Myr duration for the basin inversion (16 to 8 Ma). For the southern Puysegur, the analytical model yields a larger t_{SI} (> 30 Myr) given the small V_x (≈ 0.2 cm/yr) and young subducting plate (5 Myr old) at 15 Ma. This prediction may over-estimate t_{SI} as during the subduction initiation the convergent velocity V_x increases substantially from 0.2 cm/yr at 15Ma to ~ 2 cm/yr today due to the change of plate motion direction (Choi et al., 2017), and the large predicted t_{SI} sheds light on why the southern Puysegur remains under compression today – in addition to the hypothesis of southward propagation of subduction initiation proposed in Shuck, Gulick, et al. (2022).

Puysegur has other features reflective of the initiation phase as it evolved from a strike-slip boundary to transpressional since 16 Ma, in particular a sliver of oceanic crust (Hightower, Gurnis, and Van Avendonk, 2020) trapped at the Puysegur Trench, bounded by a vertical fault and an oblique thrust fault (J. Y. Collot et al., 1995; Shuck, Gulick, et al., 2022). East of the Puysegur Trench, the morphology of the Puysegur Fault through the central part of the southern Puysegur Ridge is sharp and consistent

with present-day activity (Shuck, Van Avendonk, et al., 2021). The 2009 Mw 7.8 Dusky Sound earthquake below Fiordland, the strike-slip onshore extension of the nascent subduction zone, showed that nearly all of the relative motion, including the strike-slip motion, was accommodated on the thrust interface (Beavan et al., 2010). Consequently, the seismic imaging and 2009 event for Puysegur shows that it has a structure, morphology, and strain partitioning consistent with that shown in Figure 3.8, that is with substantial strike-slip motion on the thrust interface, and the entrapment of an oceanic sliver between the newly formed thrust interface and the strike-slip fault.

Subduction along IBM initiated at the boundary between the Pacific Plate and the smaller West Philippine Sea Plate along the Kyushu Palau Ridge (Fig. 3.1C). The new subduction zone is inferred to have formed between 52 and 50 Ma as indicated by ages within the forearc (Reagan et al., 2019) and basement of the West Philippine Sea Plate (Ishizuka et al., 2018). IBM is often viewed as a type locality for studying subduction initiation because of the rock record on the IBM fore–arc and an association with changes in Pacific Plate motion during the Cenozoic (Stern and Bloomer, 1992; Arculus et al., 2019). The IBM subduction zone may be an example of spontaneous subduction initiation (Stern and Bloomer, 1992), with a short, rapid burst of localized extension (Reagan et al., 2019). The overriding Philippine Sea Plate had a relic arc with thick buoyant crust adjacent to the old, cold Pacific plate at the location of apparent subduction initiation and this may have played a role in its initiation (Leng and Gurnis, 2015). Computational models suggest that compression of the incipient plate margin needs to overcome a large resisting force associated with bending the incipient slab (Gurnis, C. Hall, and Lavier, 2004; Y. Li and Gurnis, 2022), but there is debate in the literature on the significance of the compression. On the one hand, Maunder et al. (2020) argued that early compression cannot lead to near–field extension and boninite formation and that a large vertical force is needed for such extension, a force which only can exsit if there is pre-existing subduction. Moreover, a recent interpretation of Baron isotope systematics on IBM forearc recovered samples apparently indicate an initial low–angle phase of thrusting prior to the formation of the distinctive basalt to boninite sequence (H.-.-Y. Li et al., 2022).

Although not widely discussed, several lines of evidence suggest that there was a strong component of strike-slip motion during IBM inception. Paleomagnetic observations show that since 50 Ma, the Philippine Sea Plate experienced nearly

90° of clockwise rotation (R. Hall et al., 1995); since the orientation of the Kyushu-Palau Ridge (the relic arc that formed at the new boundary) is currently N-S, it would have been more E-W during subduction initiation. The orientation of convergence between the West Philippine Sea and Pacific Plates depends on the absolute motion of the Pacific Plate, but the Pacific moved by the overriding plate in a mostly strike-slip orientation with velocities of about 5 cm/yr for at least five million years before initiation (Fig. 3.1 B,C), with V_{SS} and V_x varying substantially along strike due to the curved plate boundary. Independently, detailed bathymetry just to the west of the Kyushu Palau Ridge reveal a strike–slip fault subparallel and normal faults perpendicular to the ridge in which the basement dates to the time of subduction inception, 49 Ma (Gurnis, 2023). This is consistent with transverse motion along the KPR at the time of initiation. Nearly identical forearc volcanic stratigraphy near the Bonin Islands and near Gaum Islands, 500 km apart when plate tectonic motions are accounted for (Leng and Gurnis, 2015), could have been further seperated by strike slip motion.

The strike-slip model of induced subduction initiation can be applied to IBM. With subducting plate age varying between 40 and 60 Myr old at 50 Ma (C. E. Hall et al., 2003; Lallemand and Arcay, 2021), the analytical model yields a range of initiation times (Fig 3.4). At 55 Ma, the predicted t_{SI} range from 5 to 10 Myr with V_{SS} =3 to 6 cm/yr. At 50 Ma, the reconstruction gives a larger range of V_{SS} (0 to 6 cm/yr), and the analytical model predicts a $t_{SI} \approx 3$ to 5 Myr. Using the plate tectonic constraints at 55 Ma and 50 Ma, we estimate the time for the IBM to experience conversion from compression to extension to be around 50 to 45 Ma, a 5 Myr duration slightly larger than the 2 Myr inferred from fore–arc opening determined from $^{40}Ar/^{39}Ar$ and U-Pb ages of the boninite-basalt sequence in the IBM fore–arc (52 to 50 Ma) (Reagan et al., 2019).

IBM subduction initiation may be associated with the shift in Pacific Plate motion from more northerly before 50 Ma to more westerly after 50 Ma, as evident from plate reconstructions and the bend in the Hawaiian–Emperor Seamount chain (e.g. Torsvik et al. (2017) and Müller et al. (2019)). Hu, Gurnis, et al. (2022) showed that Pacific Plate motion could change by about 10° (from more northerly to northwesterly) with introduction of the IBM slab from 55 to 50 Ma. Most of the required change in absolute Pacific Plate motion must come from elsewhere, and Hu, Gurnis, et al. (2022) show that this can be accomplished with termination of intra-oceanic subduction in the north Pacific between 55 and 50 Ma. Other

west Pacific subduction zones forming during the Cenozoic, however, may have initially been induced, including the Tonga-Kermadec subduction zone that underwent vertical motions and folding within the future back-arc region prior to and contemporaneously with subduction initiation, indicating a strong compressive force during initiation (Sutherland, Dickens, et al., 2020). Strike–slip motion between Pacific and West Phillipine Sea Plates, along with compression along this boundary due to rearrangement of Pacific Plate driving forces can lead to IBM subduction initiation. The models favor an induced mode of subduction initiation, as the minimum stress (Fig. 3.6 solid lines) never vanishes independent of the magnitude of V_{SS}.

The Vanuatu subduction zone initiated between 12 and 10 Ma, following the collision of the Ontong-Java Plateau with the Vitiaz subduction zone at 16 Ma (Mann and Taira, 2004) and may be an example of induced subduction polarity reversal (Auzende, Lafoy, and Marsset, 1988; Yang, 2022). Soon after Vanuatu subduction initiation, the Fiji basin opens at ~ 8 Ma, indicating a short initiation time (Auzende, Lafoy, and Marsset, 1988; Lallemand and Arcay, 2021). The plate reconstructions show a strong component of strike-slip motion (5 – 8 cm/yr), Fig 3.1.B dashed blue curve) between the Australian and Pacific plates along the Vanuatu incipient boundary (Fig. 3.1B,D) The strike-slip mechanical model yields a small value for t_{SI} ($\approx$ 3 Myr, Fig 3.4), because of the large strike-slip velocity V_{SS}, large convergent velocity V_x and the young plate age (Lallemand and Arcay, 2021).

3.6 Conclusion

Three Cenozoic subduction zones – Puysegur, IBM and Vanuatu – all show substantial components of strike–slip motion prior to and during initiation. Application of the mechanical model developed here using plate reconstruction constraints all yield estimates of initiation times consistent with values estimated independently from geological observations. Together, the models and observations suggest that subduction initiation can be triggered when margins become progressively weakened to the point that the resisting forces become smaller than the driving forces. Despite the strike-slip velocity having a relatively minor influence on the evolution of plate stress and initiation time compared to the plate convergent velocity, it can still dramatically lower the force required to induce subduction initiation, thereby providing a favorable condition for subduction initiation.

3.7 Supplementary material

3.8 Analytical Solution

We modify the formulation in (Y. Li and Gurnis, 2022) to evaluate the force evolution in a subduction system with strike slip motion. For the no-strike-slip case, the formulation is the same as (Y. Li and Gurnis, 2022) eq. 13:

$$F_{xx} = (2\eta\frac{L_P}{d_a} + K_b)u + T_S - H\Delta\rho\sin\theta\ell + N_{HZ} + F_I \tag{3.6}$$

Where T_S is the friction at the plate boundary, dominantly governed by a linear plastic weakening process.

$$T_S = \int_0^{\frac{H}{\sin\theta}} \tau_y ds = (\tau_{y0} + \frac{(\tau_{yf} - \tau_{y0})\ell}{\delta\varepsilon_{P0}})\frac{H}{\sin\theta} + \ell\frac{\tau_{y0} - \tau_{yf}}{\delta\varepsilon_{P0}}\ell = A - B\ell + C\ell^2 \tag{3.7}$$

Here $A = \frac{\tau_{y0}H}{\sin\theta}$, $B = \frac{\tau_{y0}}{\delta\varepsilon_{P0}} \cdot \frac{H}{\sin\theta}$, and $C = \frac{\tau_{y0}}{\delta\varepsilon_{P0}}$. After $s > \delta\varepsilon_{P0}$, where δ is the fault thickness,

$$T_S = \int_0^{\frac{H}{\sin\theta}} \tau_y ds = \tau_{yf}\frac{H}{\sin\theta} + \delta\varepsilon_{P0}(\tau_{y0} - \tau_{yf}) = D \tag{3.8}$$

The presence of strike slip motion effectively accelerate the plastic weakening process, hence reduces the effective weakening rate. For the cases of boundary velocity (Dirichlet boundary condition), both convergence velocity V_x and strike slip velocity V_{SS} are constant throughout the whole time. Thereby, we can easily account for the effect of strike slip motion by introducing an effective weakening rate $\varepsilon_{P0\_eff} = \varepsilon_{P0}\frac{V_x}{\sqrt{{V_x}^2+{V_{SS}}^2}}$. By replacing all the ε_{P0} with ε_{P0_eff} in eq 3.7 and eq 3.8 we get the modified expression of force evolution incorporating the strike slip velocity.

3.9 Model Resolution

In addition to the factors discussed above, the resolution of the finite element models also has an influence on the plate decoupling process and thereby influences the formation of subduction (Gurnis, C. Hall, and Lavier, 2004). We recalculated the models with the same parametric grid search (Fig. 3.7) but with a lower resolution (1.7 km/el vs. 3.5 km/el) near the fault zone (Fig. SoM). The minimum force to initiate subduction (thick solid lines) increases by less than 10% when V_{SS} is close to 0, but with larger strike slip velocity, identical models with different resolution predict a similar minimum force. The finer structure of faulting is investigated by computing several cases with a high resolution near the plate boundary (0.8 km/el).

Symbol	Definition	Value	Symbol	Definition	Value
n	non-Newtonian exponent Olivine Mantle	3	E	Activation energy Olivine Mantle	540 kJ/mol
A	pre-exponent Olivine Mantle	2.4×10^3Pa · s	n	Activation energy Quartzitic Crust	4
E	Activation energy Quartzitic Crust	223 kJ/mol	A	pre-exponent Quartzitic Crust	3.3×10^4Pa · s
n	non-Newtonian exponent Eclogite	3.4	E	Activation energy Eclogite	480 kJ/mol
A	pre-exponent Eclogite	9.8×10^6Pa · s	τ_{yf}	minimum yield stress	3 MPa
τ_{y0}	maximum yield stress subducting plate	150 MPa	τ_{y0}	maximum yield stress upper plate	300 MPa
η_{min}	minimum viscosity	10^{19} Pa · s	η_{max}	maximum viscosity	10^{25} Pa · s
t_2	subducting plate age	40 Myr	t_1	overriding plate age	20 Myr
μ	shear modulus	3×10^{10} Pa	ε_{P0}	reference plastic strain	$1 \sim 8$
$\dot{\varepsilon}_0$	reference strain rate	10^{-15} s^{-1}	α	thermal expansivity	3×10^{-5} C^{-1}
ΔC_1	continental crustal thickness	25 km	ΔC_2	oceanic crustal thickness	8 km
κ	thermal diffusivity	10^{-6} m^2 · s^{-1}	H	plate mechanical thickness	60 km
T_0	Surface temperature	0°C	δ	fault thickness	20 km
T_1	mantle temperature	1400° C	θ	fault dip angle	45°
C_0	initial cohesion	44 MPa	μ_{y0}	initial friction coefficient	0.6
η_{st}	sticky air viscosity	10^{19}Pa · s	μ_{st}	shear modulus sticky air	3×10^{10} Pa
d_{st}	sticky air thickness	40km	κ_{st}	thermal diffusivity sticky air	10^{-5} m^2 · s^{-1}
C_0	initial cohesion	44MPa	C_f	final cohesion	3MPa
ϕ_0	initial friction angle	0.6	ϕ_f	final friction angle	0

Table 3.1: Model Parameters mainly inherit from Y. Li and Gurnis, 2022 with an addition of weak overriding plate cases. Non-Newtonian parameters of Olivine mantle, Quartzitic crust and Eclogite are from Karato and Wu, 1993; Gleason and Tullis, 1995; Jin et al., 2001.

References

Arculus, R. J. et al. (2019). "How to create new subduction zones: A global perspective". In: *Oceanography* 32, pp. 160–174. DOI: 10.5670/oceanog.2019.140.

Auzende, Jean-Marie, Yves Lafoy, and Bruno Marsset (1988). "Recent geodynamic evolution of the north Fiji basin (southwest Pacific)". In: *Geology* 16.10, pp. 925–929.

Beavan, J. et al. (2010). "Oblique slip on the Puysegur subduction interface in the 2009 July Mw 7.8 Dusky Sound earthquake from GPS and InSAR observations:

implications for the tectonics of southwestern New Zealand". In: *Geophys. J. Int.* 183, pp. 1265–1286. DOI: 10.1111/j.1365-246X.2010.04798.x.

Bercovici, D. and Y. Ricard (2014). "Plate tectonics, damage and inheritance". In: *Nature* 508, pp. 513–516. DOI: 10.1038/nature13072.

Bott, M. H. P. (1991). "Ridge push and associated plate interior stress in normal and hotspot regions". In: *Tectonophysics* 200, pp. 17–32.

Brune, J. N., T. L. Henyey, and R. F. Roy (1969). "Heat flow, stress, and rate of slip along the San Andreas Fault, California". In: *J. Geophys. Res.* 74.15, pp. 3821–3827. DOI: https://doi.org/10.1029/JB074i015p03821.

Choi, Hakkyum et al. (2017). "The kinematic evolution of the Macquarie Plate: A case study for the fragmentation of oceanic lithosphere". In: *Earth and Planetary Science Letters* 478, pp. 132–142.

Collot, J. Y. et al. (1995). "Morphostructure of an incipient subduction zone along a transform plate boundary - Puysegur Ridge and Trench". In: *Geology* 23.6, pp. 519–522. ISSN: 0091-7613. DOI: Doi10.1130/0091-7613(1995)023<0519:Moaisz>2.3.Co;2. URL: %3CGo%20to%20ISI%3E://WOS:A1995RB22200010.

Crameri, F. et al. (2020). "A transdisciplinary and community-driven database to unravel subduction zone initiation". In: *Nature communications* 11.1, pp. 1–14.

Faulkner, D. R. et al. (2011). "Scaling of fault damage zones with displacement and the implications for fault growth processes". In: *Journal of Geophysical Research: Solid Earth* 116.B5. DOI: https://doi.org/10.1029/2010JB007788. eprint: https://agupubs.onlinelibrary.wiley.com/doi/pdf/10.1029/2010JB007788. URL: https://agupubs.onlinelibrary.wiley.com/doi/abs/10.1029/2010JB007788.

Gleason, Gayle C and Jan Tullis (1995). "A flow law for dislocation creep of quartz aggregates determined with the molten salt cell". In: *Tectonophysics* 247.1-4, pp. 1–23.

Gurnis, M. (2023). "An evolutionary perspective on subduction initiation". In: *Dynamics of Plate Tectonics and Mantle Convection*. Ed. by J. C. Duarte. Amsterdam: Elsevier, pp. 357–383. DOI: 10.1016/B978-0-323-85733-8.00003-2.

Gurnis, M., C. Hall, and L. Lavier (2004). "Evolving force balance during incipient subduction". In: *Geochemistry Geophysics Geosystems* 5. ISSN: 1525-2027. DOI: ArtnQ0700110.1029/2003gc000681. URL: %3CGo%20to%20ISI%3E://WOS:000222653900002.

Hall, Chad E. et al. (July 2003). "Catastrophic initiation of subduction following forced convergence across fracture zones". In: *Earth and Planetary Science Letters* 212.1, pp. 15–30. ISSN: 0012821X. DOI: 10.1016/S0012-821X(03)00242-5. URL: https://linkinghub.elsevier.com/retrieve/pii/S0012821X03002425 (visited on 02/16/2024).

Hall, R. et al. (1995). "Origin and motion history of the Philippine Sea Plate". In: *Tectonophysics* 251.1-4, pp. 229–250. ISSN: 0040–1951. DOI: Doi10.1016/0040-1951(95)00038-0. URL: %3CGo%20to%20ISI%3E://WOS:A1995TM47600010.

Hightower, E., M. Gurnis, and H. Van Avendonk (2020). "A Bayesian 3-D linear gravity inversion for complex density distributions: application to the Puysegur subduction system". In: *Geophys. J. Int.* 223.3, pp. 1899–1918.

Hirth, G. and D. L. Kohlstedt (1996). "Water in the oceanic upper mantle: implications for rheology, melt extraction and the evolution of the lithosphere". In: *Earth Planet. Sci. Lett.* 144, pp. 93–108.

Hu, J. and M. Gurnis (2020). "Subduction duration and slab dip". In: *Geochemistry, Geophysics, Geosystems* 21. DOI: 10.1029/2019GC008862.

Hu, J., M. Gurnis, et al. (2022). "Dynamics of abrupt change in Pacific Plate motion around 50 Ma". In: *Nature Geoscience* 15, pp. 74–78. DOI: 10.1038/s41561-021-00862-6.

Humphreys, E. D. and R. W. Clayton (1990). "Tomographic image of the southern California mantle". In: *J. Geophys. Res.* 95, pp. 19725–19746.

Ishizuka, O. et al. (2018). "Age of Izu Bonin Mariana arc basement". In: *Earth Planet. Sci. Lett.* 481, pp. 80–90. DOI: 10.1016/j.epsl.2017.10.023.

Ismail-Zadeh, A. and P. J. Tackley (2010). *Computational Methods for Geodynamics*. Cambridge, U.K.: Cambridge University Press.

Jin, Z-M et al. (2001). "Eclogite rheology: implications for subducted lithosphere". In: *Geology* 29.8, pp. 667–670.

Karato, S. and P. Wu (1993). "Rheology of the Upper Mantle - a Synthesis". In: *Science* 260.5109, pp. 771–778. ISSN: 0036-8075. DOI: DOI10.1126/science.260.5109.771. URL: %3CGo%20to%20ISI%3E://WOS:A1993LA74400020.

Kohlstedt, D. L., B. Evans, and S. J. Mackwell (1995). "Strength of the lithosphere: Constraints imposed by laboratory experiments". In: *J. Geophys. Res.* 100, pp. 17, 587–17602.

Lallemand, Serge and Diane Arcay (2021). "Subduction initiation from the earliest stages to self-sustained subduction: Insights from the analysis of 70 Cenozoic sites". In: *Earth-Science Reviews* 221, p. 103779.

Lamarche, G. and J.-F. Lebrun (2000). "Transition from strike-slip faulting to oblique subduction: active tectonics at the Puysegur margin, south New Zealand." In: *Tectonophysics* 316, pp. 67–89.

Lebrun, Jean-Frédéric, Geoffroy Lamarche, and Jean-Yves Collot (2003). "Subduction initiation at a strike-slip plate boundary: The Cenozoic Pacific-Australian plate boundary, south of New Zealand". In: *Journal of Geophysical Research: Solid Earth* 108.B9.

Leng, W. and M. Gurnis (2011). "Dynamics of subduction initiation with different evolutionary pathways". In: *Geochem. Geophys. Geosys.* 12. ISSN: 1525-2027. DOI: 10.1029/2011gc003877. URL: %3CGo%20to%20ISI%3E://WOS:000298748600003.

Leng, W. and M. Gurnis (2015). "Subduction initiation at relic arcs". In: *Geophysical Research Letters* 42.17, pp. 7014–7021. ISSN: 0094-8276. DOI: 10.1002/2015gl064985. URL: %3CGo%20to%20ISI%3E://WOS:000363411200019.

Li, H.–Y. et al. (2022). "Boron isotopes in boninites document rapid changes in slab inputs during subduction initiation". In: *Nature communications* 13.1, pp. 1–10.

Li, Y. and M. Gurnis (2022). "A simple force balance model of subduction initiation". In: *Geophysical Journal International* 232.1, pp. 128–146.

Mann, Paul and Asahiko Taira (2004). "Global tectonic significance of the Solomon Islands and Ontong Java Plateau convergent zone". In: *Tectonophysics* 389.3-4, pp. 137–190.

Mansour, J. et al. (Sept. 2019). *underworldcode/underworld2: v2.8.1b*. Version v2.8.1b. DOI: 10.5281/zenodo.3384283. URL: https://doi.org/10.5281/zenodo.3384283.

Maunder, B et al. (2020). "Rapid subduction initiation and magmatism in the Western Pacific driven by internal vertical forces". In: *Nature Communications* 11.1, p. 1874.

McKenzie, D.P. (1977). "The initiation of trenches: a finite amplitude instability". In: *Island arcs, deep sea trenches and back-arc basins, Maurice Ewing Series*. Ed. by M Talwani and WC Pitman. Vol. 1. Washington, DC: American Geophysical Union, pp. 57–61.

Moresi, L., F. Dufour, and H. B. Muhlhaus (2003). "A Lagrangian integration point finite element method for large deformation modeling of viscoelastic geomaterials". In: *Journal of Computational Physics* 184.2, pp. 476–497. ISSN: 0021-9991. DOI: PiiS0021-9991(02)00031-1Doi10.1016/S0021-9991(02)00031-1. URL: %3CGo%20to%20ISI%3E://WOS:000181402800007.

Moresi, L., M. Gurnis, and S. Zhong (2000). "Plate tectonics and convection in the Earth's mantle: Toward a numerical simulation". In: *Comp. Sci. Engin.* 2.3, pp. 22–33.

Müller, R Dietmar et al. (2019). "A global plate model including lithospheric deformation along major rifts and orogens since the Triassic". In: *Tectonics* 38.6, pp. 1884–1907.

Nikolaeva, K, TV Gerya, and FO Marques (2010). "Subduction initiation at passive margins: Numerical modeling". In: *J. Geophys. Res.* 115.B03406. DOI: 10.1029/2009JB006549.

Patriat, M. et al. (2019). "Subduction initiation terranes exposed at the front of a 2 Ma volcanically–active subduction zone". In: *Earth Planet. Sci. Lett.* 508, pp. 30–40. DOI: 10.1016/j.epsl.2018.12.011.

Qing, Jiarong et al. (2021). "Dynamic evolution of induced subduction through the inversion of spreading ridges". In: *Journal of Geophysical Research: Solid Earth* 126.3, e2020JB020965.

Reagan, M. K. et al. (2019). "Forearc ages reveal extensive short–lived and rapid seafloor spreading following subduction initiation". In: *Earth Planet. Sci. Lett.* 506, pp. 520–529. DOI: 10.1016/j.epsl.2018.11.020.

Savage, H. M. and E. E. Brodsky (2011). "Collateral damage: Evolution with displacement of fracture distribution and secondary fault strands in fault damage zones". In: *Journal of Geophysical Research: Solid Earth* 116.B3. DOI: https://doi.org/10.1029/2010JB007665. eprint: https://agupubs.onlinelibrary.wiley.com/doi/pdf/10.1029/2010JB007665. URL: https://agupubs.onlinelibrary.wiley.com/doi/abs/10.1029/2010JB007665.

Shuck, B., S. P. S. Gulick, et al. (2022). "Stress transition from horizontal to vertical forces during subduction initiation". In: *Nature Geoscience* 15.2, pp. 149–155.

Shuck, B., H. Van Avendonk, et al. (2021). "Strike-Slip Enables Subduction initiation beneath a failed rift: New seismic constraints from Puysegur margin, New Zealand". In: *Tectonics* 40.5, e2020TC006436.

Stern, R. J. and S. H. Bloomer (1992). "Subduction zone infancy - examples from the Eocene Izu–Bonin–Mariana and Jurassic California Arcs". In: *Geol. Soc. Am. Bull.* 104.12, pp. 1621–1636. ISSN: 0016-7606. DOI: Doi10.1130/0016-7606(1992)104<1621:Szieft>2.3.Co;2. URL: %3CGo%20to%20ISI%3E://WOS:A1992KC40300006.

Sutherland, R., P. Barnes, and C. Uruski (2006). "Miocene-Recent deformation, surface elevation, and volcanic intrusion of the overriding plate during subduction initiation, offshore southern Fiordland, Puysegur margin, southwest New Zealand". In: *N.Z. J. Geol. Geophys.* 49, pp. 131–149.

Sutherland, R., G. R. Dickens, et al. (2020). "Continental-scale geographic change across Zealandia during Paleogene subduction initiation". In: *Geology* 48. DOI: 10.1130/G47008.1.

Thielmann, M. and B. J. P. Kaus (2012). "Shear heating induced lithospheric-scale localization: Does it result in subduction?" In: *Earth Planet. Sci. Lett.* 359, pp. 1–13. DOI: 10.1016/j.epsl.2012.10.002.

Torsvik, T. H. et al. (2017). "Pacific plate motion change caused the Hawaiian-Emperor bend". In: *Nature Communications* 8.15660. URL: https://www.nature.com/articles/ncomms15660.

Toth, J. and M. Gurnis (1998). “Dynamics of subduction initiation at preexisting fault zones”. In: *Journal of Geophysical Research-Solid Earth* 103.B8, pp. 18053–18067. ISSN: 2169-9313. DOI: Doi10.1029/98jb01076. URL: %3CGo%20to%20ISI%3E://WOS:000075299700020.

Whittaker, J. M. et al. (2007). “Major Australian–Antarctic plate reorganization at Hawaiian–Emperor bend time”. In: *Science* 318.5847, pp. 83–86. ISSN: 0036-8075. DOI: 10.1126/science.1143769. URL: %3CGo%20to%20ISI%3E://WOS:000249915400044.

Yang, Gaoxue (2022). “Subduction initiation triggered by collision: A review based on examples and models”. In: *Earth-Science Reviews*, p. 104129.

Zhong, X. and Z.–H. Li (2019). “Forced Subduction Initiation at Passive Continental Margins: Velocity-Driven Versus Stress-Driven”. In: *Geophys. Res. Lett.* 46.20, pp. 11054–11064.

Zhong, Xinyi and Zhong-Hai Li (2023). “Compression at Strike-Slip Fault Is a Favorable Condition for Subduction Initiation”. In: *Geophysical Research Letters* 50.4, e2022GL102171.

Zhou, X. et al. (2018). “Subduction initiation dynamics along a transform fault control trench curvature and ophiolite ages”. In: *Geology* 46.7, pp. 607–610. DOI: 10.1130/G40154.1.

Zoback, M. D. et al. (1987). “New Evidence on the State of Stress of the San Andreas Fault System”. In: *Science* 238.4830, pp. 1105–1111. DOI: 10.1126/science.238.4830.1105. eprint: https://www.science.org/doi/pdf/10.1126/science.238.4830.1105. URL: https://www.science.org/doi/abs/10.1126/science.238.4830.1105.

Chapter 4

BOUNDS ON FAULT WEAKENING AND DYNAMIC PROCESSES DURING SUBDUCTION INITIATION

Note: This chapter is based on work submitted as a paper titled "Rapid shear zone weakening during subduction initiation" to PNAS on March 9, 2024 and is currently under peer review.

Slab pull at subduction zones is arguably the dominant driving force for plate motion and mantle convection. For mature subduction zones, slab pull is sufficiently large for the convective system to be self-sustaining, but when a new subduction zone forms, slab pull is typically insufficient to overcome the resistance to plate motion that occurs within nascent plate boundaries. How subduction initiation can be triggered with an initially insufficient driving force remains a fundamental, open question in geodynamics and plate tectonics. Arguably, the key reason for this uncertainty is that the strain required to weaken plate boundaries has not been constrained for initiation.

Based on mechanical models and the geology and geophysics where subduction has initiated, a variety of initiation mechanisms have been proposed, including compression-induced (Toth and Gurnis, 1998), plume-induced (Gerya, R. J. Stern, et al., 2015), spontaneous initiation (R. Stern, 2004), and collapse of passive margins (Zhang, Leng, and Chen, 2023). Despite the variability and complex tectonics that often surrounds subduction initiation, the mechanisms share much in common through the balance of forces (Li and Gurnis, 2022), such that a reduction of resisting or an increase of driving forces provide more favorable conditions for subduction initiation. Therefore, either external forces, which supply additional driving force, or small yield stresses, which reduces the resistance, have been invoked in previous subduction initiation scenarios. Strain weakening is nearly universally advanced in models as a means to lower the strength of rocks within evolving plate boundaries (Gurnis, Hall, and Lavier, 2004; Gerya, D. Bercovici, and Becker, 2021; Zhang and Leng, 2021)Despite proposals like grain size reduction (David Bercovici and Ricard, 2014) and shear heating (Thielmann and B. J. Kaus, 2012), the rate at which a margin loses its strength with strain has been a crucial quantity that has been unconstrained for known examples of subduction initiation. Here, we overcome

this fundamental limitation with observations of the well-constrained Puysegur subduction zone within the context of four-dimensional dynamic models, place bounds on this critical weakening for the first time, and then compare this rate to values predicted by the principal physical models of weakening.

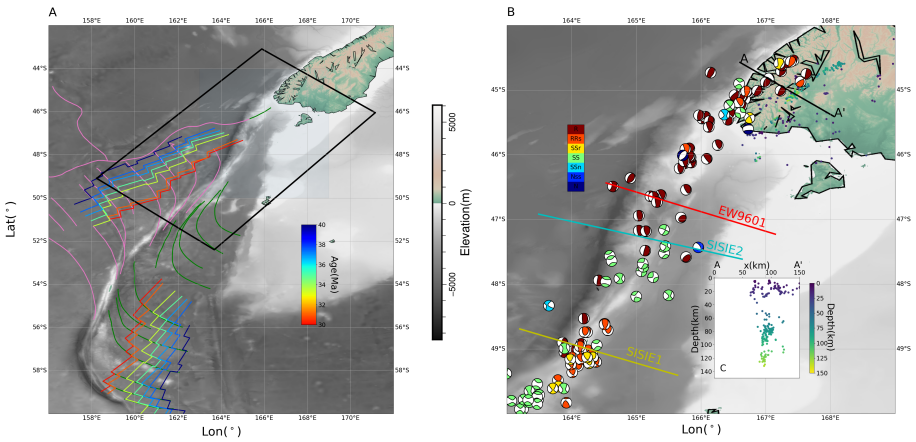

Figure 4.1: Observation summary of Puysegur trench. A. Fracture zones and seafloor magnetic lineations (color-coded with age). Black box shows the geodynamic model domain. B. Focal mechanisms from GCMT catalogue (Ekstrom, Nettles, and Dziewoński, 2012) with classified fault types (Alvarez-Gomez, 2019) for shallow earthquake(< 30 km deep), and seismicity under Fiordland(colored dots near AA' line). C, the cross-section AA' of seismicity (Seebeck et al., 2023) under Fiordland.

The Puysegur Trench (Fig 4.1), located south of New Zealand, is an extant example of subduction initiation, as the subduction zone is experiencing ongoing subduction initiation since 15 Ma. Well defined by magnetic lineations and fracture zones (Fig 4.1A), the kinematics is extraordinarily well known(**keller_william_r_cenozoic_2005**; Cande and Stock, 2004; Choi et al., 2017) with the plate boundary between the Australian and Pacific Plates experiences a transition from oceanic spreading (40 to 25 Ma), to strike-slip motion (25 to 15 Ma), and eventually transpression and subduction (15 Ma to the present). Recently, targeted multi-channel seismic imaging in which specific seismic horizons were dated using constraints from offshore drilling, placed bounds on a progressive transition of the in-plane stress at the nucleating boundary(Shuck et al., 2022). Specifically, the northern Puysegur Trench started with compression between 15 Ma and 8 Ma, but switched to extension after 8 Ma, while for southern Puysegur compression started at 8 Ma, but has yet to experience a reversal in stress. This observation is consistent with the earlier inference of uplift followed by subsidence of the Pyusegur Ridge by $\approx$ 1.5 km in the northern section

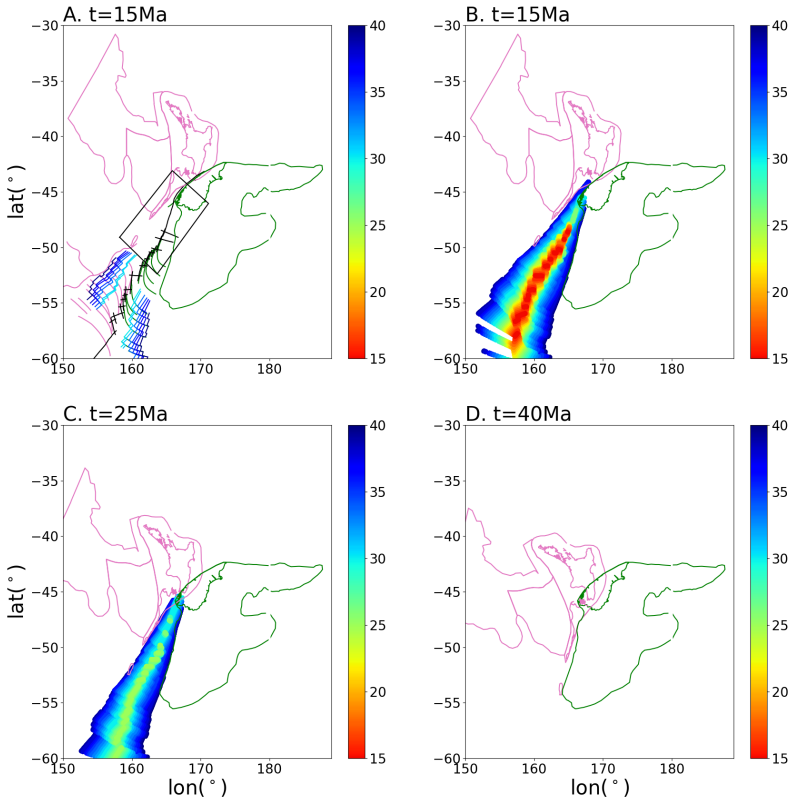

Figure 4.2: Plate reconstruction of Australia-Pacific boundary south of New Zealand. A. Reconstructed features at 15Ma. Magnetic lineations are color-coded with age. Black segments are located spreading centers and transform faults according to the magnetic lineations and curve fracture zones. B,C,D, the reconstruction with age grid at 15Ma, 25Ma and 40Ma. Age grid are color-coded with seafloor age newly generated from the spreading centers since 40Ma using *Track Tec*(Karlsen et al., 2020).

and only uplift in the southern (Collot et al., 1995) as well as the strong free-air gravity anomalies along the ridge (Hightower, Gurnis, and Van Avendonk, 2020). The vertical motions and compression-extension transition is a characteristic feature of induced subduction initiation, indicating a slab pull that increases and eventually dominates as the driving force, making the system self-sustaining. The 8 Myr phase lag between the northern and southern sections of Puysegur Trench may indicate the nucleation of Puysegur subduction starting in the north while propagating southward (Shuck et al., 2022). Today, the northern part of Puysegur is becoming a more

mature subduction zone, with the seismicity (Sutherland, Barnes, and Uruski, 2006) of the slab reaching more than 130 km depth below Fiordland, the immediate onshore region of South Island, New Zealand (Fig. 4.1C), while the southern Puysegur has strain partitioning as a consequence of transpression (Lebrun, Lamarche, and Collot, 2003) . Although Puysegur subduction initiated at the boundary of stretched continental crust and young oceanic lithosphere, a sliver of oceanic crust became trapped between the vertical strike-slip Puysegur fault and the dipping Puysegur megathrust (Lebrun, Lamarche, and Collot, 2003; Gurnis, Van Avendonk, et al., 2019).

Together, these observations provide a globally unique data set spanning the four-dimensional nature of subduction initiation from the nascent state with known antecedent tectonics, well–constrained plate kinematics during the entire period of initiation, state-of-stress in time and space along the plate boundary, and present-day structural controls from topography, gravity and seismology. Together, Puysegur is a globally unique natural experiment to constrain a key unknown in the mechanics of initiation, the weakening which we define as the strain, ε_{P0}, required for a plate boundary to loose most of its strength.

The dynamics of Puysegur subduction initiation is studied in a model in which the mechanics is merged with the tight plate kinematic and structural controls while matching outcomes of evolution to observed structure, stress and topography. The time-dependent 3D formulation (Fig 4.1A) starts at 15 Ma and is integrated to the present. The rheology is non-linear and uses realistic dislocation creep and plastic failure. The initial and boundary conditions are based on a Pacific-Australia reconstruction since 40 Ma using magnetic lineations and fracture zones (Fig 4.2). The top of the domain is a free surface and the evolution of topography is tracked. We perform a parametric search on key rheological parameters, including the weakening strain, ε_{P0}, and maximum yield stress of the upper plate, τ_u, and evaluate the correctness of the models with respect to geophysical observations to find the best set of parameters.

Typically, with best-fitting models (Fig 4.3), the behavior is consistent with previous generic, 2-D models (Li and Gurnis, 2023), except now the outcomes are explicitly in time and space that can be compared with observations. Just after the model starts with Australian Plate moving northward the plate boundary is approximately a vertical strike-slip fault with some diffuse deformation in the lower lithosphere (Fig. 4.3). With time, by 4 Myr of motion deformation continues to localize with a

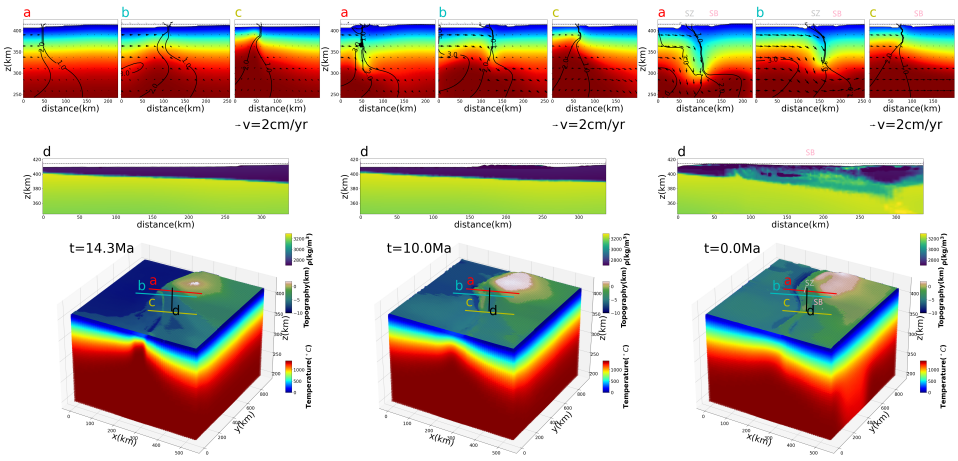

Figure 4.3: Time evolution of the case $\varepsilon_{P0} = 0.5, \tau_u = 500MPa$. Three columns represent the beginning (14.3Ma), middle(10Ma), and final stage(0Ma) of the model evolution. The top two rows are the cross sections at line a, b, c, and d. In line a, b, and c, vectors are in-plane velocity, contours are normal-to-plane(strike-slip) velocity, and temperature is color-coded. In line d, density is color-coded.

pronounced uplift on the Pacific Plate edge and some initial descent of the Australian Plate below the ridge in the northern section. Strain becomes distributed with some dipping thrust adjacent to the Ridge. As time progresses, the slab extends downward below the ridge with the formerly uplifted ridge now subsiding, consistent with the vertical motion observed along the Puysegur Ridge (Collot et al., 1995). Starting at around 10 Myr, the stress transitions on the northern edge from growing more compressive to becoming less compressive, while the state of compression in the south shows more constant values.

In the present-day, the modelled topography (Fig. 4.3), reproduces broad-scale features such as the Puysegur Trench (PT), Puysegur Ridge (PR), Puysegur Bank (PB), and Solander Basin (SB). Importantly, a small-scale topographic low underlain by thicker crust is captured in some models (Fig 4.3) and correlates with the Snares Zone (SZ), which has these same characteristics (Hightower, Gurnis, and Van Avendonk, 2020). The strain partitioning fault system comprising the Puysegur trench and the strike-slip Puysegur ridge is a dynamic outcome of an induced subduction initiation at a transpressional plate boundary (Li and Gurnis, 2023), where a piece of oceanic crust becomes trapped between the trench and the Puysegur fault. The computations demonstrate the transfer of strike-slip motion from the initial vertical fault onto the oblique subduction zone (Fig. 4.3).

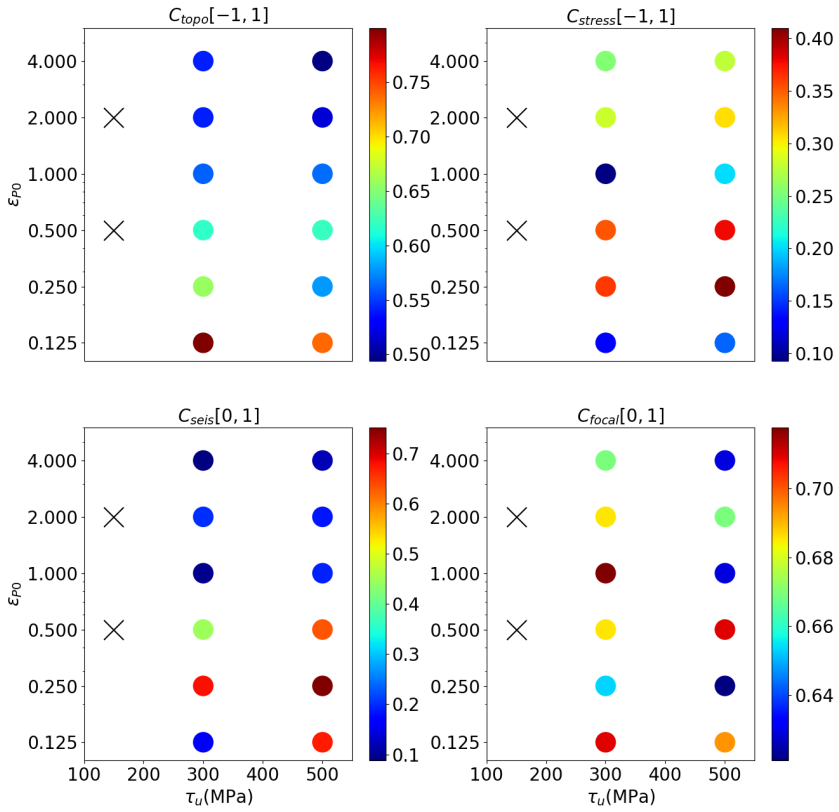

Figure 4.4: Model fitting to observations. A, the correlation coefficient of topography between models and observation. The values range from -1 to 1, with -1 being anti-correlated and 1 being perfectly correlated. B, the correlation coefficient of stress evolution between models and data. C, the correctness of location of seismicity, evaluated as the proportion of intermediate depth seismicity falling within the seismogenic zone predicted by models. The value ranges from 0 to 1, with 1 being a perfectly predicted seismogenic zone. D, correctness of focal mechanism prediction, evaluated as the proportion of correct fault types predicted by the model with respect to the GCMT catalog.

We quantify how models fit with observations by either correlation (topography and stress), correctness (focal mechanisms, seismicity), or a combination of both. Although different observations give rise to different best-fitting outcomes (Fig 4.4), the data fits are best for fast rates of weakening ($\varepsilon_{P0} \leq 1$). Combining all the model correctnesses, we get the best-fitting case with $[\varepsilon_{P0}, \tau_u] = [0.25, 500MPa]$ (Fig 4.5), while case $[\varepsilon_{P0}, \tau_u]$ = [0.25,300 MPa] or [0.5,500 MPa] fit the data almost equally well. The successful initiation of subduction requires that the upper plate's

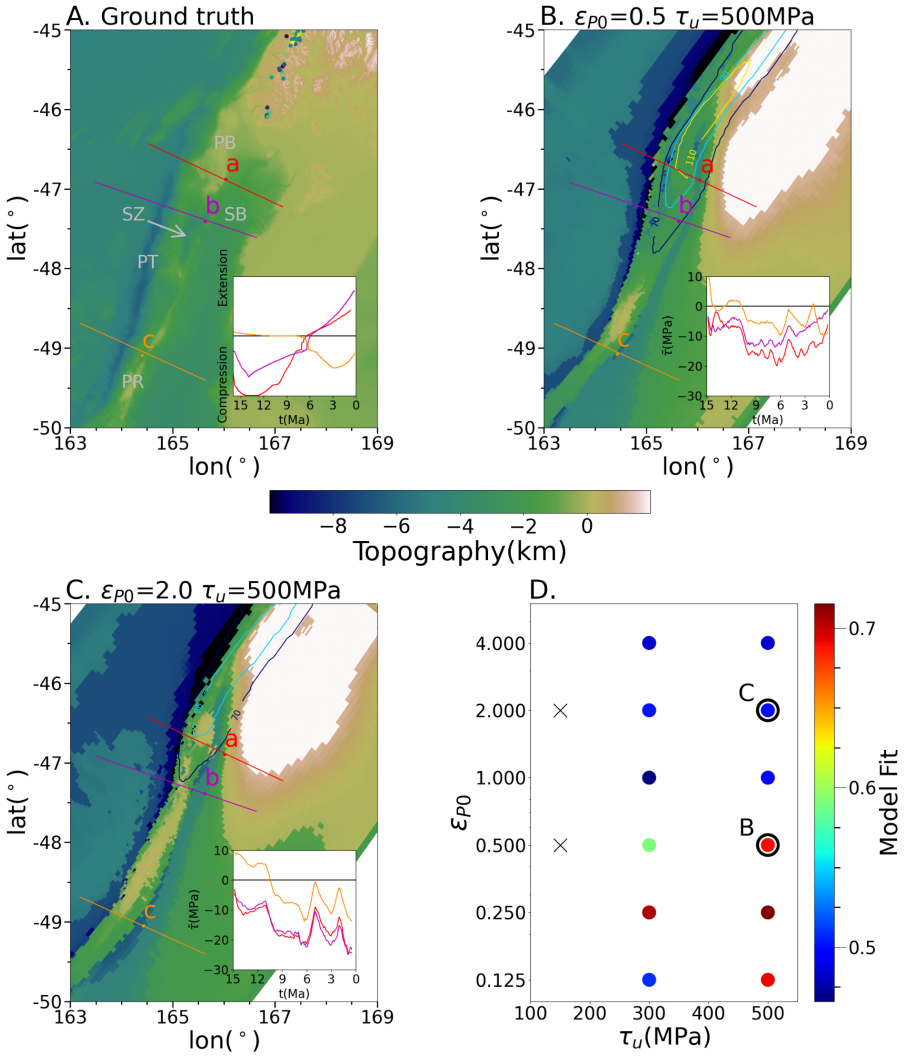

Figure 4.5: Comparisons between observation and models at present day. A. observed bathymetry topography (background color), seismicity (dots color-coded with depth), and stress evolution (sub-panel) modified from (Shuck et al., 2022). B. modeled present-day bathymetry topography, depth of seismogenic zone (contours color-coded with depth using the same colormap as the seismicity in A), and measured stress evolution at a,b,c (sub-panel) from case $\varepsilon_{P0} = 0.5, \tau_u = 500MPa$. C. same as B but from case $\varepsilon_{P0} = 2, \tau_u = 500MPa$. D. the total model correctness with varied ε_{P0} and τ_u. "X" stands for no subduction initiation. The correctness ranges from 0 to 1, with 1 being a perfect fit to observed data. PT, Puysegur trench; PR, Puysegur ridge; PB, Puysegur bank; SZ, Snares zone; SB, Solander basin.

yield stress (τ_u) exceeds that of the subducting plate, 150 MPa. In instances where both the upper plate and the subducting plate share identical yield stress (Fig 4.5D,

marked X), subduction initiation fails as the plate boundary is incapable of initiating the formation of a slab. Instead, a vertical plate boundary persists, resulting in the subducting plate being pushed horizontally beneath the upper crust (Fig 4.6). This outcome is inconsistent with observed seismicity beneath Fiordland where we see a vertically dipping slab (Fig. 4.1C).

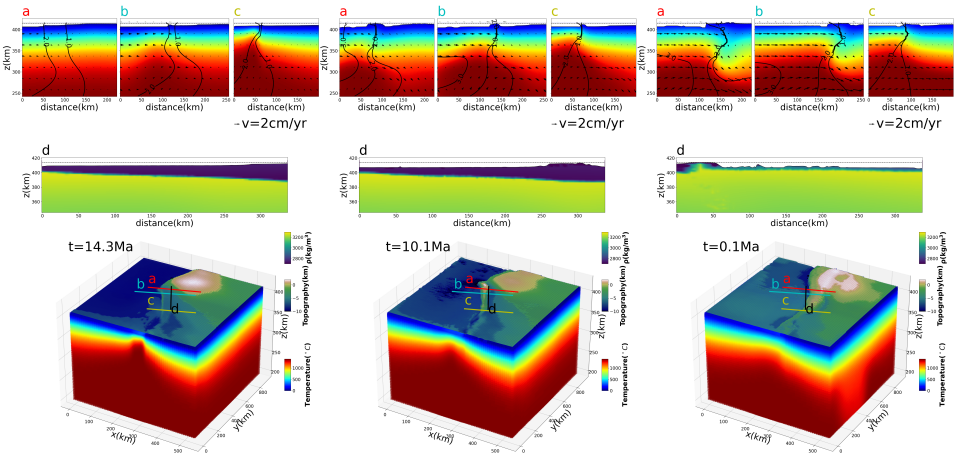

Figure 4.6: Time evolution of the case $\varepsilon_{P0} = 2, \tau_u = 150MPa$ where subduction fails to initiate.

Despite the variance among best-fitting models, there is a clear tendency from all observations to prefer a small ε_{P0}, typically $\varepsilon_{P0} < 1$. In terms of topography, a strong correlation between ε_{P0} and the width of an oceanic sliver is found, marked by the topography high between the Solander basin and Puysegur Trench. For instance, the width of the oceanic sliver at the latitude of line a is around 60 km (Fig. 4.5A), consistent with the case of $\varepsilon_{P0} = 0.5$ (Fig. 4.5B) but exceeds that observed width when $\varepsilon_{P0} = 2$ (Fig. 4.5C). The intermediate-depth seismicity indicates how deep the cold slab (defined in models as mantle $< 850°$ C) penetrates into the mantle. A large ε_{P0}, slower weakening, tends to produce a shallow slab, and only when ε_{P0} is as small as 0.25 do the computations give a slab deeper than 130 km. Predicted focal mechanisms (Fig. 4.7) and stress evolution are both influenced by ε_{P0} through plate-coupling. Although models may produce complete compression-extension reversals, cases with smaller ε_{P0} tend to predict a relaxation of horizontal compression since 6 Ma (Fig. 4.5B), while those with large ε_{P0} show strong compression persisting to the present day along the northern lines (a and b). The fault type from the seismic focal mechanism (Ekstrom, Nettles, and Dziewoński, 2012) shows an overall compression-transpression stress state existing in the whole domain, while the fault type near the Snares Zone is dominantly strike-

slip. Underneath Fiordland and Puysegur Bank, there is normal faulting, potentially indicative of a change from induced compression to pulling by the slab. Cases with larger ε_{P0} typically over-predict the extent of compression with thrust faulting throughout (Fig. 4.7C), while smaller ε_{P0}, i.e. faster weakening, produces the transpressional to strike-slip faulting as well as an extensional stress state(normal faulting) beneath Fiordland (Fig. 4.7B,D). Fits to the observed focal mechanisms and stress evolution together indicate a fast weakening, i.e. smaller ε_{P0}, is preferred.

The rheology of continental crust also influences model fit to observations. Two end-members for this rheology, one with a weak lower crust composed of wet quartzite(Brace and Kohlstedt, 1980) and a second with a strong lower crust composed of dry feldspar(Jackson, 2002), are considered. All the cases just described have a weaker quartzitic lower crust, and we test cases with a strong lower crust. The strong lower crust models yield equally good fits to the topography, seismicity, earthquake focal mechanisms and stress evolution) as the weak crust counterparts did (Fig 4.8,4.9). However, a notable discrepancy emerges: in the weaker crust models, the predicted slab position is beneath Fiordland, whereas in the stronger crust models, the slab shifts west of Fiordland. This discrepancy originates from the differing deformation behavior. A weaker lower crust in the upper plate leads to deformation primarily on the upper plate, while a stronger lower crust in the upper plate favors deformation on the subducting plate. Given that seismicity is observed beneath Fiordland, a weaker lower crust rheology is preferred.

A variety of mechanisms have been advanced to explain the progressive weakening of faults and shear zones, chief among them thermal weakening, grain size reduction, and fluid pressurization. Unfortunately, there has not been a sufficiently complete set of observations – spanning space and time – to distinguish among them in models of subduction initiation. Now, with an observationally-based bound on weakening, we determine if the parameterized weakening, ε_{P0}, is consistent with the proposed physical processes. We test three possible physical mechanisms for strain weakening, shear heating, grain-size reduction, and pore fluid pressure, with zero-dimensional systems as a function of time (see Methods section for details) in order to follow the reduction of strength with the underlying parameters. Given the many parameters which would need to be explored, adding the detailed physical processes to the 4D mechanical/data model would make the problem computationally intractable.

Weakening from shear heating arises when viscous dissipation heats the rock and reduces its creep strength. We consider a system with initial temperature, T_0, that

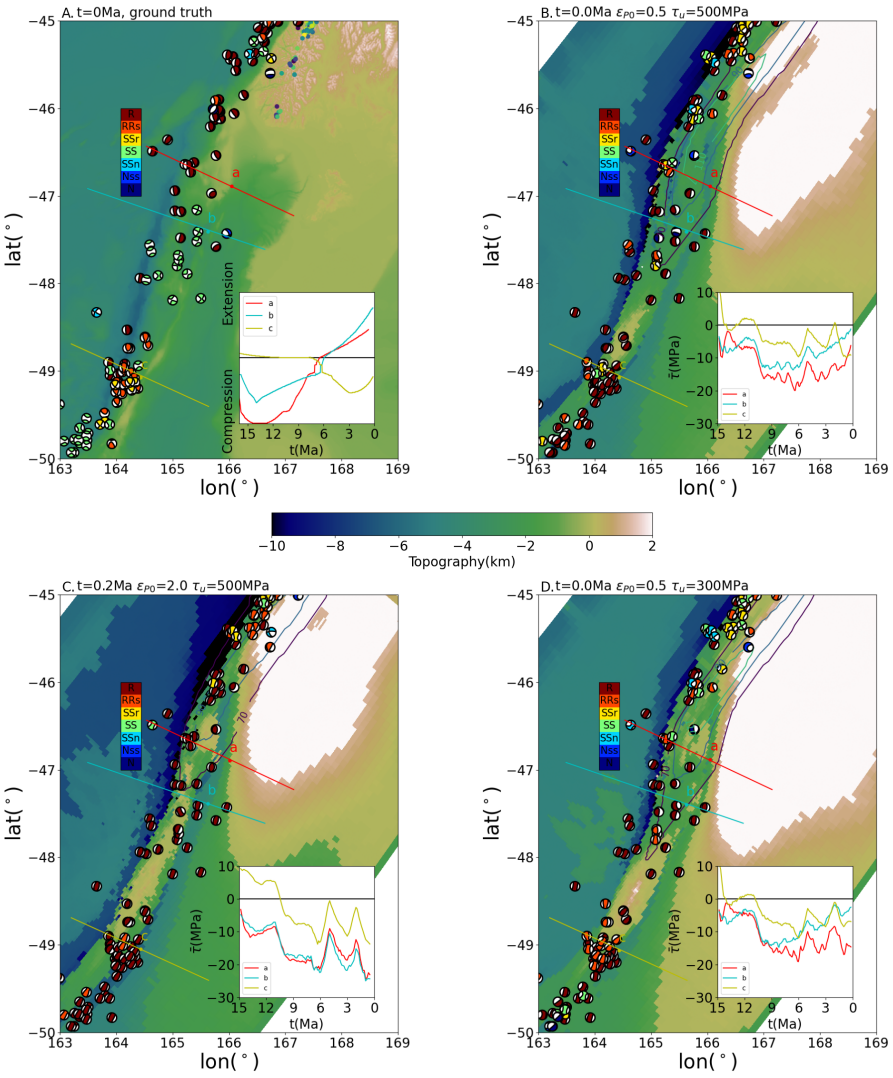

Figure 4.7: Comparison of focal mechanisms. A. focal mechanisms from GCMT((Ekstrom, Nettles, and Dziewoński, 2012)) catalog. B. focal mechanisms at the same hypocenters as A from case $\varepsilon_{P0} = 0.5, \tau_u = 500MPa$. C. same as B but from the case $\varepsilon_{P0} = 2, \tau_u = 500MPa$. D. same as B but from the case $\varepsilon_{P0} = 0.5, \tau_u = 300MPa$.

heats due to shearing. The dominant rheology experiences a transition from plastic-yielding with constant stress, to dislocation and diffusion creep with a constant strain rate, $\dot{\varepsilon}$. Predicted ε_{P0} range from 40 to 70 under the physical range of $T_0 - \dot{\varepsilon}$ from the numerical models (Fig. 4.10A) at least two orders of magnitude larger than the data-constrained value, $0.25 < \varepsilon_{P0} < 0.5$). As our calculation assumes a perfect efficiency and without heat loss, the weakening rate would only be slower (larger

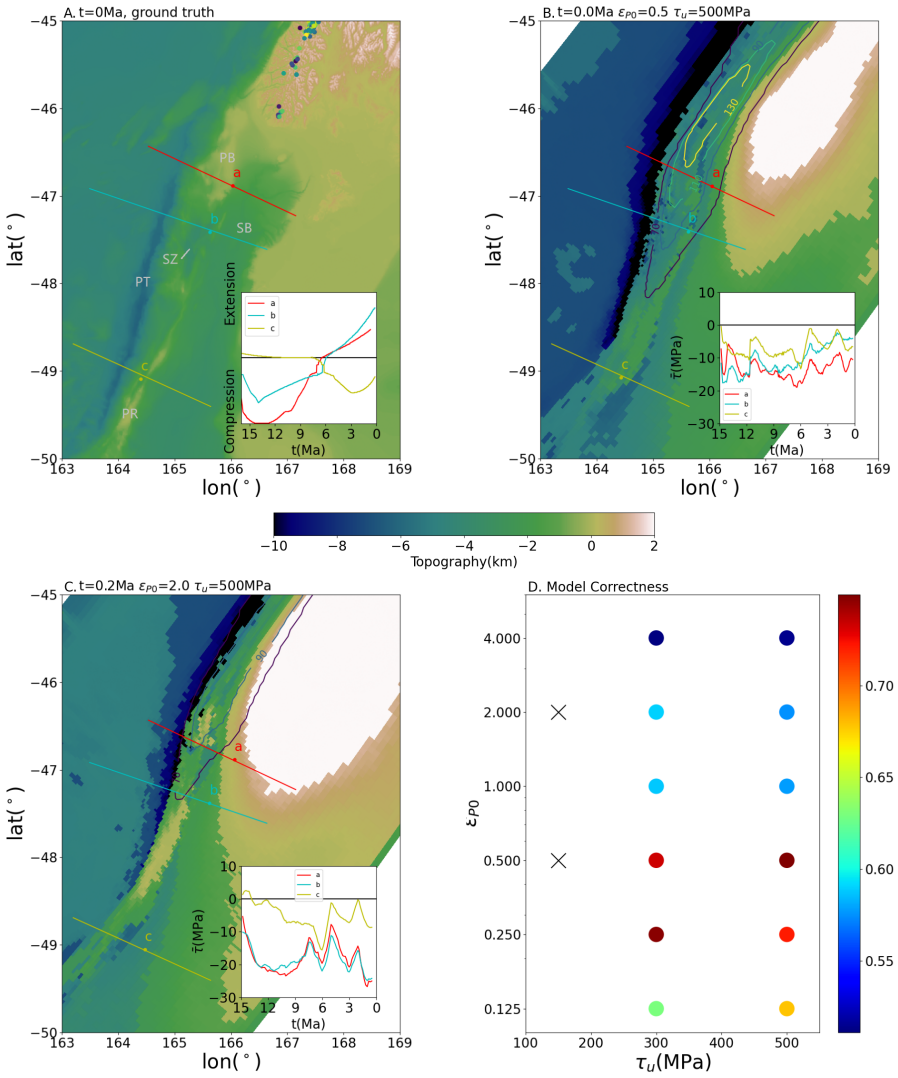

Figure 4.8: Equivalent to Figure 4.5 but from the cases with dry feldspar (strong) crust model.

ε_{P0}). Consequently, shear heating alone is insufficient to explain the weakening needed to fit the Puysegur observations.

Grain-size reduction is often invoked as a mechanism to weaken plate boundaries. When grain size decreases, diffusion creep increases and relaxes the stresses within the rock. Considering a two-phase peridotite system experiencing a grain-size evolution with Zener pinning (David Bercovici and Ricard, 2014), the governing rheology transitions from plastic failure (with constant stress) initially with large grain-size, to diffusion creep (with constant strain rate) when grain size is reduced.

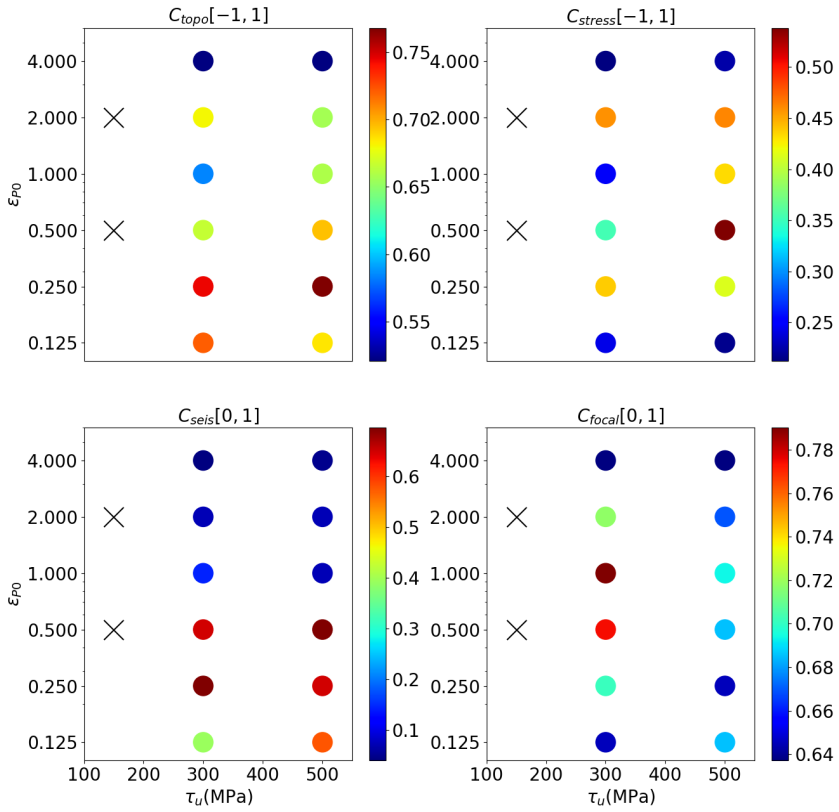

Figure 4.9: Equivalent to Figure 4.4 but from the cases with dry feldspar(strong) crust model.

The predicted ε_{P0} varies from 10^{-1} to 10^{2} under different temperature and strain rate ($T - \dot{\varepsilon}$) conditions (Fig. 4.10B). As the grain size evolution is governed by two competing mechanisms, grain growth and grain-size reduction, for a certain low-temperature region of the $T - \dot{\varepsilon}$ domain (Fig. 4.10B "insufficient reduction" region), the equilibrium grain size (Fig 4.11 blue curves) exceeds the desired grain size for the targeted stress or strain levels (Fig. 4.11 black solid curves), meaning that the desired grain size is unattainable in this temperature range. In the high-temperature domain (Fig. 4.10B "inherent weakness" zone), the weakness of the rock is already low with the initial grain size, rendering any further weakening unnecessary. The Puysegur-inferred weakening rate, $\varepsilon_{P0} < 1$, encompasses part of the grain-size reduction ε_{P0} diagram and this part corresponds to the condition of the mid-lower lithosphere ($T > 600°$C) in the Puysegur model. However, the grain-size reduction is inadequate in explaining the strain weakening for the shallow

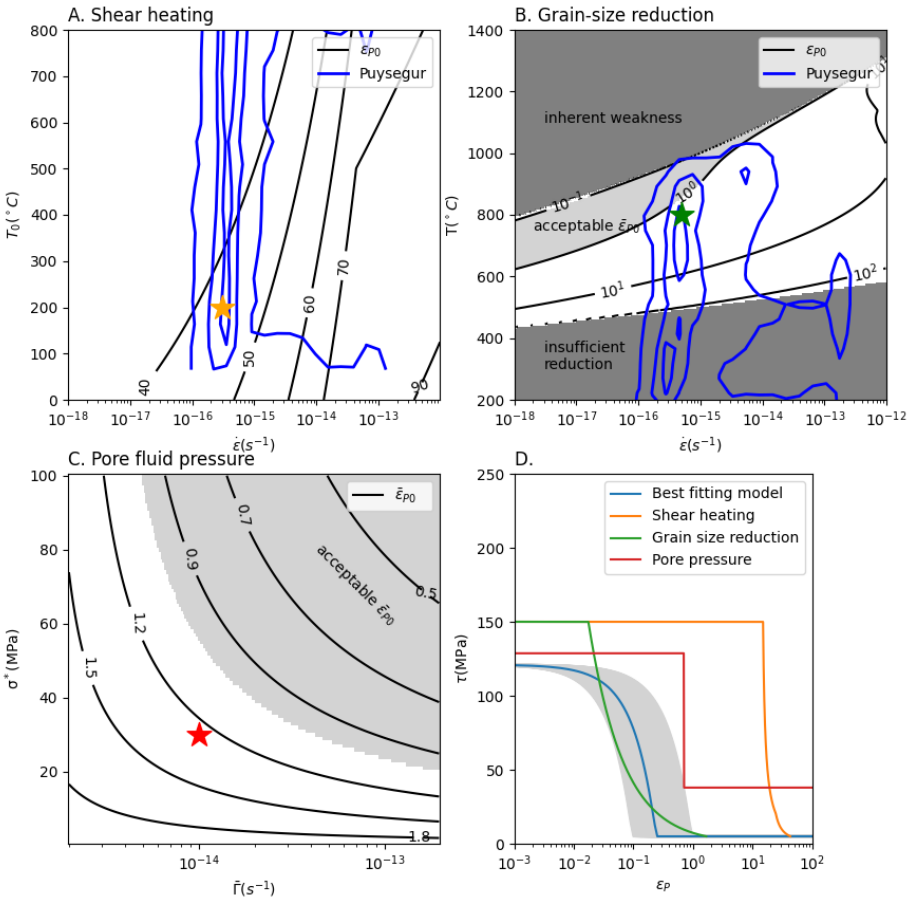

Figure 4.10: Physical models for strain-weakening. A. Shear heating with ε_{P0} (contoured in black). Blue contours represent the density distribution of T & $\dot{\varepsilon}$ in the lithosphere from the Puysegur model (beginning at 15 Ma for case $\varepsilon_{P0} = 0.5, \tau_u = 300$ MPa). T_0 is the initial temperature. B. ε_{P0} by grain-size reduction (black contours). Colored contours are the same as A except from the end (0 Ma) of case $\varepsilon_{P0} = 0.5, \tau_u = 300$ MPa. Dark gray shaded regions in B represent the grain-size reduction is either unneeded or insufficient. C. The averaged weakening rate $\bar{\varepsilon}$ from pore pressure weakening; σ^* is the pressure-permeability exponential scaling factor and $\bar{\Gamma}$ the average fluid production rate in the top 10 km. D. Typical strain weakening paths for different weakening mechanisms compared with the best fitting Puysegur models. Three physical mechanisms' parameters are taken from 3 stars with corresponding colors in A, B, and C. The paths of pore pressure and best fitting numerical model sample a point at the depth of 5 km. The light gray shaded regions are for $0.1 \leq \varepsilon_{P0} \leq 1$.

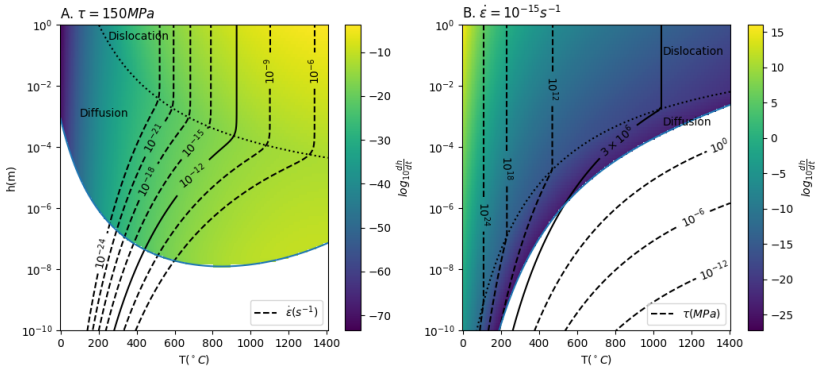

Figure 4.11: Roughness evolution r from grain-size evolution model. Background color for log scale roughness reduction rate $log_{10}(-\frac{dr}{dt})$ for A, constant stress $\tau = 150MPa$ and B, constant strain rate $\dot{\varepsilon} = 10^{-15}s^{-1}$. Dashed contours for A, strain rate in s^{-1} and B, stress in MPa. Solid curves for the contours of the desired final stress or strain rate after weakening.

lithosphere as weakening is insufficient for the low-temperature domain.

Water is the third factor that can lead to rapid weakening. The subduction interface generally exhibits a lower yield stress compared to the crust away from the plate boundary, because fluid released from the sediment and crust along the slab interface increases the pore pressure and reduces the effective stress (Saffer and Tobin, 2011; Fagereng et al., 2018). For subduction initiation, no sediment and crust pre-exist within the mantle, but the weakness introduced by the addition of fluid pore pressure can equivalently be regarded as a weakening process. Pore pressure is governed by Darcy's flow assuming permeability scales exponentially with effective pressure, where the scaling is determined by the parameter σ^*, with larger values of σ^* indicating reduced sensitivity of permeability to effective pressure (Zhu et al., 2020). Additionally, the fluid production rate Γ significantly influences pore pressure. As such, we evaluate the average weakening rate $\bar{\varepsilon}_{P0}$ across the entire subduction interface, resulting from excess pore fluid pressure due to crust and sediment dehydration, with varying σ^* and averaged production rate $\bar{\Gamma}$.(Fig. 4.10C). The predicted $\bar{\varepsilon}_{P0}$ range from 0.5 to 2, and only with large σ^* and high fluid production rate the weakening rate falls within the constraint range ($\varepsilon_{P0} < 1$). As the subducting Australian plate is very young, the slab interface $P-T$ path crosses with dehydration from Lawsonite breakdown at a shallow depth (< 10 km, Fig 4.12), leading to large average dehydration rates (up to $10^{-14}s^{-1}$), and in turn a ε_{P0} of around 1, close but slower than from the Puysegur model. To reduce ε_{P0} even further, either unrealistic

permeability ($k_0 = 10^{-20}$) or larger fluid production rate ($\bar{\Gamma} \approx 10^{-13} s^{-1}$) are needed.

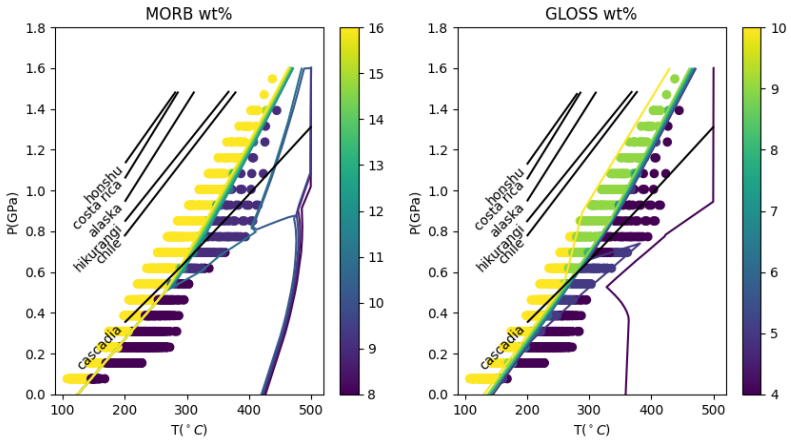

Figure 4.12: Fluid content phase diagram modified from (Fagereng et al., 2018) Figure 7. The colors of the contours and dots represent fluid content in percentage. Contours for the average fluid content in MORB (Mid-ocean ridge basalt) and GLOSS(global subducting sediment). Dots are the sampled dots at the slab interface from the last step of the case $\varepsilon_{P0} = 0.5, \tau_u = 300MPa$.

The four-dimension geodynamic model has shown great capability in fitting the different observations and provides a means to understand how plate boundaries like subduction zones nucleate and the stress, temperature, and strain rates which exist at depth, while placing constraints on key parameters like ε_{P0}. From these models, we find that a fast strain weakening is needed for Puysegur subduction initiation, with $\varepsilon_{P0} < 1$. Three possible mechanisms for strain weakening: shear heating, grain size reduction, and fluid pore pressure have been explored in light of this new constrain on weakening. We found shear heating to be too slow, grain size reduction might be fast enough but only works for high temperatures (lower lithosphere), and fluid pore pressure can produce a ε_{P0} close to the estimated weakening rate, but a perfect match requires a faster fluid production rate. Puysegur trench initiated at a vertical strike-slip boundary, and the subsequent development of weak zones varies with depth. At depths less than 10 km, pore pressure weakening likely played a significant role in the formation of the strain partitioning system. Deeper within the subsurface, grain-size reduction may have been associated with the rotation of the presumed initially vertical strike-slip fault. However, it is crucial to note that the existence of a pre-existing fault that could be reused is also indispensable for the formation of the new Puysegur subduction zone. In summary, the interplay of these factors, including fast weakening mechanisms like pore pressure weakening and

grain-size reduction, and the availability of pre-existing fault structures, contributed to the complex process leading to the initiation and evolution of subduction zones like Puysegur.

Symbol	Definition	Value	Symbol	Definition	Value
n	non-Newtonian exponent Olivine Mantle	3.5	E	Activation energy Olivine Mantle	540 kJ/mol
A	pre-exponent Olivine Mantle	2.9×10^4Pa · s	n	Activation energy Quartzitic Crust	4
E	Activation energy Quartzitic Crust	223 kJ/mol	A	pre-exponent Quartzitic Crust	3.3×10^4Pa · s
n	non-Newtonian exponent Eclogite	3.4	E	Activation energy Eclogite	480 kJ/mol
A	pre-exponent Eclogite	9.8×10^6Pa · s	τ_{yf}	minimum yield stress	3 MPa
n	non-Newtonian exponent Anorthite	4	E	Activation energy Anorthite	648 kJ/mol
A	pre-exponent Anorthite	21.15Pa · s	m	grain-size exponent Diffusion Creep	3
E_l	Activation energy Dislocation Creep	540 kJ/mol	E_f	Activation energy Diffusion Creep	375 kJ/mol
E_f	Activation energy Grain Growth	300 kJ/mol	n	non-Newtonian exponent Dislocation Creep	3
A_{disl}	pre-exponent Dislocation Creep	1.1×10^{-13}Pa^{-n}s^{-1}	A_{diff}	pre-exponent Diffusion Creep	1.5×10^{-15}m^{m}s^{-1}
τ_{y0}	maximum yield stress subducting plate	150 MPa	τ_{y0}	maximum yield stress upper plate	[150,300,500] MPa
η_{min}	minimum viscosity	10^{19} Pa · s	η_{max}	maximum viscosity	10^{24} Pa · s
$\dot{\varepsilon}_0$	reference strain rate	10^{-15} s^{-1}	α	thermal expansivity	3×10^{-5} C^{-1}
κ	thermal diffusivity	10^{-6} m^2 · s^{-1}	C_P	heat capacity	1200 J/kg/K
T_0	Surface temperature	0°C	T_1	mantle temperature	1400°C
C_0	initial cohesion	44 MPa	μ_{y0}	initial friction coefficient	0.6
η_{st}	sticky air viscosity	10^{19}Pa · s	κ_{st}	thermal diffusivity sticky air	10^{-5} m^2 · s^{-1}
d_{st}	sticky air thickness	40km	μ_0	initial friction coefficient	0.56
C_0	initial cohesion	36MPa	C_f	final cohesion	3MPa
ν	fluid viscosity	10^{-4}Pa · s	k_0	permeability zero-pressure	10^{-19}m^2
ρ	fluid density	1000kg/m^3	ρ_r	rock density	3000kg/m^3

Table 4.1: Model Parameters mainly inherit from Li and Gurnis, 2022Li and Gurnis, 2023 with an addition of weak overriding plate cases. Non-Newtonian parameters of Olivine mantle, Quartzitic crust, and Eclogite are from Karato and Wu, 1993Gleason and Tullis, 1995Jin et al., 2001Rybacki et al., 2006. Symbol A's with different composition represent pre-exponents of viscosity, i.e. $\eta = Ae^{\frac{E}{nRT}}(\dot{\varepsilon}_{II})^{\frac{1-n}{n}}$. A_{diff} and A_{disl} are the pre-exponents of strain rate(eq 4.10,4.11).

4.1 Methods

4D computational models

We perform computations in a 3D Cartesian domain as a function of time using the finite element method with the validated software *Underworld2* (Beucher et al., 2022). The approach solves the continuity and momentum equations (the Stokes system) and energy equation. The computations start at 15 Ma in a Cartesian

domain, with 540 km × 900 km horizontally (as black outline in Fig 4.1A) and 450 km vertically, including 40 km sticky-air layer which mimics a free surface. The bottom of the domain is at mantle depth of 410 km. The finest resolution near the trench is around 2.5km/element (with linear elements for the velocity). A particle-in-cell technique is implemented to trace the material composition and plastic strain.

The initial and boundary conditions are based on a plate reconstruction starting from 40 Ma (Fig. 4.2) in *pyGPlates* (Müller et al., 2018). Since 40 Ma, the Australia-Pacific plate boundary experienced a transition from a spreading center, to strike-slip motion, and eventually to subduction, so that the majority of the subducting plate is younger than 40 Ma. We reconstruct the spreading center-transform fault plate boundary system according to the magnetic lineations and fracture zones (Fig. 4.1A), and calculate the explicit, evolving age of the plates using a tracer-based algorithm *Track Tec* (Karlsen et al., 2020) implemented using *pyGPlates*. Based on the evaluated plate age model at 15 Ma, we construct the initial thermal field of the geodynamic model following half-space cooling. Crustal thickness for the upper plate (Pacific) is interpolated from crust model *CRUST 1.0* (Laske et al., 2013). Transformation from geographical to Cartesian coordinates uses a Lambert equal area projection.

The boundary conditions of the geodynamic models are based on the AUS-PAC plate finite rotation (**keller_william_r_cenozoic_2005**; Cande and Stock, 2004; Croon, Cande, and Stock, 2008; Choi et al., 2017), The bottom boundary is no-slip, and the top boundary is free-slip so that with a sticky air layer it forms a free surface on top of the plates and allows the tracking of surface topography. In four side boundaries, the velocity field is composed of two terms. In the first term, the top 100 km mantle strictly follows the plate velocity of finite rotation, and between 100 km and 410 km depth the velocity drops linearly from the plate velocity to 0. In order to conserve a mass, a second term is added as channel flow, $V_r(z) = S_0 \frac{(z-z_0)(z-z_1)}{r}$ where z_0 and z_1 are 100 km and 410 km deep, r the radial distance from the sink (trench), S_0 is a constant that guarantees that the total flux out equals the influx.

In the numerical model, we implement a visco-plastic rheology with strain weakening to mimic the realistic mantle rheology (Karato and Wu, 1993). The effective viscosity is governed by either dislocation creep or plastic-yielding

$$\eta_{eff} = \min\left(\frac{1}{2} A_{disl}^{\frac{1}{n}} e^{\frac{E_l}{nRT}} \dot{\varepsilon}_{II}^{\frac{1}{n}-1}, \frac{\tau_y}{\dot{\varepsilon}_{II}}\right) \tag{4.1}$$

Where E_l,A_{disl} and n are activation energy, prefactor and non-Newtonian exponent of dislocation creep. $\dot{\varepsilon}_{II}$ the second invariant of strain rate, and τ_y the yielding stress, defined by the Drucker-Prager failure criterion with strain weakening

$$\tau_y = \max(\min((1 - \frac{\varepsilon_P}{\varepsilon_{P0}})(\mu P + C_0), \tau_{max}), \tau_{min}) \tag{4.2}$$

Where μ and C_0 are the friction coefficient and cohesion. ε_P is the accumulated plastic strain and ε_{P0} the reference plastic strain. τ_{min} and τ_{max} the lower and upper bound of yield stress. This definition of τ_y approximates the strain weakening with a linear process until it saturates ($\varepsilon_P = \varepsilon_{P0}$). A larger ε_{P0} means a slower weakening and vice versa.

The rheology is also composition-dependent. We mainly test two end-members for the upper plate: the Jelly Sandwich model whose crust is made out of weak quartzitic crust, and the Creme Brulee model with a strong crust of dry feldspar (Bürgmann and Dresen, 2008). The two key parameters we varied in the numerical models are weakening rate ε_{P0} and the τ_{max} of the upper plate τ_u. In contrast, the τ_{max} of the subducting plate maintains 150 MPa for all the models. For the key parameters see Table 4.1

Model evaluation

Outcomes of the geodynamic model are compared against different geophysical and geological observations quantitatively. The four major observations are the bathymetry and topography, shallow earthquake focal mechanisms, intermediate depth seismicity as an inference of slab morphology, and stress evolution from stratigraphy.

In the model, the topography is derived from the interface between the mantle (crust) and sticky air, and we evaluate the similarity between model topography and the real topography with the correlation

$$C_{topo} = \frac{\int_{\Gamma_t}(T_m - \overline{T}_m)(T_o - \overline{T}_o)dxdy}{(\int_{\Gamma_t}(topo_m - \overline{T}_m)^2 dxdy)(\int_{\Gamma_t}(T_o - \overline{T}_o)^2 dxdy)} \tag{4.3}$$

Where T_m and T_o stand for the topography from model and observation. Γ_t the trench area, defined as the area within 100 km from the Puysegur trench. $\overline{T}_m$ and $\overline{T}_o$ are the average model and observed topography in the area of Γ_t. The C_T describes the similarity between model topography and observed topography in phase but not in amplitude. A perfect in-phase topography gives $C_{topo} = 1$ while a perfect anti-phase topography gives $C_{topo} = -1$.

The stress evolution is derived from seismic profiles across the Puysegur Trench (Shuck et al., 2022), which describe the time evolution of stress polarity at different locations of the trench, $\tau_i^P(t)$ where $i = 1, 2, 3$ for line a,b,c, $\tau_i^P(t) = -1$ for compression and $\tau_i^P(t) = 1$ for extension. In the model, we directly measure the stresses in the direction of the three seismic profiles $\tau_i(t)$. The similarity between modeled stress and observation is

$$C_{stress} = \frac{1}{3}\sum_{1}^{3} \frac{\int_{15Ma}^{0} \tau_i(t)\tau_i^P(t)dt}{(\int_{15Ma}^{0} \tau_i(t)^2 dt)(\int_{15Ma}^{0} \tau_i^P(t)^2 dt)} \tag{4.4}$$

Note the C_{stress} doesn't need to demean, as $\tau = 0$ has an absolute physical meaning of neutral stress.

The intermediate seismicity provides an indication of the spatial distribution of the cold slab (Benioff zone). We define the C_{seis} as the proportion of observed seismicity that falls within the area with a temperature $\leq 850°C$ (Kelemen and Hirth, 2007).

The shallow earthquake focal mechanism provides a direct inference of the stress state in the present day. We take all Mw> 5 earthquakes shallower than 30 km from GCMT catalog (Ekstrom, Nettles, and Dziewoński, 2012). In the geodynamic model, we evaluate the focal mechanism from the stress tensor measured at the same hypocenter location as the GCMT earthquakes. To assess the alignment of moment tensors between the GCMT catalog and our model prediction, we evaluate the Kagan angle (Φ) (Kagan, 2007) between them. A Kagan angle ranges from 0 to 120°, with smaller values indicating a better match between observations (GCMT) and model predictions. Similar to the seismicity, we define the correctness of focal mechanism prediction C_{focal} as the volumetric average of Kagan angles, weighted by the spatial density distribution of earthquakes:

$$C_{focal} = (120° - \sum_{i} \frac{\Phi_i/\nu_i}{1/\nu_i})/120° \tag{4.5}$$

Where Φ_i and ν_i are the Kagan angle and spatial density of earthquake i. The C_{focal} is normalized to the range [0,1], where a higher C_{focal} value indicates a more accurate model prediction.

As the C_{topo} and C_{stress} are defined as correlation ranging from -1 to 1, while C_{seis} and C_{focal} are defined as correctness ranging from 0 to 1, we define the total model correctness C as the average of the four quantities all normalized to [0,1]

$$C = ((C_{topo} + 1)/2 + (C_{stress} + 1)/2 + C_{seis} + C_{focal})/4 \tag{4.6}$$

Physical models for plate boundary weakening

Shear Heating

Shear heating is one potential strain-weakening mechanism, with the rock becoming weaker as the temperature increases with deformation. The 0-dimensional heat equation ignoring transport yields

$$\frac{dT}{dt} = \chi \frac{\tau \dot{\varepsilon}}{\rho_r C_P} \tag{4.7}$$

Where χ is the efficiency of shear heating ranging from 0 to 1 (B. J. P. Kaus and Podladchikov, 2006). We take $\chi = 1$, providing an upper limit of shear heating, such that

$$\frac{\rho_r C_P dT}{\tau} = \dot{\varepsilon} dt \tag{4.8}$$

For a fixed stress, τ, the reference strain ε_{P0} describes the total strain for complete weakening. For shear heating, we define ε_{P0} as the point when rock heats to T_1

$$\varepsilon^{\tau}_{P0}(T_0, T_1) = \int_0^{t1} \dot{\varepsilon} dt = \int_{T_0}^{T_1} \frac{\rho_r C_P}{\tau} dT = \frac{\rho_r C_P (T_1 - T_0)}{\tau} \tag{4.9}$$

For the fixed strain rate $\dot{\varepsilon}$, we follow the definition of ε_{P0} that rock is heated to T_1 through shear heating, but dislocation and diffusion creep need to be considered. Diffusion creep is:

$$\dot{\varepsilon}_{diff} = A_{diff} e^{-\frac{E_f}{RT}} h^{-m} \tau \tag{4.10}$$

Where E_f, R, m and A_{diff} are the activation energy, ideal gas constant, grain-size exponent, and prefactor of diffusion creep. Dislocation creep is

$$\dot{\varepsilon}_{disl} = A_{disl} e^{-\frac{E_l}{RT}} \tau^n \tag{4.11}$$

The maximum of these two mechanisms is taken as the dominant creep mechanism

$$\dot{\varepsilon} = \max(\dot{\varepsilon}_{disl}, \dot{\varepsilon}_{diff}) \tag{4.12}$$

As the $\dot{\varepsilon}$ is fixed, eq. 4.12 is equivalent to

$$\tau = \min\left(\frac{\dot{\varepsilon} h^m}{A_{diff} e^{-\frac{E_f}{RT}}}, \left(\frac{\dot{\varepsilon}}{A_{disl} e^{-\frac{E_l}{RT}}} \right)^{\frac{1}{n}} \right) \tag{4.13}$$

Therefore, we obtain the dislocation-diffusion transition temperature T_T

$$T_T = -\frac{nE_f - E_l}{R \ln \frac{\dot{\varepsilon}^{n-1} h^{mn} A_{disl}}{A^n_{diff}}} \tag{4.14}$$

When $T < T_T$, $\dot{\varepsilon} = \dot{\varepsilon}_{disl}$ and when $T > T_T$, $\dot{\varepsilon} = \dot{\varepsilon}_{diff}$, such that

$$\begin{aligned}
\varepsilon_{P0}^{\dot{\varepsilon}}(T_0, T_1) &= \int_0^{t1} \dot{\varepsilon} dt = \int_{T_0}^{T_1} \frac{\rho_r C_P}{\tau} dT \\
&= \int_{T_0}^{T_C} \rho_r C_P \left(\frac{A_{disl} e^{-\frac{E_l}{RT}}}{\dot{\varepsilon}} \right)^{1/n} dT + \int_{T_C}^{T_1} \rho_r C_P \frac{A_{diff} e^{-\frac{E_f}{RT}}}{\dot{\varepsilon} h^m} dT \\
&= \frac{\rho_r C_P E_l}{nR} \left(\frac{A_{disl}}{\dot{\varepsilon}} \right)^{1/n} \left(x e^{-\frac{1}{x}} + \mathrm{Ei}\left(-\frac{1}{x} \right) \right) \Bigg|_{nRT_0/E_l}^{nRT_C/E_l} \\
&+ \frac{\rho_r C_P A_{diff} E_f}{\dot{\varepsilon} R h^m} \left(x e^{-\frac{1}{x}} + \mathrm{Ei}\left(-\frac{1}{x} \right) \right) \Bigg|_{RT_C/E_f}^{RT_1/E_f}
\end{aligned} \tag{4.15}$$

Where $T_C = \max\big(T_0, \min(T_T, T_1)\big)$. Ei is the exponential integral $\mathrm{Ei}(x) = \int_{-\infty}^{x} \frac{e^t}{t} dt$.

The realistic mantle rheology follows neither fixed stress nor fixed strain rate but can be represented by a combination of fixed stress (low-temperature plasticity) and fixed strain rate (dislocation/diffusion creep). With that, eq. 4.13 is modified as

$$\tau = \min\left(\frac{\dot{\varepsilon} h^m}{A_{diff} e^{-\frac{E_f}{RT}}}, \left(\frac{\dot{\varepsilon}}{A_{disl} e^{-\frac{E_l}{RT}}} \right)^{\frac{1}{n}}, \tau_y \right) \tag{4.16}$$

Similar to eq. 4.14, we define T_{C1} and T_{C2} the transition temperature of $\dot{\varepsilon}_{disl} = \dot{\varepsilon}_y$ and $\dot{\varepsilon}_{diff} = \dot{\varepsilon}_y$.

$$T_{C1} = \max\left(T_0, \min\left(\frac{E_l}{R ln \frac{\tau_y^n A_{disl}}{\dot{\varepsilon}}}, T_1 \right) \right) \tag{4.17}$$

$$T_{C2} = \max\left(T_0, \min\left(\frac{E_f}{R ln \frac{\tau_y A_{diff}}{\dot{\varepsilon} h^m}}, T_1 \right) \right) \tag{4.18}$$

When $T_{C1} < T_{C2}$, $T_0 \xrightarrow{\text{plas}} T_{C1} \xrightarrow{\text{disl}} T_C \xrightarrow{\text{diff}} T_1$

$$\varepsilon_{P0} = \varepsilon_{P0}^{\tau_y}(T_0, T_{C1}) + \varepsilon_{P0}^{\dot{\varepsilon}}(T_{C1}, T_1) \tag{4.19}$$

When $T_{C1} > T_{C2}$,$T_0 \xrightarrow{\text{plas}} T_{C2} \xrightarrow{\text{diff}} T_1$.

$$\varepsilon_{P0} = \varepsilon_{P0}^{\tau_y}(T_0, T_{C2}) + \varepsilon_{P0}^{\dot{\varepsilon}}(T_{C2}, T_1) \tag{4.20}$$

We define T_1 as the temperature when stress reaches a lower limit $\tau_f = 3$ MPa in diffusion creep regime so that $T_1 = \frac{E_f}{R \ln \frac{A_{diff} \tau_f}{h^m \dot{\varepsilon}}}$.

The inclusion of heat transport (such as diffusive cooling) would only slow the weakening, making the estimate conservative.

Grain-size Reduction

Grain-size reduction is a physical process for strain weakening. The grain size, h, influences the rheology through diffusion creep (eq. 4.10). We follow a detailed treatment (David Bercovici and Ricard, 2012; David Bercovici and Ricard, 2014) in which the grain size evolution of peridotite (60% Olivine, $\phi_1 = 0.6$, and 40% of Pyroxene, $\phi_2 = 0.4$, where ϕ_i is the partitioning of phase i) is governed by two-phase Zener pinning (a model of surface tension-like forces at the boundary between two phases). The mean grain size can be represented by the interface roughness, r, under a pinned state ($Z_i = 0$) (David Bercovici, Schubert, and Ricard, 2015)

$$h = \sum_i r \frac{\phi_i}{\sqrt{c(1-\phi_i)}} = 1.57r \tag{4.21}$$

where the numerical value of 1.57 is for the olivine and pyroxene system with c=0.87. The evolution of r follows

$$\frac{dr}{dt} = \frac{\eta G_I}{q r^{q-1}} - \frac{f_I r^2}{\gamma_I \eta}\Phi = \frac{\eta G_I}{q r^{q-1}} - \frac{f_I r^2}{\gamma_I \eta}(\dot{\varepsilon}_{diff} + \dot{\varepsilon}_{disl})\tau \tag{4.22}$$

Where the first term on the RHS controls grain growth and the second term controls grain-size reduction. With the grain growth exponent $p = 2$, $q = 4$, and the grain interface coarsening coefficient G_I follows (Rozel, Ricard, and David Bercovici, 2011; David Bercovici and Ricard, 2013)

$$G_I = 2(\mu\text{m})^2 G_i/250 = 2(\mu\text{m})^2 (k_0 e^{-\frac{E_g}{RT}})/250 \tag{4.23}$$

Where $k_0 = 2 \times 10^4 (\mu\text{m})^p$ s^{-1} is the kinetic factor and E_g is an activation energy for the grain growth.

For grain-size reduction, the fraction of damage energy that turns into deformational work, f_I, is approximated by (David Bercovici and Ricard, 2016)

$$f_I \approx f_0 e^{-2((T+273)/1000)^{2.9}} \tag{4.24}$$

Where $f_0 = 10^{-3}$. Surface tension $\gamma_I \approx 1\text{J} \cdot \text{m}^{-1}$. With eq. 4.10, 4.11, 4.21, 4.22, 4.23, 4.24, r evolution equation yields

$$\frac{dr}{dt} = C_1 \frac{1}{r^3} - C_2 \frac{\tau^2}{r} - C_3 \tau^4 r^2 \tag{4.25}$$

Where $C_1 = 2.88 \times 10^{-23} e^{-\frac{36145}{273+T}} \text{m}^4\text{s}^{-1}$,

$C_2 = 1.077 \times 10^{-18} e^{-4\times10^{-9}(273+T)^{2.9} - \frac{45180}{273+T}} \text{m}^2\text{s}^{-1}\text{Pa}^{-2}$,

$C_3 = 3.056 \times 10^{-16} e^{-4\times10^{-9}(273+T)^{2.9} - \frac{65060}{273+T}} \text{Pa}^{-4}$.

Similar to the shear heating, we consider the deformation experiences a transition from dislocation to diffusion creep, with an initial grain size $h_0 = 5$ mm. Initially, with a large strain rate, the deformation could be governed by dislocation creep, and with the reduction of grain size, the diffusion creep eventually takes over, and the transition grain size h_T is defined by the point at which $\dot{\varepsilon}_{diff} = \dot{\varepsilon}_{disl}$. With eq. 4.10, 4.11, and 4.21, we get the transition interface roughness

$$r_T = \frac{1}{1.57}\left(\frac{A_{diff} e^{-\frac{E_f}{RT}}}{A_{disl} e^{-\frac{E_l}{RT}} \tau_T^{n-1}}\right)^{\frac{1}{m}} \tag{4.26}$$

Where the transition stress happens either plasticity (with constant yield stress τ_y) or creeping (with constant strain rate $\dot{\varepsilon}$) domain, with

$$\tau_T = \min(\tau_y, \left(A_{disl}^{-1} e^{\frac{E_l}{RT}} \dot{\varepsilon}\right)^{\frac{1}{n}}) \tag{4.27}$$

τ_y and $\dot{\varepsilon}$ are the assigned constant yield stress and strain rate for plasticity and creeping mechanism.

When dislocation creep dominates, eq. 4.25 simplifies

$$\frac{dr}{dt} = C_1/r^3 - C_3\tau^4 r^2 \tag{4.28}$$

Since the dislocation creep doesn't depend on the grain size, both the strain rate and stress remain constant during the grain size evolution, and the stress is thereby evaluated by $\tau = \tau_T$ with eq. 4.27, and with eq. 4.10 at $r = r_T$ we can evaluate strain rate $\dot{\varepsilon}$. Therefore, the total strain that causes grain roughness reduces from an initial value r_0 to a targeted value r_1 in the dislocation creep domain is

$$\varepsilon_{P0}^{disl} = \int_{t_0}^{t_1} \dot{\varepsilon} dt = \int_{r_0}^{r_1} \frac{\dot{\varepsilon}_T r^3 dr}{C_1 - C_3 \tau_T^4 r^5} \tag{4.29}$$

Where r_0 is given by the initial grain size $r_0 = h_0/1.57$, and r_1 is either the transition roughness r_T or the desired roughness which defines the completion of the weakening process.

When diffusion creep dominates, eq. 4.25 simplifies

$$\frac{dr}{dt} = C_1/r^3 - C_2\tau^2/r \tag{4.30}$$

In the context of diffusion creep, both strain rate and stress vary as the grain size evolves. In our analysis, we explore two scenarios: one in which stress remains

constant and another in which strain rate remains constant. In each scenario, we calculate the amount of strain necessary for the roughness r to transition from one state to the other.

Under the fixed stress, we define the ε_{P0} as the total strain that leads to a strain rate reaching $\dot{\varepsilon}_1 = 10^{-12}\mathrm{s}^{-1}$ due to grain-size reduction.

$$\begin{aligned}\varepsilon^{\tau}_{P0}(r_0, r_1) &= \int_{t_0}^{t_1} \dot{\varepsilon} dt = \int_{r_0}^{r_1} \frac{A_{diff} e^{-\frac{E_f}{RT}} \tau r^3}{1.57^m (C_1 - C_2 \tau^2 r^2)} dr \\ &= \frac{A_{diff} e^{-\frac{E_f}{RT}}}{2 \times 1.57^3 \sqrt{C_1 C_2}} ln \frac{r - \tau^{-1}\sqrt{C_1/C_2}}{r + \tau^{-1}\sqrt{C_1/C_2}} |_{r_1}^{r_0}\end{aligned} \tag{4.31}$$

Where r_0 and r_1 are the initial and final roughness.

Under the fixed strain rate, such that $\tau = \frac{1.57^m r^m \dot{\varepsilon}}{A_{diff}} e^{\frac{E_f}{RT}}$, we define the ε_{P0} as the total strain that leads to the stress deduced to τ_f due to grain-size reduction.

$$\begin{aligned}\varepsilon^{\dot{\varepsilon}}_{P0}(r_0, r_1) &= \int_{t_0}^{t_1} \dot{\varepsilon} dt = \int_{r_0}^{r_1} \dot{\varepsilon} \frac{r^3}{C_1 - C_2 \tau^2 r^2} dr \\ &= \frac{A_{diff} e^{-\frac{E_f}{RT}} \dot{\varepsilon}}{8\sqrt{C_1 C_2} 1.57^m \dot{\varepsilon}} ln \frac{r^4 - \sqrt{\frac{C_1}{C_2}} (\frac{A_{diff} e^{-\frac{E_f}{RT}}}{1.57^m \dot{\varepsilon}})}{r^4 + \sqrt{\frac{C_1}{C_2}} (\frac{A_{diff} e^{-\frac{E_f}{RT}}}{1.57^m \dot{\varepsilon}})} |_{r_1}^{r_0}\end{aligned} \tag{4.32}$$

Similar to shear heating, realistic rheology incorporates constant stress and constant strain to mimic the brittle to ductile transition. Initially, the flow is dominated by a constant stress, representing the flow governed by either plastic yield stress $\tau_y = 150$ MPa, or dislocation creep $\tau = \tau_T$. Determination of the stress depends on which one is smaller, i.e. $\tau = \min(\tau_y, \tau_T)$. The flow is then governed by a constant strain rate when diffusion creep takes over as grain size is reduced to r_c:

$$r_c = \frac{1}{1.57} (\frac{A_{diff} \tau e^{-\frac{E_f}{RT}}}{\dot{\varepsilon}})^{\frac{1}{m}} \tag{4.33}$$

where the $\dot{\varepsilon}$ is a constant strain the system maintains after diffusion creep dominates. The total combines the plastic deformation/dislocation creep and the diffusion creep: When $\tau_y < \tau_T$

$$\varepsilon_{P0} = \varepsilon^{disl}_{P0}(r_0, r_T) + \varepsilon^{\tau}_{P0}(r_T, r_c) + \varepsilon^{\dot{\varepsilon}}_{P0}(r_c, r_1) \tag{4.34}$$

When $\tau_y > \tau_T$

$$\varepsilon_{P0} = \varepsilon^{disl}_{P0}(r_0, r_c) + \varepsilon^{\dot{\varepsilon}}_{P0}(r_c, r_1) \tag{4.35}$$

Where $r_0 = 10^{-3}$m is the initial grain size, and $r_1 = \frac{1}{1.57}(\frac{A_{diff}\tau_f e^{-\frac{E_f}{RT}}}{\dot{\varepsilon}})^{\frac{1}{m}}$ is the final grain size that reduces stress to the target stress τ_f.

Fluid Pore Pressure

Fluid is another potential source of plate boundary weakening, as the increased fluid pore pressure reduces the effective normal stress and yield stress.

$$\tau_y = C + \mu(P - P_f) \tag{4.36}$$

Where τ_y the yielding stress, C and μ are cohesion and coefficient of friction, P and P_f are rock and pore fluid pressure. The pore pressure follows steady state Darcy's law:

$$\nabla(\frac{k\rho}{\nu}(\nabla P_f - \rho\vec{g})) + \rho\Gamma = 0 \tag{4.37}$$

Where k the permeability, ρ fluid density, ν fluid viscosity, and Γ fluid production rate. For water, we can use constant density and viscosity $\rho = 1000\text{kg/m}^3$, $\nu = 10^{-4}\text{Pa}\cdot\text{s}$, while the permeability is substantially dependent on pressure (Evans, Forster, and Goddard, 1997; Faulkner and Rutter, 2001; Dong et al., 2010; Zheng et al., 2015; Zhu et al., 2020)

$$k = k_0 e^{-\frac{\rho_r g z - P_f}{\sigma^*}} \tag{4.38}$$

where k_0 is the permeability at zero pressure, ρ_r the rock density and σ^* describes how permeability is sensitive to the change of pressure. The definition of k leads to

$$\nabla k = -\frac{k(\rho\vec{g} - \nabla P_f)}{\sigma^*} \tag{4.39}$$

$$\nabla^2 k = -\frac{1}{\sigma^*}(\nabla k \cdot \rho_r\vec{g} - \nabla k \cdot \nabla P_f - k\nabla^2 P_f) \tag{4.40}$$

With eq. 4.39 and 4.40, 4.37 yields into a linear PDE of permeability k

$$\begin{aligned}\nabla(k(\nabla P_f - \rho\vec{g}) &= \nabla k \cdot \nabla P_f + k\nabla^2 P_f - \rho\nabla k \cdot \vec{g} \\ &= \sigma^*\nabla^2 k + (\rho_r - \rho)\nabla k \cdot \vec{g} = -\nu\Gamma\end{aligned} \tag{4.41}$$

As gravity $\vec{g}$ is only in vertical direction, z, horizontally k follows diffusion equation, while vertically k is driven by the buoyancy term$(\rho_r - \rho)$, indicating the vertical transportation is much faster than horizontal. Therefore, we collapse eq 4.41 into a ODE in z dimension, assuming a point source for each column

$$k'' + \frac{(\rho_r - \rho)g}{\sigma^*}k' = -\frac{\nu\Gamma\delta(z - z_0)}{\sigma^*} \tag{4.42}$$

Where δ is the Dirac delta function, z_0 is the location of the fluid source. In our case, z_0 is the depth of sediment/crust of the mega-thrust subduction zone.

With the boundary condition $k|_{z=0} = k_0$, $k|_{z=+\infty} = 0$, we can solve eq 4.42 with Laplace transform.

$$k = \frac{\nu\Gamma}{(\rho_r - \rho)g} - \frac{\nu\Gamma - (\rho_r - \rho)gk_0}{(\rho_r - \rho)g} e^{-\frac{(\rho_r - \rho)g}{\sigma^*}z} + \frac{\nu\Gamma}{(\rho_r - \rho)g} u(z - z_0)(e^{\frac{(\rho_r - \rho)g}{\sigma^*}(z_0 - z)} - 1) \tag{4.43}$$

Where u is a heavy-side function.

In the subduction zone interface where fluid is released from sediment and oceanic crust($z = z_0$), the pore pressure P_f can be evaluated from eq 4.38 and eq 4.43:

$$P_f(z_0) = \rho_r g z_0 + \sigma^* ln(\frac{\nu\Gamma}{(\rho_r - \rho)gK_0}(1 - e^{-\frac{(\rho_r - \rho)gz_0}{\sigma^*}}) + e^{-\frac{(\rho_r - \rho)gz_0}{\sigma^*}}) \tag{4.44}$$

With no fluid source ($\Gamma = 0$), $k = k_0 e^{-\frac{(\rho_r - \rho)g}{\sigma^*}z}$ is the background permeability, with eq 4.38 we obtain background pore pressure $P_f = \rho g z$. Therefore the change of pore pressure due to the fluid release is

$$\Delta P_f = P_f - \rho g z = \sigma^* ln(\frac{\nu\Gamma}{(\rho_r - \rho)gK_0}(e^{\frac{(\rho_r - \rho)gz_0}{\sigma^*}} - 1) + 1) \tag{4.45}$$

The yield stress reduction due to the change of fluid pore pressure is

$$\Delta\tau_y = -\mu\Delta P_f \tag{4.46}$$

In subduction zones, the fluid is released from the sedimentary layer and oceanic crust through porosity loss from compaction and clay dehydration at shallow depths (top 5 km) , and hydrous mineral breakdown at deeper depth (Fagereng et al., 2018). We assign the fluid production rate following (Saffer and Tobin, 2011) assuming a 1 km thick sediment wedge (Gurnis, Van Avendonk, et al., 2019).

For subduction initiation, fluid production starts from $\Gamma = 0$ and turns non-zero, $\Gamma = \Gamma(z_0)$, once sediment reaches the depth of z_0 within the subduction channel. Within a simple shear channel flow, the total plastic strain for sediment to reach the depth of z_0 is $\varepsilon_P = \frac{z_0}{\delta sin\theta}$, with δ the channel width and θ the dip angle. In the geodynamic models, the yielding stress of the shallow depth is governed by Drucker–Prager failure criterion with a linear strain weakening

$$\tau_y = (1 - \frac{\varepsilon_P}{\varepsilon_{P0}})(\mu P_r + C_0) \tag{4.47}$$

Where μ and C_0 are the initial friction coefficient and cohesion, and $\varepsilon_P < \varepsilon_{P0}$ as strain weakening isn't saturated at shallow depth. P_r is the rock pressure, which can be approximated with $P_r = \rho_r g z_0$.

Compared to the initial stress ($\varepsilon_p = 0$), the change of yielding stress in the model is

$$\Delta\tau_y = -\frac{\varepsilon_P}{\varepsilon_{P0}}(\mu P + C_0) = -\frac{\varepsilon_P}{\varepsilon_{P0}}(\mu\rho_r g z_0 + C_0) \tag{4.48}$$

Eq 4.46 and eq 4.48 link the weakening by pore pressure change with the linear strain weakening assumption in the model

$$\Delta P_f = \frac{z_0}{\varepsilon_{P0}\delta sin\theta}(\rho_r g z_0 + \frac{C_0}{\mu}) \tag{4.49}$$

This equation predicts the relationship between $P_f \setminus P_r$ and z_0 to be linear, which is only true for small $\sigma^*(\approx 10$ MPa), meaning the linear strain weakening assumption in numerical models might not always precisely mimic the pore pressure weakening. Despite the subtle difference, we evaluate ε_{P0} by integrating eq 4.49 with depth, representing the average weakening rate throughout the whole slab interface.

$$\bar{\varepsilon}_{P0} = \frac{1}{\delta sin\theta \int_0^{z_1} \Delta P_f dz_0}(\frac{\rho_r g z_1^3}{3} + \frac{C_0 z_1^2}{2\mu}) \tag{4.50}$$

We choose the integration upper limit to be $z_1 = 10$ km, which is the depth of the strain partitioning zone.

References

Alvarez-Gomez, José A. (Jan. 2019). "FMC—Earthquake focal mechanisms data management, cluster and classification". In: *SoftwareX* 9, pp. 299–307. ISSN: 23527110. DOI: 10.1016/j.softx.2019.03.008. URL: https://linkinghub.elsevier.com/retrieve/pii/S2352711018302590 (visited on 10/15/2023).

Bercovici, David and Yanick Ricard (Aug. 2012). "Mechanisms for the generation of plate tectonics by two-phase grain-damage and pinning". In: *Physics of the Earth and Planetary Interiors* 202-203, pp. 27–55. ISSN: 00319201. DOI: 10.1016/j.pepi.2012.05.003. URL: https://linkinghub.elsevier.com/retrieve/pii/S0031920112000854 (visited on 02/16/2024).

Bercovici, David and Yanick Ricard (Mar. 2013). "Generation of plate tectonics with two-phase grain-damage and pinning: Source–sink model and toroidal flow". In: *Earth and Planetary Science Letters* 365, pp. 275–288. ISSN: 0012821X. DOI: 10.1016/j.epsl.2013.02.002. URL: https://linkinghub.elsevier.com/retrieve/pii/S0012821X13000691 (visited on 02/16/2024).

Bercovici, David and Yanick Ricard (Apr. 2014). "Plate tectonics, damage and inheritance". In: *Nature* 508.7497, pp. 513–516. ISSN: 0028-0836, 1476-4687. DOI: 10.1038/nature13072. URL: https://www.nature.com/articles/nature13072 (visited on 08/22/2023).

Bercovici, David and Yanick Ricard (Apr. 2016). "Grain-damage hysteresis and plate tectonic states". In: *Physics of the Earth and Planetary Interiors* 253, pp. 31–47. ISSN: 00319201. DOI: 10.1016/j.pepi.2016.01.005. URL: https://linkinghub.elsevier.com/retrieve/pii/S0031920116000157 (visited on 02/16/2024).

Bercovici, David, Gerald Schubert, and Yanick Ricard (Feb. 3, 2015). "Abrupt tectonics and rapid slab detachment with grain damage". In: *Proceedings of the National Academy of Sciences* 112.5, pp. 1287–1291. ISSN: 0027-8424, 1091-6490. DOI: 10.1073/pnas.1415473112. URL: https://pnas.org/doi/full/10.1073/pnas.1415473112 (visited on 08/31/2023).

Beucher, Romain et al. (Dec. 19, 2022). *Underworld2: Python Geodynamics Modelling for Desktop, HPC and Cloud*. Version v2.14.1b. DOI: 10.5281/ZENODO.7455999. URL: https://zenodo.org/record/7455999 (visited on 08/23/2023).

Brace, W. F. and D. L. Kohlstedt (Nov. 10, 1980). "Limits on lithospheric stress imposed by laboratory experiments". In: *Journal of Geophysical Research: Solid Earth* 85 (B11), pp. 6248–6252. ISSN: 0148-0227. DOI: 10.1029/JB085iB11p06248. URL: https://agupubs.onlinelibrary.wiley.com/doi/10.1029/JB085iB11p06248 (visited on 02/16/2024).

Bürgmann, Roland and Georg Dresen (May 1, 2008). "Rheology of the Lower Crust and Upper Mantle: Evidence from Rock Mechanics, Geodesy, and Field Observations". In: *Annual Review of Earth and Planetary Sciences* 36.1, pp. 531–567. ISSN: 0084-6597, 1545-4495. DOI: 10.1146/annurev.earth.36.031207.124326. URL: https://www.annualreviews.org/doi/10.1146/annurev.earth.36.031207.124326 (visited on 02/16/2024).

Cande, Steven C. and Joann M. Stock (Apr. 2004). "Pacific-Antarctic-Australia motion and the formation of the Macquarie Plate". In: *Geophysical Journal International* 157.1, pp. 399–414. ISSN: 0956540X, 1365246X. DOI: 10.1111/j.1365-246X.2004.02224.x. URL: https://academic.oup.com/gji/article-lookup/doi/10.1111/j.1365-246X.2004.02224.x (visited on 08/03/2023).

Choi, Hakkyum et al. (Nov. 2017). "The kinematic evolution of the Macquarie Plate: A case study for the fragmentation of oceanic lithosphere". In: *Earth and Planetary Science Letters* 478, pp. 132–142. ISSN: 0012821X. DOI: 10.1016/j.epsl.2017.08.035. URL: https://linkinghub.elsevier.com/retrieve/pii/S0012821X1730482X (visited on 10/14/2023).

Collot, Jean-Yves et al. (1995). "Morphostructure of an incipient subduction zone along a transform plate boundary: Puysegur Ridge and Trench". In: *Geology* 23.6, p. 519. ISSN: 0091-7613. DOI: 10.1130/0091-7613(1995)023<0519:MOAISZ>2.3.CO;2. URL: https://pubs.geoscienceworld.org/geology/article/23/6/519-522/206344 (visited on 10/26/2023).

Croon, Marcel B., Steven C. Cande, and Joann M. Stock (July 2008). "Revised Pacific-Antarctic plate motions and geophysics of the Menard Fracture Zone". In: *Geochemistry, Geophysics, Geosystems* 9.7, 2008GC002019. ISSN: 1525-2027, 1525-2027. DOI: 10.1029/2008GC002019. URL: https://agupubs.onlinelibrary.wiley.com/doi/10.1029/2008GC002019 (visited on 10/14/2023).

Dong, Jia-Jyun et al. (Oct. 2010). "Stress-dependence of the permeability and porosity of sandstone and shale from TCDP Hole-A". In: *International Journal of Rock Mechanics and Mining Sciences* 47.7, pp. 1141–1157. ISSN: 13651609. DOI: 10.1016/j.ijrmms.2010.06.019. URL: https://linkinghub.elsevier.com/retrieve/pii/S1365160910001164 (visited on 10/30/2023).

Ekstrom, G., M. Nettles, and A.M. Dziewoński (June 2012). "The global CMT project 2004–2010: Centroid-moment tensors for 13,017 earthquakes". In: *Physics of the Earth and Planetary Interiors* 200-201, pp. 1–9. ISSN: 00319201. DOI: 10.1016/j.pepi.2012.04.002. URL: https://linkinghub.elsevier.com/retrieve/pii/S0031920112000696 (visited on 10/15/2023).

Evans, James P., Craig B. Forster, and James V. Goddard (Nov. 1997). "Permeability of fault-related rocks, and implications for hydraulic structure of fault zones". In: *Journal of Structural Geology* 19.11, pp. 1393–1404. ISSN: 01918141. DOI: 10.1016/S0191-8141(97)00057-6. URL: https://linkinghub.elsevier.com/retrieve/pii/S0191814197000576 (visited on 10/30/2023).

Fagereng, Ake et al. (2018). "Fluid-related deformation processes at the up- and downdip limits of the subduction thrust seismogenic zone: What do the rocks tell us?" In: Byrne, Timothy et al. *Geology and Tectonics of Subduction Zones: A Tribute to Gaku Kimura*. Geological Society of America. ISBN: 978-0-8137-2534-5. DOI: 10.1130/2018.2534(12). URL: https://pubs.geoscienceworld.org/books/book/2074/chapter/114713690 (visited on 09/07/2023).

Faulkner, Daniel R. and Ernest H. Rutter (2001). "Can the maintenance of overpressured fluids in large strike-slip fault zones explain their apparent weakness?" In: *Geology* 29.6, p. 503. ISSN: 0091-7613. DOI: 10.1130/0091-7613(2001)029<0503:CTMOOF>2.0.CO;2. URL: https://pubs.geoscienceworld.org/geology/article/29/6/503-506/192048 (visited on 10/30/2023).

Gerya, T. V., D. Bercovici, and T. W. Becker (Nov. 11, 2021). "Dynamic slab segmentation due to brittle–ductile damage in the outer rise". In: *Nature* 599.7884, pp. 245–250. ISSN: 0028-0836, 1476-4687. DOI: 10.1038/s41586-021-03937-x. URL: https://www.nature.com/articles/s41586-021-03937-x (visited on 02/16/2024).

Gerya, T. V., R. J. Stern, et al. (Nov. 2015). "Plate tectonics on the Earth triggered by plume-induced subduction initiation". In: *Nature* 527.7577, pp. 221–225. ISSN: 0028-0836, 1476-4687. DOI: 10.1038/nature15752. URL: https://www.nature.com/articles/nature15752 (visited on 08/22/2023).

Gleason, Gayle C. and Jan Tullis (July 1995). "A flow law for dislocation creep of quartz aggregates determined with the molten salt cell". In: *Tectonophysics* 247.1, pp. 1–23. ISSN: 00401951. DOI: 10.1016/0040-1951(95)00011-B. URL: https://linkinghub.elsevier.com/retrieve/pii/004019519500011B (visited on 11/02/2023).

Gurnis, Michael, Chad Hall, and Luc Lavier (July 2004). "Evolving force balance during incipient subduction: EVOLVING FORCE BALANCE". In: *Geochemistry, Geophysics, Geosystems* 5.7. ISSN: 15252027. DOI: 10.1029/2003GC000681. URL: http://doi.wiley.com/10.1029/2003GC000681 (visited on 07/19/2022).

Gurnis, Michael, Harm Van Avendonk, et al. (Aug. 2019). "Incipient subduction at the contact with stretched continental crust: The Puysegur Trench". In: *Earth and Planetary Science Letters* 520, pp. 212–219. ISSN: 0012821X. DOI: 10.1016/j.epsl.2019.05.044. URL: https://linkinghub.elsevier.com/retrieve/pii/S0012821X19303267 (visited on 02/16/2024).

Hightower, Erin, Michael Gurnis, and Harm Van Avendonk (Oct. 15, 2020). "A Bayesian 3-D linear gravity inversion for complex density distributions: application to the Puysegur subduction system". In: *Geophysical Journal International* 223.3, pp. 1899–1918. ISSN: 0956-540X, 1365-246X. DOI: 10.1093/gji/ggaa425. URL: https://academic.oup.com/gji/article/223/3/1899/5902856 (visited on 07/20/2022).

Jackson, James (2002). "Strength of the continental lithosphere: Time to abandon the jelly sandwich?" In: *GSA Today* 12.9, p. 4. ISSN: 1052-5173. DOI: 10.1130/1052-5173(2002)012<0004:SOTCLT>2.0.CO;2. URL: http://www.geosociety.org/gsatoday/archive/12/9/pdf/i1052-5173-12-9-4.pdf (visited on 11/02/2023).

Jin, Z.-M. et al. (2001). "Eclogite rheology: Implications for subducted lithosphere". In: *Geology* 29.8, p. 667. ISSN: 0091-7613. DOI: 10.1130/0091-7613(2001)029<0667:ERIFSL>2.0.CO;2. URL: https://pubs.geoscienceworld.org/geology/article/29/8/667-670/192050 (visited on 11/02/2023).

Kagan, Yan Y. (Oct. 2007). "Simplified algorithms for calculating double-couple rotation". In: *Geophysical Journal International* 171.1, pp. 411–418. ISSN: 0956540X, 1365246X. DOI: 10.1111/j.1365-246X.2007.03538.x. URL: https://academic.oup.com/gji/article-lookup/doi/10.1111/j.1365-246X.2007.03538.x (visited on 12/19/2023).

Karato, Shun-ichiro and Patrick Wu (May 7, 1993). "Rheology of the Upper Mantle: A Synthesis". In: *Science* 260.5109, pp. 771–778. ISSN: 0036-8075, 1095-9203.

DOI: 10.1126/science.260.5109.771. URL: https://www.science.org/doi/10.1126/science.260.5109.771 (visited on 02/17/2024).

Karlsen, Krister S. et al. (July 2020). "A tracer-based algorithm for automatic generation of seafloor age grids from plate tectonic reconstructions". In: *Computers & Geosciences* 140, p. 104508. ISSN: 00983004. DOI: 10.1016/j.cageo.2020.104508. URL: https://linkinghub.elsevier.com/retrieve/pii/S0098300419308325 (visited on 08/22/2023).

Kaus, Boris J. P. and Yuri Y. Podladchikov (Apr. 2006). "Initiation of localized shear zones in viscoelastoplastic rocks". In: *Journal of Geophysical Research: Solid Earth* 111 (B4), 2005JB003652. ISSN: 0148-0227. DOI: 10.1029/2005JB003652. URL: https://agupubs.onlinelibrary.wiley.com/doi/10.1029/2005JB003652 (visited on 02/17/2024).

Kelemen, Peter B. and Greg Hirth (Apr. 2007). "A periodic shear-heating mechanism for intermediate-depth earthquakes in the mantle". In: *Nature* 446.7137, pp. 787–790. ISSN: 0028-0836, 1476-4687. DOI: 10.1038/nature05717. URL: https://www.nature.com/articles/nature05717 (visited on 09/04/2023).

Laske, Gabi et al. (Apr. 1, 2013). "Update on CRUST1.0 - A 1-degree Global Model of Earth's Crust". In: Conference Name: EGU General Assembly Conference Abstracts ADS Bibcode: 2013EGUGA..15.2658L, EGU2013–2658. URL: https://ui.adsabs.harvard.edu/abs/2013EGUGA..15.2658L (visited on 08/22/2023).

Lebrun, Jean-Frédéric, Geoffroy Lamarche, and Jean-Yves Collot (Sept. 2003). "Subduction initiation at a strike-slip plate boundary: The Cenozoic Pacific-Australian plate boundary, south of New Zealand". In: *Journal of Geophysical Research: Solid Earth* 108 (B9). ISSN: 01480227. DOI: 10.1029/2002JB002041. URL: http://doi.wiley.com/10.1029/2002JB002041 (visited on 07/19/2022).

Li, Yida and Michael Gurnis (Sept. 16, 2022). "A simple force balance model of subduction initiation". In: *Geophysical Journal International* 232.1, pp. 128–146. ISSN: 0956-540X, 1365-246X. DOI: 10.1093/gji/ggac332. URL: https://academic.oup.com/gji/article/232/1/128/6679290 (visited on 12/21/2022).

Li, Yida and Michael Gurnis (Apr. 17, 2023). "Strike slip motion and the triggering of subduction initiation". In: *Frontiers in Earth Science* 11, p. 1156034. ISSN: 2296-6463. DOI: 10.3389/feart.2023.1156034. URL: https://www.frontiersin.org/articles/10.3389/feart.2023.1156034/full (visited on 05/18/2023).

Müller, R. Dietmar et al. (July 2018). "GPlates: Building a Virtual Earth Through Deep Time". In: *Geochemistry, Geophysics, Geosystems* 19.7, pp. 2243–2261. ISSN: 1525-2027, 1525-2027. DOI: 10.1029/2018GC007584. URL: https://onlinelibrary.wiley.com/doi/10.1029/2018GC007584 (visited on 07/19/2022).

Rozel, Antoine, Yanick Ricard, and David Bercovici (Feb. 1, 2011). "A thermodynamically self-consistent damage equation for grain size evolution during dynamic recrystallization". In: *Geophysical Journal International* 184.2, pp. 719–728. ISSN: 1365-246X, 0956-540X. DOI: 10.1111/j.1365-246X.2010.04875.x. URL: https://academic.oup.com/gji/article/184/2/719/593403 (visited on 09/06/2023).

Rybacki, E. et al. (Mar. 2006). "Influence of water fugacity and activation volume on the flow properties of fine-grained anorthite aggregates". In: *Journal of Geophysical Research: Solid Earth* 111 (B3), 2005JB003663. ISSN: 0148-0227. DOI: 10.1029/2005JB003663. URL: https://agupubs.onlinelibrary.wiley.com/doi/10.1029/2005JB003663 (visited on 11/02/2023).

Saffer, Demian M. and Harold J. Tobin (May 30, 2011). "Hydrogeology and Mechanics of Subduction Zone Forearcs: Fluid Flow and Pore Pressure". In: *Annual Review of Earth and Planetary Sciences* 39.1, pp. 157–186. ISSN: 0084-6597, 1545-4495. DOI: 10.1146/annurev-earth-040610-133408. URL: https://www.annualreviews.org/doi/10.1146/annurev-earth-040610-133408 (visited on 02/17/2024).

Seebeck, Hannu et al. (Mar. 19, 2023). "The New Zealand Community Fault Model – version 1.0: an improved geological foundation for seismic hazard modelling". In: *New Zealand Journal of Geology and Geophysics*, pp. 1–21. ISSN: 0028-8306, 1175-8791. DOI: 10.1080/00288306.2023.2181362. URL: https://www.tandfonline.com/doi/full/10.1080/00288306.2023.2181362 (visited on 08/22/2023).

Shuck, Brandon et al. (Feb. 2022). "Stress transition from horizontal to vertical forces during subduction initiation". In: *Nature Geoscience* 15.2, pp. 149–155. ISSN: 1752-0894, 1752-0908. DOI: 10.1038/s41561-021-00880-4. URL: https://www.nature.com/articles/s41561-021-00880-4 (visited on 02/17/2024).

Stern, R (Oct. 15, 2004). "Subduction initiation: spontaneous and induced". In: *Earth and Planetary Science Letters* 226.3, pp. 275–292. ISSN: 0012821X. DOI: 10.1016/S0012-821X(04)00498-4. URL: https://linkinghub.elsevier.com/retrieve/pii/S0012821X04004984 (visited on 08/22/2023).

Sutherland, Rupert, Philip Barnes, and Chris Uruski (Mar. 2006). "Miocene-Recent deformation, surface elevation, and volcanic intrusion of the overriding plate during subduction initiation, offshore southern Fiordland, Puysegur margin, southwest New Zealand". In: *New Zealand Journal of Geology and Geophysics* 49.1, pp. 131–149. ISSN: 0028-8306, 1175-8791. DOI: 10.1080/00288306.2006.9515154. URL: http://www.tandfonline.com/doi/abs/10.1080/00288306.2006.9515154 (visited on 05/02/2023).

Thielmann, Marcel and Boris J.P. Kaus (Dec. 2012). "Shear heating induced lithospheric-scale localization: Does it result in subduction?" In: *Earth and Planetary Science Letters* 359-360, pp. 1–13. ISSN: 0012821X. DOI: 10.1016/j.epsl.2012.

10.002. URL: https://linkinghub.elsevier.com/retrieve/pii/S0012821X12005511 (visited on 02/17/2024).

Toth, John and Michael Gurnis (Aug. 10, 1998). "Dynamics of subduction initiation at preexisting fault zones". In: *Journal of Geophysical Research: Solid Earth* 103 (B8), pp. 18053–18067. ISSN: 01480227. DOI: 10.1029/98JB01076. URL: http://doi.wiley.com/10.1029/98JB01076 (visited on 07/19/2022).

Zhang, Shengxing and Wei Leng (June 16, 2021). "Subduction Polarity Reversal: Induced or Spontaneous?" In: *Geophysical Research Letters* 48.11, e2021GL093201. ISSN: 0094-8276, 1944-8007. DOI: 10.1029/2021GL093201. URL: https://agupubs.onlinelibrary.wiley.com/doi/10.1029/2021GL093201 (visited on 11/01/2023).

Zhang, Shengxing, Wei Leng, and Ling Chen (Aug. 2023). "Continental Tip With Thinned Lithosphere and Thickened Crust Is a Favorable Location for Subduction Initiation". In: *Journal of Geophysical Research: Solid Earth* 128.8, e2023JB027067. ISSN: 2169-9313, 2169-9356. DOI: 10.1029/2023JB027067. URL: https://agupubs.onlinelibrary.wiley.com/doi/10.1029/2023JB027067 (visited on 11/01/2023).

Zheng, Jiangtao et al. (Sept. 2015). "Relationships between permeability, porosity and effective stress for low-permeability sedimentary rock". In: *International Journal of Rock Mechanics and Mining Sciences* 78, pp. 304–318. ISSN: 13651609. DOI: 10.1016/j.ijrmms.2015.04.025. URL: https://linkinghub.elsevier.com/retrieve/pii/S1365160915001653 (visited on 10/30/2023).

Zhu, Weiqiang et al. (Sept. 24, 2020). "Fault valving and pore pressure evolution in simulations of earthquake sequences and aseismic slip". In: *Nature Communications* 11.1, p. 4833. ISSN: 2041-1723. DOI: 10.1038/s41467-020-18598-z. URL: https://www.nature.com/articles/s41467-020-18598-z (visited on 10/22/2023).

Chapter 5

SHEAR WAVE VELOCITIES IN THE SAN GABRIEL AND SAN BERNARDINO BASINS, CALIFORNIA

Li, Yida et al. (July 2023). "Shear Wave Velocities in the San Gabriel and San Bernardino Basins, California". In: *Journal of Geophysical Research: Solid Earth* 128.7, e2023JB026488. DOI: 10.1029/2023JB026488.

5.1 Abstract

We construct a new shear velocity model for the San Gabriel, Chino, and San Bernardino basins located in the northern Los Angeles area using ambient noise correlation between dense linear nodal arrays, broadband stations, and accelerometers. We observe Rayleigh and Love waves in the correlation of vertical (Z) and transverse (T) components, respectively. By combining Hilbert and Wavelet transforms, we obtain the separated fundamental and first higher mode of the Rayleigh wave dispersion curves based on their distinct particle motion polarization. Basin depths constrained by receiver functions, gravity, and borehole data are incorporated into the prior model. Our 3D shear wave velocity model covers the upper 3 to 5 km of the crust in the San Gabriel, Chino, and San Bernardino basin area. The Vs model is in agreement with the geological and geophysical cross-sections from other studies, but discrepancies exist between our model and a Southern California Earthquake Center (SCEC) community velocity model. Our shear wave velocity model shows good consistency with the CVMS 4.26 in the San Gabriel basin, but predicts a deeper and slower sedimentary basin in the San Bernardino and Chino basins than the community model.

5.2 Introduction

The San Gabriel (SG) and San Bernardino (SB) basins are sedimentary basins northeast of the city of Los Angeles (Fig. 5.1). The SG basin consists of two subbasin structures: the Raymond basin on the west and the San Gabriel basin on the east, separated by the Raymond fault. The SB region, immediately to the east of SG, is composed of three sedimentary basins: the Chino, Rialto-Colton, and San Bernardino basins from west to east. Bounded by mountains both to the north and south, the sedimentary structures in the SG and SB area were part of the opening of

the Los Angeles basin region in the Miocene.

Understanding the velocity structure of SG and SB area is important for the accurate hazard assessment of the densely populated Los Angeles region because the low-velocity basins in the SG and SB area may function as a waveguide that channels earthquake energy from the San Andreas Fault (SAF) into the Los Angeles region (Olsen et al., 2006). Numerical simulations such as the ShakeOut Scenario (Jones et al., 2008) and CyberShake (Graves et al., 2011) show events on the southern SAF may cause large ground motions in downtown Los Angeles. A study using ambient noise correlation estimate (M. A. Denolle et al., 2014) found the ground motion could be four times larger than the simulation. This implies the current Southern California Earthquake Center (SCEC) Community Velocity Model (CVM) used in the ground motion simulations do not adequately account for the channeling effect of the northern sedimentary basins (R. Clayton et al., 2019). A recent study in the Los Angeles basin constrains the velocity model using dense industry arrays correlated with broadband stations (Jia and Robert W. Clayton, 2021), and the new fine-scale velocity model's strong motion amplification performs similar to the CVMH model but better than the CVMS model, two popular community models used in seismic hazard estimates. Similarly, Ajala and Persaud, 2022 show that in contrast to the CVMH hybrid models produced by embedding high-resolution basin models into the community model, most CVMS hybrids do not produce better matching ground motions. We attribute the underestimation of ground motions in numerical simulations for downtown Los Angeles to the inaccuracy of the community velocity models in the SG and SB basins as this area is not as well constrained as the Los Angeles basin where dense industry array data and borehole measurements are more readily available.

The community model (CVMS) in this region has evolved over several generations, with the earliest version of the CVMS model comprised of rule-based basin models constrained by empirical equations and a few well logs (H. Magistrale, 2000). In the subsequent versions, a geotechnical layer was incorporated, and full waveform inversion was introduced into the model. However, due to the limited number of broadband stations deployed in the SG and SB region (black triangles in Fig. 5.1), the modification of the CVMS model through the different versions is small in this area, and the final version of the CVMS model (CVMS 4.26) retains the original CVMS model's primary characteristics from the geology and borehole dataset. In order to better constrain the velocity model in the SG and SB area, we deployed a set

of linear dense nodal arrays, and combine the ambient noise cross-correlation in this study with basin depths derived from the receiver function technique applied to this dataset, along with the Bouguer gravity anomaly and borehole datasets to construct a new shear wave velocity model. In the past few decades, the ambient noise technique has been widely applied to construct velocity models. With a homogeneous ambient noise source distribution, the cross-correlation of the ambient noise signal from two stations can provide the surface wave Empirical Green's Functions (EGF), in the causal (t>0) and anti-causal (t<0) sense, between the two stations(Sanchez-Sesma, 2006; Snieder, 2004). The correlation of different receiver components generates different surface wave EGF: the Rayleigh wave in the vertical (Z) and radial (R) components and the Love wave in the transverse (T) component (Fan-Chi Lin, Moschetti, and Ritzwoller, 2008). In this study, we extract Rayleigh wave EGF from ZZ correlation, and Love wave EGF from TT correlation. With the surface wave EGF's, group and phase velocity dispersion curves can be measured(Yao, Der Hilst, and De Hoop, 2006), which allows tomographic phase and group velocity maps to be constructed (Herrmann, 2013). These are then used to invert for shear wave velocity, Vs. Compared to the crustal-scale survey using the long-period ambient noise correlation between broadband stations, the surface wave EGF in high-frequency ambient noise correlation is less coherent due to the greater structural variations in sedimentary basins. In recent years, the deployment of dense seismic arrays makes it possible to resolve the fine-scale velocity structure of the top 5 km sedimentary layer (Castellanos and Robert W. Clayton, 2021; Jia and Robert W. Clayton, 2021; Fan-Chi Lin, D. Li, et al., 2013). In addition to the ambient noise correlation, receiver functions are also computed from the dense array datasets to constrain the basement depth within the sedimentary basins (Ma, Robert W. Clayton, and D. Li, 2016; Liu, Persaud, and Robert W. Clayton, 2018; Wang et al., 2021). Receiver functions using our linear dense arrays data have shown a coherent converted phase at the basin bottom can be observed in the SG and SB area, which provide an independent constraint on the basin structure in this area (Liu, Persaud, and Robert W. Clayton, 2018; Wang et al., 2021).

In this study, we construct a shear wave velocity model in the SG and SB area using 10 linear dense array datasets together with broadband stations and accelerometers. We correlate the vertical (ZZ) and transverse component (TT) ambient noise recordings to obtain Empirical Green's Functions and perform a dispersion analysis to extract the group and phase velocities. We developed a method to separate Rayleigh wave modes in the dispersion analysis based on the Rayleigh wave particle motion. Our Vs

model incorporates both group and phase velocity tomographic maps and starts with an initial model constrained with receiver functions, Bouguer gravity, and borehole data. We finally compare our Vs model with previous studies and the community velocity models.

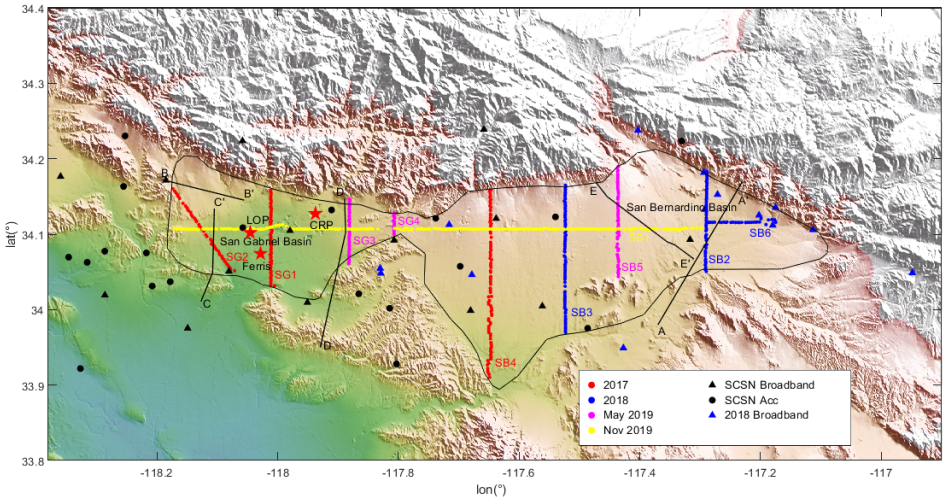

Figure 5.1: Distribution of BASIN nodal arrays (colored dots), broadband stations (black and blue triangles), and SCSN accelerometers (black dots). Color represents the deployment time for the temporary node stations. Black triangles are the permanent Southern California Seismic Network (SCSN) stations. Black lines (AA' to EE') are geological cross-sections, and red stars in the San Gabriel basin are boreholes with well logs used in this study.

5.3 Data

The dataset is made up of three different types of seismograms: 1) the temporary linear dense Basin Amplification Seismic Investigation (BASIN) nodal arrays, 2) permanent and temporary broadband stations and 3) strong-motion accelerometers. The distribution of the stations is shown in Figure 5.1. Between 2017 and 2019, 10 linear dense BASIN nodal arrays (SG1 to SG4, and SB1 to SB6) were deployed in the San Gabriel and San Bernardino basins during four deployment periods. The dense arrays consisted of lines with 14 to 260 Fairfield ZLand nodes with a standard 5 Hz 3-component geophones spaced 250 m apart. Each of the dense arrays was deployed for approximately one month. The broadband stations dataset includes the permanent Southern California Seismic Network (SCSN) stations and 14 temporary broadband stations deployed in 2018, indicated with triangles in Figure 5.1. In this study, we use the passive ambient noise method on the combined dataset, to extract

the EGF and with this construct a three-dimensional Vs model.

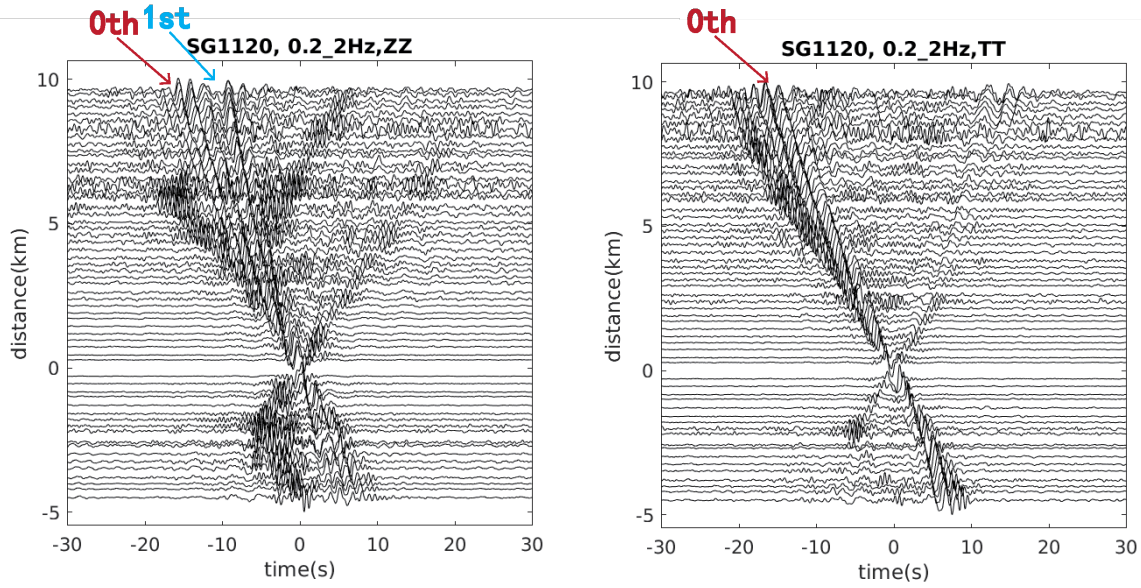

Figure 5.2: Intra-array correlation function from the SG1 dense linear array. a. The ZZ component depicts Rayleigh waves. b. The TT component with virtual source SG1120 shows Love waves. Correlation functions are filtered between 0.2 and 2 Hz.

5.4 Method

Ambient noise correlation

To estimate the shear wave velocity, we first determine the EGF between each pair of station using ambient noise correlations. The noise correlation follows the technique described in Bensen et al., 2007 and Jia and Robert W. Clayton, 2021. To reduce the influence of anthropogenic noise, we correlate only the nighttime (8:00 pm to 8:00 am, local time) ambient noise. We include all the possible ray pairs, including node to node, node to broadband, and node to accelerometer, that have overlapping recording times. The data are correlated in one-hour segments and stacked to get the final correlation. To minimize the effect of earthquakes and broaden the effective period range, we do time domain normalization and spectral whitening prior to the correlation. For the node-to-node correlation, as the stations of every pair have the same instrument response, it cancels out in the spectral whitening, and therefore the removal of the instrument response was not required in our case. For the node-to-accelerometer correlation, we will show that a $-\pi/2$ and $\pi/2$ phase shift is introduced because of the difference in the instrument response, and special care should be taken when stacking the causal and anti-causal branches of the correlation

function (Appendix A). As all of our stations are 3-component, we can extract both Rayleigh and Love waves. We rotate the components from the ZNE into the ZRT coordinate system. The Rayleigh wave particle motion is in the RZ plane and the Love wave particle motion is mainly in the T direction, and hence we correlate the Z components of the virtual source and virtual receiver, called the ZZ correlation, to get the Rayleigh wave EGF, and use the TT correlation to get Love wave EGF. In Figures 5.2 and 5.3, we show examples of the ZZ and TT correlations and ZZ dispersion curves for SG1 using station 120 as a virtual source and all stations in the SG1 line as virtual receivers. From both the Love (TT) and Rayleigh (ZZ) waves we can see two consistent dispersive fundamental modes in the t > 0 and t < 0 domain, as well as first-higher-mode Rayleigh waves. Some high frequency scattered waves are also present in the correlation functions, which interfere with the direct wave EGF signals in some cases.

Group Velocity Dispersion Picking

Our method for picking the surface wave dispersion curve from the EGF is modified from (Yao, Der Hilst, and De Hoop, 2006). We first fold the correlation function at t=0. When both the virtual source and receiver are the same type of sensor, the causal (t >0) and anti-causal (t <0) branches are symmetric, and we therefore add the two branches to enhance the signal. For velocity sensors (i.e., nodes) to accelerometer correlations, due to the phase difference in the instrument response, we subtract the causal branch from the folded anti-causal branch. Details on the derivation of this approach are provided in Appendix A. Next, we apply the Hilbert transform to a set of frequency bands (0.5-3 s) to obtain the signal envelope in terms of period, T. In Figure 5.3a, we show an example of the group velocity dispersion picking, where the signal envelope function is color-coded in the frequency (period) and group slowness (u=t/d) domain. A typical group velocity dispersion curve is picked along the peak of the envelope, which is usually continuous. Solid lines in Figure 5.3a show the dispersion curve picks for the fundamental model (red) and first higher mode (blue). However, the picking of the group velocity dispersion curve with this method is sometimes ambiguous for two main reasons: 1) When the fundamental mode is close to the higher mode, different modes may interfere with each other and the different modes cannot be separated based on the envelope alone. 2) The envelope pattern is sometimes discontinuous, e.g., the higher mode in Figure 5.3a in the period range between 1.5 s and 4 s. In order to distinguish between the fundamental mode and the first higher mode Rayleigh wave, we developed a

new technique based on the polarization of particle motion. For the Love wave, the higher mode is substantially weaker than the fundamental, therefore we only extract its fundamental mode dispersion curves.

Rayleigh Wave Mode Separation

Our identification of Rayleigh wave modes is based on the particle motion of the waves. For the fundamental mode, the Rayleigh wave particle motion is typically retrograde, while the Rayleigh wave first higher mode is prograde. The retrograde and prograde particle motions reflect the phase lag between the Z and R components. For retrograde motion, the R component is T/4 ahead of the Z component, and for prograde, it is T/4 behind. For the ambient noise correlation, the phase difference between ZZ and ZR is the same as the phase difference between Z and R (Appendix B), so the relationship between ZZ and ZR reflects the polarization of the Rayleigh wave particle motion in the same way. In a previous study, Ma, Robert W. Clayton, and D. Li, 2016 have shown that in the sedimentary basin the ZZ and ZR correlation show consistent retrograde fundamental mode and prograde first higher mode. Here we present a quantitative way of measuring the particle motion using the Continuous Wavelet Transform (CWT)

$$W_x(s,n) = (\frac{\delta t}{s})^{(1/2)} \sum_{n'=1}^{N} x_{n'} \Phi_0^*[\frac{(n'-n)\delta t}{s}] \tag{5.1}$$

Where Φ_0^* is the wavelet function (Torrence and Compo, 1998), s is the wavelet scale, and δt is the time step. As with the Fourier transform, the variation of s gives a spectral pattern in the frequency domain, but the wavelet transform also has an additional dimension, n that reflects the temporal variation. The wavelet transformation has been proven to be a powerful technique to monitor temporal variation in the coda with high precision (Mao et al., 2020). Here, we use it to evaluate the phase difference between the ZZ and ZR correlations, and when combined with the the Hilbert transform it produces a clear separation of the fundamental from the first higher mode. We apply the CWT using the Matlab Wavelet Toolbox with the Morse wavelet function Φ_0^*. The phase difference between the ZR and ZZ correlations is $\delta = arg(W_{ZR}(s,n)) - arg(W_{ZZ}(s,n))$. For a retrograde fundamental mode, this is $\pi/2$. In contrast, for the prograde first-higher mode $\delta = -\pi/2$. We plot $\sin\delta$ in Figure 5.3b to quantify the polarization of particle motion in the group slowness and period domain, where red and blue are positive ($\delta = \pi/2$) and negative ($\delta = -\pi/2$) phase shifts, respectively, corresponding to retrograde and prograde particle motion. However, as the $\sin\delta$ pattern only represents the phase difference,

noise and signal are not distinguishable in this representation. To combine the amplitude and phase information, we multiply the wave envelope from the Hilbert transformation (Figure 5.3a) and the sinδ from the wavelet transformation (Figure 5.3b) to produce the result shown in Figure 5.3c. In Figure 5.3c, red representing the retrograde fundamental (sinδ = 1) mode and blue representing the prograde first higher mode (sinδ = -1) are clearly separated, and the picking of the Rayleigh wave group velocity dispersion curve is based on this pattern. We test our method with a published correlation function (G. Li et al., 2016), which is shown in the supporting information Figure 5.5.

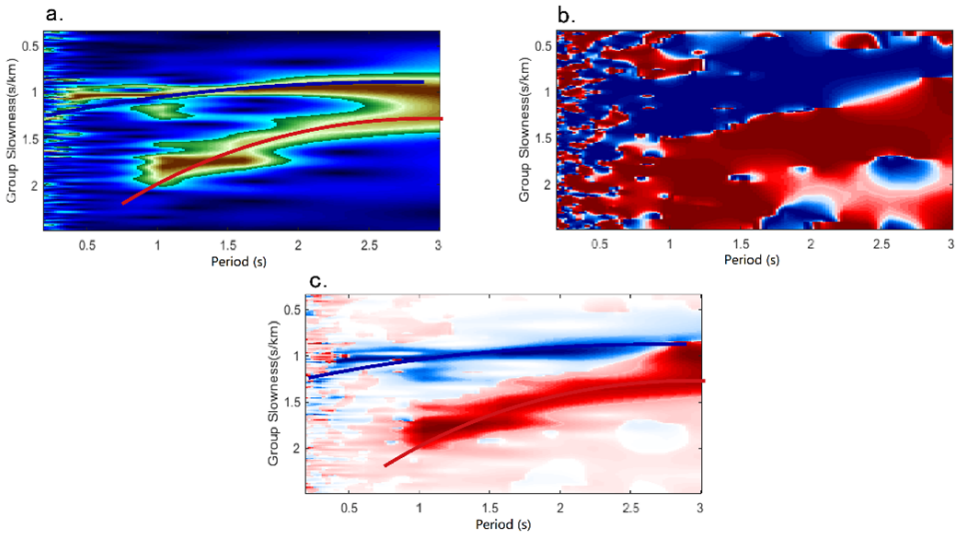

Figure 5.3: An example of Rayleigh wave group velocity dispersion analysis in the frequency-time domain. a. Hilbert transform of the ZZ correlation function. b. Phase difference δ between ZR and ZZ from the Wavelet transform. Red for δ between [0, π], retrograde particle motion. Blue for δ between [-π, 0], prograde particle motion. c. Combination of a and b. Red and blue lines are inferred retrograde fundamental mode and prograde first higher mode dispersion curves, respectively. The correlation is from station pair SG102-SG160.

Tomography

With the measured dispersion curves, we applied the straight-ray tomography method to invert the frequency dependent group velocity maps. We discretize the area into a uniform grid with 0.55 km longitudinal spacing and 0.66 km latitudinal spacing. The group velocity tomography is carried out between 0.5 s and 3 s period, using the travel times from the dispersion curves. Figure 5.4 shows

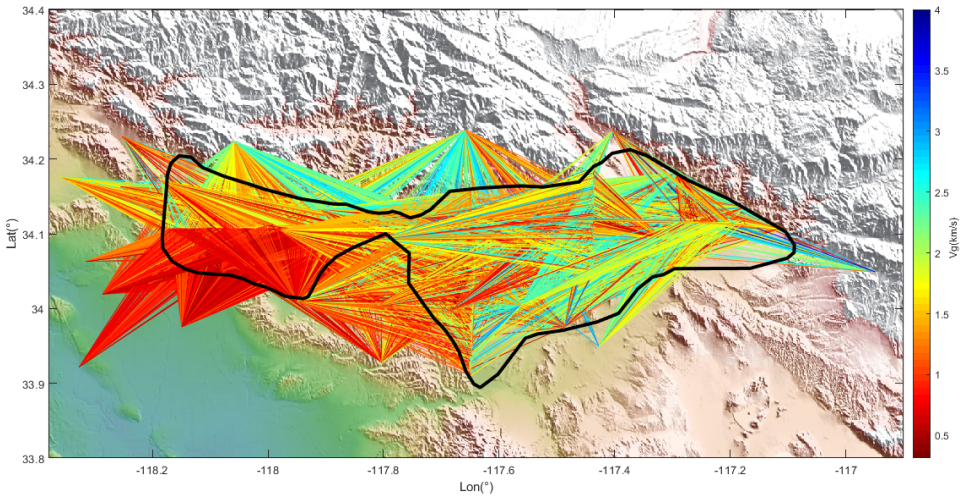

Figure 5.4: Ray coverage of the Rayleigh wave fundamental mode group velocity at T=1s. The rays are color-coded by picked group velocity.

an example of the straight ray coverage of group velocity at period T=1s, where the picked group velocity is color-coded. We evaluate the azimuthal ray coverage of every grid cell following Ekström, 2006, and the grid cells with low azimuthal ray coverage (i.e., low reliability) are eliminated by replacing the velocities in such grid cells with Nan values. We apply damping and smoothing in the inversion through regularization $|Gm - d|^2 + \alpha|m|^2 + \beta|Lm|^2$, where m the slowness vector, d the travel time and G the matrix connecting velocity with travel time, and L the Laplacian operator. α and β are the damping and smoothing coefficient, which are equal to 10 and 20, respectively, in our model. Our primary Vs model is generated by conducting 1D surface wave inversion on the dispersion curves of every pixel from the group velocity tomography, then evaluating the reference phase velocity from the primary Vs model for the subsequent phase velocity dispersion picking.

Phase Velocity Picking

We measured the phase velocity as an additional constraint for our Vs model in addition to the group velocity. We followed the method in (Yao, Der Hilst, and De Hoop, 2006) for the single-station-pair phase velocity dispersion measurement. Because of the relatively high-frequencies and large degree of lateral heterogeneity in the basins, an accurate reference phase velocity model is essential for the phase velocity dispersion picking. With a prior reference phase velocity model from the primary Vs model derived using only group velocity dispersion curves (red line in

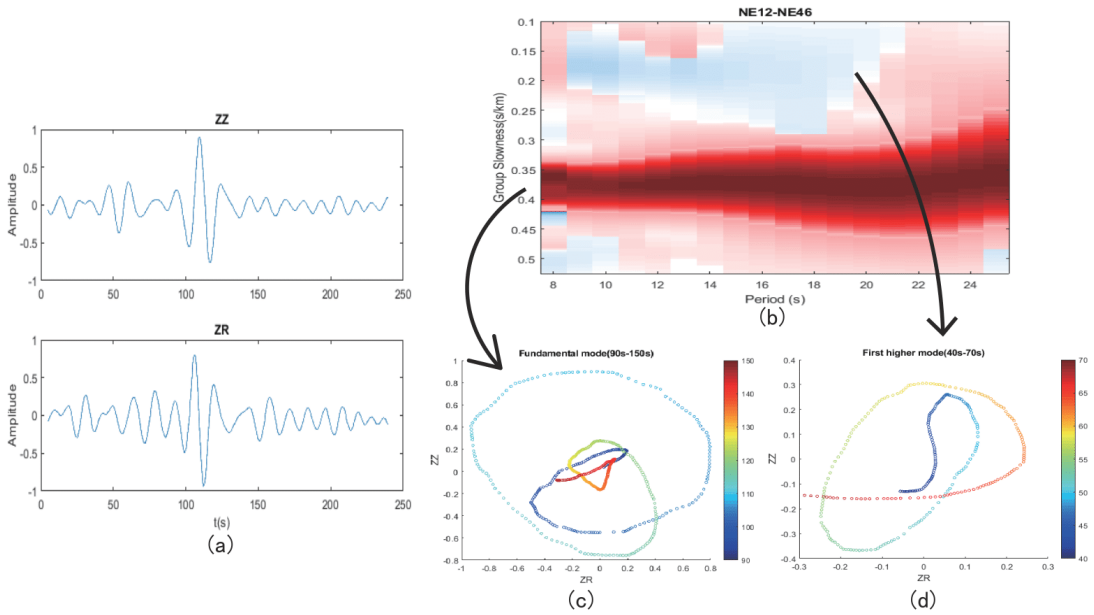

Figure 5.5: a. ZZ and ZR ambient noise correlation functions from G. Li et al., 2016. b. The Hilbert-wavelet transformation of a. c. and d. the particle motion of the blue and red parts of (b). In c and d, the time of the particle motion is color-coded, from blue (t = 0) to red.

Figure 5.6), we measure the phase velocity fundamental mode dispersion curves for every available station pair (Figure 5.6). Rayleigh wave and Love wave fundamental mode phase velocity are measured from ZZ and TT correlation, and phase velocity tomography is conducted in the same way as the group velocity. The final inversion for the Vs model incorporates both phase and group velocity dispersion curves for both Rayleigh and Love waves.

Initial Vs Model

The inversion for the Vs model from dispersion curves is highly dependent on the initial model. We construct our initial model based on the prior basin depth (PBD) model from (Villa et al., 2023) shown in Figure 5.7. The PBD model integrates multiple observations including receiver functions, Bouguer gravity, and borehole data. The receiver function times from every linear array (Ghose, Persaud, and Robert W. Clayton, 2023; Liu, Persaud, and Robert W. Clayton, 2018; Wang et al., 2021) are used to constrain the depths to the sediment-basement interface beneath the linear dense arrays, and the Bouguer gravity is used to extrapolate the receiver function constraints along the seismic profiles into a 3-D model. Times are converted

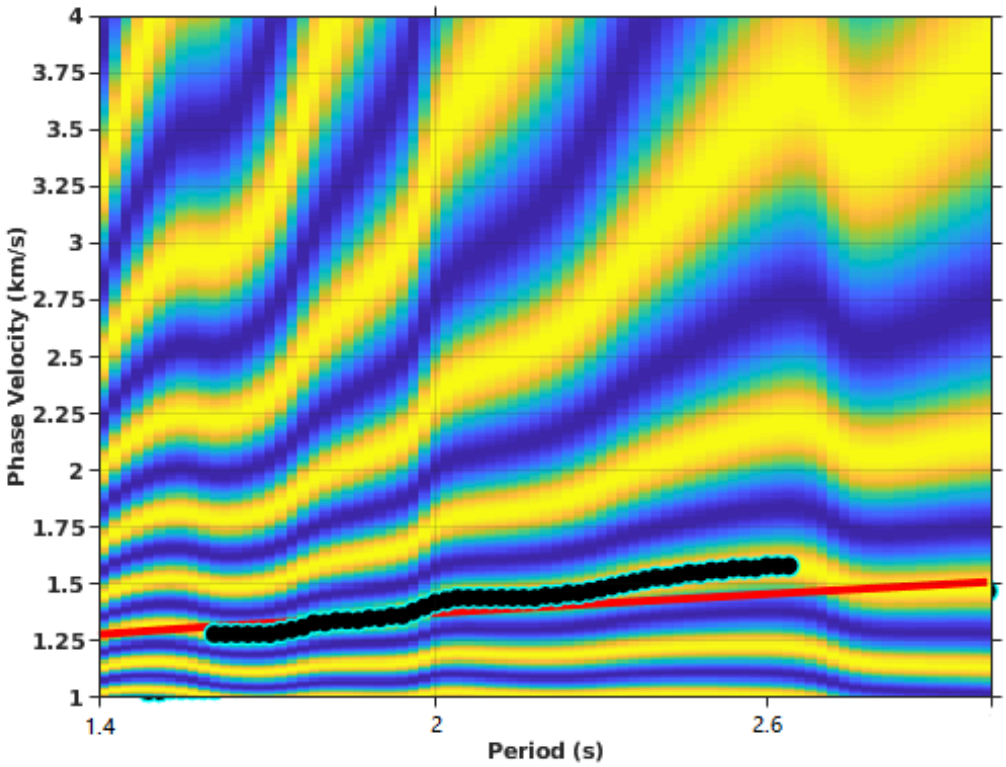

Figure 5.6: An example of phase velocity dispersion picking. The red line is the reference fundamental mode phase velocity evaluated from the group velocity model. The black dots are the picks.

to depths using our VS model. Data from 17 boreholes are also used to calibrate and validate the 3-D basin depth model. A detailed description of the methods for integrating the receiver function, gravity and borehole data are given in Villa et al., 2023. The initial VS model increases linearly with depth, from 0.3 km/s at the surface to 2.3 km/s at the basin bottom defined by PBD. In addition, the prior model also contains a low-velocity zone. The low-velocity zone is a prominent feature in the San Gabriel basin, associated with the shallow marine Fernando Formation (Thomas M. Brocher et al., 1998; West et al., 1988). The CVM-S 4.26 model (Lee et al., 2014) inherits the low-velocity feature from the CVMS1-3 models (Kohler, H. Magistrale, and R. W. Clayton, 2003; Harold Magistrale, McLaughlin, and Day, 1996) in which the SG area is based on borehole data and geological models. We preserve these low-velocity features present in the CVM-S 4.26 model as a prior feature in our initial model. In the PBD model, the conversion from travel time to depth is based on the velocity model, and the Vs model is dependent on the PBD

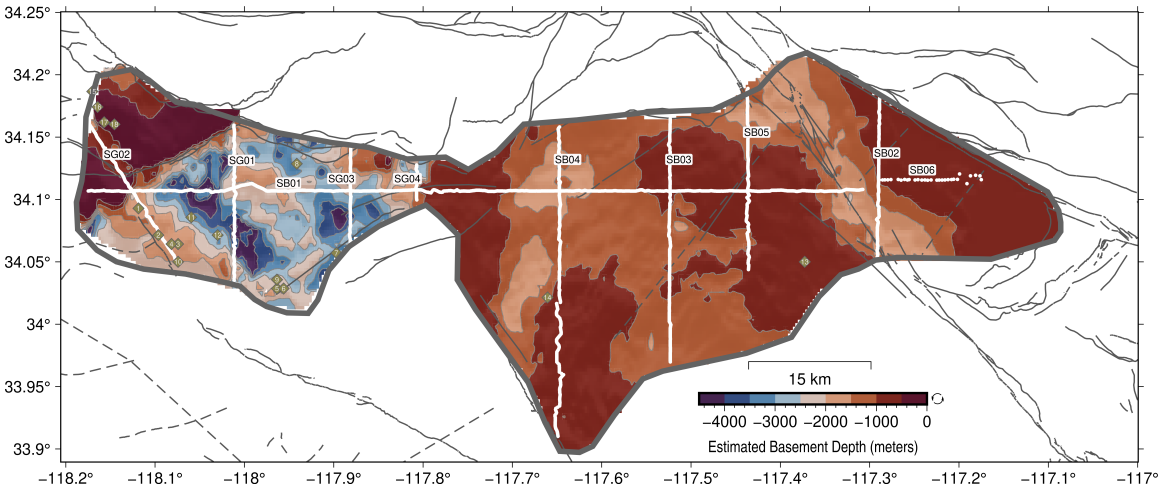

Figure 5.7: Color-coded background map is the prior basin depth model from (Villa et al., 2023). White lines are the nodal arrays. Numbered green diamonds are boreholes.

model through the initial model. We iterate over the PBD model and the Vs model until the Vs model converges.

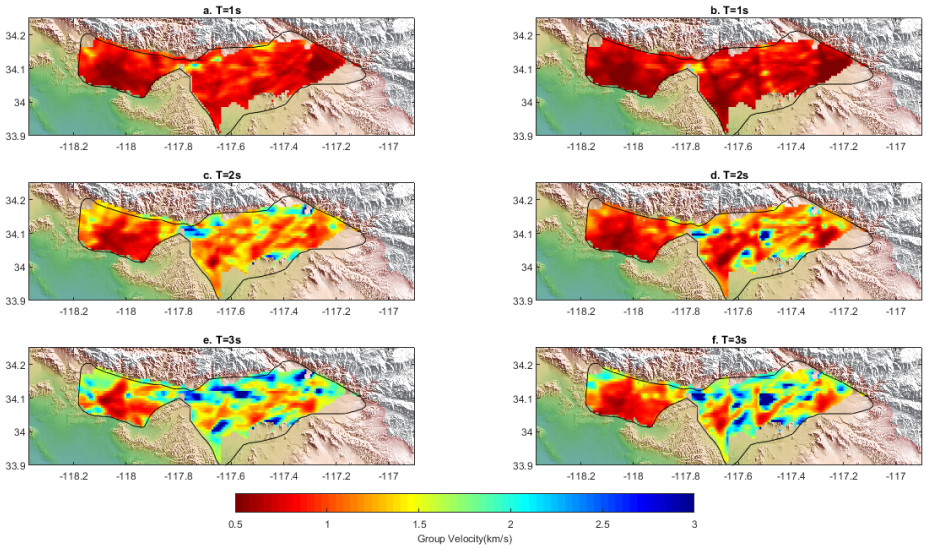

Figure 5.8: Group velocity maps for Rayleigh wave (a, c, e) and Love wave (b, d, f) at periods of 1, 2, and 3 s.

Vs Model

With the Rayleigh wave and Love wave dispersion maps (Figure 5.8), we conduct the 1D S wave velocity inversion from the dispersion curves for each grid point

using the SURF96 software (Herrmann, 2013). As mentioned above, the initial model is a linear velocity model defined by the PBD model, with a 50 m thick layer above the PBD and a homogeneous half space below. The Rayleigh and Love waves are used separately to invert for V_{SH} (Figure 5.9) and V_{SV} (Figure 5.10), and we use the radial anisotropy, γ to address the difference between VSV and VSH, with $\gamma = 2(V_{SH} - V_{SV})/(V_{SH} + V_{SV})$ (Figure 5.12) (Jaxybulatov et al., 2014). The final Vs model incorporates the phase and group velocities of Rayleigh (ZZ) and Love (TT) waves, reflecting an average of V_{SH} and V_{SV}. As the PBD model can extend beyond the sensitivity of the dispersion curves, the cutoff depth of the model is either defined by the PBD or the depth where the sensitivity kernel is below 0.02. We then merge our final Vs model on top of the CVMS 4.26 model in the region defined by the cutoff depth: the Vs above the cutoff depth is from our Vs model, and deeper than 1 km below the cutoff depth, the Vs is taken from the CVMS 4.26. Within the 1 km zone below the cutoff depth, we use a linear weighting function to smooth the transition from our Vs model to the CVMS 4.26.

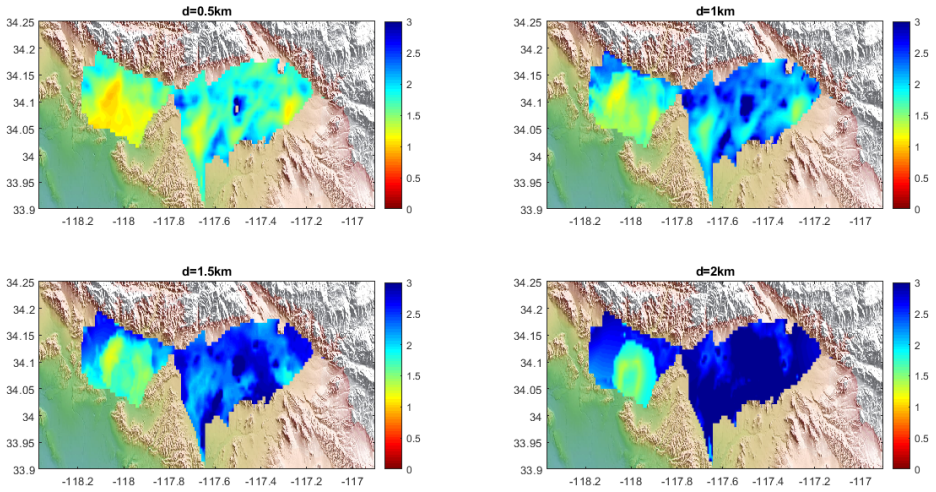

Figure 5.9: V_{SH} inverted from Love wave tomography at depths of 0.5, 1, 1.5, and 2 km.

5.5 Results

We show the group velocity maps of the fundamental Rayleigh (Figure 5.8.a, c, e) and Love (Figure 5.8.b, d, f) waves at periods of 1, 2, and 3 s. The group velocity at different periods is sensitive to different depths, and T = 1, 2, 3 s have a typical sensitivity kernel covering 0-1 km, 0-1.5 km, and 0-2.5 km depths, respectively.

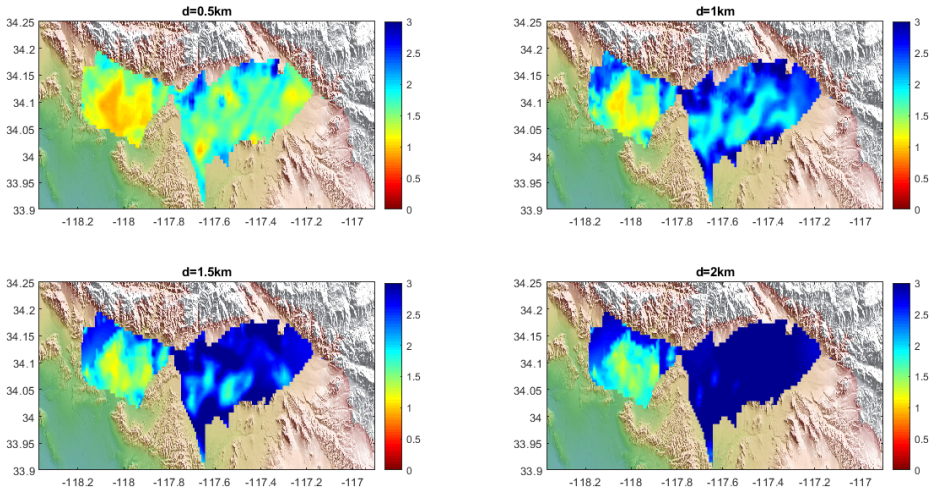

Figure 5.10: V_{SV} inverted from Rayleigh wave tomography at depths of 0.5, 1, 1.5, and 2 km.

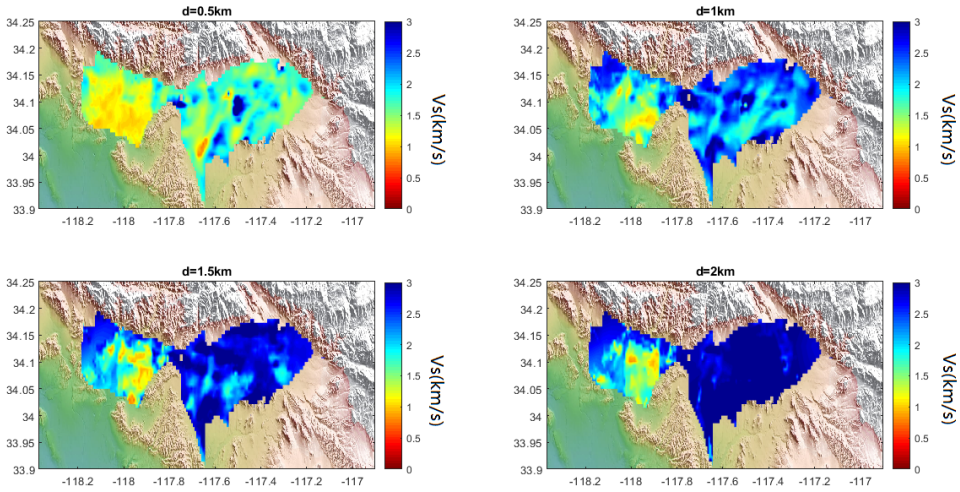

Figure 5.11: Vs model at the depths of 0.5, 1, 1.5, and 2 km.

To test the validity of the straight ray group velocity tomography, we evaluate the Eikonal arrival time along the west-east trending SB1 line using the determined group velocity model (Fan-Chi Lin, Ritzwoller, and Snieder, 2009; Qiu, Fan-Chi Lin, and Ben-Zion, 2019; White et al., 2020; Zhang et al., 2021), and the predicted travel times at different frequencies show consistency with the correlation function (Figure 5.13, 5.14, 5.15). The ray paths from the Eikonal method indicate curving of ray paths occurs when large lateral variations are present, but the curving is not

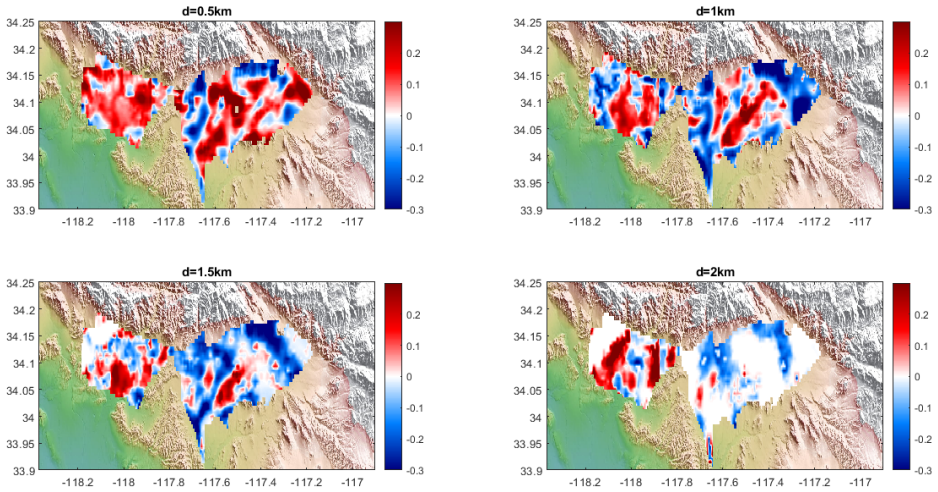

Figure 5.12: Radial anisotropy at depths of 0.5, 1, 1.5, and 2 km.

severe with limited distance (Figure 5.16). Although the curved Eikonal ray paths have longer travel distances compared to the straight ray path, the Eikonal ray path are drawn towards areas of higher velocity, resulting in higher average velocity along the path. As a result, the actual travel times between these two ray paths are similar, though a relatively big difference may occur at the edge of the basin where the velocity variation is relatively large (Figure 5.16). The group velocity dispersion is independent of the PBD model, reflecting features derived purely from the ambient noise data. Despite the large spatial variations, we see several features consistent with the PBD model. In the San Gabriel basin, a prominent low-velocity region from 1 to 3 s indicates a sedimentary basin with over 2.5 km depth. To the northwest of the San Gabriel basin, a sharp increase of group velocity for $T > 1$s, indicates a transition from the 2.5 km deep San Gabriel basin to the shallower Raymond basin (< 1 km depth) near the Raymond fault. In the San Bernardino area, the group velocity map is more complex, but prominent features are evident, such as the Chino basin in the west and the San Bernardino basin in the east with relatively low group velocities, and the Jurupa Hills in the central-southern region with high group velocities. The shear wave velocity (V_S) model is shown in Figure 5.11 at depths of 0.5, 1, 1.5, and 2 km. The spatial distribution of the low VS regions (sedimentary basins) is similar to the group velocity maps, and variations of maximum depth within the sedimentary basins can be inferred from the VS model: the Raymond basin is less than 1 km deep, the San Gabriel basin is deeper than 2 km, the Chino basin is around 1 km deep, and the San Bernardino basin is between 1 km and 2 km

deep. In addition to the ambient noise data, the VS model is also dependent on the PBD model. In the following section, we discuss and compare the VS model with the PBD model, as well as other basin depth models from geological cross-sections, other geophysical constraints, and borehole data. V_{SH} and V_{SV} are inverted in the same way as the V_S model but only using either the Love or Rayleigh wave group velocities. The cutoff depth of V_{SH} and V_{SV} is thereby determined by the Love and Rayleigh wave sensitivity kernels, respectively. The radial anisotropy (Figure 5.12) representing the difference between V_{SH} and V_{SV}, is overall positive (10% 20%) in the San Gabriel and central part of San Bernardino basin, reflecting the fact that the SH wave is overall slower than the SV wave. In some areas like the northern Chino basin and northern San Bernardino basin, the radial anisotropy is unrealistically low (-30%). As the anomalously low anisotropy areas are mainly located at the edge of the basins, where the ray coverage is sparser, the radial anisotropy in those areas likely does not reflect the real anisotropy. Besides, the V_{SH} and V_{SV} are embedded on top of the CVMS based on the Rayleigh and Love wave sensitivity kernels and the Rayleigh wave typically has a deeper sensitivity kernel than Love wave. Hence, the measured radial anisotropy may represent the difference between V_{SV} and the underlying CVMS model instead of the V_{SH}.

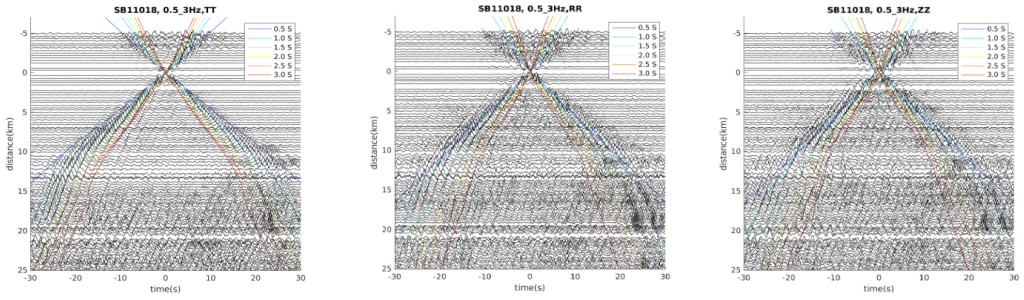

Figure 5.13: Intra-array TT, RR, and ZZ correlation functions from the SB1 dense linear array using SB1-1018 as a virtual source. Colored lines are Eikonal travel times from the group velocity map at different frequencies (color-coded by period).

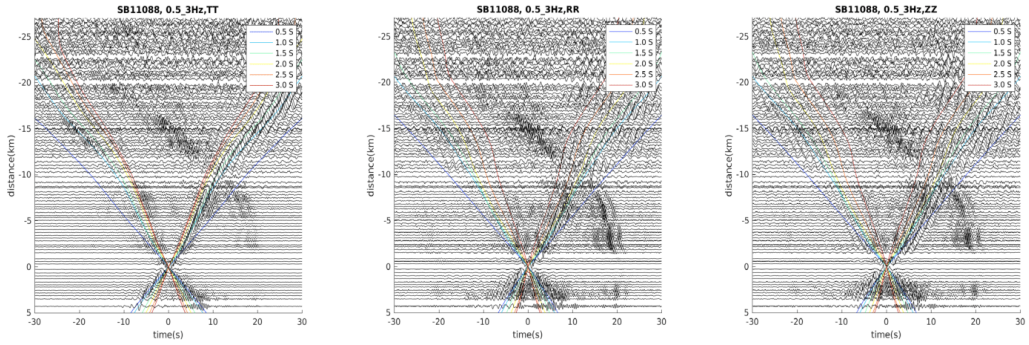

Figure 5.14: Intra-array TT, RR, and ZZ correlation functions from the SB1 dense linear array using SB1-1088 as a virtual source. Colored lines are Eikonal travel times from the group velocity map at different frequencies (color-coded by period).

5.6 Discussion

In this section, we compare our V_S model to several other independent observations to validate the robustness of the V_S model. The location of five cross-sections (black lines, AA' to EE') and three sonic boreholes well logs (red stars) are shown in Figure 5.1. The five cross-sections were analyzed in previous studies: AA' through the San Bernardino basin is from Stephenson et al., 2002, BB' is the cross-section in the Raymond basin from Buwalda, 1940, CC' and DD' are cross-sections 14 and 15 in the San Gabriel basin in Davis and Namson, 2017; *Southern California Cross Section Study Map Showing 2012 AAPG Annual Mtg Field Trip Stops* 2013 and EE' is the cross-section in Rialto-Colton basin from Paulinski, 2012; Woolfenden and Kadhim, 1997. The comparison of our Vs model with the PBD model (dashed lines) and models from other references (dotted lines) is shown in Figure 5.17. In the San Bernardino basin, the structure between 10 and 20 km distance along the AA' profile was consistently constrained by seismic reflection data and gravity-aeromagnetic modeling (Stephenson et al., 2002). From south to north along AA', the sedimentary basin depth increases sharply to 1.7 km near the San Jacinto fault (12 km from A) and slowly decreases after passing the Loma Linda fault (14 km from A). In our V_s model, a low-velocity structure shows good correlation with the basin model from Stephenson et al., 2002, both laterally and in-depth. The Raymond

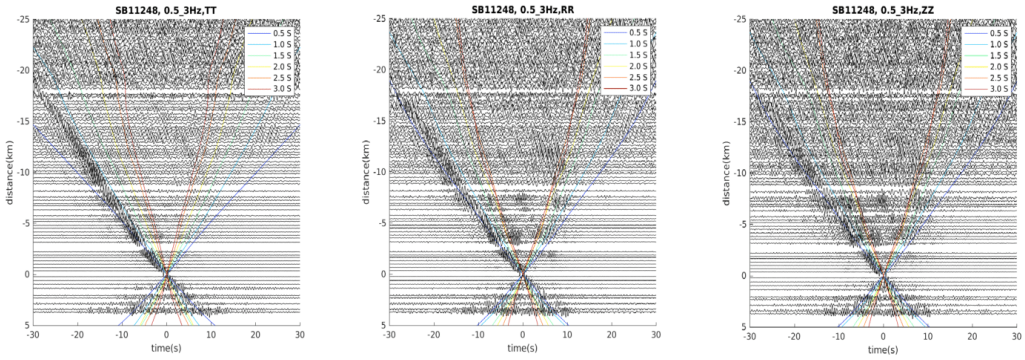

Figure 5.15: Intra-array TT, RR, and ZZ correlation functions from the SB1 dense linear array using SB1-1248 as a virtual source. Colored lines are Eikonal travel times from the group velocity map at different frequencies (color-coded by period).

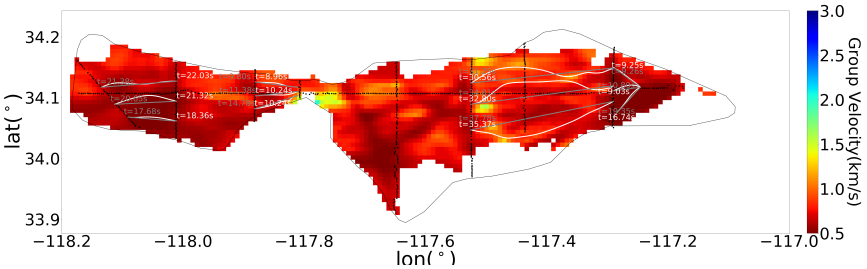

Figure 5.16: Ray paths (white curves) of the Love wave group velocity model at 1 s period from the Eikonal method. Gray straight lines represent straight ray path. Travel times of Eikonal ray path (white) and straight ray path (gray) are marked for comparison.

basin, bounded by the Raymond fault on the southeast, is a relatively shallow basin compared to the adjacent San Gabriel basin. Based on gravity and borehole data, the BB' cross-section (Buwalda, 1940) constrains the central Raymond basin depth to 1.5 km, slightly deeper than the low-velocity structure (1 km deep) from our Vs model. Across the Raymond fault, the PBD model reveals a sharp transition from the 1 km deep Raymond basin to the 3 km deep San Gabriel basin, consistent with the conspicuous reduction of group velocity at the Raymond fault, which creates a sudden deepening of the low-velocity layer in the Vs profile at a distance of 16

km in BB' profile. The CC' and DD' profiles (Davis and Namson, 2017; *Southern California Cross Section Study Map Showing 2012 AAPG Annual Mtg Field Trip Stops* 2013) constrain the depths and shapes of the western and eastern San Gabriel basin. In the CC' profile, the low-velocity layer shows a sharp decrease at 8 km from the start of the profile, coincident with the Whittier fault that offsets the sedimentary layer and basement rock in the geologic cross-section. DD' is a cross-section in the eastern part of the San Gabriel basin. The profile is bounded by the Whittier fault to the south and the Sierra Madre fault to the north. The Vs model only captures the Sierra Madre fault at a distance of 22 km from the start of the profile, while in the south, the Whittier fault is located outside the Vs model coverage. The EE' profile cuts through the Rialto-Colton basin located northwest of the San Bernardino basin. In Figure 5.17e, the dotted line represents the base of the water-bearing layer (Paulinski, 2012; Woolfenden and Kadhim, 1997) from resistivity logs. Due to the limited borehole depth (<300 m), the base of the water-bearing layer (bedrock or consolidated deposits) is not necessarily equivalent to the sedimentary basin depth. Our velocity model overall predicts a low-velocity layer comparable to the water-bearing layer, but with a much larger variation in depth. However, the location of the Barrier J and (unnamed) fault Q (Anderson, Matti, and Jachens, 2004; Lu and Danskin, 2001) coincides with the boundary of the graben-like structure in our model. In the five cross-sections, AA' to EE', our V_S model agrees with the basin depth from other references, and the fault structures inferred from sharp lateral Vs gradients agree with the fault locations that offset the sedimentary layers.

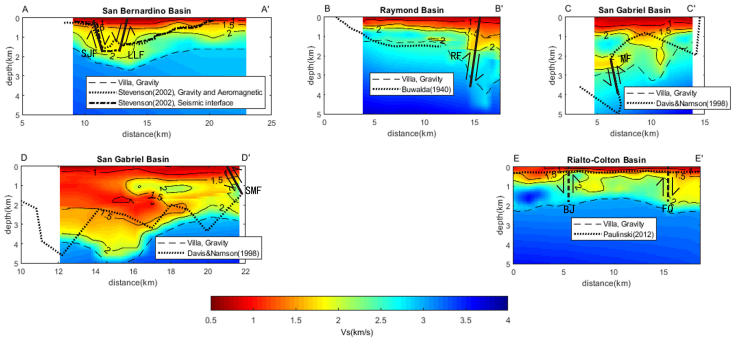

Figure 5.17: Cross-sections of Vs model compared against prior basin model (dashed line) and basin model constraint from other references (dotted line). Locations of the cross-sections are shown in Figure 5.1 with black lines. Abbreviations for faults: SJF-San Jacinto fault; LLF-Loma Linda fault; RF-Raymond fault; SMF-Sierra Madre fault; BJ-Barrier J; FQ- fault Q.

The radial anisotropy γ is derived from the difference between $V^{--}SH$ and V_{SV}

from the Love and Rayleigh wave respectively(Fig 5.12). In this area, the sedimentary basin structure varies greatly among different basins, leading to large lateral and vertical variation in radial anisotropy. We observe strong positive radial anisotropy in the San Gabriel basin and eastern part of Chino basin, indicating a well-stratified sedimentary layer (Backus, 1962). In the San Bernardino basin, the negative anisotropy highly correlates with the San Jacinto fault zone, indicating that the vertical cracking caused by the San Jacinto fault could be the potential source of the negative radial anisotropy (Jiang and Marine A. Denolle, 2022; Nakata and Snieder, 2012). Sonic velocities from well logs provides ground truth of the velocity structure of the sedimentary layers. We compare our Vs model in the San Gabriel basin to three available sonic well logs (Fig. 5.12), with the VS computed from the measured VP using an empirical relationship (T. M. Brocher, 2005). One prominent feature in the sonic velocity logs is the low-velocity zones in the Ferris borehole at 1800 m and in Live Oak Park (LOP) borehole at 1200 m depth (locations shown on Figure 5.1). The low-velocity layer is associated with the Fernando formation, a ubiquitous marine layer in San Gabriel and Los Angeles basins that underlies the non-marine Duarte Conglomerate (Yeats, 2004). As the earlier version of the CVMS model is constructed based on the geology (Harold Magistrale, McLaughlin, and Day, 1996) and the three borehole logs (H. Magistrale, 2000) in San Gabriel basin, and the current CVMS 4.26 Vs model (Lee et al., 2014) is developed with full waveform modelling using the earlier version as a starting model, it's not surprising that the CVMS 4.26 agrees well with the borehole velocity (Figure 5.27, dots vs. red curves). In our Vs model, the prior model is a linear model based on the PBD model with a low-velocity feature inherited from the CVMS 4.26 (Figure 5.27 dashed curves). Despite the large difference in the initial model, the final Vs model converges to the CVMS model and borehole data in the top 1 2 km, and the preservation of the low-velocity zone makes it consistent with the borehole data and CVMS 4.26.

Besides the incorporation of the low-velocity zone from the CVMS 4.26 model as a prior feature in the initial model used in our inversion, the construction of the Vs model is mainly based on the PBD model and the dispersion curves, both of which are independent of the CVMS model. We compare a set of the group velocity dispersion curves in the San Gabriel basin predicted from our Vs model to the CVMS model prediction (Fig. 5.18, 5.19, 5.20, 5.21). In the San Gabriel basin, both models predict slower group velocities in the south compared to the north, but overall, the dispersion curve generated from CVMS 4.26 is faster than

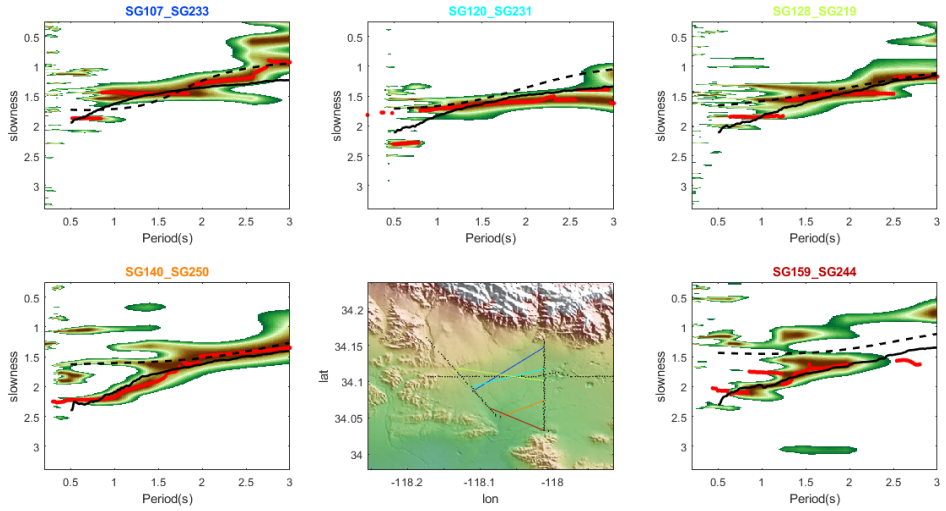

Figure 5.18: Love wave group velocity dispersion curves in the San Gabriel basin predicted by our model (black solid line) and CVMS model (black dashed line). The background is the envelope from the correlation function, and the red curves are the actual picks.

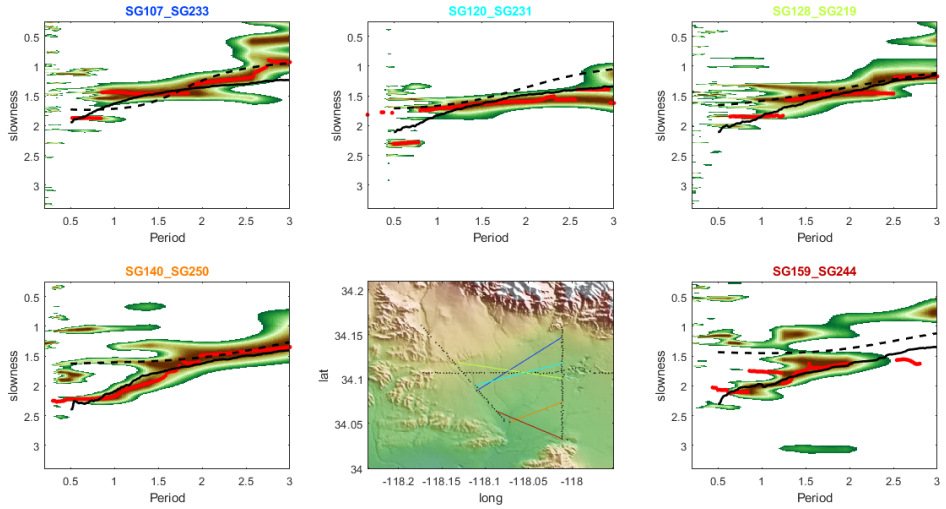

Figure 5.19: Rayleigh wave group velocity dispersion curves in the western San Gabriel basin (SG1-SG2) predicted by our model (black solid line) and CVM-S model (black dashed line). The background is the envelope from the correlation function, and the red curves are the actual picks.

our measured dispersion curves. In the San Bernardino basin, the CVMS 4.26 model's dispersion curves do not show much variation across the basin and is overall lower than the observed dispersion curve (Figure 5.22, 5.23, 5.24, 5.25).

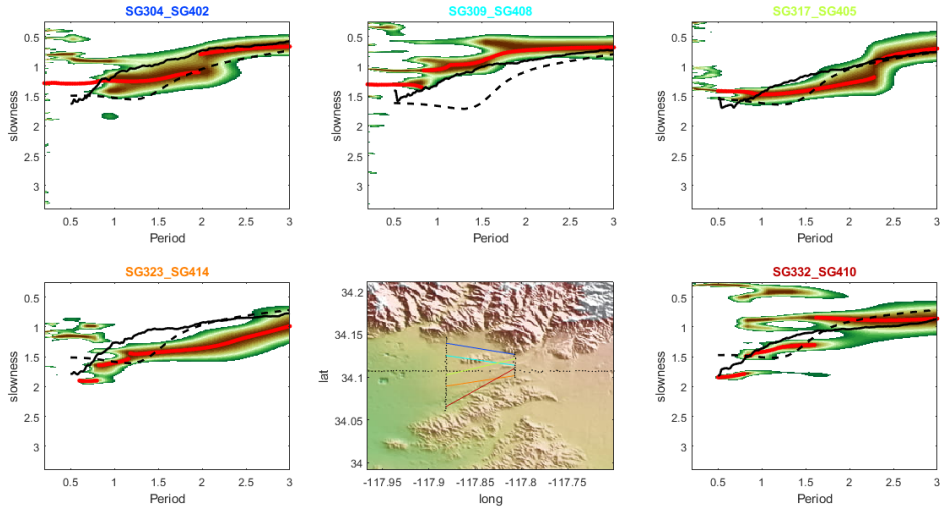

Figure 5.20: Love wave group velocity dispersion curves in the eastern San Gabriel basin (SG3-SG4) predicted by our model (black solid line) and CVM-S model (black dashed line). The background is the envelope from the correlation function, and the red curves are the actual picks.

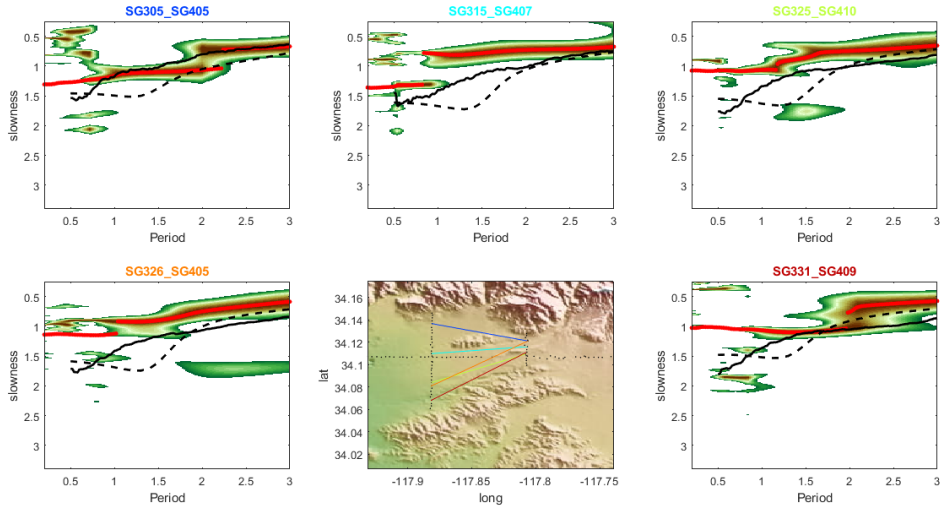

Figure 5.21: Rayleigh wave group velocity dispersion curves in the eastern San Gabriel basin (SG3-SG4) predicted by our model (black solid line) and CVM-S model (black dashed line). The background is the envelope from the correlation function, and the red curves are the actual picks.

Compared to the CVMS 4.26 model, our Vs model resolves the observed dispersion curves better in the San Bernardino basin. In the dispersion comparison (Fig 5.19, 5.20, 5.21, 5.22, 5.23, 5.24, 5.25), the model prediction does not always fit

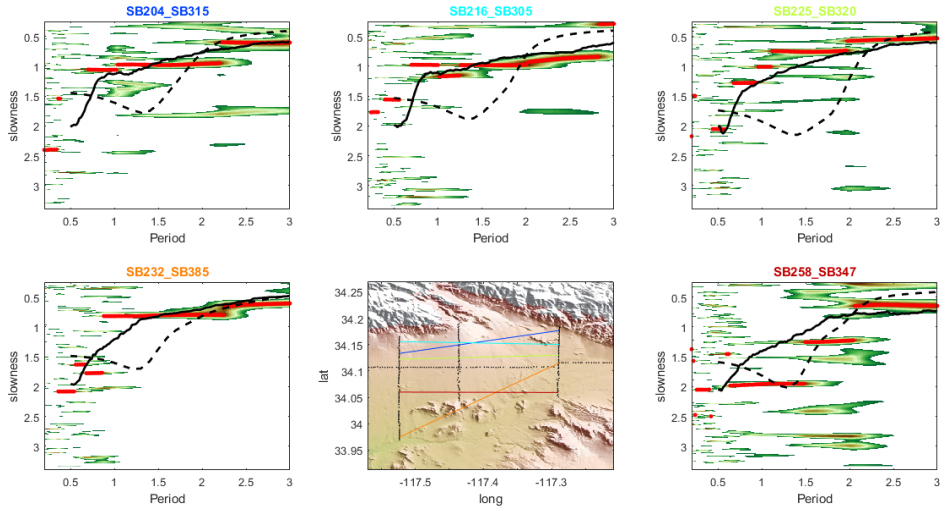

Figure 5.22: Love wave group velocity dispersion curves in the San Bernardino and Chino basins (SB2-SB3) predicted by our model (black solid line) and CVM-S model (black dashed line). The background is the envelope from the correlation function, and the red curves are the actual picks.

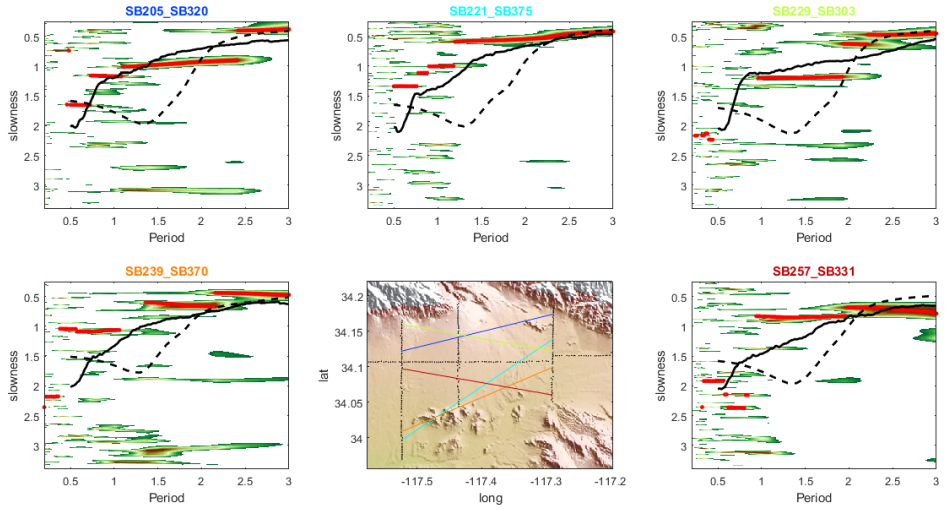

Figure 5.23: Rayleigh wave group velocity dispersion curves in the San Bernardino and Chino basins (SB2-SB3) predicted by our model (black solid line) and CVM-S model (black dashed line). The background is the envelope from the correlation function, and the red curves are the actual picks.

with the data. The uncertainty of the model may originate from a few aspects, including the insufficient ray coverage, inconsistent dispersion picking and violation of straight ray assumption. The checkerboard resolution tests (Fig 5.26) show

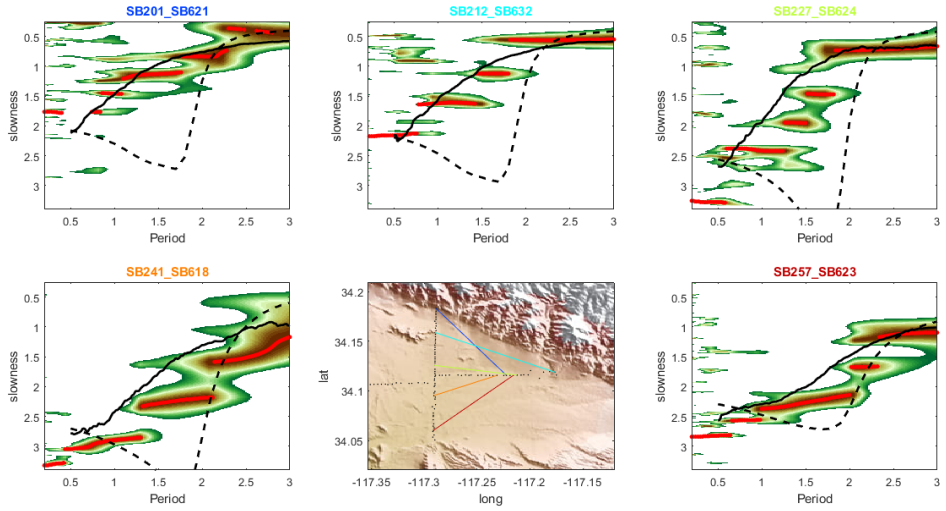

Figure 5.24: Love wave group velocity dispersion curves in the San Bernardino basin (SB2-SB6) predicted by our model (black solid line) and CVM-S model (black dashed line). The background is the envelope from the correlation function, and the red curves are the actual picks.

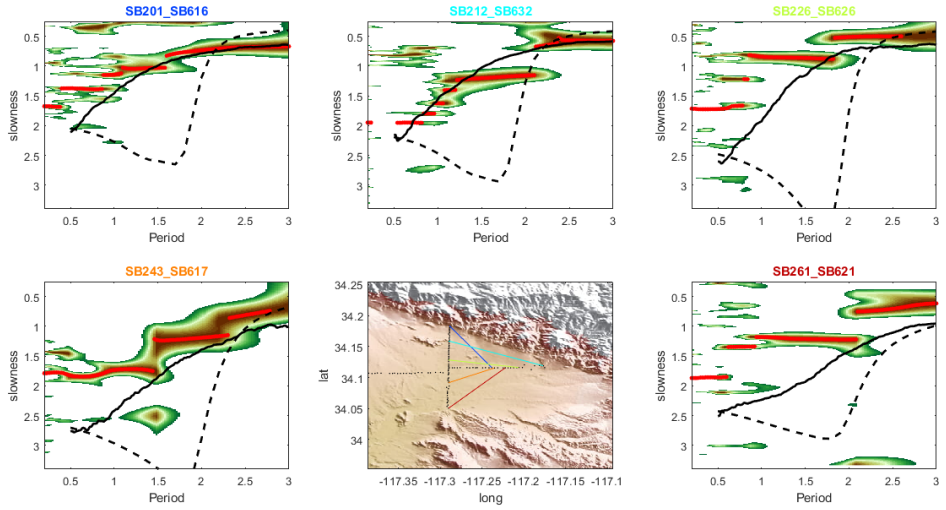

Figure 5.25: Rayleigh wave group velocity dispersion curves in the San Bernardino basin (SB2-SB6) predicted by our model (black solid line) and CVM-S model (black dashed line). The background is the envelope from the correlation function, and the red curves are the actual picks.

the ray coverages of Rayleigh and Love wave are overall good in the basin area (bounded by black curves in Fig 5.26). The inconsistency in dispersion pickings usually present in the correlation functions with the ray paths being either very long

or crossing the edge of the basins, which violates the assumption of a horizontal layered medium and the surface wave could interfere with the body wave (Ma, Robert W. Clayton, and D. Li, 2016). The violation of straight ray path has been discussed in the previous chapter, and we conclude that the violation mainly occurs at the basin edge where the velocity has a large lateral variation.

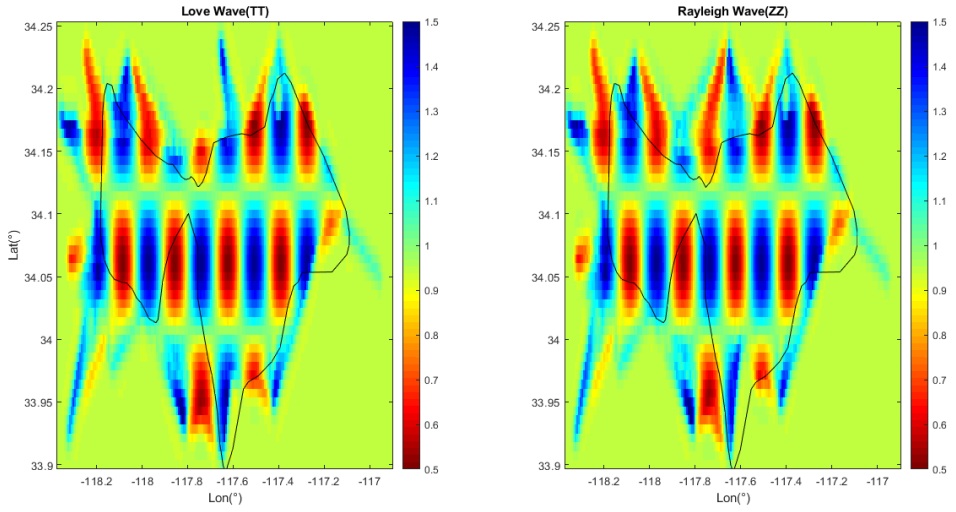

Figure 5.26: Love and Rayleigh wave resolution test from ray coverage of TT and ZZ correlation at T=2s.

A direct comparison of our Vs model and CVMS 4.26 in the different basin areas (Fig. 5.28) illustrates the difference between the models. In the San Gabriel basin, the CVMS model behaves similar to our model, in terms of fitting the dispersion curves (Fig 5.18, Fig 5.19, 5.20, 5.21) and borehole data (Fig 5.27), indicating the CVMS model is well constrained in this area. However, in the Chino and San Bernardino basins, probably due to lack of seismic and borehole data, the CVMS model has a laterally homogeneous velocity field. The prediction of dispersion curves from CVMS model can barely fit the observed dispersion curves (Fig 5.22, 5.23, 5.24, 5.25). In our model, we see the sedimentary basins are in general deeper with lower seismic velocities, and the variation of velocity with depth is always smoother than in the CVMS model. The deeper and slower sedimentary basins can enhance the focusing effect and potentially resolve the underestimation of ground motion simulation using the CVMS model.

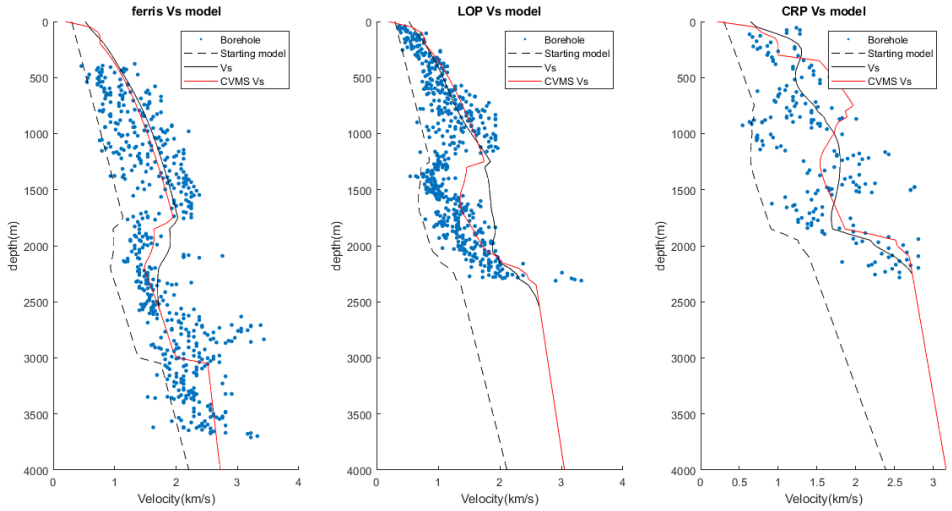

Figure 5.27: VS derived from sonic well logs from the Ferris, LOP, and CRP boreholes compared with our Vs model (black dashed lines for starting model, black solid lines for final model) and CVMS 4.26 (red). Locations of the boreholes are shown with red stars in Figure 5.1.

5.7 Conclusion

We cross-correlate the ambient noise between 10 linear nodal arrays, SCSN broadband stations, 18 temporary broadband stations, and strong motion accelerometers. We obtain the Rayleigh wave and Love wave EGF from the ZZ and TT component ambient noise cross-correlation. In the dispersion analysis, the Rayleigh wave fundamental mode and first higher mode were separated using Rayleigh wave particle motion polarization. We constructed the Vs model by incorporating group and phase velocity tomography, and basin depth from receiver functions and Bouguer gravity datasets. Our Vs model is consistent with geological and geophysical cross-sections from independent studies and the sonic borehole dataset in terms of basement depth and fault locations. Compared to the SCEC CVMS community model, our Vs model generally contains deeper and slower basin structures, especially in the San Bernardino area. This discrepancy might resolve the underestimation of ground motion predicted in future seismic wavefield simulations.

5.8 Model Product

The results of this study are designed to seamlessly fit into the CVMS4.26 model. They are available as a rectilinear block of shear wave velocities between longitude 116.90°W and 118.37°W, and latitude between 33.90°N and 34.25°N. Since the

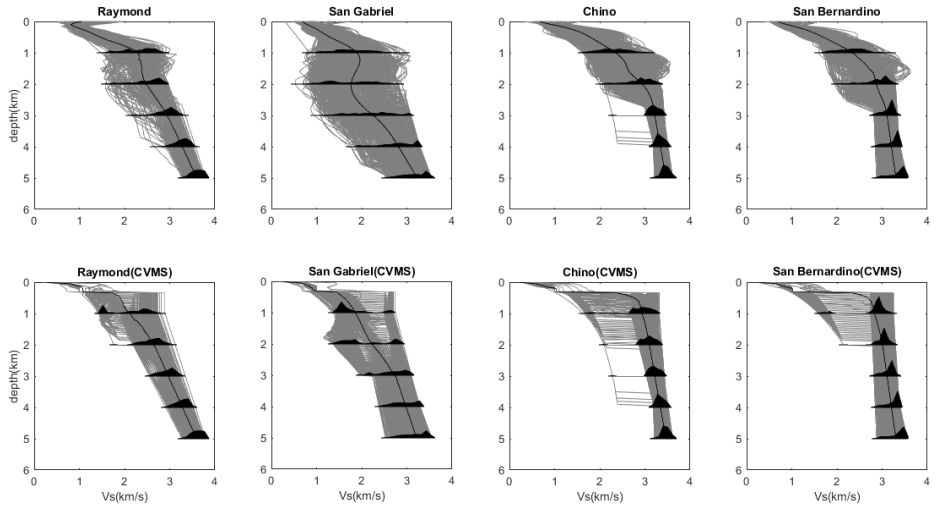

Figure 5.28: Compilation and distribution of Vs with depth in the Raymond, San Gabriel, Chino, and San Bernardino basins (gray lines) from our Vs model (upper panels) and CVMS 4.26 (lower panels). The black shaded regions show the distribution of Vs values at different depths.

CVMS4.26 was used as the starting model, this block can be used as a direct replacement for the corresponding block in the CVMS4.26 model. This will increase the resolution and details in the San Gabriel, Chino, and San Bernardino basins without disturbing the CVMS4.26 model outside of these basins.

5.9 Appedix A: Instrumental response for seismogram to accelerometer correlation.

In the ambient noise correlation, the removal of instrumental response is unnecessary when the two stations have the same instrumental response. In the frequency domain, the correlation function $C_{XY}(\omega) = \frac{X(\omega)I(\omega)}{|X(\omega)I(\omega)|}\frac{\bar{Y}(\omega)\bar{I}(\omega)}{|\bar{Y}(\omega)\bar{I}(\omega)|}$ where $X(\omega)$,$Y(\omega)$ are the Fourier transformation of ambient noise waveform, $I(\omega)$ is the Fourier transformation of instrumental response, bar for conjugate, and the modulus in the denominator is due to spectrum whitening. As $\frac{I(\omega)}{|I(\omega)|}\frac{\bar{I}(\omega)}{|\bar{I}(\omega)|} = 1$, $C_{XY}(\omega) = \frac{X(\omega)}{|X(\omega)|}\frac{\bar{Y}(\omega)}{|\bar{Y}(\omega)|}$, so that the instrumental response has no effect on the dense array- dense array correlation.

For the correlation between dense array and accelerometer, however, the instrumental response causes a non-trivial phase lag. Assuming the station x is a seismogram, which records the velocity x(t), and station y is an accelerometer recording the acceleration dy(t)/dt. The correlation $C_{XY}(\omega) = \frac{X(\omega)}{|X(\omega)|}\frac{i\omega\bar{Y}(\omega)}{|i\omega\bar{Y}(\omega)|} = \frac{X(\omega)}{|X(\omega)|}\frac{i\bar{Y}(\omega)}{|\bar{Y}(\omega)|}$, where

the $i\omega$ comes from the time-derivative operator. Assuming the causal (t>0) and anti-causal (t<0) branches of correlation function are symmetric in the waveform, we fold the waveform at t=0 and stack the causal and anti-causal parts before dispersion analysis (Fig 5.29.a). However, the correlation between seismogram and accelerometer has a $\pi/2$ phase shift due to the i in the frequency domain. The $\pi/2$ shift leads to a π (half period) shift when we fold the waveform at t=0, meaning a flip of sign between causal and anti-causal branches (Fig 5.29.b). Therefore, we subtract the causal by the anti-causal branch to account for instrumental response when stacking the correlation function from seismogram-accelerometer cross-correlation.

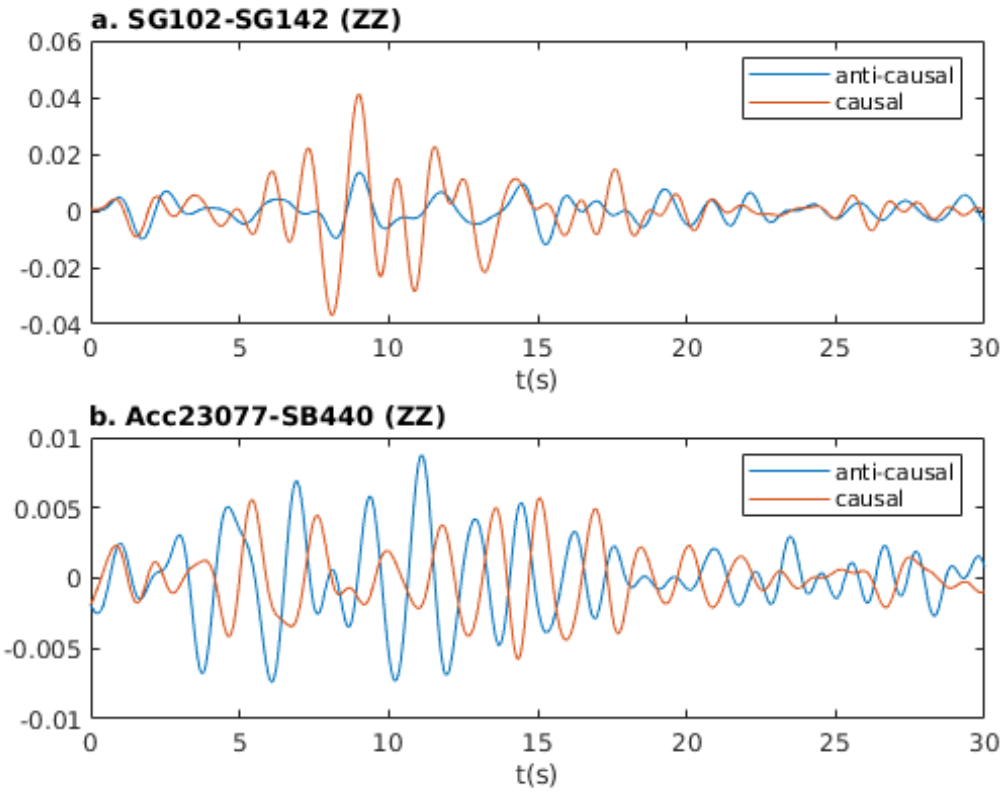

Figure 5.29: Example of correlation functions folded at t = 0 s from a) a seismogram-to-seismogram cross correlation and b) a seismogram-to-accelerometer cross correlation. In a) the causal and anti-causal branch show coherent phase, and in b) the causal and anti-causal display a half period (π phase) shift.

5.10 Appendix B: ZZ and ZR phase difference is the same as Z and R phase difference.

In the dispersion analysis, we use the phase lag between the Z and R components in the path of Rayleigh wave propagation to quantify the Rayleigh wave particle motion.

In this section, we show the phase difference between ZZ and ZR in ambient noise correlation is equivalent to the Z and R phase difference. With a given noise source, signals in different components can be written as $s_1(t) = cos(wt + \phi_1))$ and $s_2(t) = cos(wt + \phi_2))$. For receivers, the recorded waveform from s_1 at station x is $x_1(t) = cos(w(t - \frac{r_1}{c}) + \phi_1)$, and the recorded waveform from s_2 at station y is $y_1(t) = cos(w(t - \frac{r_2}{c}) + \phi_2)$, where r_1 and r_2 are the distances from source to the two receivers and c is the velocity. The correlation between the two receivers is

$$C_{xy} = \frac{1}{2T}\int_{-T}^{T} cos(w(\tau - \frac{r_1}{c}) + \phi_1)cos(w(t + \tau - \frac{r_2}{c}) + \phi_2)d\tau = \frac{1}{2}cos(w(t - \frac{r_2 - r_1}{c}) + \phi_2 - \phi_1)(T >> 1) \tag{5.2}$$

For ZZ correlation, $\phi_1 = \phi_2$; for ZR correlation, $\phi_1 = \phi_Z$, $\phi_2 = \phi_R$. $C_{ZR} = \frac{1}{2}cos(w(t - \frac{r_2 - r_1}{c}) + \phi_R - \phi_Z)$, $C_{ZZ} = \frac{1}{2}cos(w(t - \frac{r_2 - r_1}{c}))$. Therefore, we proved that the phase difference between ZZ and ZR is $\phi_Z - \phi_R$, equal to the phase difference between the Z and R components of the source.

5.11 Supplementary Material

Rayleigh Wave Mode Separation

As described in Section 3.3, we combine the amplitude information coming from the Hilbert transformation and the phase difference between Z and R component from a wavelet transformation to separate the Rayleigh wave modes and pick the Rayleigh wave group velocity dispersion curves. Here we apply the method to published correlation functions (Figure 5.5). The correlation functions are ZZ and ZR correlation of NE12-NE46 (Figure 5.5a), two temporary broadband stations of the NECESSArray filtered at 8 s and 25 s period (G. Li et al., 2016). By applying the Hilbert-wavelet combined method described in the main text, we get a clearly separated red fundamental mode and blue first higher mode (Figure 5.5b). With identified fundamental mode between t 90-150 s and first higher mode between t 40-70 s, we plotted out the particle motion (ZZ vs ZR) with time color-coded in Figure 5.5c-d. From blue to red, the fundamental model particle motion is counterclockwise (retrograde) and first higher mode particle motion is clockwise (prograde), in agreement with Figure 5.5c-d.

References

Ajala, Rasheed and Patricia Persaud (Aug. 10, 2022). “Ground-Motion Evaluation of Hybrid Seismic Velocity Models”. In: *The Seismic Record* 2.3, pp. 186–196. ISSN: 2694-4006. DOI: 10.1785/0320220022. URL: https://doi.org/10.1785/0320220022 (visited on 08/10/2022).

Anderson, Megan, Jonathan Matti, and Robert Jachens (Apr. 2004). "Structural model of the San Bernardino basin, California, from analysis of gravity, aeromagnetic, and seismicity data: STRUCTURE OF THE SAN BERNARDINO BASIN". In: *Journal of Geophysical Research: Solid Earth* 109 (B4). ISSN: 01480227. DOI: 10.1029/2003JB002544. URL: http://doi.wiley.com/10.1029/2003JB002544 (visited on 06/16/2022).

Backus, George E. (Oct. 1962). "Long-wave elastic anisotropy produced by horizontal layering". In: *Journal of Geophysical Research* 67.11, pp. 4427–4440. ISSN: 01480227. DOI: 10.1029/JZ067i011p04427. URL: http://doi.wiley.com/10.1029/JZ067i011p04427 (visited on 04/21/2023).

Bensen, G. D. et al. (June 2007). "Processing seismic ambient noise data to obtain reliable broad-band surface wave dispersion measurements". In: *Geophysical Journal International* 169.3, pp. 1239–1260. ISSN: 0956540X, 1365246X. DOI: 10.1111/j.1365-246X.2007.03374.x. URL: https://academic.oup.com/gji/article-lookup/doi/10.1111/j.1365-246X.2007.03374.x (visited on 01/25/2022).

Brocher, T. M. (Dec. 1, 2005). "Empirical Relations between Elastic Wavespeeds and Density in the Earth's Crust". In: *Bulletin of the Seismological Society of America* 95.6, pp. 2081–2092. ISSN: 0037-1106. DOI: 10.1785/0120050077. URL: https://pubs.geoscienceworld.org/bssa/article/95/6/2081-2092/146858 (visited on 01/26/2023).

Brocher, Thomas M. et al. (1998). "Compilation of 20 sonic and density logs from 12 oil test wells along LARSE Lines 1 and 2, Los Angeles region, California". In: *US Geol. Surv. Open-File Rept. 98* 366, p. 53.

Buwalda, John Peter (1940). *Geology of the Raymond Basin*. California Institute of Technology. (pp. 1–131). URL: http://doi.org/10.22002/D1.20258.

Castellanos, Jorge C. and Robert W. Clayton (Dec. 2021). "The Fine-Scale Structure of Long Beach, California, and Its Impact on Ground Motion Acceleration". In: *Journal of Geophysical Research: Solid Earth* 126.12. ISSN: 2169-9313, 2169-9356. DOI: 10.1029/2021JB022462. URL: https://onlinelibrary.wiley.com/doi/10.1029/2021JB022462 (visited on 04/05/2022).

Clayton, Robert et al. (Oct. 10, 2019). "Exposing Los Angeles's Shaky Geologic Underbelly". In: *Eos* 100. ISSN: 2324-9250. DOI: 10.1029/2019EO135099. URL: https://eos.org/science-updates/exposing-los-angeless-shaky-geologic-underbelly (visited on 03/29/2022).

Davis, Thomas L. and Jay S. Namson (Apr. 2017). "Field excursion: Petroleum traps and structures along the San Andreas convergent strike-slip plate boundary, California". In: *AAPG Bulletin* 101.4, pp. 607–615. ISSN: 0149-1423. DOI: 10.1306/011817DIG17040. URL: http://archives.datapages.com/data/doi/10.1306/011817DIG17040 (visited on 08/01/2022).

Denolle, M. A. et al. (Jan. 24, 2014). “Strong Ground Motion Prediction Using Virtual Earthquakes”. In: *Science* 343.6169, pp. 399–403. ISSN: 0036-8075, 1095-9203. DOI: 10.1126/science.1245678. URL: https://www.science.org/doi/10.1126/science.1245678 (visited on 03/04/2022).

Ekström, Göran (2006). “Global detection and location of seismic sources by using surface waves”. In: *Bulletin of the Seismological Society of America* 96.4. ISBN: 1943-3573 Publisher: Seismological Society of America, pp. 1201–1212.

Ghose, Ritu, Patricia Persaud, and Robert W. Clayton (Oct. 24, 2023). “Basin Structure for Earthquake Ground Motion Estimates in Urban Los Angeles Mapped with Nodal Receiver Functions”. In: *Geosciences* 13.11, p. 320. ISSN: 2076-3263. DOI: 10.3390/geosciences13110320. URL: https://www.mdpi.com/2076-3263/13/11/320 (visited on 10/31/2023).

Graves, Robert et al. (Mar. 2011). “CyberShake: A Physics-Based Seismic Hazard Model for Southern California”. In: *Pure and Applied Geophysics* 168.3, pp. 367–381. ISSN: 0033-4553, 1420-9136. DOI: 10.1007/s00024-010-0161-6. URL: http://link.springer.com/10.1007/s00024-010-0161-6 (visited on 03/04/2022).

Herrmann, Robert B. (2013). “Computer programs in seismology: An evolving tool for instruction and research”. In: *Seismological Research Letters* 84.6. ISBN: 1938-2057 Publisher: Seismological Society of America, pp. 1081–1088.

Jaxybulatov, K. et al. (Oct. 31, 2014). “A large magmatic sill complex beneath the Toba caldera”. In: *Science* 346.6209, pp. 617–619. ISSN: 0036-8075, 1095-9203. DOI: 10.1126/science.1258582. URL: https://www.sciencemag.org/lookup/doi/10.1126/science.1258582 (visited on 01/24/2023).

Jia, Zhe and Robert W. Clayton (2021). “Determination of Near Surface Shear-Wave Velocities in the Central Los Angeles Basin With Dense Arrays”. In: *Journal of Geophysical Research: Solid Earth* 126.5. ISBN: 2169-9313 Publisher: Wiley Online Library, e2020JB021369.

Jiang, Chengxin and Marine A. Denolle (Aug. 2022). “Pronounced Seismic Anisotropy in Kanto Sedimentary Basin: A Case Study of Using Dense Arrays, Ambient Noise Seismology, and Multi-Modal Surface-Wave Imaging”. In: *Journal of Geophysical Research: Solid Earth* 127.8. ISSN: 2169-9313, 2169-9356. DOI: 10.1029/2022JB024613. URL: https://onlinelibrary.wiley.com/doi/10.1029/2022JB024613 (visited on 04/18/2023).

Jones, Lucile M. et al. (2008). *The ShakeOut Scenario*. Open-File Report 2008-1150. Series: Open-File Report. Reston, VA: U.S. Geological Survey. URL: 10.3133/ofr20081150.

Kohler, M. D., H. Magistrale, and R. W. Clayton (2003). “Mantle heterogeneities and the SCEC reference three-dimensional seismic velocity model version 3”. In: *Bulletin of the Seismological Society of America* 93.2. ISBN: 1943-3573 Publisher: Seismological Society of America, pp. 757–774.

Lee, En-Jui et al. (2014). "Full-3-D tomography for crustal structure in southern California based on the scattering-integral and the adjoint-wavefield methods". In: *Journal of Geophysical Research: Solid Earth* 119.8. ISBN: 2169-9313 Publisher: Wiley Online Library, pp. 6421–6451.

Li, Guoliang et al. (Feb. 2016). "Measurement of Rayleigh wave ellipticity and its application to the joint inversion of high-resolution *S* wave velocity structure beneath northeast China". In: *Journal of Geophysical Research: Solid Earth* 121.2, pp. 864–880. ISSN: 2169-9313, 2169-9356. DOI: 10.1002/2015JB012459. URL: https://onlinelibrary.wiley.com/doi/10.1002/2015JB012459 (visited on 01/23/2023).

Lin, Fan-Chi, Dunzhu Li, et al. (July 1, 2013). "High-resolution 3D shallow crustal structure in Long Beach, California: Application of ambient noise tomography on a dense seismic array". In: *GEOPHYSICS* 78.4, Q45–Q56. ISSN: 0016-8033, 1942-2156. DOI: 10.1190/geo2012-0453.1. URL: https://library.seg.org/doi/10.1190/geo2012-0453.1 (visited on 04/05/2022).

Lin, Fan-Chi, Morgan P. Moschetti, and Michael H. Ritzwoller (Apr. 2008). "Surface wave tomography of the western United States from ambient seismic noise: Rayleigh and Love wave phase velocity maps". In: *Geophysical Journal International* 173.1, pp. 281–298. ISSN: 0956540X, 1365246X. DOI: 10.1111/j.1365-246X.2008.03720.x. URL: https://academic.oup.com/gji/article-lookup/doi/10.1111/j.1365-246X.2008.03720.x (visited on 04/03/2022).

Lin, Fan-Chi, Michael H. Ritzwoller, and Roel Snieder (June 2009). "Eikonal tomography: surface wave tomography by phase front tracking across a regional broadband seismic array". In: *Geophysical Journal International* 177.3, pp. 1091–1110. ISSN: 0956540X, 1365246X. DOI: 10.1111/j.1365-246X.2009.04105.x. URL: https://academic.oup.com/gji/article-lookup/doi/10.1111/j.1365-246X.2009.04105.x (visited on 01/26/2023).

Liu, Guibao, Patricia Persaud, and Robert W. Clayton (Sept. 2018). "Structure of the Northern Los Angeles Basins Revealed in Teleseismic Receiver Functions from Short-Term Nodal Seismic Arrays". In: *Seismological Research Letters* 89.5, pp. 1680–1689. ISSN: 0895-0695, 1938-2057. DOI: 10.1785/0220180071. URL: https://pubs.geoscienceworld.org/ssa/srl/article/89/5/1680/544475/Structure-of-the-Northern-Los-Angeles-Basins (visited on 04/05/2022).

Lu, Zhong and Wesley R. Danskin (July 1, 2001). "InSAR analysis of natural recharge to define structure of a ground-water basin, San Bernardino, California". In: *Geophysical Research Letters* 28.13, pp. 2661–2664. ISSN: 00948276. DOI: 10.1029/2000GL012753. URL: http://doi.wiley.com/10.1029/2000GL012753 (visited on 06/16/2022).

Ma, Yiran, Robert W. Clayton, and Dunzhu Li (2016). "Higher-mode ambient-noise Rayleigh waves in sedimentary basins". In: *Geophysical Journal International* 206.3. ISBN: 1365-246X Publisher: Oxford University Press, pp. 1634–1644.

Magistrale, H. (Dec. 1, 2000). "The SCEC Southern California Reference Three-Dimensional Seismic Velocity Model Version 2". In: *Bulletin of the Seismological Society of America* 90.6, S65–S76. ISSN: 0037-1106. DOI: 10.1785/0120000510. URL: https://pubs.geoscienceworld.org/bssa/article/90/6B/S65-S76/147009 (visited on 02/25/2022).

Magistrale, Harold, Keith McLaughlin, and Steven Day (1996). "A geology-based 3D velocity model of the Los Angeles basin sediments". In: *Bulletin of the Seismological Society of America* 86.4. ISBN: 1943-3573 Publisher: The Seismological Society of America, pp. 1161–1166.

Mao, Shujuan et al. (2020). "On the measurement of seismic traveltime changes in the time–frequency domain with wavelet cross-spectrum analysis". In: *Geophysical Journal International* 221.1. ISBN: 0956-540X Publisher: Oxford University Press, pp. 550–568.

Nakata, Nori and Roel Snieder (June 2012). "Time-lapse change in anisotropy in Japan's near surface after the 2011 Tohoku-Oki earthquake: S-WAVE SPLITTING CAUSED BY THE TOHOKU EQ". In: *Geophysical Research Letters* 39.11, n/a–n/a. ISSN: 00948276. DOI: 10.1029/2012GL051979. URL: http://doi.wiley.com/10.1029/2012GL051979 (visited on 04/21/2023).

Olsen, K. B. et al. (2006). "Strong shaking in Los Angeles expected from southern San Andreas earthquake". In: *Geophysical Research Letters* 33.7, p. L07305. ISSN: 0094-8276. DOI: 10.1029/2005GL025472. URL: http://doi.wiley.com/10.1029/2005GL025472 (visited on 03/04/2022).

Paulinski, Scott (2012). "Structural, hydrogeologic framework, and textural model of the Rialto-Colton Basin and the Chino and North Riverside area". In: *Doctoral dissertation, California State University, Sacramento*.

Qiu, Hongrui, Fan-Chi Lin, and Yehuda Ben-Zion (Sept. 2019). "Eikonal Tomography of the Southern California Plate Boundary Region". In: *Journal of Geophysical Research: Solid Earth* 124.9, pp. 9755–9779. ISSN: 2169-9313, 2169-9356. DOI: 10.1029/2019JB017806. URL: https://onlinelibrary.wiley.com/doi/10.1029/2019JB017806 (visited on 01/26/2023).

Sanchez-Sesma, F. J. (June 1, 2006). "Retrieval of the Green's Function from Cross Correlation: The Canonical Elastic Problem". In: *Bulletin of the Seismological Society of America* 96.3, pp. 1182–1191. ISSN: 0037-1106. DOI: 10.1785/0120050181. URL: https://pubs.geoscienceworld.org/bssa/article/96/3/1182-1191/146787 (visited on 01/30/2023).

Snieder, Roel (Apr. 29, 2004). "Extracting the Green's function from the correlation of coda waves: A derivation based on stationary phase". In: *Physical Review E* 69.4, p. 046610. ISSN: 1539-3755, 1550-2376. DOI: 10.1103/PhysRevE.69.

046610. URL: https://link.aps.org/doi/10.1103/PhysRevE.69.046610 (visited on 04/03/2022).

Southern California Cross Section Study Map Showing 2012 AAPG Annual Mtg Field Trip Stops (May 24, 2013). In collab. with Thomas Davis and Jay Namson. URL: https://thomasldavisgeologist.com/cross-sections/.

Stephenson, W. J. et al. (2002). "Delineation of faulting and basin geometry along a seismic reflection transect in urbanized San Bernardino Valley, California". In: *Bulletin of the Seismological Society of America* 92.6. ISBN: 1943-3573 Publisher: Seismological Society of America, pp. 2504–2520.

Torrence, Christopher and Gilbert P. Compo (1998). "A practical guide to wavelet analysis". In: *Bulletin of the American Meteorological society* 79.1. ISBN: 0003-0007 Publisher: American Meteorological Society, pp. 61–78.

Villa, Valeria et al. (July 2023). "Three-Dimensional Basin Depth Map of the Northern Los Angeles Basins From Gravity and Seismic Measurements". In: *Journal of Geophysical Research: Solid Earth* 128.7, e2022JB025425. ISSN: 2169-9313, 2169-9356. DOI: 10.1029/2022JB025425. URL: https://agupubs.onlinelibrary.wiley.com/doi/10.1029/2022JB025425 (visited on 10/31/2023).

Wang, Xin et al. (Sept. 2021). "Urban Basin Structure Imaging Based on Dense Arrays and Bayesian Array-Based Coherent Receiver Functions". In: *Journal of Geophysical Research: Solid Earth* 126.9. ISSN: 2169-9313, 2169-9356. DOI: 10.1029/2021JB022279. URL: https://onlinelibrary.wiley.com/doi/10.1029/2021JB022279 (visited on 04/05/2022).

West, J. C. et al. (1988). "Correlation section across Los Angeles basin from Palos Verdes Hills to San Gabriel Mountains". In: *Correlation Section CS 3R*.

White, Malcolm C. A. et al. (July 1, 2020). "PyKonal: A Python Package for Solving the Eikonal Equation in Spherical and Cartesian Coordinates Using the Fast Marching Method". In: *Seismological Research Letters* 91.4, pp. 2378–2389. ISSN: 0895-0695, 1938-2057. DOI: 10.1785/0220190318. URL: https://pubs.geoscienceworld.org/ssa/srl/article/91/4/2378/586804/PyKonal-A-Python-Package-for-Solving-the-Eikonal (visited on 01/26/2023).

Woolfenden, Linda and Dina Kadhim (1997). *Geohydrology and water chemistry in the Rialto-Colton Basin, San Bernardino County, California*. USGS Numbered Series. DOI: 10.3133/wri974012. URL: http://pubs.er.usgs.gov/publication/wri974012 (visited on 06/16/2022).

Yao, Huajian, Robert D. van Der Hilst, and Maarten V. De Hoop (2006). "Surface-wave array tomography in SE Tibet from ambient seismic noise and two-station analysis—I. Phase velocity maps". In: *Geophysical Journal International* 166.2. ISBN: 1365-246X Publisher: Blackwell Publishing Ltd Oxford, UK, pp. 732–744.

Yeats, Robert S. (2004). “Tectonics of the San Gabriel Basin and surroundings, southern California”. In: *Geological Society of America Bulletin* 116.9, p. 1158. ISSN: 0016-7606. DOI: 10.1130/B25346.1. URL: https://pubs.geoscienceworld.org/gsabulletin/article/116/9-10/1158-1182/2118 (visited on 02/25/2022).

Zhang, Zhen-dong et al. (Nov. 2021). “Rayleigh Wave Dispersion Spectrum Inversion Across Scales”. In: *Surveys in Geophysics* 42.6, pp. 1281–1303. ISSN: 0169-3298, 1573-0956. DOI: 10.1007/s10712-021-09667-z. URL: https://link.springer.com/10.1007/s10712-021-09667-z (visited on 01/26/2023).

Chapter 6

MAPPING THE NEAR-FIELD SCATTERING ENERGY FROM AMBIENT NOISE SPURIOUS ARRIVAL IN SEDIMENTARY BASINS

6.1 Introduction

Ambient noise correlation is a widely employed technique in seismology. With the assumption of homogeneously distributed diffuse sources, the cross-correlation of the recorded random field at two stations produces an approximation of Green's function between the two stations. The Green's function describes how signals originating at one station propagate and are recorded at the other station, and information of the medium encoded in the Green's function can be extracted to invert for underground velocity structure. This methodology, known as ambient noise tomography, has been widely applied to a variety of scenarios, spanning from global-scale studies to the Earth's crust and sedimentary basins.

In addition to the expected Empirical Green's function, the violation of the homogeneous source distribution assumption incurs additional phases in the correlograms. For instance, a strong near-field secondary source results in precursory energy in the correlogram, often referred to as spurious arrivals. Similarly, a strong near-field reflector gives rise to coda waves within the correlogram. The sources of such spurious arrivals encompass various mechanisms, including volcanic tremor(Zeng and Ni, 2010), scattering associated with magma chamber(Ma et al., 2013), scattering at the boundary between the sedimentary basin and base rock(Retailleau and Beroza, 2021) and scattering from the fault zone(Yang et al., 2022). Notably, scattering at the edge of sedimentary basins(Retailleau, Boué, et al., 2017) and within fault zones(Yang et al., 2022) also contributes to the generation of coda waves observed in the correlograms.

As information about the near-field source/scatterer is encoded in the precursory signals, inversion methodologies are employed to discern and extract information about the ambient noise source. For a linear dense array, back projection is used to image the source distribution along the 1D profile(Retailleau and Beroza, 2021; Yang et al., 2022). For a curved linear array or a 2D dense array, a grid-search-based method is used to pinpoint the location of a single scatterer(Ma et al., 2013). In

this paper, we introduce an inversion method to map the 2D spatial distribution of the near-field noise source. In the correlation functions from the nodal dense arrays in northern LA basins, we observe very strong scattering and apply the inversion technique to map the near-field noise source distribution. The noise source distribution shows a strong correlation with the shape of the geological element boundaries and fault zones. Finally, we test the frequency dependency of the noise source, which sheds light on the depth of the noise source.

6.2 Ambient Noise Correlation and Inversion Method

We correlate the ambient noise recorded by the seismic nodal arrays of the BASIN project(Basin Amplification Seismic Investigation) (Fig 6.1a). This project aims to improve the community velocity model in the area of the San Gabriel and San Bernardino basins, with 10 linear nodal arrays deployed between 2017 and 2019. Based on the gravity(Villa et al., 2022), receiver function(Liu, Persaud, and R. W. Clayton, 2018; Wang et al., 2021) and ambient noise correlation, a new velocity model is established for this region(Li, Villa, R. Clayton, et al., 2022). Following (Bensen et al., 2007; Lin et al., 2013), (Li, Villa, R. Clayton, et al., 2022) construct the ambient noise tomography involving the correlation of different components, including the ZZ(vertical) correlation for the Rayleigh wave and the TT(transverse) correlation for the Love wave. In ZZ correlation, they report a presence of fundamental mode co-existing with the first higher mode in the Rayleigh wave Green's function, well-distinguished by the particle motion. In TT correlation, only an obvious fundamental mode exists. In this paper, we focus on the TT correlation, so that we avoid the interference between the higher mode and the precursors.

In addition to the direct wave Green's function, a series of precursory spurious arrivals are present in the correlation functions(black arrow in Fig 6.1b,c). The spurious arrivals branch out from the anti-causal branch of Green's function(t<0) and the wave package migrates with distance in the direction of the causal branch of Green's function(t>0). We see no coda wave as a continuation of spurious arrivals, indicating that spurious arrivals are more likely to be caused by secondary sources instead of reflectors(Yang et al., 2022).

For a given point source, the cross-correlation process results in the wave arriving at the time corresponding to the travel time difference $t_1 - t_2$, where t_1 and t_2 represent the travel times from the source to two receivers. In the case of a uniform noise field, the spatial integration of noise sources preserves the stationary phase at the

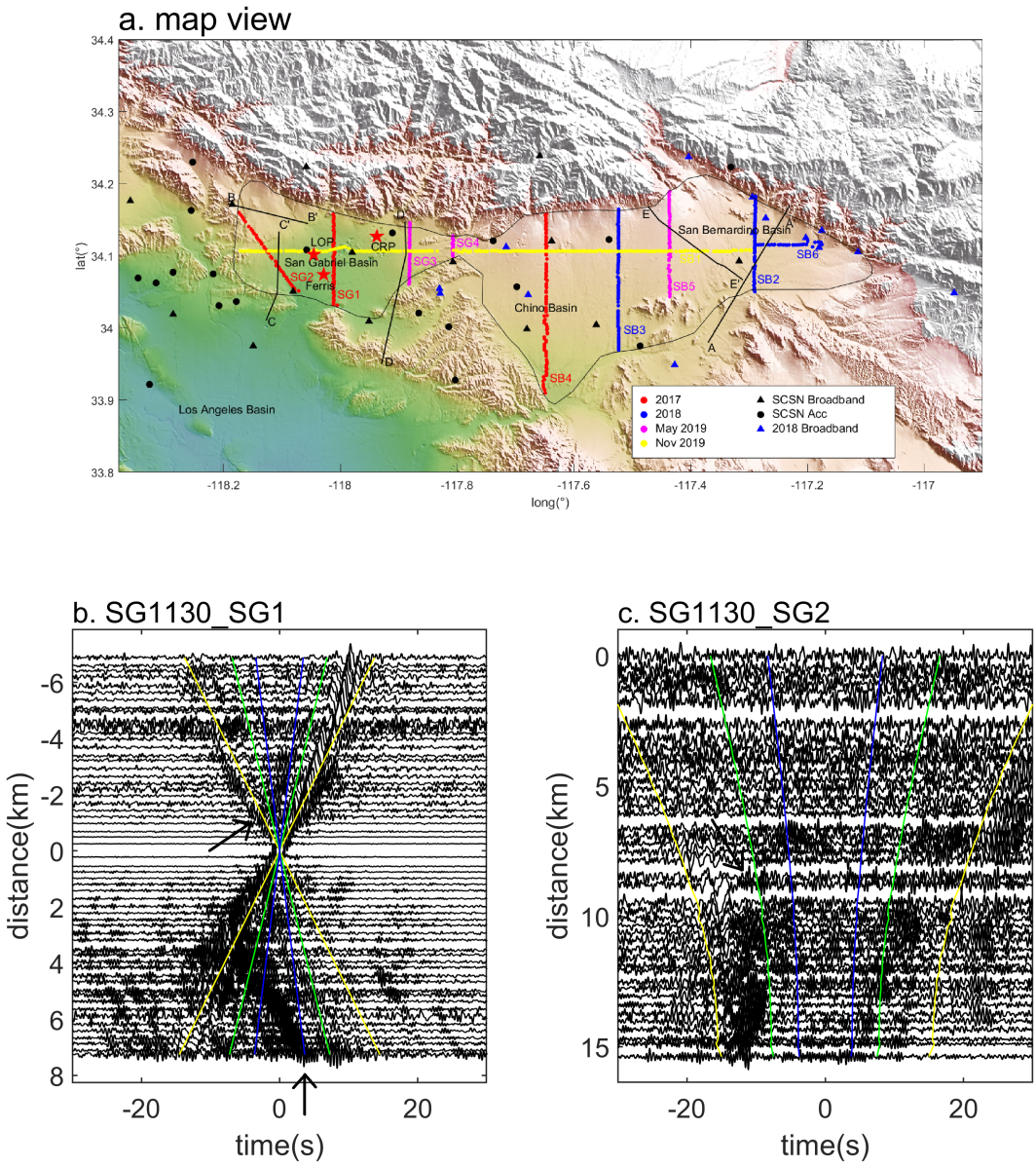

Figure 6.1: a. Mapview of study area with dense array distribution. In total 750 stations in 10 lines wer4e deployed Li, Villa, R. W. Clayton, et al., 2023 b. An example of SG1-SG1 intra-array correlations using SG130 as a virtual source. c. An example of SG1-SG2 inter-array correlations using SG130 as a virtual source. Yellow, green and blue curves for the estimated direct arrival at speed of 0.5, 1 and 2km/s respectively. Black arrows mark the possible spurious arrivals.

time corresponding to the travel time between the two stations, denoted as $t = \pm t_{12}$. This time serves as an approximation of Green's function. The presence of a strong near-field source contributes energy at $t = t_1 - t_2 \leq t_{12}$, which is the reason why we observe precursory arrivals (at $-t_{12} \leq t \leq t_{12}$).

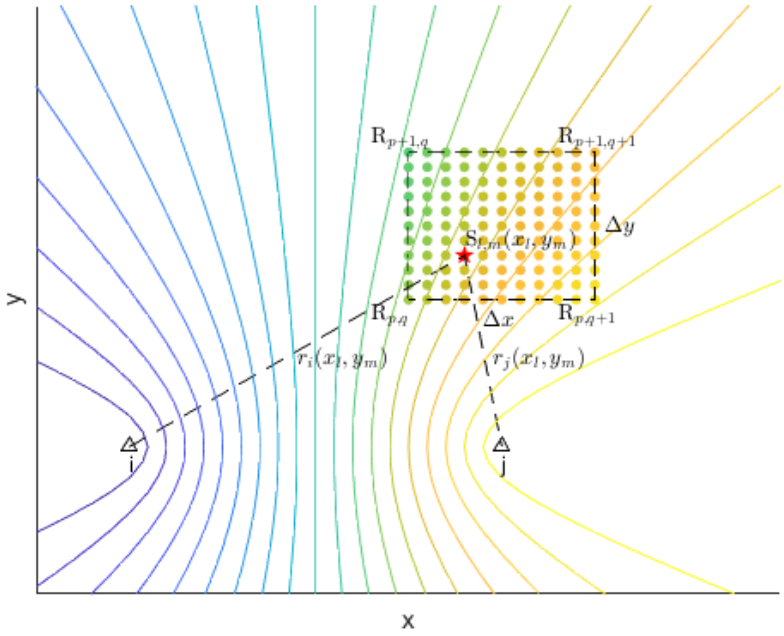

Figure 6.2: Illustration of the inversion method. Triangle i and j stand for the station i,j. Color-coded hyperbolas are the contours of the travel time difference. Each contour contributes to the same time point in the cross-correlation between station i and j. Solid circles stand for dense noise source S_{lm} at the location of (x_l, y_m), with the color-coded travel time difference from each source to station i and j. The dashed square depicts a domain of sparser noise source R_{pq}, with all the dots interior the square governed by the four corners' R.

We develop a method to invert the spatial distribution of the near-field noise source from the precursory waveform of ambient noise correlation. Assuming a set of station pairs, with virtual sources and virtual receivers indexed with i and j, the amplitude of the correlation is $A_{ij}(t)$, where t is the correlation time. Considering a 2D domain with x-y axis, the noise source contributes to the correlation only when $t = \Delta t_{ij}(x, y) = t_i(x, y) - t_j(x, y)$, where x,y are the source location, t_i and t_j the travel time from source to station i and j, and Δt_{ij} is the travel time difference. Assuming the strength of the noise source to be $S(x, y)$ and accounting for the geometric spreading, we get

$$A_{ij}(t) = \int \frac{S(x, y)\delta(t - \Delta t_{ij}(x, y))}{\sqrt{r_i(x, y)r_j(x, y)}} dxdy \tag{6.1}$$

Where $r_i(x, y)$, $r_j(x, y)$ the distance from source location (x,y) to station i and j. In real data, the time is equally discretized ($t = t_k$), so that the target is to invert for

$S(x, y)$ given $A_{ij}(t_k)$, where k is the time index. As illustrated in Figure 6.2, we further discretize variables in the space domain by replacing (x, y) with (x_l, y_m), an equally-spaced mesh grid (dots in Figure 6.2), such that $S_{lm} = S(x_l, y_m)$. Under a constant velocity field, the travel time difference $\Delta t_{ij}(x, y)$ is contoured with hyperbolic curves (colored curves in Figure 6.2). Only when the dot (x_l, y_m) falls within the area bounded by the two hyperbolas contouring $t = t_k \pm \frac{\Delta t}{2}$, the noise source S_{lm} contributes to the correlation at $t = t_k$. This leads to

$$A_{ij}(t_k) = \sum_{lm} w1_{lm}^{ijk} S_{lm} \tag{6.2}$$

With

$$w1_{lm}^{ijk} = \begin{cases} \frac{\delta x \delta y}{\sqrt{r_i(x_l, y_m) r_j(x_l, y_m)}} & |t_k - \Delta t_{ij}(x_l, y_m)| < \frac{\Delta t}{2} \\ 0 & otherwise \end{cases} \tag{6.3}$$

Where δx, δy, and Δt are the spacing of x_l,y_m and t_k.

As the spatial density of the mesh grid (x_l, y_m) needs to be much denser than the contours of $t_k = \Delta t(x_l, y_m)$, the unknown variable to be solved S_{lm} has a large degree of freedom. To make the problem practically solvable, we reduce the degree of freedom of the noise source mesh system by introducing R_{pq}, the source strength on a coarser mesh system (Figure6.2, dashed squares). The finer S_{lm} and coarser $R_{pq} = R(x_p, y_q)$ mesh system are bridged with an interpolation method

$$S_{lm} = \sum_{pq} w2_{pq}^{lm} R_{pq} \tag{6.4}$$

Where

$$w2_{pq}^{lm} = \begin{cases} \frac{(\Delta x - |x_l - x_p|)(\Delta y - |y_m - y_q|)}{\Delta x \Delta y} & |x_l - x_p| < \Delta x, |y_m - y_q| < \Delta y \\ 0 & otherwise \end{cases} \tag{6.5}$$

In this interpolation, the value S_{lm} is taken from four corners of R_{pq} the S_{lm} belongs to, and it guarentees $S_{lm} = R_{pq}$ when $(x_l, y_m) = (x_p, y_q)$. With equation 6.2 and equation 6.4, we establish a relationship between the correlation wave amplitude $A_{ij}(t_k)$ and noise source strength distribution R_{pq}

$$A_{ij}(t_k) = \sum_{lm} \sum_{pq} w1_{lm}^{ijk} w2_{pq}^{lm} R_{pq} \tag{6.6}$$

In the matrix form, we have

$$A = W1W2R = WR \tag{6.7}$$

As every row of A corresponds to a given time point (t_k) for a given station pair (i, j), the row number of A is the total number of time points of all the correlation between any given ray pairs, which is much larger than the row number of R, which corresponds to the total number of mesh point in R_{pq} system. This makes the equation 6.7 over-determined, and we solve for it with the least square method. Besides, similar to seismic tomography, we can add damping and smoothing regularization terms to the matrix, and equation 6.7 becomes

$$\begin{bmatrix} WR - A \\ \alpha I \\ \beta L \end{bmatrix} = 0 \tag{6.8}$$

Where α and β are the damping and smoothing coefficient, I and L are the identical matrix and Laplacian operator.

One more physical constrain is that the strength of the source R cannot be negative, therefore we solve for equation 6.8 with the non-negative least square method(Bill White, 2023). Furthermore, it is important to note that the evaluation of the travel time difference ($t_1 - t_2$) does not strictly demand a homogeneous velocity field. Our method accommodates variable velocity fields as an input.

We validate the robustness of our method through a series of benchmark tests, as illustrated in Figure 6.3 and Figure 6.4. In each test scenario, we employ finite difference simulations of the two-dimensional (2D) acoustic wave equation utilizing *Devito* (Louboutin et al., 2019). Within the model domain, we introduce a checkerboard velocity field, depicted by the background color in Figure 6.3 and Figure 6.4a. To emulate ambient noise, we position a set of point sources (red stars) in a circular arrangement around the receivers (black circles). Additionally, we introduce a few point sources near the receivers to mimic near-field sources. Each source is active for a defined duration, and only one source is active at any given time, thus simulating a scenario where each source operates independently.

For the intra-array and inter-array correlation tests, we deploy either one or two sets of linear receivers (black circles). We perform correlations between the virtual source (black star) and all virtual receivers (same array for intra-array test, adjacent array for inter-array test), resulting in the correlation function, as illustrated in Figure 6.3 and Figure 6.4c (black waveforms). Using the velocity field and the obtained correlation waveforms as input data, we execute the inversion process to deduce the spatial distributions of the near-field noise sources. These inferred distributions

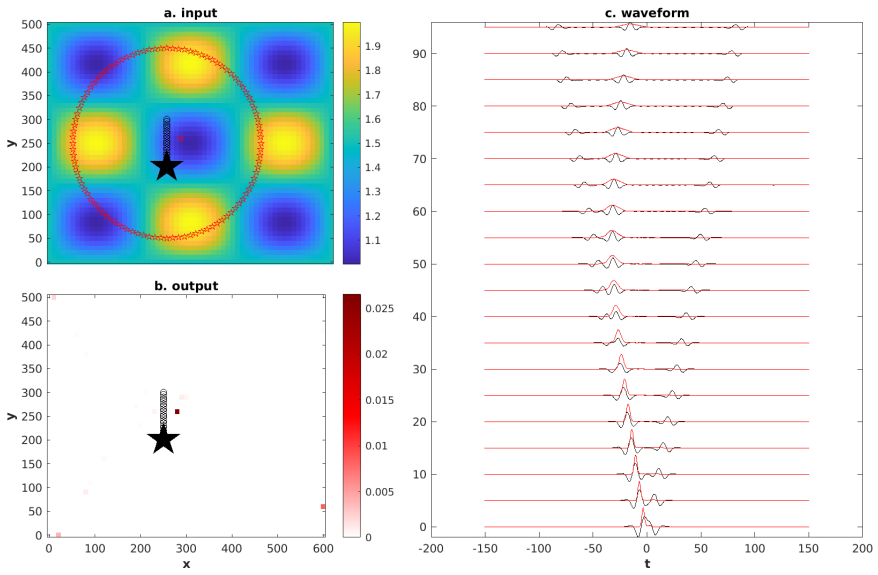

Figure 6.3: A benchmark test of intra-array correlation. a. Noise source(red stars), stations(black circles) and velocity model(background color) in map view. b. Inverted noise source distribution(background color). c. Correlation functions from finite difference model(black) as an input for the inversion vs. synthetic wave envelops from inversion output. The virtual source of c is the black star in b.

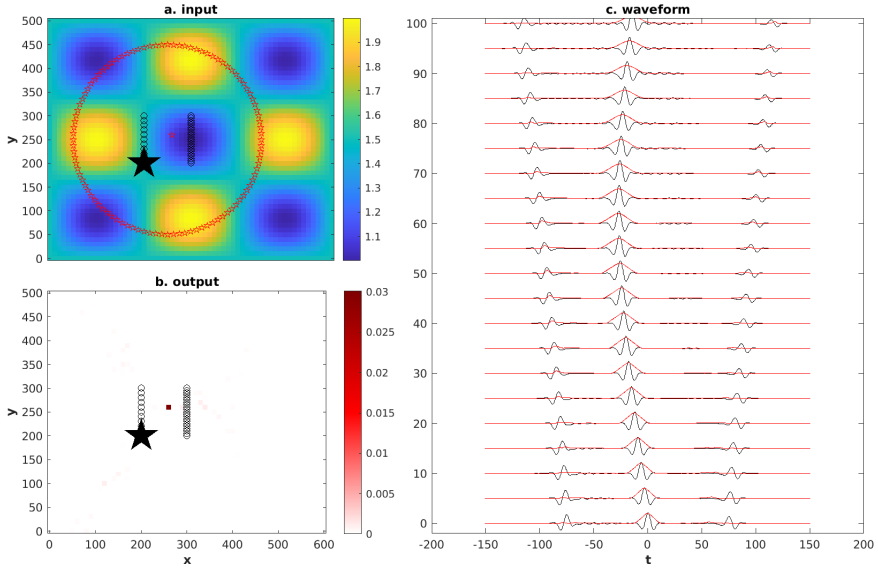

Figure 6.4: A benchmark test of inter-array correlation. Equivalent to Figure 6.3 but using the inter-array correlation for the inversion.

are presented in Figure 6.3 and Figure 6.4b, while the corresponding synthetic

waveforms are showcased in red in Figure 6.3 and Figure 6.4c. In both the intra-array (Figure 6.3) and inter-array (Figure 6.4) test cases, our inversion method successfully retrieves the locations of the near-field sources, and the synthetic waveforms closely match the observed correlation functions, confirming the efficacy and accuracy of our approach.

6.3 Result and Discussion

We take the inter-array correlation for those array pairs sharing the same deployment time period, specifically SG1-SG2, SG3-SG4, SB2-SB6, and SB3-SB6. As we see a strong first higher mode in the Rayleigh wave (ZZ), which can potentially interfere with spurious arrivals, we opt to utilize only the Love wave (TT component) since its higher mode remains indistinct. Given that spurious arrivals are predominantly associated with high frequencies, we incorporate the Love wave group velocity at $T = 0.5s$ obtained from the direct wave Green's function (Li, Villa, R. Clayton, et al., 2022) as the input velocity model. For each pair of dense arrays, we define smaller domains that only incorporate the region covered by that pair. Then, we separately analyze the data for each pair within its own coverage domain. Instead of putting all the data from all the dense arrays into one big analysis, we gather and combine the results from these separate inversions (Figure 6.5.a).

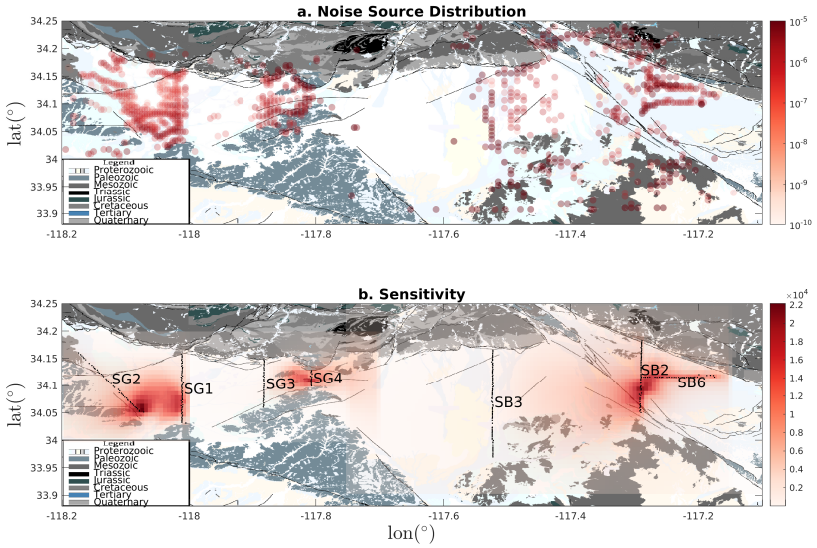

Figure 6.5: a. The combined inverted noise source distribution from correlation SG1-SG2, SG3-SG4, SB2-SB6, and SB3-SB6. b. The combined model sensitivity from the same correlation dataset as a.

The sensitivity quantifies how changes in the noise source R are affected by variations in the data. The employed least-square method minimizes the loss function $L = (A - WR)^T(A - WR)$, thus we define the sensitivity as $\frac{\partial L}{\partial R}$. In the vicinity of the least-squares solution, where $W^TA \approx W^TWR$, the loss function simplifies to $L \approx A^TA - R^TW^TWR$, so that the sensitivity $\frac{\partial L}{\partial R} \approx 2W^TWR$. Unlike tomography whose sensitivity only exists in the area where ray paths cover, the sensitivity of the noise source represents the coverage of the contours of the travel time differences (hyperbolas in Figure 6.2), which is non-zero everywhere. However, due to the geometric spreading the sensitivity decays with the distance to the dense arrays. The composite sensitivity (Figure 6.5.b) demonstrates the inversion is sensitive to the areas between the dense array pairs, and the gaps of noise sources between SG1 and SG3, and between SG4 and SB3 are due to a lack of ray coverage.

In regions with robust ray coverage, a clear and consistent correlation emerges between the inverted noise sources and geological features. Within the SG1-SG2 domain(Fig 6.6.a), the inverted noise sources span the area between the two arrays. Some of these noise sources align with the edges of the San Gabriel basin to the north and south, while others cluster between the younger and older Quaternary alluvial elements on the west. On the south, two swarms of east-west trending linear scattering sources are easily identified in the map view(Fig 6.7.a). The southern swarm correlates with the southern edge of the San Gabriel basin bounded by the Puente hills, while the northern linear swarm does not correlate with any known geological structure. However, in the correlation function(Fig 6.6b black lines), the branch of precursor intersects with the acausal(t<0) branch of the empirical Green's function at the distance of 12km, co-located with the northern swarm of the inverted scattering source and confirms the existence of the coherent scattering energy. In the SG3-SG4 area(Fig 6.7.a), the noise sources exhibit a strong alignment with the boundaries of the San Gabriel basin. Notably, to the north, the noise source closely traces the Sierra Madre fault at the base of the San Gabriel Mountains. To the south, numerous scattered source points coincide with the San Jose fault. The waveform amplitude of the correlation function between SG3 and SG4, filtered into a high-frequency band (2 to 3 Hz), exhibits significantly stronger precursors compared to direct arrivals(Fig 6.7.b, black). Based on the velocity model predictions, the average velocity in this region at 2 Hz is approximately 0.5 to 1 km/s (between the green and yellow lines). However, the strong correlation extends over the time range from -10 s to 0 s, suggesting an apparent velocity ranging from 1 km/s to infinity if these strong signals were interpreted merely as direct waves. Using our method to

interpret these strong signals as precursory spurious arrivals, we get the source distribution(Fig 6.7.a) and its corresponding synthetic waveform amplitude(Fig 6.7.b, red). The close match between the synthetic waveform amplitude and the correlation function confirms that the observed strong signal, characterized by a rapid apparent velocity, is indeed a spurious arrival generated by near-field sources. Furthermore, the spatial coherence between the source distribution and the basin edges suggests that the near-field noise field is likely generated by scattering at the basin edge, where there is a strong velocity contrast. Within the region constrained by SB2, SB3, and SB6(Fig 6.8.a), the noise sources similarly demonstrate a correlation with sedimentary basin boundaries. Along the northwestern edge of the San Bernardino basin, the noise source follows the trajectory of the Cucamonga fault, while along the northeastern edge, it distributes itself along the San Andreas fault. To the south, where the edge of the San Bernardino basin is less well-defined, the noise sources scatter within the mountain range. Inside the basin, a cluster of sources is mapped in the San Jacinto fault zone.

In addition to the noise sources linked to geological features, we also observe sources in close proximity to the dense arrays. These noise sources are likely a result of direct arrival contamination, where the inversion mistakenly identifies direct arrivals as precursors and relocates the sources near the dense array locations to align with the observed data. This misidentification could be attributed to inaccuracies in predicting arrival times caused by inaccuracies in the velocity model, which forces the sources to be positioned near the dense arrays.

We finally study the frequency dependence of the noise source by performing a 1D source inversion. Through the back-projection of the precursory wave envelope from the SG1-SG1 correlation function (Fig. 6.1.a) onto different frequency bands along the SG1 line, we acquired a frequency-dependent 1D noise source distribution along SG1 that results in the precursory energy observed in the SG1-SG1 correlation (Fig 6.9a). In the normalized 1D source distribution, we identified two prominent peaks in the high-frequency range ($T < 1$ s), while the energy levels in the low-frequency bands remained relatively constant along the SG1 line. This observation suggests that the near-field noise source is primarily associated with the high-frequency components. When combined with the sensitivity kernel of Love waves in the San Gabriel basin (Fig 6.9c), derived from the velocity model, it becomes evident that high-frequency Love waves ($T < 1$ s) are primarily sensitive to depths shallower than 200m. Consequently, our results indicate that the near-field noise

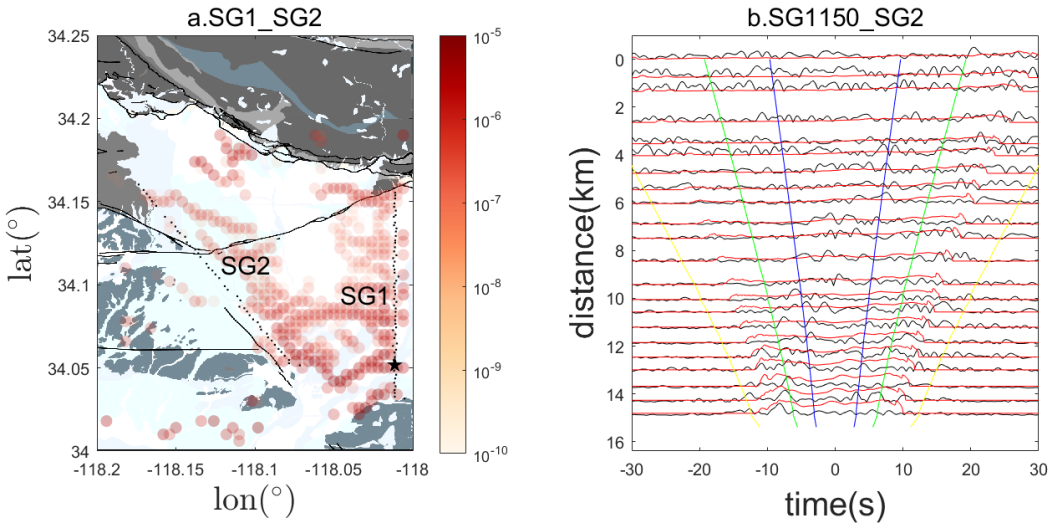

Figure 6.6: a. Zoom-in of inverted noise source distribution from SG1-SG2 region. b. Waveform amplitude of ambient noise correlation(black) vs. synthetic correlation(red). The virtual source is SG1-150(black star in a.) and the virtual receivers are the nodes of SG2 line. Yellow, green and blue lines are the direct arrivals at the speed of 0.5, 1 and 2km/s. All waveforms(black) in b. are filtered by a bandpass filter with a frequency band of 2 Hz to 3 Hz.

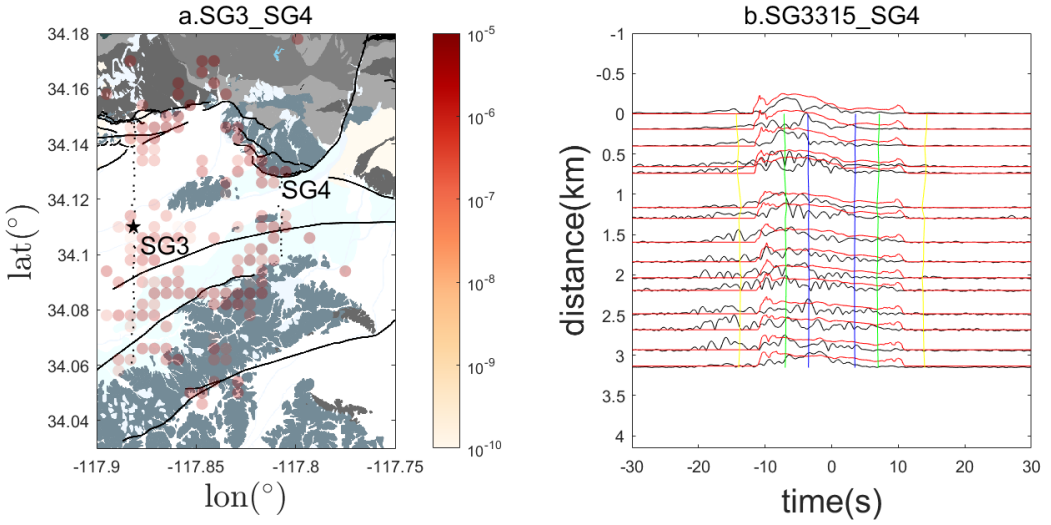

Figure 6.7: a. Zoom-in of inverted noise source distribution from SG3-SG4 region. b. Waveform amplitude of ambient noise correlation(black) vs. synthetic correlation(red). The virtual source is SG3-315(black star in a.) and the virtual receivers are the nodes of SG4 line. Yellow, green and blue lines are the direct arrivals at the speed of 0.5, 1 and 2km/s. All waveforms in b. are filtered by a bandpass filter with a frequency band of 2 Hz to 3 Hz.

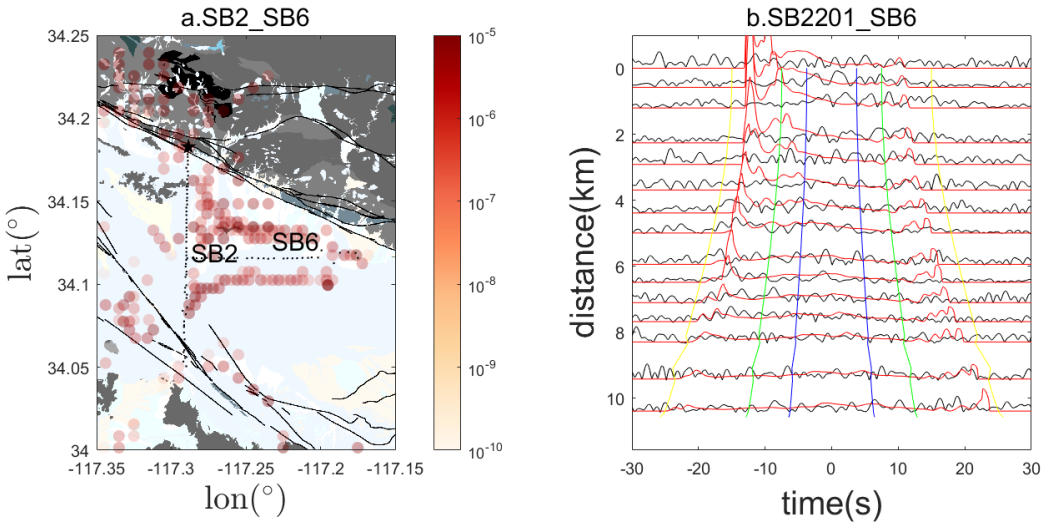

Figure 6.8: a. Zoom-in of inverted noise source distribution from SB2-SB6 region. b. Waveform amplitude of ambient noise correlation(black) vs. synthetic correlation(red). The virtual source is SB2-201(black star in a.) and the virtual receivers are the nodes of SB6 line. Yellow, green and blue lines are the direct arrivals at the speed of 0.5, 1 and 2km/s. All waveforms in b. are filtered by a bandpass filter with a frequency band of 2 Hz to 3 Hz.

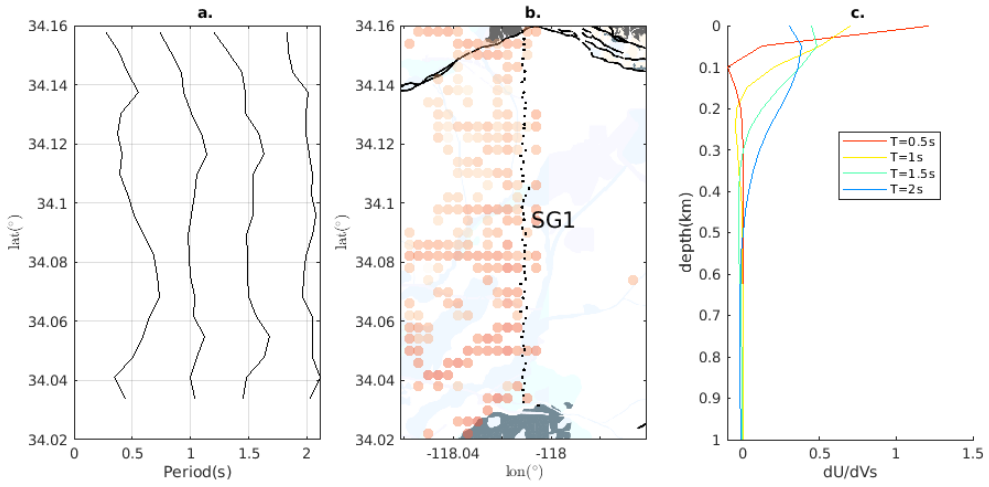

Figure 6.9: a. 1D noise source distribution from SG1-SG1 correlation with different periods color-coded. Black arrows mark the two possible peaks of noise source in high frequency. b. Zoom in of the noise source distribution near SG1 from the SG1-SG2 correlation. c. Love wave group velocity sensitivity kernels in the San Gabriel basin with different periods.

source originates at relatively shallow depths.

In conclusion, we developed a new method that's able to map the 2D ambient noise

source from the precursory spurious arrival from the ambient noise correlation. Applying the technique to the dense-array correlation dataset in the San Gabriel and San Bernardino basins, the noise source distribution shows a strong correlation with some geological features, like the sedimentary basin edge and fault, indicating the noise source could originate from a structure with strong velocity contrast that scatters the seismic energy, and a 1D inversion in spectrum reveals those scattering to have a shallow source.

In summary, we developed a new method that can map the 2D ambient noise source using precursory spurious arrivals derived from ambient noise correlations. When applied to the dense-array correlation dataset in the San Gabriel and San Bernardino basins, our results have revealed a correlation between the noise source distribution and prominent geological features, such as the edges of sedimentary basins and fault zones. This correlation suggests that the noise source may originate from structures with significant velocity contrasts, resulting in the scattering of seismic energy. Our spectral analysis further indicates that these scattering sources predominantly exist at shallow depths. This new method provides a promising way for imaging underground structures in 3D using the spurious arrivals of ambient noise correlations.

References

Bensen, G. D. et al. (June 2007). "Processing seismic ambient noise data to obtain reliable broad-band surface wave dispersion measurements". In: *Geophysical Journal International* 169.3, pp. 1239–1260. ISSN: 0956540X, 1365246X. DOI: 10.1111/j.1365-246X.2007.03374.x. URL: https://academic.oup.com/gji/article-lookup/doi/10.1111/j.1365-246X.2007.03374.x (visited on 01/25/2022).

Bill White (2023). *nnls - Non negative least squares*. URL: https://www.mathworks.com/matlabcentral/fileexchange/38003-nnls-non-negative-least-squares.

Li, Yida, Valeria Villa, Robert Clayton, et al. (Aug. 1, 2022). *Shear Wave Velocities in the San Gabriel and San Bernardino Basins, California*. Version 1.0. DOI: 10.22002/D1.20248. URL: https://data.caltech.edu/records/20248 (visited on 05/10/2023).

Li, Yida, Valeria Villa, Robert W. Clayton, et al. (July 2023). "Shear Wave Velocities in the San Gabriel and San Bernardino Basins, California". In: *Journal of Geophysical Research: Solid Earth* 128.7, e2023JB026488. ISSN: 2169-9313, 2169-9356. DOI: 10.1029/2023JB026488. URL: https://agupubs.

onlinelibrary.wiley.com/doi/10.1029/2023JB026488 (visited on 11/06/2023).

Lin, Fan-Chi et al. (July 1, 2013). "High-resolution 3D shallow crustal structure in Long Beach, California: Application of ambient noise tomography on a dense seismic array". In: *GEOPHYSICS* 78.4, Q45–Q56. ISSN: 0016-8033, 1942-2156. DOI: 10.1190/geo2012-0453.1. URL: https://library.seg.org/doi/10.1190/geo2012-0453.1 (visited on 04/05/2022).

Liu, Guibao, Patricia Persaud, and Robert W. Clayton (Sept. 2018). "Structure of the Northern Los Angeles Basins Revealed in Teleseismic Receiver Functions from Short-Term Nodal Seismic Arrays". In: *Seismological Research Letters* 89.5, pp. 1680–1689. ISSN: 0895-0695, 1938-2057. DOI: 10.1785/0220180071. URL: https://pubs.geoscienceworld.org/ssa/srl/article/89/5/1680/544475/Structure-of-the-Northern-Los-Angeles-Basins (visited on 04/05/2022).

Louboutin, Mathias et al. (Mar. 27, 2019). "Devito (v3.1.0): an embedded domain-specific language for finite differences and geophysical exploration". In: *Geoscientific Model Development* 12.3, pp. 1165–1187. ISSN: 1991-9603. DOI: 10.5194/gmd-12-1165-2019. URL: https://gmd.copernicus.org/articles/12/1165/2019/ (visited on 10/27/2023).

Ma, Yiran et al. (Mar. 1, 2013). "Locating a scatterer in the active volcanic area of Southern Peru from ambient noise cross-correlation". In: *Geophysical Journal International* 192.3, pp. 1332–1341. ISSN: 1365-246X, 0956-540X. DOI: 10.1093/gji/ggs103. URL: http://academic.oup.com/gji/article/192/3/1332/826604/Locating-a-scatterer-in-the-active-volcanic-area (visited on 10/23/2023).

Retailleau, Lise and Gregory C Beroza (Mar. 12, 2021). "Towards structural imaging using seismic ambient field correlation artefacts". In: *Geophysical Journal International* 225.2, pp. 1453–1465. ISSN: 0956-540X, 1365-246X. DOI: 10.1093/gji/ggab038. URL: https://academic.oup.com/gji/article/225/2/1453/6119910 (visited on 10/24/2023).

Retailleau, Lise, Pierre Boué, et al. (Oct. 2017). "Locating Microseism Sources Using Spurious Arrivals in Intercontinental Noise Correlations". In: *Journal of Geophysical Research: Solid Earth* 122.10, pp. 8107–8120. ISSN: 2169-9313, 2169-9356. DOI: 10.1002/2017JB014593. URL: https://agupubs.onlinelibrary.wiley.com/doi/10.1002/2017JB014593 (visited on 10/23/2023).

Villa, Valeria et al. (Aug. 13, 2022). *Three-Dimensional Basin Depth Map of the Northern Los Angeles Basins from Gravity and Seismic Measurements*. preprint. Geophysics. DOI: 10.1002/essoar.10512148.1. URL: http://www.essoar.org/doi/10.1002/essoar.10512148.1 (visited on 08/14/2022).

Wang, Xin et al. (Sept. 2021). “Urban Basin Structure Imaging Based on Dense Arrays and Bayesian Array-Based Coherent Receiver Functions”. In: *Journal of Geophysical Research: Solid Earth* 126.9. ISSN: 2169-9313, 2169-9356. DOI: 10.1029/2021JB022279. URL: https://onlinelibrary.wiley.com/doi/10.1029/2021JB022279 (visited on 04/05/2022).

Yang, Yan et al. (June 2022). “Fault Zone Imaging With Distributed Acoustic Sensing: Surface-To-Surface Wave Scattering”. In: *Journal of Geophysical Research: Solid Earth* 127.6, e2022JB024329. ISSN: 2169-9313, 2169-9356. DOI: 10.1029/2022JB024329. URL: https://agupubs.onlinelibrary.wiley.com/doi/10.1029/2022JB024329 (visited on 10/23/2023).

Zeng, Xiangfang and Sidao Ni (Dec. 2010). “A persistent localized microseismic source near the Kyushu Island, Japan: PL MICROSEISMIC SOURCE NEAR KYUSHU”. In: *Geophysical Research Letters* 37.24, n/a–n/a. ISSN: 00948276. DOI: 10.1029/2010GL045774. URL: http://doi.wiley.com/10.1029/2010GL045774 (visited on 10/23/2023).

Chapter 7

CONCLUSIONS AND FUTURE DIRECTION

In Chapters 2,3, and 4, we systematically studied the dynamic process of subduction initiation, from analytical solutions to numerical models, from theory to observation, and from simplified 2D perspectives to the realism of the 3D world.

In Chapter 2, we started with a simple 2D problem. We established a set of analytical formulations that describe the force balance of the subducting plate in an induced subduction initiation system and validated the equations with geodynamic models. Those simple formulations provided us with some physical intuition on the subduction initiation system. Firstly, the widely observed compression-extension transition in the stress state results from the slab pull taking over the far-field compression as the major driving force when subduction initiates. Secondly, the strain weakening rate is a governing factor that controls the initiation time and energy.

Chapter 3 follows up on the theory established in Chapter 2. By extending the model domain into sliced 3D, we accounted for the component of strike-slip motion. With analytical and numerical approaches, we demonstrated the addition of strike-slip makes subduction easier to occur. By modifying the weakening rate, the effect of strike-slip velocity can be easily accounted for. We also discovered a strain partitioning system can emerge as a natural consequence of subduction initiation at a strike-slip boundary. Finally, we compared the initiation time, which marks when compression turns into an extension interior of the plate, from the theory against the observation. The first-order agreement in initiation time between the analytical prediction and the geological observations serves as a validation of our theory.

Despite the alignment with data, 2D or sliced 3D models are still over-simplified from the real world. Therefore we moved on to the realistic 3D geodynamic models with a case study of the Puysegur trench offshore New Zealand. As the initial and boundary conditions are well-constrained by the regional plate reconstructions, the geodynamic models, starting from 15 Ma, are able to fit current-day observations surprisingly well. The models are even capable of reproducing small-scale topographic features, like the Snares zone, whose formation mechanism is still not entirely clear. By comparing a variety of geophysical and geological observations,

we find a fast weakening rate is required to produce Puysegur subduction initiation. Such a fast weakening rate might correspond to pore pressure weakening in the shallow depth and grain size reduction in the deeper depth.

In the first three chapters, we study the same topic, the subduction initiation, with distinct methodology and philosophy. On the one hand, simple models and theories are able to capture first-order physics and make some large-scale predictions that agree with observations. On the other hand, sophisticated 3D models exhibit an enormous capacity in matching small-scale observations. Success in fitting all the data leads to a "best fitting" model, and from a "best fitting" model we can learn more about the mechanisms of plate boundary weakening.

The second half of the thesis is about a distinct topic, the ambient noise correlation in northern Los Angeles sedimentary basins. In Chapters 5 and 6, we analyzed two parts of the ambient noise correlation function: the direct arrivals and the spurious arrivals. From the direct arrivals, we extracted Empirical Green's function and established a shear wave velocity model for the northern LA basins. We also developed a technique to identify the fundamental and higher mode of Rayleigh waves based on particle motion. With the new dense array dataset, we see a lower velocity in the northern LA basins than in previous models, which may explain why previous ground-shaking models underestimated the ground motion in LA region when a large earthquake occurs from San Andreas faults. In Chapter 6, we developed a method that maps the ambient noise source from the spurious arrivals in correlation functions. In north LA basins, the inverted noise source distribution shows a correlation with the structures with strong velocity contrast, like basin edge and faults. With this technique, spurious arrivals, a widespread but long-ignored signal, can be used to illuminate more underground structures.

INDEX

T
tables, 13, 71, 92